1-1-1995

The chemical and physical structure of giant molecular cloud cores.

Edwin A. Bergin
University of Massachusetts Amherst

The Chemical and Physical Structure of Giant Molecular Cloud Cores

A Dissertation Presented

by

Edwin A. Bergin

Submitted to the Graduate School of the
University of Massachusetts Amherst in partial fulfillment
of the requirements for the degree of

Doctor of Philosophy

September 1995

Department of Physics and Astronomy

The Chemical and Physical Structure of Giant Molecular Cloud Cores

A Dissertation Presented

by

Edwin A. Bergin

Approved as to style and content by:

Paul F. Goldsmith, Co-Chair

Ronald L. Snell, Co-Chair

William D. Langer, Member

Monroe Rabin, Member

John F. Dubach, Department Head
Department of Physics and Astronomy

Acknowlegment

Over the past six years I have really enjoyed my time in Amherst. I imagine some (sister!) would say at times I enjoyed it a little too much and would never leave. Much of this "enjoyment", and many times some hard learning, is due to the many people, both staff and students, at UMass that I have had the pleasure of being associated with. Foremost among these are my two advisors Paul Goldsmith and Ron Snell. From the summer day 5 years ago when I first started working with a research assistantship for SWAS, with the words something like "I don't know anything about radio astronomy and molecules", Paul and Ron have shown tremendous patience and guidance while I sat and learned everything I could about molecular astrophysics.

I would like to thank Paul for being a great advisor from the start. I have learned to greatly appreciate his exhaustive knowledge and perspective on how to approach problems. I believe that a large measure of my success has been due to his guidance. On the personal level Paul and Sheryl have been great friends and I have enjoyed their company and conversation both on this side of the Atlantic and on the other side in Italia. Grazie di tutto!

Ron has also been a great source of knowledge and guidance. I think that one of Ron's great qualities is his ability to talk about anything with little notice. Many times I remember walking into his office with "can I ask you a stupid question"; thanks for providing answers Ron. I would also like to thank Ron and Karen for their kindness and friendship on many occasions, and Ron for putting a light hearted attitude into almost any discussion.

The other member of my committee who I feel also deserves alot of credit is Bill Langer. Five years ago I started working on my chemical model with only 17 species

and 40 reactions. I now have over 300 species and 3000 reactions and I could not have done it without Bill's help. I certainly hope that kind of progress is achievable in the future! Bill has also been a good friend, anytime I have gone out to Los Angeles I have both enjoyed myself and learned quite a bit. Thanks Bill. I have always felt that with a committee composed of Paul, Ron, and Bill that one cannot do any better.

I also wish to thank Hans Ungerechts, Bill Irvine, and Pete Schloerb for helping me at various stages and for providing many useful ideas. There are many others whose friendship and help at various times is deeply appreciated, Zak for his help with C and postscript (and for many walks around the pond), Doug for his help in any number of areas, John Carpenter for helping me with wip and various other things. Sally, Denise, Barb, and Pam have also been incredibly efficient and have provided a dose of sanity throughout the insane existence of graduate school. Thanks to Nimesh and Preethi for many useful discussions about science.

One the personal side I am grateful to Mark, Susan, Mike, Murali, Lori, Pat, James, and I can't forget Louma (for many reasons) for being really great friends. You all made the past six years a good and bearable experience. There are many many others who I have spent fewer years with but deserve mention Meg, Jess, Jeff, TJ, and Nance to name a few. I also have to mention my friends for life from PA: Matt and Lina (you're the best), Mark, Ellen, Pat, Joe, Rich, and Johnny M, who have all made grade school, high school, college, and graduate school worthwhile. Given my current state I can't help but bring up the good conversation and expensive dinners in the North End with Mark, Susan, John, Jess, and Ingrid. Thanks for helping me learn about Italian wines! One person deserves special notice for being a wonderful person to spend as much time as I can with and for providing immense amounts of support over the past two plus years since I met her, thanks Ingrid. I hope I can repay you in your next three years at Penn. I should probably express

my gratitude to her for making sure that I will never have to go out and "buy" an animal, since I will already have more than I can imagine.

Last, but not least, I have to thank the ones who made all this possible: my parents. Mom and Dad from the start you let me go my own way but provided all the support and help whenever I needed it. I just plain could not have done this without you. My sister Cindy and brother Tom have also been a source of support and laughter. I wish you both the very best whenever or wherever you go. Given the closeness of my extended family I have to thank my aunts, uncles, and cousins for their support throughout the years. Finally this work is dedicated in memory of Msgr. Peter J. Cruise and Mary Agnes Bergin, two people who I wish could have seen me finish.

Abstract

The Chemical and Physical Structure of Giant Molecular Cloud Cores

September 1995

Edwin A. Bergin, B.S., Villanova University

Ph.D., University of Massachusetts Amherst

Directed by: Professors Paul F. Goldsmith

& Ronald L. Snell

We present the results of a study of the emission from 33 molecular transitions in the GMC cores Orion A, M17, and Cepheus A. We have mapped the emission over a $4' \times 12'$ area in Orion, and a $4' \times 5'$ area in M17 and Cepheus A. We have used these observations to probe the physical and chemical structure within each core.

To derive the temperature we have used the $J = 6 \rightarrow 5$ (K = 0,1,2) transitions of CH_3C_2H and the $J = 1 \rightarrow 0$ transition of ^{12}CO. A comparison of temperatures obtained from the two thermometers in Orion and M17 show significant differences, which we propose are the result of a line of sight temperature gradient. Densities were determined through a multitransitional study of HC_3N. The density structure within each core is similar, showing no evidence of large scale variations, with values typically $n(H_2) \sim 10^6$ cm^{-3}.

The temperatures and densities determined directly from CH_3C_2H and HC_3N were used to derive abundances for 12 species in six positions in Orion A, and two positions in M17 and Cepheus A. Although abundance differences exist, in general, chemical abundances are found to be similar both within and among GMC cores. We have constructed a chemical model of GMC cores, accounting for variations with A_V, to compare with measured abundances. This model was found to be unable

to reproduce the abundances of many molecules for any particular time. Both the inclusion of clumps and variations in the gas-phase C/O ratio within the model were examined to obtain between agreement with observations.

We found that the inclusion of clumps into the chemical model can reproduce the observed abundances of C^+ and C. However, due to the greater weight placed on the photon dominated region in smaller clumps, clumps have a detrimental effect on reproducing the abundances of other species. Models with a range of C/O ratios were also compared to the abundances measured in each cloud. Good agreement between model and observations was found for early times ($t \sim 10^5$ yr) and for $C/O \sim 0.8$.

Table of Contents

List of Tables

List of Figures

Chapter 1

Introduction

Giant molecular cloud (GMC) cores are regions of high density and column density, located within more diffuse extended clouds, that are often associated with massive star formation. Current evidence indicates that these cores are composed of numerous small dense condensations of gas and dust or "clumps" (Mundy et al 1986; Stutzki & Gusten 1990; Tauber and Goldsmith 1993). The study of the chemical and physical conditions in the dense cores therefore probes the chemistry and physics of the clumps and provides important clues to the beginnings of star formation. While the links between the physical state (density and temperature) of molecular cores and star formation is the subject of many ongoing studies, the relationship between chemical processes and star formation is less often examined. An example of a possible link between chemistry and the formation of stars is through the processes of ambi-polar diffusion which depends on the ionization fraction in the cloud (McKee 1989).

In addition to understanding the formation of stars, the knowledge of chemical processes is also necessary in order to physically interpret molecular observations of the ISM. Such basic quantities as the masses of clouds and densities, which are determined from observations of molecular emission lines, often require *apriori* knowledge of molecular abundances. The link between chemical abundances and the physical state of molecular clouds is complex; for example, a drop in the gas phase abundances of an important coolant, such as H_2O (Goldsmith & Langer 1978) will alter the thermal balance of the cloud, raising the gas temperature, and possibly affecting the formation of cores and stars. Thus the physical evolution of molecular clouds is closely intertwined with their chemical evolution.

Dense cores in molecular clouds are diverse environments, and the chemical processes occurring within these regions are dependent on many variables in addition to strictly chemical interactions. Variations in such parameters as density, temperature, degree of ionization, or even the actual age of the cloud can drive molecular compositions in different directions. Of particular interest is the effect of star formation on the chemistry of the surrounding material. High temperatures induced by the radiation from the newly formed stars can open up new reaction pathways as well as warming up grain mantles possibly releasing molecules frozen on the grain surfaces. Systematic studies of the chemistry in star-forming regions are lacking. Chemical analyses of a large number of species have been limited to a single position in a few sources such as OMC-1 or TMC-1. To what extent these regions are representative of other molecular clouds or even other positions within the same cloud is an open question (van Dishoeck *et al.*, 1991). Indeed, studies of star-forming regions with a small set of different molecular tracers show significant abundance gradients and morphological differences within one source. Examples are L134N (Swade, 1989 a,b; Swade and Schloerb 1992); NGC 2071 (Zhou *et al.*, 1990; Goldsmith *et al.*, 1992); and Sgr B2 (Vogel *et al.*, 1987; Goldsmith *et al.*, 1987). An understanding of the chemical and physical processes that underly the observed abundance gradients and morphological differences is critical since the inferred cloud structure may be quite different depending on which tracer is being used (Goldsmith, 1991).

Previous studies of star forming regions have been limited to either analyzing a small number of molecules over a large spatial extent in a source (such as the study of NGC 2071 by Goldsmith et al 1992) or unbiased searched of the millimeter wave spectrum in typically one or two positions in a source (such as the 70-150 GHz survey of Sgr B2 by Cummins et al 1986 and the surveys of Orion KL by Blake et al 1987 and Sutton et al 1995). Thus even though abundances are

predicted by chemical models to vary depending on numerous factors little observational data are available to test these models.

In this thesis we extend and improve upon previous efforts by presenting a combined study of the chemical and physical structure of three dense giant cloud cores: Orion A, M 17, and Cepheus A. We present observations of 26 different molecular transitions (13 molecules and 7 isotopic variants) in these sources using the Five College Radio Astronomy Observatory (FCRAO) 14m telescope equipped with a 15-element focal plane array. The sources in Orion, M 17, and Cepheus are all dense cores in close proximity to newly formed stars. The maps of the 26 transitions cover large regions in each source and consist of hundreds of individual spectra; the maps extend over both the known star forming sites as well as more quiescent material. By examining the abundance gradients and variations in each source in a large number of species we are able to examine the effects of star formation on the surrounding material as well as the evolution of regions which are relatively unaffected by forming stars. In addition to studying possible abundance variations the determination of abundances for a large number of molecules will allow for greater constraints to be placed on chemical models.

In the following sections we introduce the various aspects of the thesis, which also includes the development and use of a theoretical chemical model. In Section 1.1 we present and discuss the molecular transitions observed for this study and their importance in limiting chemical processes and physical conditions. In Section 1.2 we briefly introduce each source, discussing the principle star forming sites and any previous chemical results. Section 1.3 introduces the theoretical chemical model, which includes >300 species coupled through >3000 reactions. Section 1.4 outlines the overall method and goals.

1.1 Chemical Survey of GMC Cores

1.1.1 Molecular Transitions

Table 1.1 lists the molecular transitions observed for this survey, the table includes the frequency, upper state energy, and an estimate of the critical density for each transition. This lists includes some of the traditional tracers of column density ($C^{18}O$), density ($C^{34}S$), and temperature (^{12}CO) as well as key molecules that can be used as diagnostics of chemical processes. In modeling the gas phase chemistry of molecular clouds, observations of ions are important, since dominant reactions are thought to involve ions and neutral molecules. We have observed two molecular ions HCO^+ and N_2H^+ and will use these species to constrain the abundance of ions. The simple radicals CN and C_2H react without barriers with some neutral species as well as with ions and hence play an active role in the gas phase chemistry. Observations of the abundances of the simple carbon- and nitrogen-bearing species HCN and HNC are also important for gas phase chemical models and the ratio of these species is correlated with the kinetic temperature (Goldsmith et al., 1986).

The sulfur bearing molecules SO, and SO_2 have enhanced abundances near high mass star-forming regions where high temperature chemistry or grain mantle evaporation are thought to be important processes (Prasad et al., 1987). Solid methanol (CH_3OH) has been identified on grain mantles (Grim et al., 1991; Allamandola et al 1992), and the abundant gas-phase methanol observed near the embedded sources in Orion could arise from evaporation of grain mantles (Blake et al 1987). Therefore CH_3OH may prove to be important in delimiting grain processes.

To determine molecular abundances the observed molecular line intensities must be converted into column densities, which enables a comparison with theoretical predictions. Therefore we must determine if the molecular emission we

Table 1.1. Molecular Line Parameters for GMC Survey

Species	Transition	ν (GHz)	E_u (K)	n_{cr} (cm^{-3})
CO	$J = 1 \rightarrow 0$	115.271203	5.53	1×10^3
^{13}CO	$J = 1 \rightarrow 0$	110.201370	5.29	1×10^3
$C^{18}O$	$J = 1 \rightarrow 0$	109.782182	5.27	1×10^3
CS	$J = 2 \rightarrow 1$	97.981011	7.05	3×10^5
$C^{34}S$	$J = 2 \rightarrow 1$	96.412962	6.94	3×10^5
HCO^+	$J = 1 \rightarrow 0$	89.188523	4.28	3×10^5
$H^{13}CO^+$	$J = 1 \rightarrow 0$	86.754329	4.16	3×10^5
N_2H^+	$J = 1 \rightarrow 0$			
	$F = 1 \rightarrow 1$	93.17195	4.47	2×10^5
	$F = 2 \rightarrow 1$	93.17375	4.47	
	$F = 0 \rightarrow 1$	93.17631	4.47	
CN	$N = 1 \rightarrow 0$			
	$J = 3/2 \rightarrow 1/2$			
	$F = 3/2 \rightarrow 1/2$	113.488140	5.45	10^{5-6}
	$F = 5/2 \rightarrow 3/2$	113.490982	5.45	
C_2H	$N = 1 \rightarrow 0$			
	$J = 1/2 \rightarrow 1/2$			
	$F = 1 \rightarrow 1$	87.402004	4.20	
	$F = 0 \rightarrow 1$	87.407165	4.20	
SO	$J_K = 3_2 \rightarrow 2_1$	99.299875	9.20	10^5
SO	$J_K = 2_3 \rightarrow 1_2$	109.252134	21.1	
SO	$J_K = 4_5 \rightarrow 4_4$	100.029627	38.6	
^{34}SO	$J_K = 3_2 \rightarrow 2_1$	97.715390	9.20	10^5
HCN	$J = 1 \rightarrow 0$	88.631847	4.25	2×10^6
$H^{13}CN$	$J = 1 \rightarrow 0$	86.340184	4.14	2×10^6
HNC	$J = 1 \rightarrow 0$	90.663593	4.35	2×10^6
$HN^{13}C$	$J = 1 \rightarrow 0$	87.090851	4.18	2×10^6
CH_3OH	$J_K = 2_{-1} \rightarrow 1_{-1}E$	96.73939	11.6	7×10^3
CH_3OH	$J_K = 2_0 \rightarrow 1_0A^+$	96.74142	6.97	
CH_3OH	$J_K = 2_0 \rightarrow 1_0E$	96.74458	19.15	
CH_3OH	$J_K = 2_1 \rightarrow 1_1E$	96.75551	27.07	
C_3H_2	$J_{K^+,K^-} = 2_{1,2} \rightarrow 1_{0,1}$	85.33890	4.1	
HC_3N	$J = 10 \rightarrow 9$	90.979023	24.0	7×10^5
HC_3N	$J = 12 \rightarrow 11$	109.173634	34.1	1×10^6
CH_3C_2H	$J_K = 6_0 \rightarrow 5_0$	102.547983	17.2	2×10^4
CH_3C_2H	$J_K = 6_1 \rightarrow 5_1$	102.546023	24.2	
CH_3C_2H	$J_K = 6_2 \rightarrow 5_2$	102.540143	45.2	
SO_2	$J_{K^+,K^-} = 3_{1,3} \rightarrow 2_{0,2}$	104.02942	8	

are observing is tracing the entire column density along the line of sight, i.e. whether the emission is optically thin. In practice this involves observing rare isotopes of the same species or using hyperfine line ratios to obtain estimates of the line optical depth. Table 1.1 shows that for many species we have observed isotopic variants and for other species (eg. CN, C_2H, N_2H^+) we can use the hyperfine structure to estimate the opacity. Thus for 10 of the species observed we believe the emission is optically thin or can readily correct for the effects of optical depth.

Another important factor in comparing molecular abundances is whether each molecule is tracing the same component along the line of sight. To minimize this concern we have observed only transitions with similar critical densities, $n_{cr} \gtrsim 10^4$ cm^{-3}, and upper state energies, $4 < E_u < 30$ K. The only transitions in Table 1.1 that do not fulfill this requirement are CO and its isotopic variants, and the highest excited transitions of CH_3C_2H and SO. We discuss in Chapter 3 whether the $C^{18}O$ emission is from the same dense layer as other molecules or is possibly arising from a lower density component as well, while the higher transitions of CH_3C_2H are primarily used to determine the temperature. For the transitions meeting these excitation conditions it is likely that emission from each is probing the same region along the line of sight.

1.1.2 Temperature and Density

The observed column densities reflect the population in the upper state of the transition in question, one must therefore make assumptions about the molecular excitation in order to compute the total column density of a species from the observations. Since it is collisions with molecular hydrogen (H_2) that excite the molecular transitions this requires knowledge of density as well as the kinetic temperature. We can determine these parameters using the emission from the symmetric top molecule CH_3C_2H to estimate the gas temperature and the emission from the linear molecule HC_3N to estimate densities.

We derive values, for both density and temperature, in as many positions in each core as is possible. In this fashion we will produce maps of the physical conditions for each cloud. This enables us to examine the physical structure, the dependence of density and temperature with position, in each core. These estimates will then be used to derive accurate molecular abundances and determine whether the emission variations are the result of abundance gradients or solely due to variations in the density or temperature. The temperatures derived from CH_3C_2H are also compared to the temperature determined using CO, allowing a direct determination of whether a single temperature characterizes the lines of sight in these clouds.

1.2 Sources

The three GMC cores studied are each in regions of high mass star formation. In fact, the dense cloud cores are in close proximity to newly formed stars and are receiving UV flux that is a factor of $10^4 - 10^5$ higher than the solar neighborhood radiation field. The enhanced flux will have the effect of dissociating and ionizing molecules as well as warming dust grains. The UV flux also may be keeping some fraction of carbon in atomic form and enhancing ionization of certain species. Regions with these characteristics are called photon dominated regions (PDRs). Below we provide a brief description of each source.

1.2.1 Orion A

The Orion molecular cloud, located at a distance of 480 pc, is the nearest massive star forming region (Genzel et al 1981). The strongest emission in the cloud is in the direction of the Orion A H II region (M42) and is often labeled as the Orion A cloud or OMC-1 core. In the direction of the H II region is a complex of embedded sources (Orion KL/BN) that are significantly influencing the local molecular environment through both high velocity and low velocity outflows. The

strongest infrared source in this region is IRc2, which is presumably the source of the high velocity flows (Genzel and Stutzki 1989). The Orion A H II region, powered by several OB stars (in particular the O6 star θ^1C Ori), is located in front of the cloud on the plane of the sky (Zuckerman 1973).

The lines of sight toward the IRc2 exhibits several velocity components that trace at least three physically distinct regions. The separate components can be distinguished by the characteristics of their velocity profiles, and are denoted the "plateau", "hot core", and the "quiescent ridge". These disparate regions have been shown to have considerable chemical complexity with species such as CH_3OH, HCN, and HC_3N having enhanced abundances in the hot core, while other molecules such as SO are enhanced in the plateau, still other species, C_2H, CN, HNC are observed only in the quiescent ridge component (Blake et al 1987).

The ridge feature is associated with the extended quiescent cloud, which extends $\sim 5'$ north and south of KL/BN, and is relatively unaffected by the star formation in the KL/BN region. Significant differences among the distribution of molecules along the Orion ridge have been known for many years (Turner and Thaddeus 1977; Goldsmith et al 1986a). In particular the molecular ion N_2H^+ and radicals, CN and C_2H, peak $\sim 3'$N of KL/BN. C_2H and N_2H^+ actually have an emission minimum at the star forming sites in sharp contrast to other species such as $C^{18}O$ or CS. The emission variations for the CN and C_2H radicals has been suggested by Greaves et al (1992) to be due to lower temperatures at the "radical-ion" peak, which is $3'$N ($\sim$ 0.4 pc) of the heating sources (Orion A, KL/BN). The area observed for this study is a $4' \times 12'$ region centered on the KL/BN star forming core. We are primarily interested in the chemistry in the extended quiescent ridge component and will examine abundance gradients along the ridge proceeding away from the star forming sites.

1.2.2 M17

The dense core in M17 is located to the southwest of the optical M17 H II region. Since the H II region/molecular cloud interface is seen nearly edge on (Gatley et al 1979; Icke et al 1980) an examination of the effects of an H II region on the structure and evolution of a dense molecular cloud can be readily undertaken. Observations of FIR continuum, atomic fine structure lines (Meixner et al 1992; Stutzki et al 1988), and high-J CO and CS lines (Harris et al 1987; Stutzki et al 1988) have suggested that UV photons penetrate deep into the molecular cloud. These observations provide some of the strongest evidence for clumpy cloud structure.

Although this source has a greater column density than Orion (Goldsmith, Bergin, & Lis 1995), there exists little information on chemical abundances. The area we have mapped in all transitions is a $4' \times 5'$ (120 positions) region that includes the H II region/molecular cloud interface. Although, the M 17 core ($d \sim$ 2.2 kpc) is more distant than Orion, providing much lower spatial resolution, the edge-on geometry should provide an important gauge on the effects of distance from the ionizing source on chemistry. The structure of this source may provide clues to possible chemical differences that could exist along the line of sight in Orion, which has a face-on geometry.

1.2.3 Cepheus A

Cepheus A is a dense condensation in a much larger molecular complex directly to the south of the Cepheus OB3 stellar association (Sargent 1977). Maps of CO emission at high and low resolution (Hayashi, Hasegawa, & Kaifu 1988; Rodriguez, Ho, & Moran 1980) reveal an energetic bipolar outflow which is oriented east-west. At the centroid of the outflow a cluster of deeply embedded ultracompact H II regions has been found (Beichmann, Becklin, & Wynn-Williams

1979; Simon & Joyce 1983; Hughes & Wouterlout 1984). These sources, labeled as HW 1-7 (Hughes & Wouterlout 1984), form a Y with one chain of H II regions extending northeast-southwest, and the other pointing east-southwest (Staude & Elsasser 1993).

Little chemical information exists for the Cepheus A core. HCN (Weliachew et al 1985), NH_3 (Ho et al 1982; Gusten, Chini, & Neckel 1984, Torrelles et al 1986), and CS (Hayashi, Kaifu, & Hasegawa 1986; Moriarty-Schieven et al 1991) have been observed, but these observations have tended to be directed to studying the relationship between the dense gas and the outflow evident in the CO emission. The outflow does not appear to have directly altered the abundances of NH_3, CS, and HCN and these molecules are suggested to be probing pre-existing condensations of gas surrounding the high-velocity flow (Staude & Elsasser 1993).

The region we have mapped is a $4' \times 5'$ region centered on the compact radio continuum source HW-2. Given the characteristics of this source we will examine whether the outflow, which is extended over several arc-minutes at low velocities (Hayashi et al 1988), affects the chemistry of the core. In addition the comparison of the physical conditions and chemical abundances of this core with Orion and M 17 allows for a direct examination of the similarities and differences in the processes that are ongoing in GMC cores.

1.3 Chemical Model

In order to make the maximum use of this data set we have developed a time dependent chemical model. The chemical reaction network for gas-phase reactions consists of the major formation pathways for carbon-, oxygen-, nitrogen-, and sulfur-bearing molecules, encompassing all the species in the survey. Because the chemical model is applied to dense cores that are exposed to enhanced UV flux the model treats the effects of cloud depth on the chemistry accounting for the

photodissociation and photoionization of atomic and molecular species, including a treatment of CO self-shielding.

We will also be able to use the densities and temperatures derived from the observations as inputs for the chemical models. This direct coupling of observations and theory has not been attempted previously and may provide further information on the chemical processes that are prevalent in GMC cores.

1.4 Goals of Thesis

We have discussed the importance of understanding chemical and physical evolution in star forming regions. We have outlined a project that will use observations in conjunction with models of the physical and chemical properties of molecular clouds to further our understanding of the evolution occurring in these dense regions. Below we outline the goals of this thesis:

1. **GMC Survey** - Observations of 26 molecular transitions of 14 species and isotopic variants are presented for 3 giant molecular cloud cores in Orion A, M 17, and Cepheus A. By mapping a large number of molecules over a large spatial region in each source we will be able to improve constraints on the chemistry and examine variations in abundance from near star forming sites to more quiescent material. To date there has been no systematic chemical survey of cores that includes both the extended quiescent regions as well as the regions near the star-forming sites.

2. **Physical Structure**

   We use the symmetric top molecule CH_3C_2H to determine the temperature of the dense gas and the high-dipole moment molecule HC_3N to derive the density of molecular hydrogen. These observations enable a detailed examination to be made of the physical state of these clouds and provide critical information on the conditions for molecular excitation.

3. **Chemical Structure**

We utilize the temperature and density determinations to estimate total column densities, which are converted to relative abundances. The determination of abundances for many positions in each cloud allows for a comparison to be made of abundances *both within a given cloud and among the three cores.* Thus we will be able to examine whether each core (and possibly each position) is chemically unique or whether the cores are chemically homogeneous.

4. **Combination of Theory and Data**

The final aspect of this work is a comparison of the relative abundances to the results of a theoretical chemical model. The modeling will attempt to address two key questions. First, we will examine whether a pure gas-phase model is able to reproduce the observed abundances. Second we examine whether the abundance variations are related to changes in the physical conditions, such as density, temperature, or strength of the ultraviolet radiation. If the gas-phase chemistry provides an inadequate match to the data, then we will examine whether grain surface reactions could play an active or supporting role in the chemical interactions.

Chapter 2

Temperature Structure in GMC Cores

2.1 Introduction

As mentioned earlier, knowledge of the gas temperature is required in order to determine accurate molecular abundances. In this chapter we will examine two different methods of measuring the temperature in molecular clouds and ask the following question: which is more appropriate for the dense gas containing most of the molecules included in our study?

One common method to determine gas temperatures in molecular clouds is observation of the emission from ^{12}CO. The carbon monoxide molecule is very abundant and, due to its low dipole moment, readily excited. These factors underly the widespread use of this molecular species to map molecular clouds. The low lying rotational transitions of CO are expected to be optically thick and with the effects of radiative trapping, the excitation temperature is expected to be close to the gas temperature, even at densities as low as 10^{2-3} cm^{-3}. Thus, if the CO emission is assumed to be in local thermodynamic equilibrium (LTE) and optically thick, the observed antenna temperature can be directly used to estimate the gas temperature. However, since the lines are optically thick, there has always been a concern whether the CO emission is indicative of the gas temperature for the entire volume of the cloud or only at its surface (e.g. Castets et al. 1990).

It is not surprising that molecular clouds may not be characterized by a single temperature along a given line of sight. It is, after all, a balance of the heating and cooling processes that determines the gas temperature, and these processes certainly vary as function of position or depth into a cloud. Observations of CO

self-absorption in low-J transitions provide direct evidence of line of sight excitation gradients and possible temperature gradients (Phillips et al. 1981). Other observations of ^{12}CO line ratios in Orion by Tauber and Goldsmith (1990) attribute the increasing intensity of CO lines with increasing J to temperature gradients within the source. Another way to look for these effects is to use two separate molecules as thermometers, preferably molecules that require quite different excitation conditions and whose emission arises from different regions along a single line of sight. We examine this question by using the symmetric top molecule methyl acetylene (CH_3C_2H) as a thermometer in the dense regions of molecular cloud cores and compare these results with the traditional method employing the CO $J = 1 \rightarrow 0$ antenna temperature as a temperature probe, which plausibly traces the temperature in the lower density regimes.

The symmetric top molecules CH_3C_2H, NH_3, and CH_3CN have been used as probes of kinetic temperature in molecular clouds because it is possible to separate the effects of density and temperature in their excitation (Ho & Townes 1983; Walmsley & Ungerechts 1983; Batrla et al. 1983; Cummins et al. 1983; Loren & Mundy 1984; Sutton et al. 1986; Churchwell & Hollis 1984; Askne et al. 1984; Kuiper et al. 1984). For these symmetric top molecules the line frequencies are nearly the same for transitions having different values of J but which are in different K ladders. Therefore lines which arise from widely different energy levels have nearly the same frequency and thus can be observed simultaneously, reducing uncertainties due to telescope calibration. The molecules are effective thermometers because the separate K ladders are connected only through collisions, and the total population in each K ladder is a function only of the kinetic temperature of the gas. Although the populations of a given J-level within a K ladder will depend on the density, the relative populations of the K ladders should be a fairly direct measure of the kinetic temperature.

Askne et al. (1984) examined the use of CH_3C_2H to determine temperatures in molecular clouds via a statistical equilibrium analysis. They have shown that (due to the low dipole moment of methyl acetylene: $\mu = 0.78\ D$) a thermal population distribution should exist under conditions present in the dense cores of molecular clouds. If the CH_3C_2H emission is optically thin, a simple rotation diagram analysis plotting line intensity as a function of the energy of the level above the ground state will give an estimate of the kinetic temperature for $n_{H_2} > 10^4$ cm^{-3}.

In this chapter we re-examine the use of CH_3C_2H as a temperature probe extending upon previous studies in several fashions. We first present the results of a statistical equilibrium analysis using more accurate collision rates computed by Green (1986). We then use these results to analyze the temperature of the dense gas in three dense cloud cores: Orion, M17, and Cepheus A. We have mapped the $J = 6 \rightarrow 5$ ($K = 0, 1, 2$) transitions of CH_3C_2H in each of the sources using the FCRAO 14 m telescope. These observations represent the first attempt to map the distribution of CH_3C_2H emission over a large extent in several sources. In addition we have also mapped the same sources at FCRAO in the CO $J = 1 \rightarrow 0$ transition. A comparison of these two tracers allows a direct determination of whether a single temperature characterizes a given line of sight in these clouds, or to what extent each tracer probes a different region, having a different kinetic temperature.

2.2 Observations

The CH_3C_2H and CO observations were carried out during the 1991 and 1992 observing seasons using the 15-element QUARRY focal plane array (Erickson et al. 1992) mounted at the Cassegrain focus of the 14 m Five College Radio Astronomy Observatory (FCRAO) telescope. The two spectrometers used were 32 channel filterbanks with resolutions of 250 kHz and 1 MHz, thus providing velocity resolutions of 0.73 km s^{-1} and 2.9 km s^{-1}, respectively for methyl acetylene and 0.65 km s^{-1} and 2.6 km s^{-1} for carbon monoxide. The observed lines and

Table 2.1. Observed Molecular Line Parameters

Species	Transition	ν (GHz)	E_u (K)	Beam Size ($''$)
CO	$1 \rightarrow 0$	115.271	5.5	45
CH_3C_2H	$6 \rightarrow 5$ $(K = 0)$	102.547	17.2	50
CH_3C_2H	$6 \rightarrow 5$ $(K = 1)$	102.546	24.2	50
CH_3C_2H	$6 \rightarrow 5$ $(K = 2)$	102.540	45.1	50

frequencies are listed in Table 2.1. A single reference position was used for each source. The reference positions were examined separately and found to be free of emission. The standard chopper wheel method used for calibrations places all observations on the T_A^* scale. The main beam efficiency η_{MB} then relates T_A^* to the radiation temperature T_R of a uniform source which fills only the main beam of the antenna (Kutner & Ulich 1981). The methyl acetylene observations are uncorrected for antenna efficiency and are presented on the T_A^* scale; since all analysis is done with line ratios the absolute calibration is not important. For the CO observations the strongest emission for all of the sources is confined to a small area $\ll 30'$. There are also velocity gradients which limit the size of the region contributing at any specific velocity. Hence we believe the correction by the main beam efficiency is more appropriate for these observations than the forward scattering and spillover efficiency. The CO observations are therefore presented on the T_R ($T_R = T_A^*/\eta_{MB}$) scale using a main beam efficiency of 0.45. Since the total bandwidth of the 250 kHz filter banks is only 8 MHz only the CH_3C_2H $K = 0$ and $K = 1$ lines appear within a given spectra. Observations of the weaker $K = 2$ component were alternated with those of $K = 0$, 1 and then combined to form a single 64 channel spectrum. The beamwidth of the antenna at the observed frequencies are shown in Table 2.1. All of the maps were sampled on a $25''$ grid.

2.2.1 Orion

The Orion Molecular Cloud, the nearest massive star forming region, is located at a distance of 480 pc (Genzel et al. 1981). The region covered by this survey is

the central portion of the southern cloud associated with Orion A (M42) and the BN/KL cluster. The region mapped is $4.5' \times 12'$ in extent centered on the embedded Orion BN/KL complex at $\alpha(1950) = 5^h32^m46.8^s$, $\delta(1950) = -5°24'28''$.

Figure 2.1a-d show the CH_3C_2H and CO data in the form of contour maps. Figures 2.1a-c present the integrated intensity for each of the CH_3C_2H $J = 6 \rightarrow 5$ K-components observed and Figure 2.1d shows the CO peak T_R map for comparison. The distribution of methyl acetylene emission shown in Figure 2.1a clearly defines the dense molecular ridge. The strongest emission is found slightly northward of the BN/KL region and a secondary peak is found at the position of the southern star forming region: Orion S (Ziurys et al. 1981; Keene, Hildebrand, & Whitcomb 1982). The $K = 1$ and $K = 2$ maps show similar morphology, although the emission becomes progressively weaker. The velocity gradient present around BN/KL results in peak velocities that vary from ~ 8 km s^{-1} south of the source to ~ 10 km s^{-1} north of the source (Genzel & Stutzki 1989) is evident in the CH_3C_2H emission. The CH_3C_2H linewidths near BN/KL and Orion S are $3 - 4$ km s^{-1}, however further north and south along the ridge the linewidths decrease to $\simeq 2$ km s^{-1}, a value that is characteristic of the quiescent ridge. Both the velocity gradient and the linewidth variations are similar to the observations of the $J = 5 \rightarrow 4$ transition by Wang, Wouterloot, & Wilson (1993). In general the largest linewidths are associated with the known regions of star formation.

We are primarily interested in using CH_3C_2H as a tracer of the temperature structure in dense regions. Since this represents one of the first efforts to map the distribution of methyl acetylene emission it is worthwhile to compare its extent with that of more standard tracers of the dense gas. A simple comparison between the morphology of the methyl acetylene emission with that of other species may provide an insight into possible chemical differences. Ungerechts et al. (1992) present these data along with the maps of other species including the optically

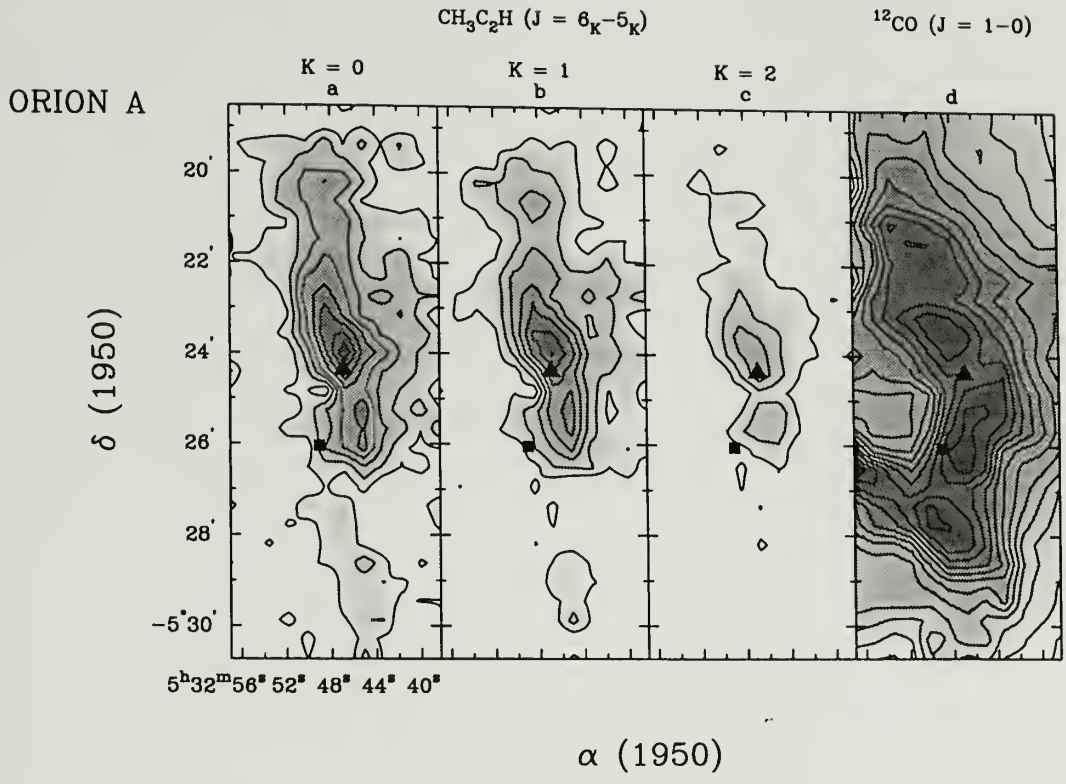

Figure 2.1. (a-c) Distribution of the CH_3C_2H $J = 6 \rightarrow 5$ ($K = 0, 1, 2$) integrated intensity in Orion. The lowest contour and the spacing are 0.2 K km s^{-1} for all maps. The filled triangle indicates the position of the embedded BN/KL cluster and the filled square denotes the position of $\theta^1 C$ Ori. (d) Map of the CO peak T_R, the highest contour is 90 K and the spacing is 5 K. CH_3C_2H integrated intensities are presented on the T_A^* scale while the CO temperatures are on the T_R scale.

thin isotopes of CO and CS (in particular $C^{18}O$ and $C^{34}S$). They show that the morphology of the CH_3C_2H emission is similar to that of the standard tracers of column density and space density. While this simplistic analysis does not discriminate between differing excitation conditions and possible abundance variations, it does provide some evidence that CH_3C_2H does not have a peculiar chemistry and can be used in a general sense as a probe of the dense material.

A discussion of the subtleties in the CO emission seen in Figure 2.1d is beyond the scope of this study; several studies have been done on the large scale distribution of this ubiquitous tracer (see Schloerb, Goldsmith, & Scoville 1982; Genzel & Stutzki 1989; Heyer et al. 1992 and references therein). It should be noted that the CO map shown here has a local minimum in the emission towards Orion KL; this is due to the limitations of the 32 channel 250 kHz filterbanks which have insufficient bandwidth to include the broad line wings observed in the CO emission towards KL. Only the few positions near BN/KL that contain the high velocity emission are affected and the other features seen in the map are in agreement with previous studies. It does appear, however, that there is no local maximum of radiation temperature in ^{12}CO at the position of BN/KL.

2.2.2 M17

We have mapped the central $4' \times 5'$ of the M17 giant molecular cloud including the H II region/molecular cloud interface. Figure 2.2a-c presents the contour maps of the methyl acetylene $J = 6 \rightarrow 5$ ($K = 0, 1, 2$) integrated intensity and Figure 2.2d the CO $J = 1 \rightarrow 0$ peak T_R.

Radio continuum observations by Felli, Churchwell, & Massi (1984) show that the extended H II region is located in the northeast corner of the contour maps where the CH_3C_2H and CO emission sharply decreases. The emission is strongly peaked near the H II region/molecular cloud interface in all 3 K-components of CH_3C_2H. To the south and west the $K = 0$ and $K = 1$ components show weak,

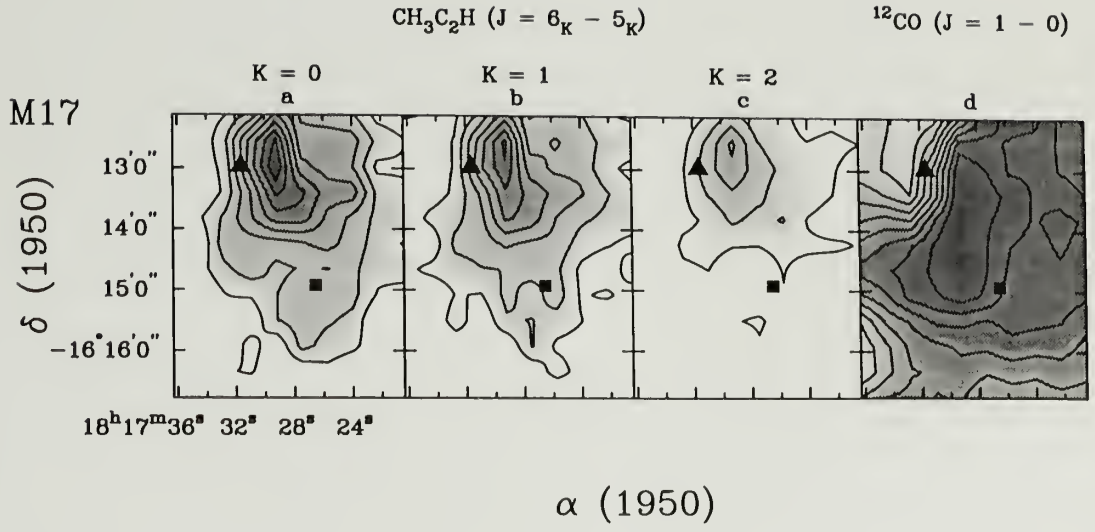

Figure 2.2. (a-c) Distribution of the CH_3C_2H $J = 6 \rightarrow 5$ ($K = 0, 1, 2$) integrated intensity in M17. The lowest contour and the spacing are 0.4 K km s^{-1} for all maps. The filled triangle indicates the position of the ultracompact source UC1 and the filled square denotes the position the embedded KW object. (d) Map of the CO peak T_R, the highest contour is 60 K and the spacing is 5 K. CH_3C_2H integrated intensities are presented on the T_A^* scale while the CO temperatures are on the T_R scale.

extended emission. The maximum integrated intensity is found $\sim 30''$ away from the position of the ultra-compact H II region UC1 (Felli, Churchwell, & Massi 1984) and is spatially coincident with the "northern condensation" peak seen in the emission of the $C^{18}O$ $J = 2 \rightarrow 1$ and $C^{34}S$ $J = 3 \rightarrow 2$ lines observed by Stutzki & Güsten (1990). This is in contrast to the $C^{18}O$ $J = 1 \rightarrow 0$ and $C^{34}S$ $J = 2 \rightarrow 1$ emission in which the maxima is observed further to the south away from the interface (Ungerechts et al. 1993b). The emission from another symmetric top molecule, NH_3 (Güsten & Fiebig 1988), correlates with the lower rotational transitions of $C^{18}O$ and CS and not with the methyl acetylene emission. The differences between the CH_3C_2H and NH_3 emission may be due to chemical differences between these species across the interface and into the cloud. The CH_3C_2H linewidths do not show any systematic variation with position and are typically ~ 3.5 km s^{-1}.

2.2.3 Cepheus A

We have mapped a $4' \times 5'$ area of the dense core region of Cepheus A in the CH_3C_2H $J = 6 \rightarrow 5$ ($K = 0, 1, 2$) and CO $J = 1 \rightarrow 0$ transitions. The center of the map corresponds to the FIR continuum peak at $\alpha(1950) = 22^h54^m19^s$, $\delta(1950) = 61°45'47''$ (Moriarty-Schieven, Snell, & Hughes 1991). Figure 2.3a-d presents the contour maps of the CH_3C_2H $J = 6 \rightarrow 5$ ($K = 0, 1, 2$) integrated intensity and CO $J = 1 \rightarrow 0$ peak T_R.

The CH_3C_2H $K = 0$ emission shown in Figure 2.3a has two peaks located on opposite sides of the FIR source. The $K = 1$ component shows a slightly more compact morphology, while the $K = 2$ emission is very weak and only observed near the embedded sources at the center of the dense core. The typical linewidth of the methyl acetylene emission is ~ 2.5 km s^{-1}. The distribution of ammonia once again is significantly different when compared to that of CH_3C_2H. Single dish observations by Güsten, Chini, & Neckel (1984) show that the NH_3 emission is

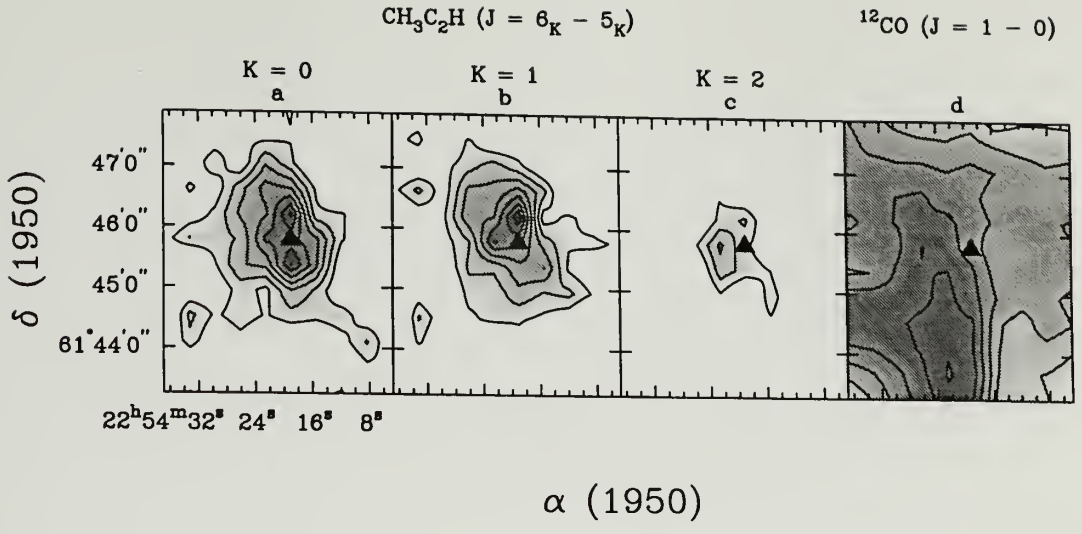

Figure 2.3. (a-c) Distribution of the CH_3C_2H $J = 6 \rightarrow 5$ ($K = 0, 1, 2$) integrated intensity in Cepheus A. The lowest contour and the spacing are 0.2 K km s^{-1} for all maps. The filled triangle denotes the position of the FIR continuum peak. (d) Map of the CO peak T_R, the highest contour is 26 K and the spacing is 2 K. CH_3C_2H integrated intensities are presented on the T_A^* scale while the CO temperatures are on the T_R scale.

more extended to the northeast. There is no evidence of high velocity emission in our CH_3C_2H data.

2.3 Analysis

2.3.1 CH_3C_2H

2.3.1.1 Molecular Theory

Two of the principal moments of inertia of a symmetric top molecule are equal. As discussed in detail by Townes & Schawlow (1955), the molecular rotational energy levels are described by two quantum numbers: J the total angular momentum, and K the component of J along the axis of symmetry. The energy levels are then grouped according to the K quantum number into separate ladders.

Since K is a component of J, the lowest energy level in each K ladder is that with $J = K$.

As CH_3C_2H is a prolate symmetric top, the energy for each J level is shifted to higher energy with increasing K. The frequencies for radiative transitions are weakly dependent on K due to centrifugal distortion, and higher K transitions occur at successively lower frequencies. An additional effect of the symmetry is that there is no dipole moment perpendicular to the symmetry axis. As a consequence, radiative transitions cannot change the angular momentum along the symmetry axis. Hence there are no radiative transitions across K ladders; only dipole transitions between adjacent J levels within a given K ladder are permitted. Because of this selection rule the K ladders are connected *only* through collisions and the population of one K ladder relative to another should reflect a thermal distribution at the kinetic temperature.

The effects of nuclear spin divide the molecule into two distinct species depending on the relative orientation of the spins of the hydrogen atoms (labeled A and E symmetry states). Rotational levels with $K = 3n$ (n = 0, 1, 2...) belong to the A species and levels with $K = 3n + 1, 3n + 2$ (n = 0, 1, 2...) belong to the E species. This is similar to the ortho and para forms of H_2 and NH_3 with the A species of methyl acetylene designated as *ortho* and the E species as *para*. The two species are independent since both collisional and radiative transitions between them are forbidden. The formation process is unlikely to discriminate between these two species and therefore we assume equal abundances.

2.3.1.2 Rotation Diagram

With the assumption of optically thin emission the integrated intensity is proportional to the column density in the upper state of the observed transition. The excitation temperature is defined by the Boltzmann factor relating the populations of the upper and the lower states:

$$\frac{N_u}{N_l} = \frac{g_u}{g_l} exp\left(-\frac{\Delta E_{ul}}{kT_{ex}}\right) \tag{2.1}$$

where N_u, N_l, g_u, and g_l are the column densities and degeneracies of the upper and lower states respectively, ΔE_{ul} is the energy difference, and T_{ex} is the excitation temperature. All pairs of levels by definition can be characterized by eqn. 2.1 but in general T_{ex} will be different for different pairs of levels. However, if the populations of all levels are in LTE, the total column density is related to a single temperature via the following relation:

$$\frac{3k \int T_A \delta v}{8\pi^3 \nu S \mu^2} = \frac{N_{tot}}{Z} exp\left(-\frac{E_u}{kT}\right), \tag{2.2}$$

where S and ν are the line strength and frequency of a transition, E_u the upper state energy, μ is the dipole moment, N_{tot} is the total column density and Z the partition function, $\int T_A \delta v$ is the integrated intensity for a given transition. For a more complete derivation of equation 2.2 see e.g. Cummins et al. (1986).

When observing more than one transition the "rotation diagram" is formed by taking the logarithm of eqn. 2.2 and plotting $log(\int T_A \delta v / S\nu)$ against the energy of the upper state of each transition. In general any transition can be included in this plot. For this work we plot only same J transitions of the different K ladders. Since the abscissa is proportional to the column density in the upper state if the K ladders are excited similarly then the plot represents the relative populations of the K ladders. Due to the molecular characteristics discussed in the previous section, it is very easy to bring the relative populations of various K levels for a given J into LTE. We then expect a straight line when the populations are plotted. The slope in this case is proportional to the inverse of the "rotational temperature" (T_{rot}) of the K-levels for a given J which should equal the gas kinetic temperature.

2.3.1.3 Statistical Equilibrium Calculations

Statistical equilibrium models of the excitation of CH_3C_2H $J = 6 \rightarrow 5$ ($K = 0$, 1, 2) transitions were calculated to verify that the "rotational temperature" discussed in the previous section is a measure of the kinetic temperature. We used the large velocity gradient(LVG) approximation in our calculations to include the effects of trapping; however, since the emission from CH_3C_2H is optically thin (Wang et al. 1993), trapping is not very important and our results are insensitive to the details of our assumptions about the gas velocity field. Three parameters were varied in the calculation: density (n_{H_2}), kinetic temperature (T_K), and total CH_3C_2H column density per unit line width ($N_{A+E}/\Delta v$) where $N_{A+E} \equiv N_A + N_E$. The column density parameter was therefore fixed at a value that ensured the optical depth for each transition was small. The value chosen was $N_{A+E}/\Delta v = 1.0 \times 10^{14}$ cm^{-2} / km s^{-1} (with $N_A/N_E = 1$). The background temperature was fixed at a value of 2.7 K. We have used theoretical collisional rates calculated by Green (1986) for CH_3CN-H_2 (further discussion presented by Sutton et al. 1986). These collision rates are different than those used by Askne et al (1984) since the rates coupling the separate K ladders (i.e. collisional transitions with $\Delta K \neq 0$) are smaller. For rates used, typical values for $\Delta K = 0$ are $\sim 10^{-10}$ cm^3 s^{-1} and for $\Delta K \neq 0$ are $\sim 10^{-13}$ cm^3 s^{-1}. Molecular constants were taken from Bauer *et al.* (1979).

We have used these models to predict the intensities of the $J = 6 \rightarrow 5$, $K = 0$, 1, and 2 transitions as a function of T_K and n_{H_2}. These theoretical results were then used to form a rotational diagram to deduce the gas kinetic temperature. Figure 2.4a shows theoretical rotation diagrams for various values of the molecular hydrogen density and $T_K = 30$ K. The derived rotational temperature and the excitation temperatures (as defined by equation 1) for each transition are shown in Figure 2.4b. These figures demonstrate the unique ability of symmetric tops: to

separate the effects of density and temperature on excitation. While the excitation temperature for any single transition is thermalized only for $n_{H_2} > 10^5$ cm^{-3}, *the derived rotational temperature provides good measure, to within 10%, of* T_K *for all values of* n_{H_2}. Figure 2.5 shows T_{rot} as a function of both density and temperature. For $T_K < 50$ K the rotational temperature closely approximates the kinetic temperature and is fairly insensitive to the molecular hydrogen density. For temperatures greater than 50 K using the $J = 6 \rightarrow 5$ ($K = 0, 1, 2$) transitions will somewhat underestimate T_K for most values of n_{H_2}.

The above analysis was limited to $K = 0$, 1, and 2 since our data include only these lines. Ideally one would like to observe all K components of a single J transition in order to increase the range in energy above the ground state and therefore increase the sensitivity to higher temperatures. Therefore we have examined the use of rotation diagrams for the full range of K transitions. Figure 2.6 shows the rotational temperature as a function of density for $T_K = 30$ K with all the components of the $J = 6 \rightarrow 5$ transition included. The behavior of T_{rot} becomes somewhat more sensitive to density than in the previous case and T_{rot} overestimates the true temperature for densities below 10^4 cm^{-3}. At low densities a particular J-level is overpopulated in the high K levels because the higher ladders have fewer rotational levels over which the population is distributed. Thus, at low density, the gas temperature is better estimated by fitting only the first three K transitions. However for values of $n_{H_2} > 10^3$ cm^{-3} the rotational temperature using all K transitions for a given J of CH_3C_2H yields a good estimate of the kinetic temperature.

2.3.1.4 Temperature Determinations

To determine rotational temperatures from the observations of methyl acetylene, we fit the spectra using a multi-component Gaussian fit that fixes the separation between each component to determine the integrated intensities and

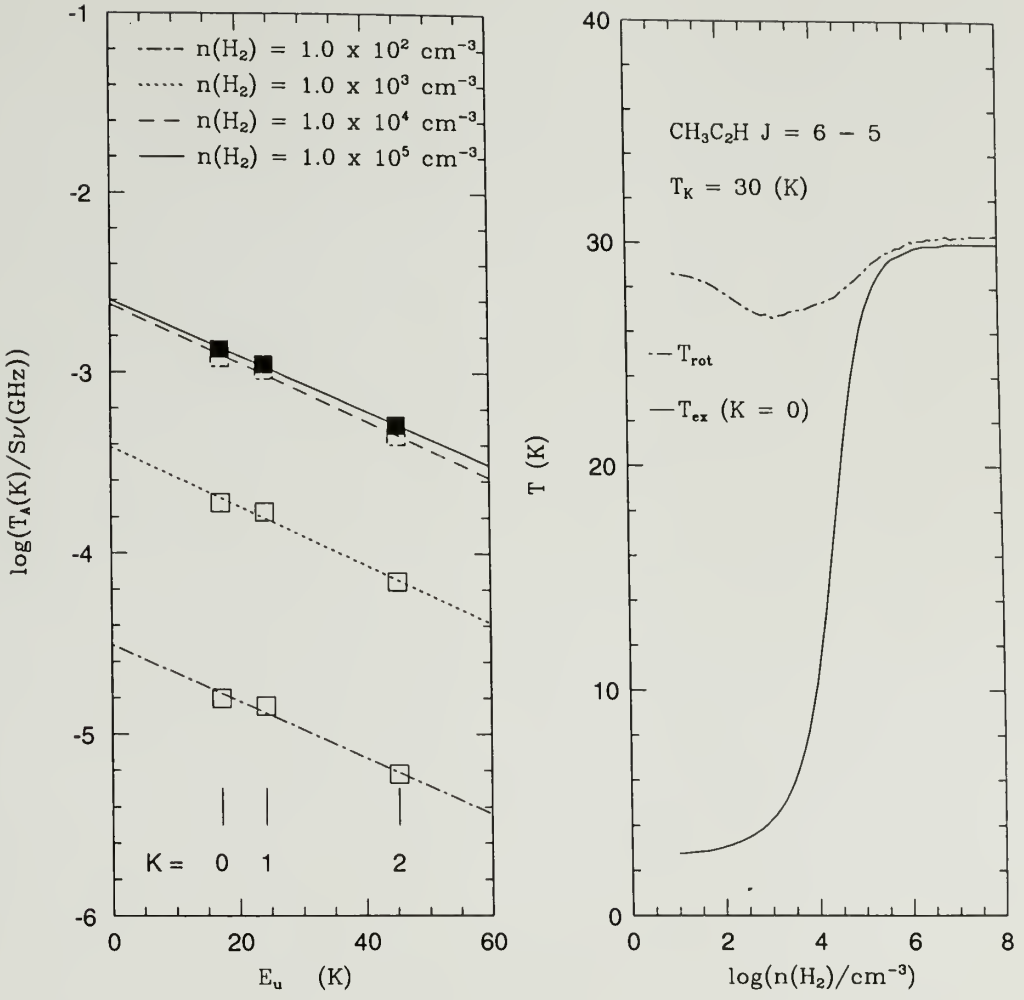

Figure 2.4. (a) Theoretical rotation diagrams for various values of n_{H_2} at $T_k = 30$ K. The lines shown in the rotation diagram are the best fit straight lines. (b) CH_3C_2H $J = 6 \rightarrow 5$ ($K = 0, 1, 2$) excitation temperatures (T_{ex}) and rotational temperature (T_{rot}) from statistical equilibrium calculations are shown as a function of n_{H_2} for $T_k = 30$ K. The $K = 1$ and $K = 2$ excitation temperatures are equal to the K = 0 for all values of n_{H_2}

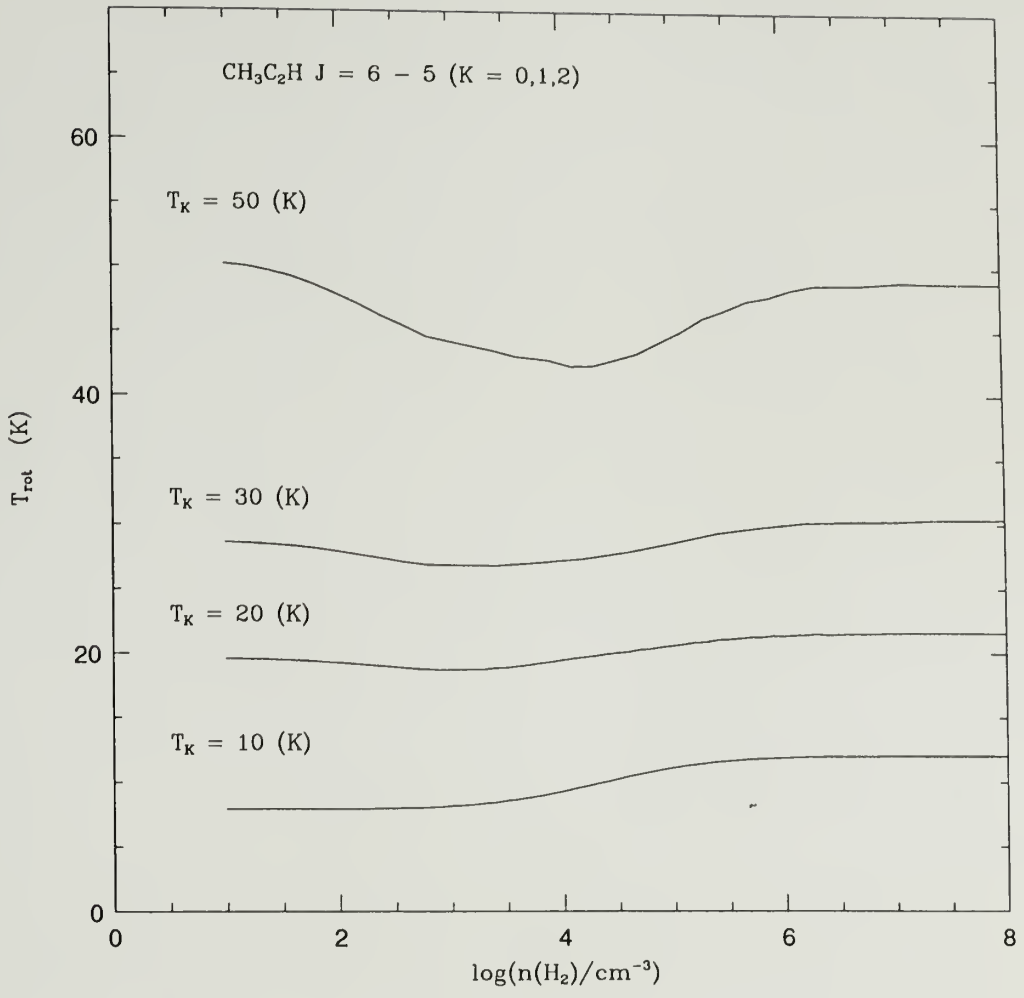

Figure 2.5. CH_3C_2H $J = 6 \rightarrow 5$ $(K = 0, 1, 2)$ rotational temperature as a function of temperature and density.

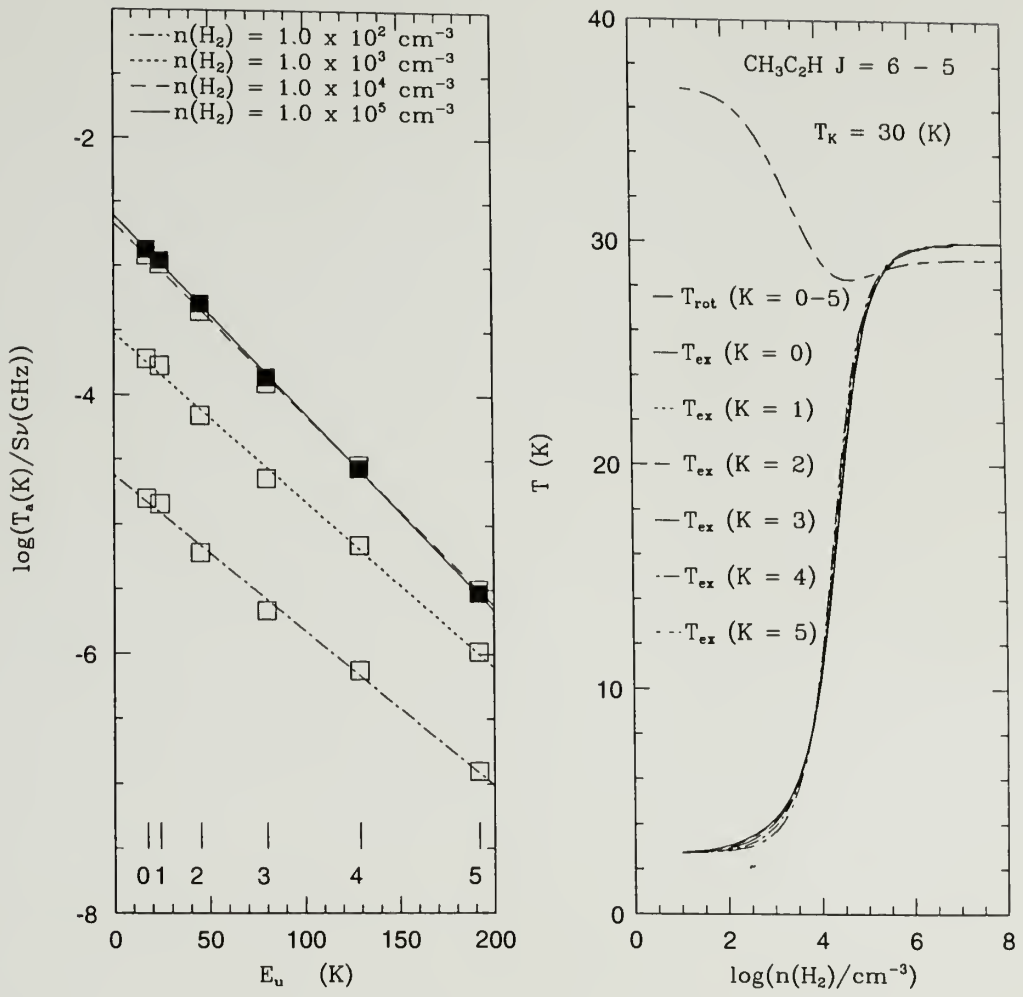

Figure 2.6. (a) Theoretical rotation diagrams for various values of n_{H_2} at $T_k = 30$ K. The lines shown in the rotation diagram are the best fit straight lines. (b) CH_3C_2H $J = 6 \rightarrow 5$ ($K = 0, 1, 2, 3, 4, 5$) excitation temperatures (T_{ex}) and rotational temperature (T_{rot}) from statistical equilibrium calculations are shown as a function of n_{H_2} for $T_k = 30$ K.

associated errors for each K component. The five fitted parameters are then the line width, line center velocity, and the intensity of each of the three K-components. Implicit in this method is the assumption that all three lines originate from the same volume. The rotational temperature is determined by fitting the exponential in eqn 2.2. In order to determine reliable temperatures we calculate rotational temperatures only for positions in which the $K = 0$ and $K = 1$ components have computed integrated intensities that are at least 5σ. This procedure has been carried out for all 3 sources. As an additional constraint, we exclude from discussion all positions in which the uncertainty in the rotational temperature exceeded 15 K in Orion, and 10 K in M17 and Cepheus A.

2.3.2 CO

The CO molecule has a low dipole moment and therefore is easily excited. For the $J = 1 \rightarrow 0$ transition the critical density is only $n_{crit} \sim 10^3$ cm^{-3}. Due to the high abundance the lowest transitions are expected to be optically thick and the effects of radiative trapping will then drive the excitation temperature towards the kinetic temperature of the gas. It is well known (c.f. Snell, 1981) that, due to radiative trapping in the lines of CO which have $\tau \gg 1$, the $J = 1 \rightarrow 0$ transition will be thermalized ($T_{ex} = T_k$) at densities $\leq n_{crit}$. Thus, as long as $n_{H_2} > 10^2$ cm^{-3} the excitation temperature of the $J = 1 \rightarrow 0$ transition is approximately equal to the kinetic temperature. In the following paragraph we derive the expression relating the CO excitation temperature to the observed radiation temperature.

The result of position switched or frequency switched observations is an observed excess intensity which can be expressed as

$$\Delta I_\nu = [B_\nu(T_{ex}) - B_\nu(T_{bg})](1 - exp(-\tau_\nu)) \tag{2.3}$$

where $B_\nu(T)$ is the Planck function at the temperature T, T_{bg} is the temperature of the background radiation, and τ_ν is the optical depth of the transition. The radiation temperature is defined as

$$T_R \equiv \frac{\lambda^2}{2k}\Delta I_\nu \tag{2.4}$$

where λ is the observed wavelength. Combining equations (3) and (4), the radiation temperature can also be given by

$$T_R = \frac{\lambda^2}{2k}[B_\nu(T_{ex}) - B_\nu(T_{bg})](1 - exp(-\tau_\nu)). \tag{2.5}$$

If we assume $\tau_\nu \gg 1$ and $T_{bg} = 2.77$ K the observed excitation temperature, which for the CO $J = 1 \rightarrow 0$ transition is expected to be equal to the kinetic temperature, can be easily solved for, and is

$$T_k = \frac{5.54}{ln\left[\left(\frac{5.54}{T_R+0.87}\right)+1\right]}. \tag{2.6}$$

2.4 Results

2.4.1 Temperature Structure in Orion

The contour map of the CO ($J = 1 \rightarrow 0$) T_R, shown in Figure 2.1d, can essentially be considered a temperature map and therefore should follow the distribution of the heating sources. The temperatures are much higher, with values typically near 80-90 K, near the possible heating sources, BN/KL and the Trapezium stars and decreasing to $\sim$ 60 K away from these luminous sources. The most prominent feature in this temperature map is the U shaped feature in the contour map that surrounds the O6 star θ^1C Ori. This feature is even more pronounced in the [C II] 158 μ m map of the same region by Stacey et al. (1993). This correspondence between the intensity distribution of [C II] and CO indicates that the CO and ionized carbon emission originate in the same gas layer (Stacey et

al. 1993). Since the [C II] arises from the photodissociated gas at the interface between the H II region and the molecular cloud, this is suggestive of the Trapezium stars dominating the heating seen in the CO emission as proposed by Schloerb, Goldsmith, & Scoville (1982) and Padman et al (1985).

Figure 2.7 shows four examples of CH_3C_2H spectra in Orion and the associated rotational diagrams. One of the key assumptions when using the rotational diagram to determine T_{rot} for CH_3C_2H is that the optical depths in each transition are small, otherwise a more detailed excitation analysis would be required. At this point it is worthwhile to examine the validity of this assumption. Density determinations from both CS and HC_3N show that densities $> 10^5$ cm^{-3} are present for most positions along the Orion ridge (Goldsmith et al. 1980; Vanden Bout et al. 1983; Rodriguez-Franco et al. 1991). Since the global distribution of emission of CH_3C_2H and that of CS and HC_3N are similar (Ungerechts et al. 1992), it is likely that the methyl acetylene emission is tracing the same dense layers as CS and HC_3N, and thus the CH_3C_2H transitions are likely to be close to thermalization. All of the spectra in Orion have weak emission with $T_A^* < 0.5$ K in all three components, thus, unless the filling factor is extremely low, the opacity of these lines must be $\ll 1$. Examining the top three spectra in Figure 2.7, we see that data from positions near the northern ion-radical peak, Orion KL, and Orion S are fit well by a single rotational temperature. The last spectra exhibits weak emission and the fit is somewhat poorer, although the temperature is well determined.

As argued in Section 2.3.1.3 the rotational temperature from the $J = 6 \rightarrow 5$ ($K = 0$,1, and 2) transitions is an excellent probe of the kinetic temperature. A map of the gas temperatures in Orion is presented in Figure 2.8 where the rotational temperatures are shown overlaid on the $J = 6 \rightarrow 5$ ($K = 0$) integrated intensity map. To a first approximation the gas temperature has a maximum near

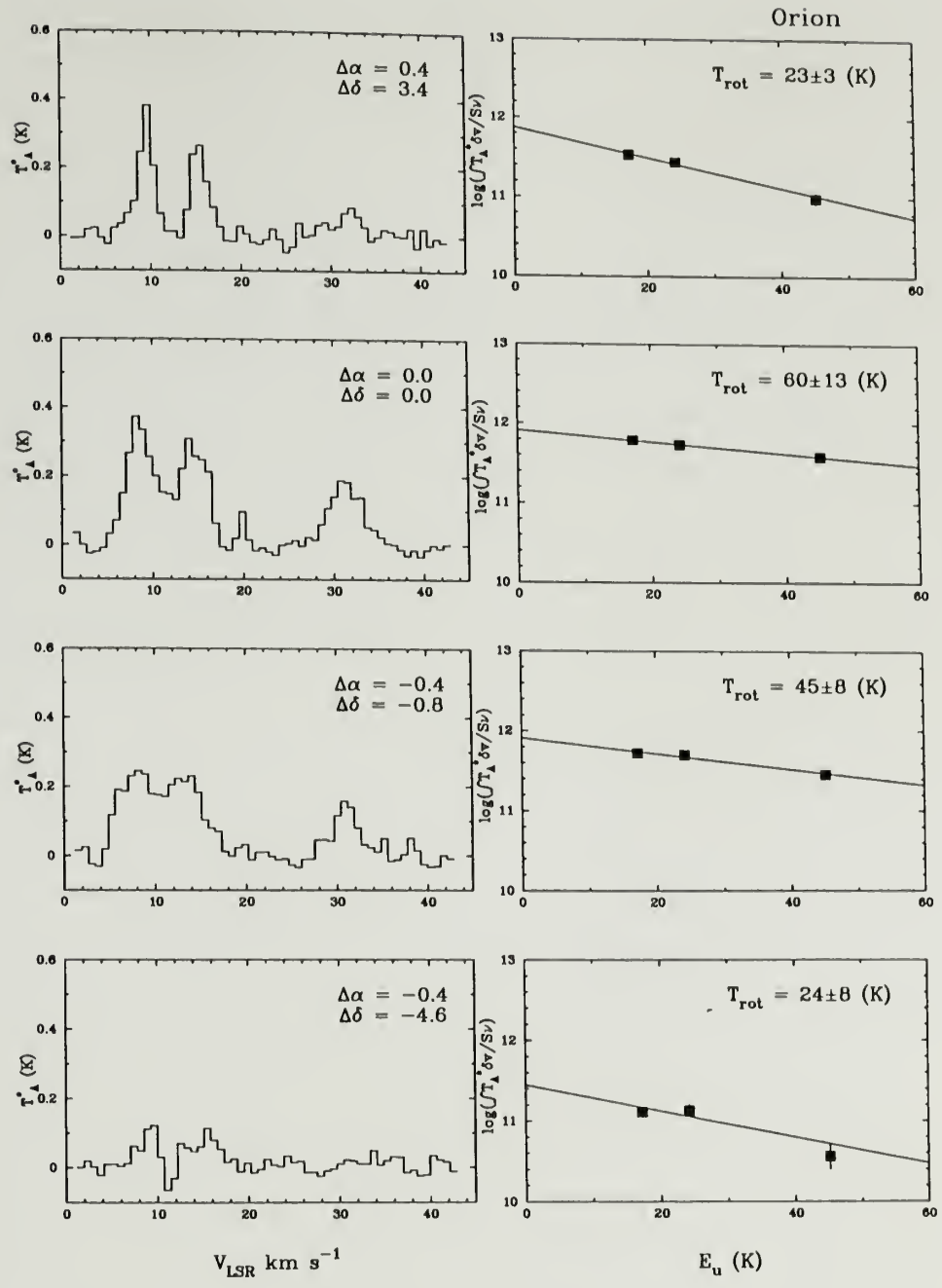

Figure 2.7. Sample CH_3C_2H spectra in Orion shown with rotation diagrams and rotational temperatures. Errorbars for the data points are included, but in many cases they are smaller than the square which denotes the data point.

BN/KL and $\theta^1 C$ of $40 - 60$ K and gradually decreases with distance from these objects. Temperatures as low as $\sim 15 - 25$ K are found far to the south and north of the embedded sources and the Trapezium stars.

Previous determinations of the CH_3C_2H rotational temperature in Orion by Churchwell & Hollis (1984), Goldsmith et al. (1986) and Wang, Wouterloot, & Wilson (1993) show similar gradients in temperature. Our value of the temperature toward Orion KL of 60 ± 13 K is in good agreement with the other temperatures derived from CH_3C_2H. However the improved sensitivity of this study combined with a more extensive map provides the most detailed view to date of the temperature structure in the cloud.

2.4.2 Temperature Structure in M17

The steep gradient in emission seen in the northeast corner of the CO T_R map in Figure 2.2d delineates the H II region/molecular cloud interface. T_R rapidly rises from ~ 15 K near the ultracompact source where the radio continuum emission coincides with the molecular emission to ~ 60 K less than an arc minute away. Away from the interface the temperature slowly falls off. The embedded IR source (Kleinmann & Wright 1973) does not appear as a temperature maximum in this map suggesting that the embedded star does not play a large role in the energetics of the gas sampled by CO.

Figure 2.9 presents two of the CH_3C_2H spectra observed toward M17, one near the HII region/molecular cloud interface region and the other in the quiescent cloud, and their rotational diagrams. Both spectra, from near the interface region and in the center of the cloud show no deviations from a single rotational temperature within the uncertainties. Density determinations also exist for M17 from Snell et al. (1986). This study examined the density distribution using several CS transitions and covered a region slightly smaller than the one mapped here. For all positions examined the densities were $> 10^5$ cm^{-3}. Given these high

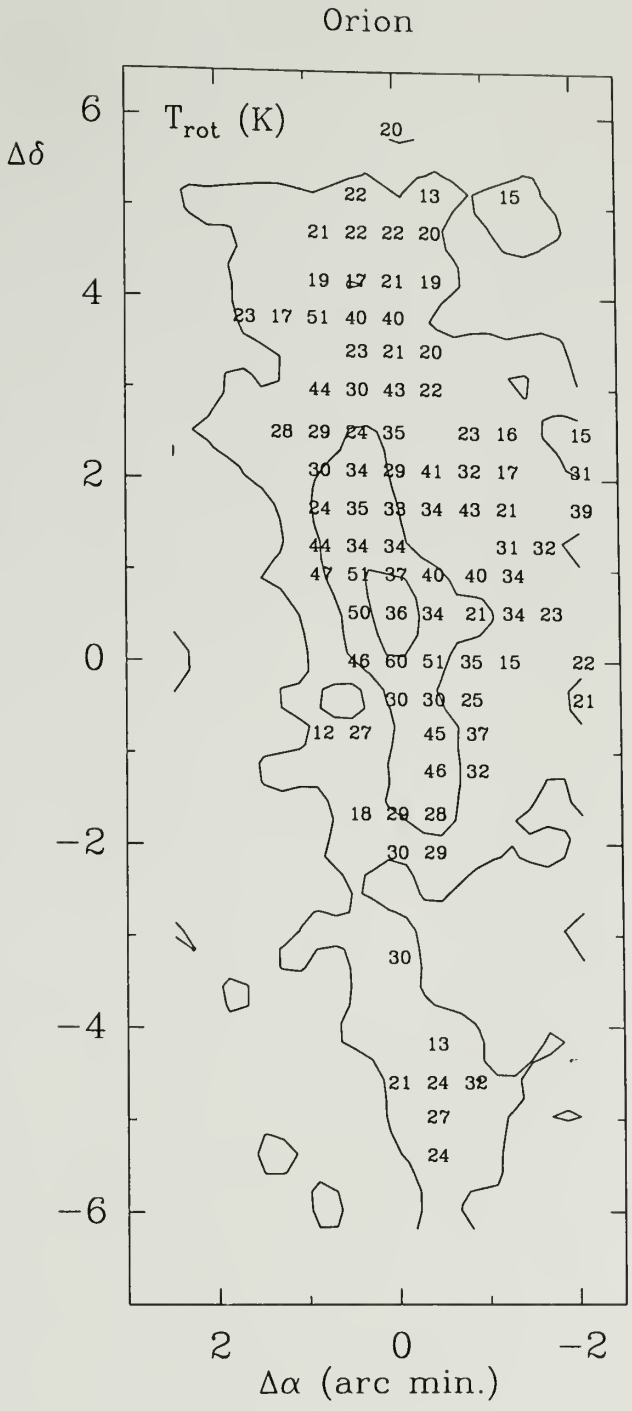

Figure 2.8. A map of the rotational temperatures in Orion. The temperatures are overlaid on the CH_3C_2H $J = 6_0 \rightarrow 5_0$ integrated intensity contours of 0.2, 0.8, and 1.4 K km s^{-1} which are intended as a guide to the morphology of the CH_3C_2H emission.

densities and the observed weak emission seen in Figure 2.9 and Figures 2.2a-c we expect that the CH_3C_2H emission is optically thin.

The gas temperature map in M17 is shown in Figure 2.10 overlaid on the $K = 0$ integrated intensity map. The gas temperature is highest near the H II region/molecular cloud interface and then smoothly decrease with distance. The positions where the gas temperatures are highest correspond to the positions where the radio continuum emission from the H II region is coincident with the molecular emission. The observed CH_3C_2H rotational temperatures decrease away from the ionization front, and are in good agreement with the temperature determinations using NH_3 by Güsten & Fiebig (1988).

2.4.3 Temperature Structure in Cepheus A

The CO peak T_R map in Figure 2.3d shows a relatively featureless morphology, with T_R ranging from 15 K at the edge of the map rising to a broad peak in the south near 28 K. Using this map as a guide to the gas temperature is problematic since the observed CO spectra exhibit obvious self-absorption features. The presence of self absorption makes the determination of a peak temperature quite difficult because the true line profile is unknown. We have used the peak temperature taken directly from the observed spectra and make no corrections for self absorption. Hence the observed temperatures are lower limits to the maximum temperature along the line of sight (Phillips et al. 1981).

Also shown in Figure 2.9 are two CH_3C_2H spectra from Cepheus A. The emission of methyl acetylene from Cepheus A is much weaker than the two previous sources with $T_A^* < 0.2$ K for most positions. The gas temperature distribution in Cepheus A, presented in Figure 2.11, shows the highest gas temperatures $\sim 20 - 30$ K near the center of the map and close to the embedded young stellar objects. In general the outlying positions are much colder with values typically < 20 K. This pattern suggests that the gas heating is dominated by the

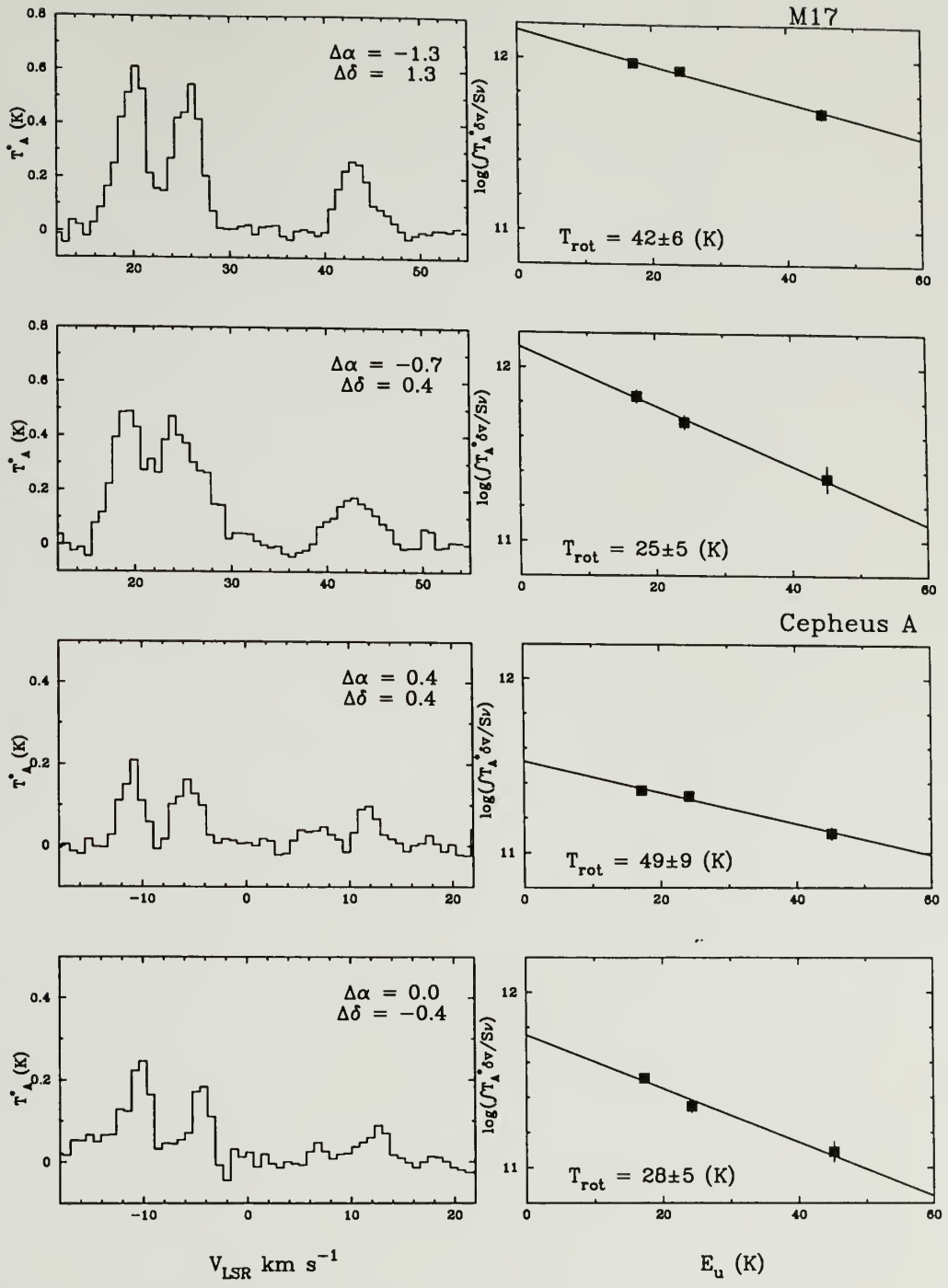

Figure 2.9. Sample CH_3C_2H spectra in M17 and Cepheus A shown with their respective rotational fits.

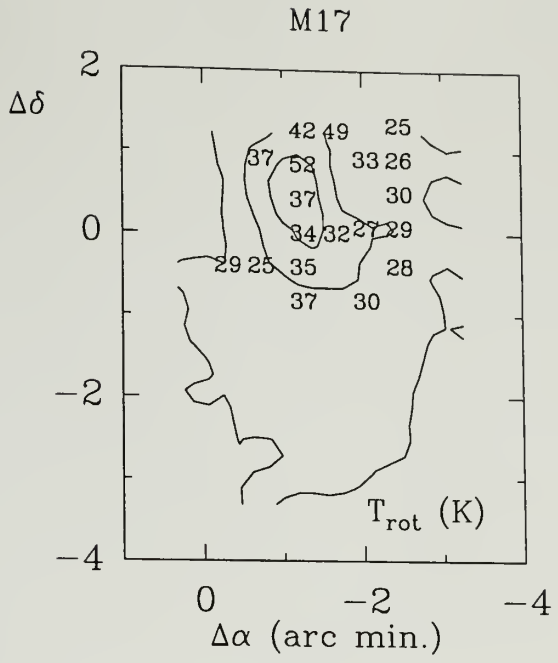

Figure 2.10. A map of the rotational temperatures in M17. The temperatures are overlaid on the CH_3C_2H $J = 6_0 \rightarrow 5_0$ integrated intensity contours of 0.4, 1.6, and 2.8 K km s^{-1} which are intended as a guide to the morphology of the CH_3C_2H emission.

embedded young stars. A similar temperature distribution using ammonia inversion transitions was observed by Güsten, Chini, & Neckel (1984).

2.5 Discussion

2.5.1 Orion

A point by point comparison of the temperature estimates from CO and CH_3C_2H for the Orion ridge is presented in Figure 2.12. In Orion, where we have the greatest number of positions, the contrast between the temperatures inferred from these two thermometers is striking: for all positions, the methyl acetylene rotational temperatures are much less than the temperature from CO.

One obvious explanation for the observed differences is that we are using an incorrect coupling efficiency when we convert the CO antenna temperatures to the

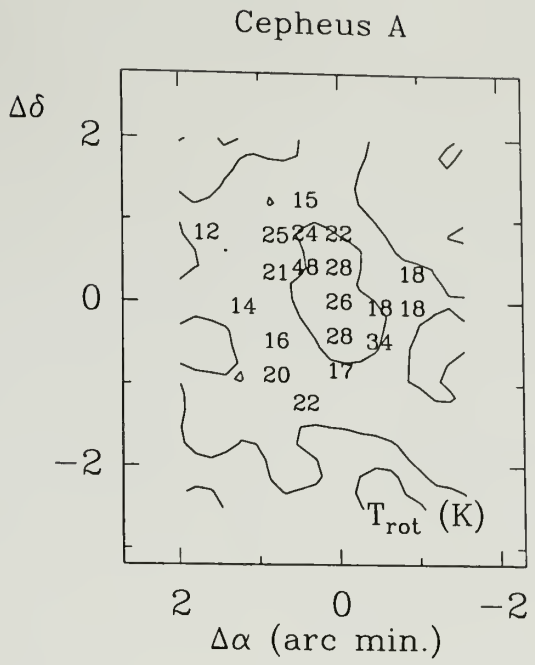

Figure 2.11. Same as Fig. 2.8 for Cepheus A. The contour levels are 0.1 and 0.5 K km s^{-1}.

T_R scale. As stated in section 2 we have assumed the coupling efficiency of the antenna is the main beam efficiency ($\eta_{MB} = 45\%$). If there is significant emission outside the main beam of the antenna then some of the power may be coupled through the error beam and sidelobes of the telescope. However, the error beam of the telescope is large and the sidelobe levels are low. We do not expect this to be a major source of error since the CO emission in Orion is relatively compact and there are velocity gradients which limit the size of any region contributing at a specific velocity.

A plausible explanation for this temperature discrepancy is that methyl acetylene predominately traces a *different* region along the line of sight than does CO. Given other considerations, this result may not be surprising. Observations suggest a density gradient between the layers traced by the CO emission and the layers probed by species with higher critical densities. Density determinations from

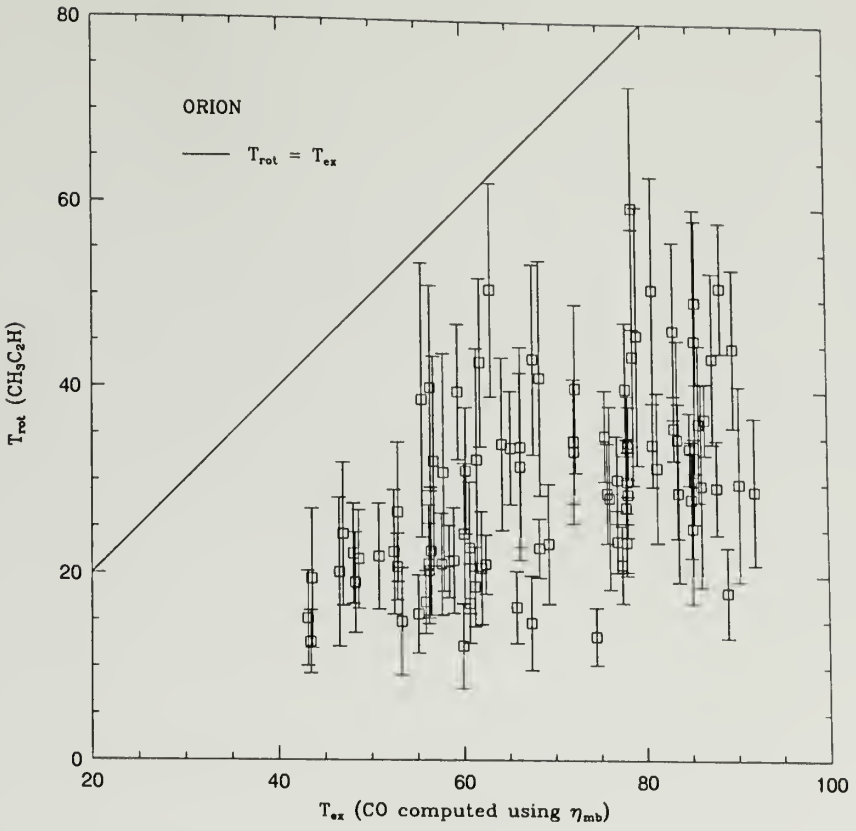

Figure 2.12. Comparison of gas temperature determinations using CH_3C_2H and CO in Orion. The solid line indicates equal temperatures obtained from the two tracers. The units for both axes are K.

the optically thin isotope ^{13}CO (Goldsmith et al. 1982; Castets et al. 1990) exhibit molecular hydrogen densities between 1000 and 6000 cm^{-3} much less then values estimated by the high dipole moment molecules such as CS and HC_3N (Goldsmith et al. 1980; Vanden Bout et al. 1983; Rodriguez-Franco et al. 1991) suggesting that the CO molecule is tracing only the outer low density envelopes of dense cores.

Methyl acetylene has a higher dipole moment than CO and therefore requires higher densities for excitation. Examination of the CH_3C_2H $J = 6 \rightarrow 5$ excitation temperatures from Figure 2.1b shows that densities $\gg 10^3$ cm^{-3} are required to obtain appreciable emission from the $J = 6$ levels. The CH_3C_2H emission is also optically thin, sampling the entire line of sight, including the dense cold regions far removed from any heating source. Therefore the rotational temperature is a

complicated weighting of the temperature along the line of sight presumably dominated by gas with $n_{H_2} > 10^4$ cm^{-3}. These observations thus support a temperature gradient in Orion between the relatively warmer low density gas, traced by CO, and the cooler high density gas traced by CH_3C_2H.

CH_3C_2H has a higher dipole moment than CO, but CH_3C_2H is much easier to excite than most of the molecules that are used to delineate the dense ridge in Orion. The extended emission observed in Orion from the high dipole moment molecules such as CS, HC_3N, and HCN require densities greater than 10^5 cm^{-3}. It may be questioned whether the CH_3C_2H emission is sampling the same dense regions as these molecules or is perhaps excited in gas of intermediate density. To examine this issue we have compared the centroid of emission and linewidths of methyl acetylene with observations of HC_3N $J = 10 \rightarrow 9$ in Orion observed at the same positions as CH_3C_2H (Ungerechts et al. 1992). HC_3N is an excellent choice for comparison with CH_3C_2H, because both are complex carbon chain molecules and the HC_3N emission is also thought to be optically thin (Vanden Bout et al. 1983), which is not true for CS or HCN. The critical density of the $J = 10 \rightarrow 9$ transition of HC_3N is $> 10^5$ cm^{-3}, and the observed emission is presumably dominated by high density material. If the observed velocity centroids and linewidths of CH_3C_2H and HC_3N agree then it is reasonable to assume that the lines originate from the same volume of gas.

Figure 2.13 shows the CO and CH_3C_2H linewidths plotted against the HC_3N linewidth. In general, the observed CH_3C_2H and HC_3N linewidths are in good agreement, while the CO lines are almost a factor of 2 broader. In Figure 2.14 we show a histogram of the differences in the line center velocities of CO $J = 1 \rightarrow 0$ and CH_3C_2H $J = 6 \rightarrow 5$ $(K = 0)$ transitions relative to the velocities of HC_3N $J = 10 \rightarrow 9$. The unshaded histogram, which corresponds to $V(CH_3C_2H) - V(HC_3N)$, is narrow and centered about zero implying that the velocities agree

within the measured uncertainties (1 channel $\sim$ 0.8 km s^{-1}). The shaded part of the histogram, which corresponds to V(CO) − V(HC_3N), shows that the CO and HC_3N velocities have significant differences and that on average the HC_3N velocities are higher than the CO velocities. Given the differences in line width and line center velocity of CO compared to HC_3N it is unlikely the emission from these two species arises from the same gas. Thus, we believe that the CO lines are formed in the low density gas while the emission from CH_3C_2H and HC_3N is predominantly from the dense gas deeper in the cloud.

The temperature gradient from the low density to high density gas can be accounted for by the CO emission originating on the surface of the clouds, excited by the ultraviolet emission from the H II region. This assertion is also supported by the correspondence in the intensity distribution of CO and ionized carbon (see section 4.1). An additional study by Tauber & Goldsmith (1990) examined the CO $J = 3 \rightarrow 2$ and $J = 1 \rightarrow 0$ line ratio in the Orion cloud. They found that the CO line ratio implied the existence of a temperature gradient throughout the region. These authors argue that given the current evidence for clumpy structure in Orion (c.f. Mundy et al. 1986; Stacey et al. 1993) these gradients must exist within the individual clumps. If the heating source were located at the center of the cloud the portions of clumps along the line of sight which are heated would be hidden, since the CO emission from an individual clump is optically thick. Only if the heating source (Orion A) were located on the surface of the cloud would CO exhibit these observed ratios over an extended area.

Due to self shielding, the CO molecule is more chemically robust than CH_3C_2H. At moderate depths ($A_V = 3.0$), the timescale for photodestruction of CO is a factor of 10^5 greater than for methyl acetylene, using a typical CO abundance of $\sim 8 \times 10^{-5}$ (Irvine, Goldsmith & Hjalmarson 1986) and the photodissociation rates given by van Dishoeck & Black 1988 for CO and Roberge

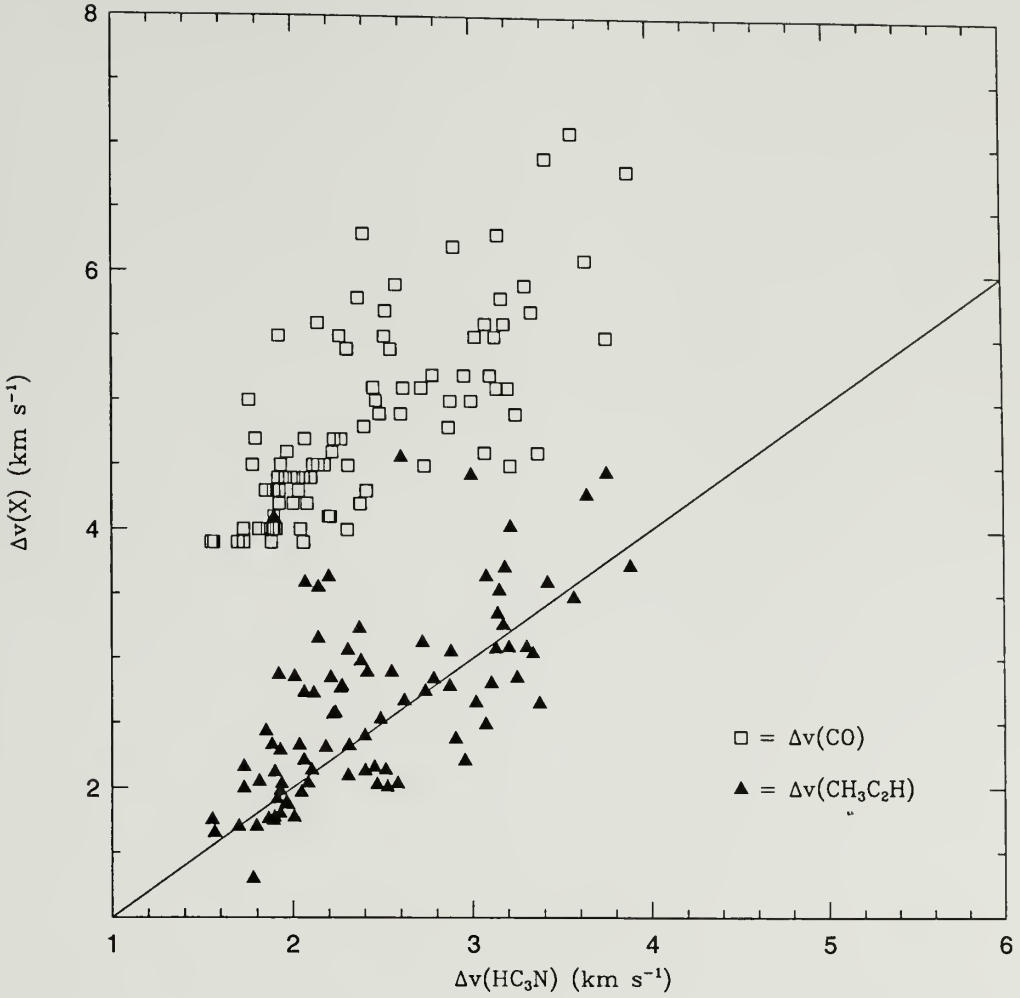

Figure 2.13. Comparison of CO and CH_3C_2H linewidths with those of the high density tracer HC_3N. The solid line denotes linewidths equal to that of HC_3N.

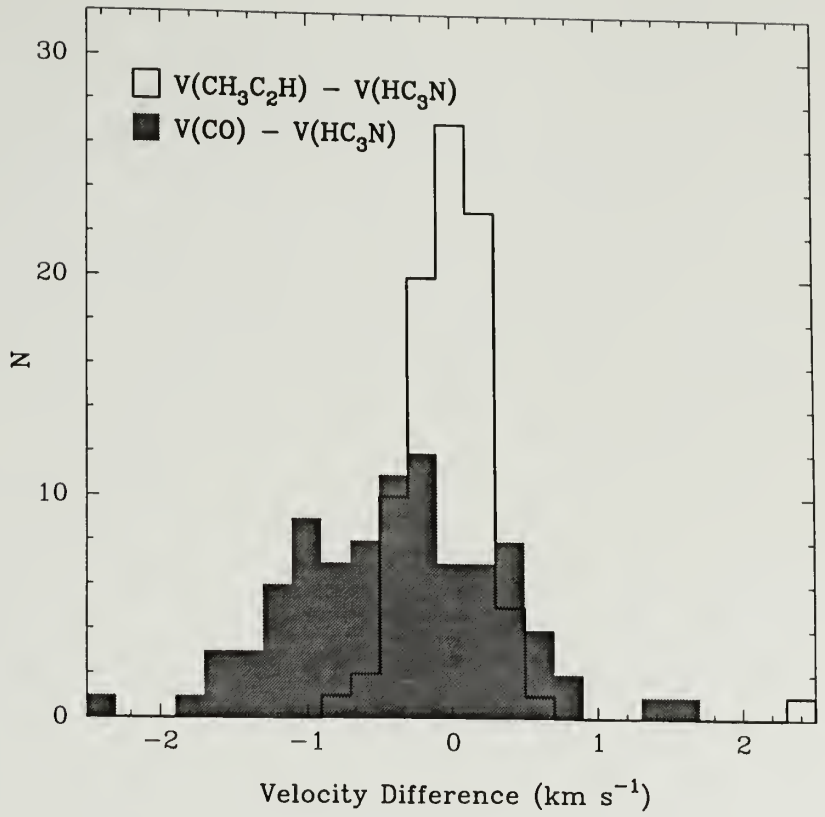

Figure 2.14. Histogram of the line center velocity difference. The vertical axis is the number of positions where a given velocity difference is observed. The shaded region represents V(CO) - V(HC_3N) while the unshaded histogram is V(CH_3C_2H) - V(HC_3N).

et al. 1991 for CH_3C_2H. This difference is independent of the radiation field enhancement since increasing the radiation field will decrease the CO and CH_3C_2H photodissociation timescales in a similar fashion. With such a large difference in destruction timescales and the large enhancement of the UV radiation field in Orion (Tielens & Hollenbach 1985) it is possible that the emission region for the CO $J = 1 \rightarrow 0$ line may actually be chemically distinct from the CH_3C_2H emission zone. Since the CO molecule is strongly self shielding, it is able to survive in a zone with a rich photo-chemistry, while CH_3C_2H requires a reduced radiation field to survive.

The dominant heating mechanism for the gas in these dense regions is expected to be collisional coupling of the gas to dust grains that absorb the radiation from the stars. The dust color temperature observed from the 50μm/100μm flux ratio shows a peak around BN/KL and the Trapezium stars with values $\sim$ 90 K, decreasing to 40-50 K away from the heating sources. The temperature as traced by CH_3C_2H has a similar distribution ranging from 60 K near BN/KL to 20 K several arc-minutes away. Using the heating and cooling expressions at $n_{H_2} = 10^5$ cm^{-3} from Goldsmith and Langer (1978) a dust temperature of 90 K will heat the gas to a temperature of 60 K. Given the high densities along the ridge and the similarities between the gas and dust temperature distributions, the gas and dust in this region appear to be thermally coupled.

However, at low densities where the CO line presumably originates, the density is not high enough to collisionally couple the molecules to the dust grains. To further emphasize this point, a CO excitation temperature of 80 K is observed toward the BN/KL position. Again using the expressions from Goldsmith and Langer (1978) at $n_{H_2} = 10^4$ cm^{-3} the gas temperature, from gas dust coupling, would be 31 K, significantly below the observed value. Therefore the observed excitation temperatures cannot be accounted for even if the CO lines were

originating from a high density layer with warm dust. If the CO lines originate in a low density region a mechanism to directly heat the gas is required.

Heating mechanisms such as the photoelectric effect, and H_2 photodissociation can directly couple the gas to the FUV radiation field from the M42 H II region. The thermal balance of both high density and low density photodissociation regions has been examined by Burton, Hollenbach, & Tielens (1990), Hollenbach, Takahashi, & Tielens (1991), and Meixner and Tielens (1993). These models can reproduce the observed gas temperatures with photoelectric heating as the dominant mechanism, provided the low-J CO emission arises from regions at the cloud surface (where the temperatures range from 50 K to 100 K), as our observations suggest, rather than the colder interior. Another possible heating mechanism, UV pumping of H_2 molecules, will be relatively unimportant at low densities ($\sim 10^3$ cm^{-3}) because the collisional de-excitation, which transfers internal energy to kinetic energy, has a rate which depends on the square of the density (Hollenbach, Takahashi, & Tielens 1991).

2.5.2 M17

The CO and CH_3C_2H temperature comparison for M17 is shown in Figure 2.15. In a majority of the positions $T_{ex}(CO) > T_{rot}(CH_3C_2H)$ in agreement with our observations in Orion. The picture is complicated by five positions where the temperature derived from methyl acetylene is equal to or greater than the temperature derived from CO. These positions are located in the northeastern corner of the map where the H II region overlaps the molecular material. These include the four positions where $T_{rot}(CH_3C_2H)$ is between 37 and 52 K, in addition to one position where $T_{rot} = 29$ K on the eastern edge of the map. The rest of the molecular cloud, away from the interface, shows $T_{rot}(CH_3C_2H) < T_{ex}(CO)$. However, high angular resolution observations of CO $J = 2 \rightarrow 1$ by Stutzki and Güsten (1990) find strong self absorption in many positions *including* the positions

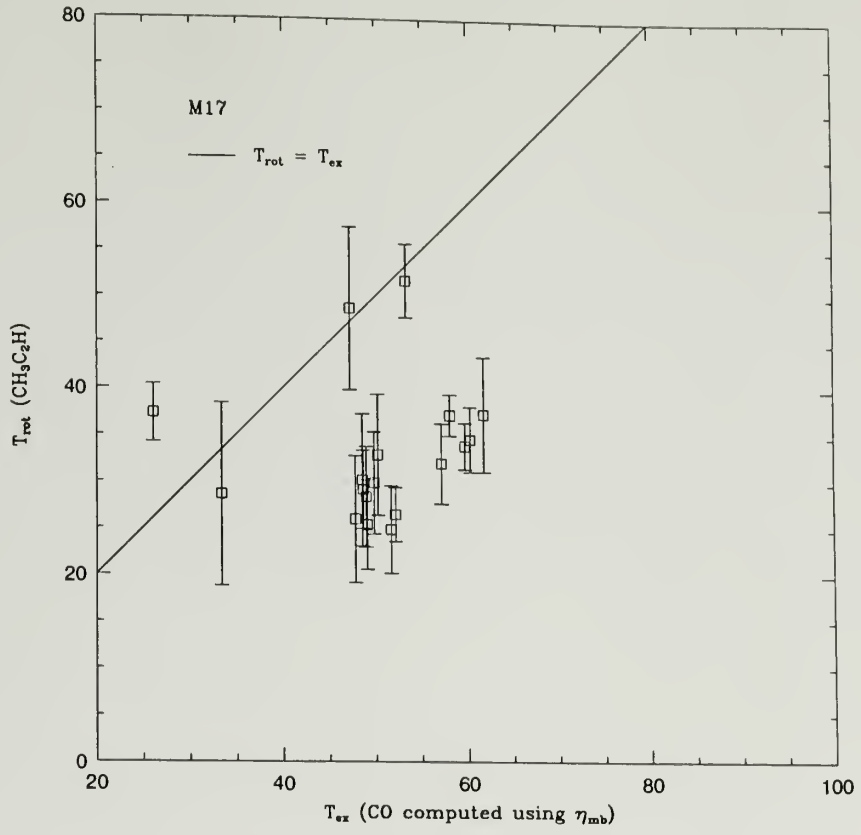

Figure 2.15. Same as Fig. 2.12 for M17.

where we find $T_{rot}(CH_3C_2H) \sim T_{ex}(CO)$. Correcting for this self absorption will lead to higher CO temperatures and the M17 observations are thus similar to those of Orion with temperatures derived with methyl acetylene being below the temperatures derived from CO.

The similarities and differences between the Orion cloud and M17 are notable. The heating in M17, for both high density and low density tracers, is dominated by the M17 OB stellar cluster, as is evidenced by the regular decline in temperature away from the interface region seen in both tracers (see Section 2.4.2). In Orion, the temperatures derived from CH_3C_2H decline with distance from the heating sources but the CO emission exhibits a more complex morphology that is similar to the ionized emission (Stacey et al. 1992). However, the geometry of these sources is quite different, in M17 the ionization front/molecular cloud interface is

perpendicular to the plane of the sky, as compared to in Orion where the H II region appears in front of the molecular cloud. Therefore, it is plausible to expect that the CO emission in M17 will not exhibit all of the complexities seen in Orion but will decrease in a relatively simple fashion with distance from the heating source. Observations of M17 show a similar intensity distribution for the extended [C II] emission and the CO $J = 1 \rightarrow 0$ transition (Stutzki et al. 1988). Similar to Orion the majority of positions in M17 exhibit $T_{rot}(CH_3C_2H) < T_{ex}(CO)$. Since both of these sources have luminous external heating sources, a plausible explanation for these observations is again that the CO and CH_3C_2H emission are tracing different components along the line of sight and that the CO emission arises from surfaces heated by the external H II region.

These observations also require two heating mechanisms for the different density regimes. Temperatures inferred from CO are typically ~ 50 K throughout the M17 cloud core. Provided the dust and gas are thermally coupled this would require dust temperatures in excess of 70 K using the expressions from Goldsmith & Langer (1978) for $n_{H_2} = 10^4$ cm^{-3}. The dust color temperature (inferred from the $50\mu m/100\mu m$ ratio) of ~ 50 K near the interface is too low to heat the gas to the observed temperature. Thus we suggest that the low density gas traced by the CO $J = 1 \rightarrow 0$ transition is directly heated via the photoelectric effect and H_2 photodissociation, as suggested in section 5.1 for Orion. While the colder high density regime traced by methyl acetylene the dust and gas are presumably thermally coupled.

2.5.3 Cepheus A

The temperature comparison in Cepheus A is presented in Table 2.2. Given the geometry of this source compared to Orion or M17 one might expect the dense gas, which is closer to the heating source, to be warmer than the low density material. However, whereas the previous sources show dramatic differences

between the two thermometers, in Cepheus A the two tracers appear to be in good agreement. This result is complicated by self absorption features seen in the CO spectra. If we correct for the self absorption it is possible that T_{ex} (CO) $> T_{rot}(CH_3C_2H)$, but the magnitude of the correction is highly uncertain. The average rotational temperature in Cepheus A is ~ 22 K compared to the average CO excitation temperature of ~ 24 K. A 50% increase in the CO excitation temperature would be required to obtain results similar to the differences observed between CO and CH_3C_2H in M17. Thus, if the correction for self absorption is $<$ 50% the temperature estimates in Cepheus A would still be in better agreement than either Orion or M17.

The temperature distribution observed from the CH_3C_2H rotational temperatures and the self-reversals in the CO profiles suggest that the embedded sources are responsible for the observed emission from the various species. Moriarty-Schieven, Snell, Hughes (1991) determined an average dust temperature for the core of $30 - 40$ K which, with the high densities $> 10^6$ cm^{-3} (Moriarty-Schieven, Snell, & Hughes 1991), is high enough to couple the gas to the dust.

2.6 Summary

We have presented statistical equilibrium calculations for the symmetric top molecule CH_3C_2H. These models show that this molecular species is an excellent tracer of kinetic temperature in molecular clouds. Due to its low dipole moment and low opacity CH_3C_2H should be a powerful tool in probing the temperatures of dense clouds.

We have presented observations of two different molecules used as temperature probes: the CO $J = 1 \rightarrow 0$ transition and the CH_3C_2H $J = 6 \rightarrow 5$ ($K = 0, 1, 2$) transitions in Orion, M17, and Cepheus A. The observations offer a detailed view of the gas temperature in all three sources.

Table 2.2. Temperature Estimates in Cepheus A

$\Delta\alpha$ (′)	$\Delta\delta$ (′)	T_{rot} (K)	CO T_{ex} (K)
0.42	1.24	15.8±4.6	21.6±0.27
1.66	0.83	12.5±5.5	23.1±0.37
0.42	0.83	24.0±3.9	22.4±0.33
−0.00	0.83	22.6±2.9	21.9±0.02
0.79	0.80	25.1±6.9	23.9±0.18
0.42	0.42	48.7±8.5	24.4±0.30
0.00	0.42	28.1±4.0	22.1±0.22
0.79	0.35	21.2±3.6	23.9±0.01
−0.91	0.35	18.8±4.3	21.5±0.18
0.00	0.00	26.1±2.9	22.6±0.34
1.21	−0.07	14.7±3.1	23.1±0.12
−0.50	−0.07	18.2±3.3	19.9±0.31
−0.91	−0.07	18.5±5.2	20.2±0.50
0.00	−0.42	28.4±4.6	24.0±0.22
0.79	−0.48	16.9±4.4	25.4±0.02
−0.50	−0.48	34.1±6.6	20.7±0.03
0.00	−0.84	17.5±4.9	24.3±0.17
0.79	−0.90	20.0±7.8	25.2±0.01
0.42	−1.24	22.2±6.0	26.5±0.16

In Orion the temperature distribution peaks near the BN/KL nebula and the Trapezium and smoothly decreases with distance from these sources. The comparison of the two thermometers shows significant differences, with CO excitation temperatures much larger than those inferred from methyl acetylene. Along the Orion ridge, the CH_3C_2H emission is shown to be tracing the same high density layer as the emission from the high dipole moment molecule, HC_3N. The observed temperature difference between CO and CH_3C_2H reflects differences in the emission regions along the line of sight. The CO lines are formed in the warmer low density foreground gas while the methyl acetylene emission arises from cooler dense gas deeper in the clouds. Observations of another high density thermometer such as CH_3CN would be useful in confirming this trend of temperature decreasing with increasing density.

A similar picture emerges in M17, where temperatures peak near the H II region and fall off with increasing distance. The temperature comparison shows the same pattern as Orion where $T_{ex}(\mathrm{CO}) > T_{rot}(\mathrm{CH_3C_2H})$. These observations support the picture that in Orion and M17, the CO emission arises from surface heating by the luminous external sources. The temperature disparity between low density and high density regions also suggests that different heating mechanisms are required for the two regimes. A direct gas heating mechanism is suggested for the low density medium while the gas in high density regions is indirectly heated by collisions with dust grains.

The temperature distribution in Cepheus A shows a peak near the embedded sources and then a smooth decrease away from the sources. The CO excitation temperatures are close to the $\mathrm{CH_3C_2H}$ rotational temperatures, although the comparison is complicated by the self-absorbed CO line profiles that are observed.

Chapter 3

Density Structure in GMC Cores

3.1 Introduction

Several studies of the density structure in molecular clouds have been performed with reasonable success (Snell et al 1984, Snell et al 1986; Mundy et al 1987, Wang et al 1993). The technique used involves observing several (at least two) transitions of a single molecule, such as CS or H_2CO. These molecular species have high dipole moments and therefore are excited only in the densest regions of molecular clouds. The observations are then interpreted using a non-LTE model, which includes the effects of radiative trapping. The line intensities are fit for the best density and column density assuming a gas temperature.

A less often utilized density probe of GMC cores is the linear molecule cyanoacetylene (HC_3N), although this molecule has several characteristics that make it ideal for this purpose. HC_3N ($\mu = 3.6$ D) has a higher dipole moment than either CS or H_2CO. With a large dipole moment cyanoacetylene is only excited in the densest regions of molecular clouds, typically with $n_{H_2} > 10^4$ cm^{-3}. In addition, HC_3N is a heavy linear molecule with a small molecular rotational constant ($B_0 \simeq 4.5$ GHz) providing numerous lines, sampling different levels of excitation, scattered throughout the millimeter and sub-millimeter spectrum. The low cyanoacetylene abundance suggests that the emission should be optically thin in most cloud cores. This is in contrast to the other common high-density probes, CS and H_2CO, which are more abundant and often suffer from high opacities and thus complicate the excitation analysis, which makes the radiative transfer effects more important. Morris et al (1976), Morris, Snell, & Vanden Bout (1977),

Vanden Bout et al (1983), and Schloerb et al (1983) examined the use of HC_3N as a density probe and found that HC_3N is an excellent tracer of the molecular hydrogen density.

CS, H_2CO, and HC_3N have been used in multitransition studies to derive densities in various molecular cloud cores, including Orion and M 17, and have yielded similar results (Snell et al 1984, Snell et al 1986; Mundy et al 1987, Rodriguez-Franco et al 1993, Wang et al 1993). In general, the densities derived are $> 10^5$ cm^{-3} and there is no evidence of large scale systematic variations. This featureless morphology is observed in spite of the fact that the observed column density in some cases varies by an order of magnitude over the region studied (Snell et al 1984). The lack of correlation between the volume density and the column density can be explained if the emission arises from dense clumps that are smaller than the spatial resolution of the observations, with the filling factor of dense clumps increasing towards the regions of higher column density. Although most of the previous work has been undertaken with moderate resolution of $\sim 1'$, a recent multitransition examination of CS excitation in M 17 by Wang et al (1993) at high resolution ($\sim 20''$) obtained virtually the same flat density structure as previous studies.

In this chapter we present a study of the density structure in molecular cloud cores using observations of 4 transitions of HC_3N. As noted earlier, the HC_3N emission is believed to be optically thin, which permits a simpler excitation analysis requiring no assumptions about radiative effects. Hence a re-examination of the density in these regions with greater signal to noise, over many positions, and with a more robust optically thin tracer is warranted. Previous studies assumed a constant temperature for the cloud as a whole usually based on CO observations, while noting that gradients in temperature could exist. In Chapter 2 we have shown that the temperature structure in these same cloud cores is indeed

Table 3.1. Observed HC_3N Molecular Line Parameters

Transition	ν (GHz)	E_u (K)	Telescope	Beam Size ($''$)
$4 \rightarrow 3$	36.392	4.37	Haystack(37m)	60
$10 \rightarrow 9$	90.979	19.7	FCRAO(14m)	57
$12 \rightarrow 11$	109.173	28.8	FCRAO(14m)	48
$16 \rightarrow 15$	145.560	52.4	NRAO(12m)	45

complex since temperature gradients were found both across the face of the cloud and along the line-of-sight. Knowledge of the temperature of the dense gas is required for density determinations because the effects of density and temperature on excitation are similar and as such it is hard to differentiate between them. Using the temperatures for the dense gas derived in Chapter 2 we are able to derive more accurately the average density along each line of sight.

3.2 Observations

Maps of Orion, M 17, and Cepheus A were obtained on the same grid of positions for each source at three separate observatories in the J = 16 $\rightarrow$ 15 (NRAO), J = 12 $\rightarrow$ 11, J = 10 $\rightarrow$ 9 (FCRAO), and J = 4 $\rightarrow$ 3 (Haystack) transitions of HC_3N. A summary of the observation parameters is provided in Table 3.1. All observations were obtained using position switching with a single reference position for each source. The reference positions were examined and found to be free of emission. A common problem in multitransitional studies is that the observations at separate frequencies leads to differing resolutions at each frequency making direct comparisons difficult to interpret. The combination of telescopes and transitions listed in Table 3.1 provides similar beam sizes for the entire data set allowing direct comparisons to be made.

The calibration of the telescope for each transition puts the data on the T_A^* scale. These data were corrected for the main beam efficiency (η_{MB}), which assumes that the source fills the main beam of the antenna but not the error pattern. This places all observations on the T_R ($T_R = T_A^*/\eta_{MB}$) scale of Kutner

and Ulich (1981). We believe that the correction for the main beam efficiency is appropriate for these observations because the size of the emitting region in each source, while exceeding the beam width of the main beam is still relatively limited ($\ll 10'$). In the following sections we discuss the velocity resolutions and efficiencies for the individual transitions.

3.2.1 HC_3N J = 16 $\rightarrow$ 15

The HC_3N J = 16 $\rightarrow$ 15 data were obtained at the National Radio Astronomy Observatory 12m telescope in October 1993. The dual channel 2mm SiS receiver was utilized and typical system temperatures were between 200 and 250 K. A combination of backends was used with the 100 and 500 kHz filterbanks combined with the hybrid correlator operating with 37.5 MHz bandwidth and 97.7 kHz channel spacing. The 100 kHz data is presented here and was used in the analysis. This provided a velocity resolution of 0.2 km s^{-1} for these data. The main beam efficiency was estimated to be $\eta_{MB} \sim 0.72$ from NRAO measurements.

3.2.2 HC_3N J = 12 $\rightarrow$ 11 and J = 10 $\rightarrow$ 9

The 3mm observations were carried out during the 1991 and 1992 observing seasons using the 15-element focal plane array (Erickson et al 1992) mounted at the Cassegrain focus of the 14 m Five College Radio Astronomy Observatory (FCRAO) telescope. The two spectrometers used contained 32 channels per array element with resolutions of 250 kHz and 1 MHz. We have utilized the 250 kHz data for most of the analysis except for the 9 positions surrounding Orion KL where the 32 channels in the 250 kHz filterbanks did not provide enough bandwidth to establish a good baseline. For these 9 positions the 1 MHz data were substituted for the 250 kHz data. The corresponding velocity resolutions were 0.82 (250 kHz) and 3.82 (1 MHz) km s^{-1} at 90.9 GHz and 0.69 and 2.76 km s^{-1} at

109.2 GHz. The main beam efficiency at FCRAO during the 1991 and 1992 observing seasons was estimated to be $\eta_{MB} \sim 0.45$ at both frequencies.

3.2.3 HC_3N J = 4 → 3

The J = 4 → 3 observations of HC_3N were obtained in November 1993 using the Haystack 37m antenna. An autocorrelator was used for these observations with a bandwidth of 17.8 MHz providing a resolution of 15 kHz or 0.04 km s^{-1}. To increase the signal to noise in the spectra, and allow for ease in comparison with the other transitions, the J = 4 → 3 data were smoothed to a resolution of 0.6 km $^{-1}$. The hyperfine splitting in the J = 4 → 3 transition is the largest of the four transitions, however, because of the 2 − 5 km s^{-1} linewidths associated with giant cloud cores the hyperfine structure for this transition is unresolved. The main beam efficiency was estimated using observations of Mars and Jupiter and was found to be $\eta_{MB} \sim 0.33$. This is in agreement with independent measurements at the same frequency by Fuller and Myers (1993).

3.3 Results

3.3.1 Orion A

The region observed in Orion is a 4′ × 12′ (360 positions) region centered on the Orion KL/BN star forming core at $\alpha(1950) = 5^h32^m46.8^s$ and $\delta(1950) = -5°24'28''$. The map size and spacing are the same as the CH_3C_2H observations presented in the previous chapter.

Figure 3.1 shows the HC_3N integrated intensity of each transition in the form of contour maps. The J = 10 → 9 and J = 12 → 11 transitions, in the middle two panels, clearly show the extended quiescent ridge, with the strongest emission appearing near the Orion KL/BN star forming core. HC_3N is known to have strong emission in both the hot core and plateau, two features which are associated with star formation activity near KL/BN (Masson & Mundy 1988).

The line profiles observed exhibit evidence of the hot core feature (Goldsmith et al 1982), but as the beam size of the FCRAO observations ($\sim 50''$) is much larger than the size of the hot core ($\sim 10''$, Masson & Mundy 1988, Mangum et al 1990) the emission from the hot core is severely beam diluted.

Although the morphology of the HC_3N J = 4 $\rightarrow$ 3 emission is similar to that of other transitions, the emission peaks are located north and south of KL/BN, while the other 3 transitions peak directly at the star forming core. Emission from the J = 4 $\rightarrow$ 3 transition is important because it has the lowest critical density, $n_{cr} \sim 10^4$ cm^{-3}, and is therefore the most sensitive to low density material along the line of sight. The emission from this transition is weaker than the higher transitions. However, the extent of the observed J = 4 $\rightarrow$ 3 emission is similar to that of higher transitions (with higher critical densities), therefore it is likely that the different transitions are probing the same dense layer and the weak emission can be explained simply as an effect of the excitation.

The J = 16 $\rightarrow$ 15 emission shows structure similar to that observed in the J = 10 $\rightarrow$ 9 and J = 12 $\rightarrow$ 11 transitions. The main difference observed is that the J = 16 $\rightarrow$ 15 integrated intensity is stronger than any other transition at the KL/BN position and at the southern star forming site ($\sim 1.5'$ S). This is probably due to a combination of two effects. First, the beam size of the J = 16 $\rightarrow$ 15 transition is the smallest of our sample of HC_3N transitions and is therefore the least sensitive to effects of beam dilution. Second, the hot core is warmer ($T_K > 250$ K; Wilner, Wright, & Plambeck 1994) compared to the quiescent ridge ($T_K \sim 60$ K; Chapter 2) which will increase the populations in the higher energy states ($E_{J=16}/k = 52$ K).

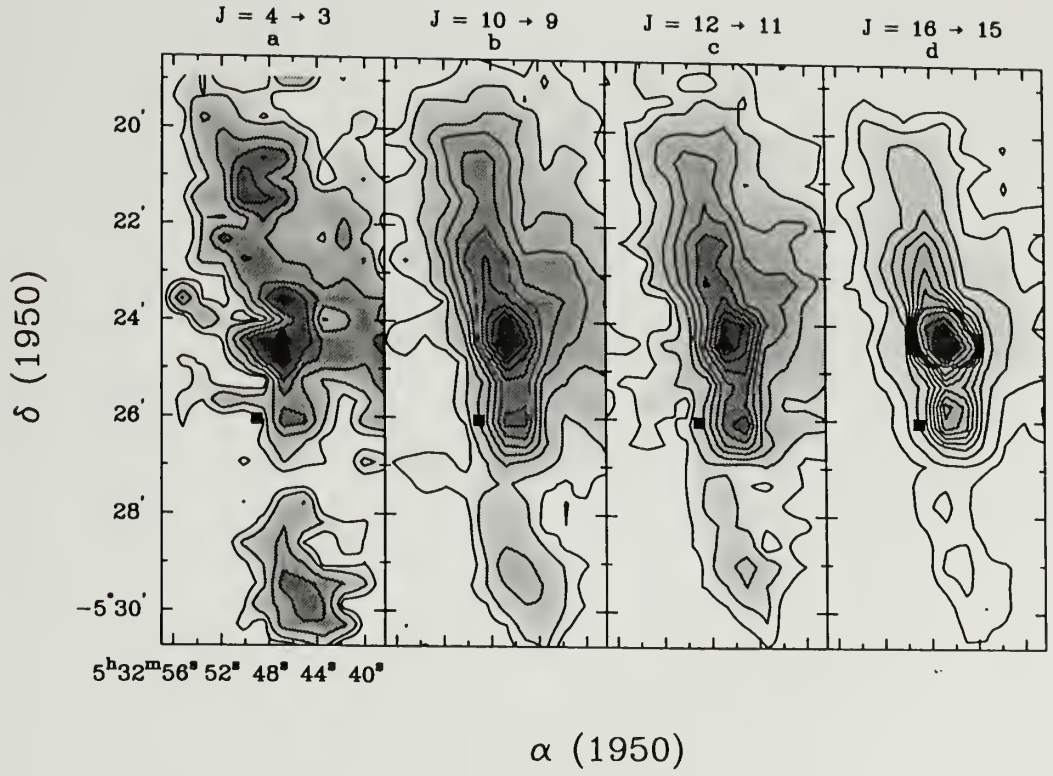

Figure 3.1. Distribution of the HC_3N integrated intensities for four transitions in Orion. For the J = 4 → 3 transition the lowest contour and the spacing are 0.5 K km s^{-1}. For the other transitions the lowest two contours are 1 and 2 K km s^{-1} and the subsequent spacing is 2 K km s^{-1}. The filled triangle indicates the position of the embedded BN/KL cluster and the filled square denotes the position of $\theta^1 C$ Ori.

Since our combinations of telescope and frequencies have slightly varied responses to the KL/BN line of sight, we have fit the spectra of all transitions in the nine positions surrounding KL/BN with multiple gaussian components and have only included the quiescent ridge component in our analysis. Thus, this paper will concentrate solely on the density structure within the extended quiescent ridge. Away from the star forming sites and along the extended ridge the J = 10 $\rightarrow$ 9 and J = 12 $\rightarrow$ 11 integrated intensities are typically greater than observed in the J = 16 $\rightarrow$ 15 and the J = 4 $\rightarrow$ 3 transitions suggesting that with this choice of transitions we have, for the most part, determined the distribution of molecular excitation and will be able to make accurate determinations of the density.

3.3.2 M 17

We have mapped a 4′× 5′ (120 positions) region covering the same grid as the CH_3C_2H observations in Chapter 2. Figures 3.2 present the contour maps of the HC_3N integrated intensity. There are some apparent differences in morphology of emission between the four transitions. The three higher rotational transitions observed exhibit similar morphologies with emission strongest to the northeast adjacent H II region region. However, the J = 4 $\rightarrow$ 3 transition, shown in Figure 3.2, has two emission peaks, with the northern peak displaced somewhat from the emission peaks seen in the higher rotational transitions. The strong emission in the northeastern corner of the map is quite prominent in the high resolution $C^{18}O$ and CS study of Stutzki & Gusten (1990) and has been labeled as the "northern condensation".

These morphological differences are similar to the variations in CS emission observed in the multitransition study of CS performed by Wang et al (1993). In that study, the J = 1 $\rightarrow$ 0 emission is intense towards the central part of the core, while the higher transitions (J > 2) have structure similar to that observed in the HC_3N J > 10 transitions. Wang et al suggested that a portion of the morphological

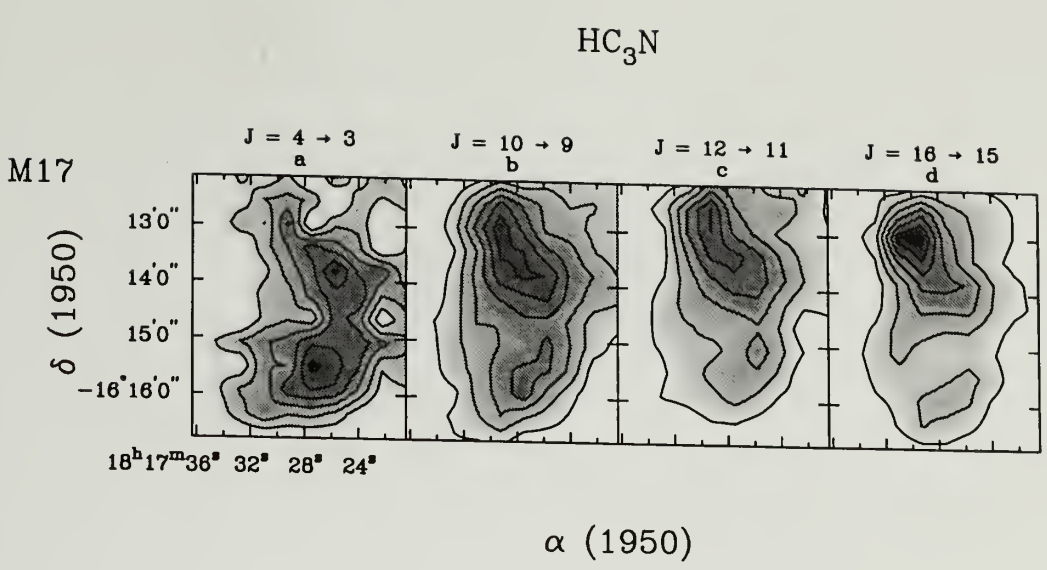

Figure 3.2. Distribution of the HC_3N integrated intensities for four transitions in M 17. For the J = 4 → 3 transition the lowest contour and the spacing are 1.0 K km s^{-1}. For the other transitions the lowest contour and the spacing is 2 K km s^{-1}.

differences was due to optical depth, while some of the differences were inferred to be the result of excitation. If the emission from HC_3N is optically thin, these differences could be the result of variations in excitation. The temperature in the northern condensation ($T_K \sim 50$ K), as inferred by CH_3C_2H in Chapter 2, is higher than in the central regions of the cloud ($T_K \sim 30$ K) confirming that the excitation does vary and may account for the HC_3N morphological differences.

3.3.3 Cepheus A

We have mapped a $4' \times 5'$ region (120 positions) centered on the FIR continuum peak (Moriarty-Schieven et al 1991) and including the compact H II regions. Figure ?? presents the integrated intensity maps for all four transitions of HC_3N observed in Cepheus A. As observed in M 17, the transitions with J > 10 have similar patterns in their emission, with the strongest emission at the dust

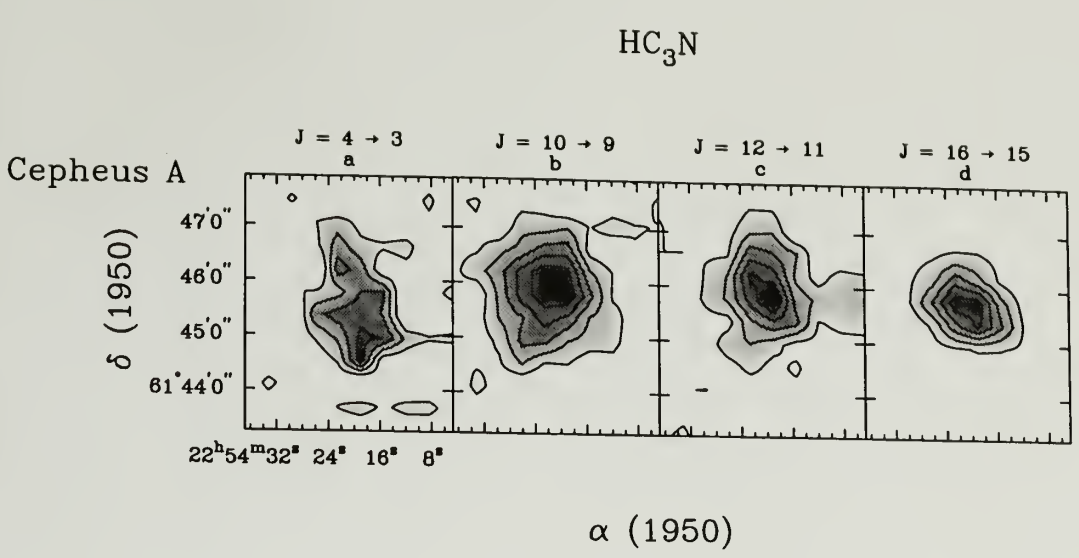

Figure 3.3. Distribution of the HC_3N integrated intensities for four transitions in Cepheus A. For the J = 4 → 3 transition the lowest contour and the spacing are 0.5 K km s^{-1}. For the other transitions the lowest contour and the spacing is 1 K km s^{-1}.

continuum peak. The J = 10 → 9 transition has the highest intensity and the most extended emission, while the higher-J transitions have intensities that are decreasing and exhibit successively more compact emission morphologies. In contrast, the J = 4 → 3 transition peaks to the south and north of the FIR continuum peak.

These differences in the emission may be due to changes in the temperature of the cloud which is highest near the map center ($T_K \sim 50$ K) and decrease sharply away from the central position to lower temperatures ($T_K \sim 20$ K; Chapter 2). This kind of temperature structure will favor the lines with low excitation, such as the J = 4 → 3, which are relatively more intense at low temperatures. The higher-J lines will be preferentially populated at higher temperatures and therefore should have the strongest emission near the regions traced by the warm dust. A density that decreases from the center to the edge could also result in a similar

morphology for the emission. These questions will be examined in the following sections.

3.4 Density Determinations

3.4.1 Model Fitting

We have used a non-LTE model to fit the observed lines of HC_3N. The statistical equilibrium calculations include radiative trapping, which is computed using the large velocity gradient approximation (LVG). Since the HC_3N optical depths are small the effects of radiative trapping is also small. We have used the collision rates computed by Green and Chapman (1978) for HC_3N with helium.

The resulting integrated intensities from our model depend on four parameters: the density of molecular hydrogen, n_{H_2}, the kinetic temperature, T_K, the column density of HC_3N and the line width. For the linewidth we have used an average of the J = 10 $\rightarrow$ 9 and J = 12 $\rightarrow$ 11 linewidths and for the temperature we used the temperatures derived from CH_3C_2H in Chapter 2. The gas temperature for all 3 cloud cores has large variations with position in each cloud, with the temperatures of the dense gas typically higher near the star forming sites. While including these temperature variations across the face of the cloud should be a better approximation to density determinations, there is one concern, which is whether the temperatures derived from methyl acetylene are appropriate for the region being probed by HC_3N. The dipole moment of CH_3C_2H is only $\mu = 0.78$ Debye, much smaller than the dipole moment of HC_3N. Therefore the emission from these two molecules may not be probing the same gas. To examine this question we compared the line widths and line center velocities of the HC_3N J = 10 $\rightarrow$ 9 transition to those of the CH_3C_2H J = 6 $\rightarrow$ 5 (K = 0) in Orion (see Figures 2.13 and 2.14). These figures show that the line widths and centroids of emission of these two species are in agreement and suggest that it is reasonable to

assume that the lines originate in the same volume of gas. Thus two of the four free parameters, temperature and line width, can be fixed.

The four HC_3N integrated intensities were fitted to a grid of LVG models which minimized χ^2 by varying the column density of HC_3N and the density of molecular hydrogen. In order to obtain reliable estimates of the density we only included those positions that have $J = 10 \rightarrow 9$ and $J = 12 \rightarrow 11$ integrated intensities that were at least 5σ. Temperature estimates for these positions were taken from Chapter 2. Several positions lacked a value for the temperature. For these positions we used temperatures interpolated from the closest neighbors. Each transition was weighted by the quadratic sum of the errors in calibration and the statistical error as determined via a baseline fit to each spectrum. The uncertainty in the calibration was assumed to be 20% for each transition.

Since the HC_3N lines are likely to be optically thin (see following section), the column density and density determinations are nearly decoupled. The column density of HC_3N is determined primarily by the integrated line intensities, while the density is constrained by the intensity ratios. Thus for density determinations, the $J = 4 \rightarrow 3$ and $J = 16 \rightarrow 15$ transitions are particularly important because these two transitions anchor the upper and lower bound of the excitation curve. It can also be expected that each line of sight may not be ascribed a single density and that instead a range of densities may exist. Since the emission from HC_3N is optically thin it samples the entire line of sight, with the majority of the emission presumably weighted towards the highest densities. Therefore the density derived from HC_3N (like the temperature; see Chapter 2) is an average value for the line of sight weighted towards the denser regions (Snell et al 1984).

3.4.2 Results

The results of the fits: density, column density of HC_3N, and the reduced χ^2 (χ^2/ν; where the number of degrees of freedom $\nu = 2$) are presented in Table 3.2

for Orion, Table 3.3 for M 17, and Table 3.4 for Cepheus A. In order to remove bad fits to the HC_3N intensities from the data sample we have used several cutoffs to insure the quality of the results. As a first constraint we present here only those fits that had values of reduced $\chi^2 \leq 5$. The reduced χ^2 is a measure of the quality of the fit and a value of $\chi^2/\nu \leq 5$ is equivalent to better than a 1.5σ fit on average to each data point. Since a large fraction of positions fit these criteria we conclude that the simple statistical equilibrium fit to the intensities provides an adequate model of the data.

A sample of the model fits to the HC_3N data along three lines of sight in Orion is presented in Figure 3.4. The data shown in this figure exemplify the types of fits we found in our multitransition survey. In these positions, as observed for most positions studied, the $J = 4 \rightarrow 3$ and $J = 16 \rightarrow 15$ transitions are weaker than the two intermediate-J transitions, so the shape of the excitation curve is well defined. Although all 3 positions have reduced $\chi^2 < 0.6$, the curves giving the variation of χ^2 with density are quite different. In Figure 3.5 we have plotted for each position the reduced χ^2 as a function of density. For each density the column density was the only free parameter, thus $\nu = 3$.

For the first position ($\Delta\alpha = -0.84, \Delta\delta = 1.68$) a symmetric minimum in χ^2 is found centered at $n_{H_2} = 2 \times 10^5$ cm^{-3}. For the second position ($\Delta\alpha = 0.0$, $\Delta\delta = 2.5$) a shallow asymmetric minimum in reduced χ^2 is observed, and the reduced χ^2 increases much more slowly on the high density side. The final position ($\Delta\alpha = 0.0, \Delta\delta = 1.26$) does not even have a minimum in reduced χ^2. Instead a sharp drop in χ^2 is seen as the density increases, followed by an asymptotic

Table 3.2 Orion Ridge Densities

$\Delta\alpha$	$\Delta\delta$	T_K	$\log(n_{H_2})$	$\log(\sigma_{n_{H_2}})$		$\log(N)$	$\log(\sigma(N))$	χ^2/ν
(′)	(′)	(K)	(cm^{-3})	(cm^{-3})	(cm^{-3})	(cm^{-2})	(cm^{-2})	
0.42	5.04	21.9	>5.7			12.9	0.06	3.5
0.42	5.04	21.9	>5.7			12.9	0.06	3.5
0.84	5.04	(21.4)	5.8	−0.4	+0.9	12.9	0.06	0.02
0.00	4.62	22.2	>5.9			13.3	0.04	0.1
0.42	4.62	21.9	6.1	−0.5	+0.1	13.3	0.05	1.8
0.84	4.62	21.4	5.8	−0.4	+0.7	13.2	0.05	0.5
1.26	4.62	(21.4)	>5.8			13.2	0.04	1.6
−0.84	4.62	(22.2)	>6.1			12.7	0.06	1.3
0.00	4.20	20.8	6.0	−0.4	+0.1	13.5	0.05	0.9
0.42	4.20	17.0	>6.0			13.6	0.04	1.4
0.84	4.20	18.7	>6.2			13.6	0.04	1.6
1.26	4.20	(17.5)	>6.2			13.5	0.04	3.2
1.68	4.20	(23.4)	>6.1			13.2	0.04	0.4
−0.42	4.20	19.1	6.1	−0.4	+0.1	13.1	0.06	1.7
−0.84	4.20	(19.1)	>5.7			12.9	0.06	0.8
−1.26	4.20	(19.1)	>6.0			13.0	0.05	0.6
−1.68	4.20	(19.1)	6.1	−0.6	+0.1	12.9	0.07	0.5
0.00	3.78	40.1	5.2	−0.3	+0.3	13.5	0.05	1.6
0.42	3.78	39.7	5.4	−0.3	+0.4	13.6	0.05	2.2
0.84	3.78	50.8	5.4	−0.3	+0.4	13.5	0.05	2.1
1.26	3.78	16.5	>6.3			13.5	0.04	4.1
1.68	3.78	23.4	>6.0			13.0	0.05	2.4
−0.42	3.78	(21.8)	>6.1			13.1	0.04	1.1
−1.26	3.78	(21.8)	5.9	−0.4	+0.1	13.0	0.06	0.7
−1.68	3.78	(21.8)	5.7	−0.3	+0.4	12.9	0.07	1.6
0.00	3.36	21.1	>6.2			13.5	0.04	1.4
0.42	3.36	22.9	>6.0			13.6	0.04	0.8
0.84	3.36	(25.8)	6.2	−0.6	+0.1	13.6	0.05	2.3
1.26	3.36	(16.5)	>6.2			13.4	0.04	4.4
1.68	3.36	(23.4)	>5.9			12.9	0.04	0.1
−0.42	3.36	20.4	6.1	−0.6	+0.1	13.1	0.05	1.1

Table 3.2 (cont.)

$\Delta\alpha$	$\Delta\delta$	T_K	$\log(n_{H_2})$	$\log(\sigma_{n_{H_2}})$		$\log(N)$	$\log(\sigma(N))$	χ^2/ν
(′)	(′)	(K)	(cm^{-3})	(cm^{-3})	(cm^{-3})	(cm^{-2})	(cm^{-2})	
0.00	2.94	43.3	5.3	−0.4	+0.3	13.5	0.05	2.7
0.42	2.94	30.4	5.9	−0.4	+0.1	13.6	0.05	1.0
0.84	2.94	43.7	5.4	−0.5	+0.4	13.5	0.05	4.9
1.26	2.94	(33.5)	5.9	−0.4	+0.1	13.1	0.05	2.3
−0.42	2.94	21.5	>5.8			13.2	0.04	0.6
−0.84	2.94	(22.0)	5.6	−0.3	+0.3	13.2	0.05	0.3
−1.26	2.94	(15.7)	>5.9			13.2	0.05	0.7
−1.68	2.94	(15.7)	>6.3			13.0	0.05	4.8
−2.10	2.94	(15.7)	>6.1			12.9	0.05	4.4
0.00	2.52	34.5	6.1	−0.4	+0.1	13.5	0.05	1.1
0.42	2.52	23.6	>6.1			13.6	0.04	1.1
0.84	2.52	28.8	>5.8			13.4	0.04	1.0
1.26	2.52	28.4	>6.0			13.2	0.04	1.5
−0.42	2.52	(27.1)	5.9	−0.4	+0.8	13.2	0.05	0.4
−0.84	2.52	22.9	5.8	−0.3	+0.4	13.2	0.05	0.7
−1.26	2.52	15.7	>6.3			13.4	0.04	2.8
−1.68	2.52	(15.7)	>6.2			13.3	0.04	3.2
0.42	2.10	34.4	>6.1			13.7	0.04	2.1
0.84	2.10	30.2	>6.0			13.6	0.04	0.8
1.26	2.10	(29.9)	6.0	−0.6	+0.1	13.4	0.05	3.9
1.68	2.10	(29.9)	>5.8			13.0	0.04	1.6
−0.42	2.10	41.3	5.5	−0.2	+0.3	13.3	0.04	0.1
−0.84	2.10	31.7	6.3	−0.5	+0.1	13.2	0.05	1.9
−1.26	2.10	16.9	>6.2			13.5	0.04	1.4
−1.68	2.10	(18.3)	>6.2			13.1	0.05	3.0
−2.10	2.10	31.0	5.3	−0.2	+0.2	13.0	0.06	1.3
0.00	1.68	33.4	>6.0			13.6	0.04	1.4

Table 3.2 (cont.)

$\Delta\alpha$	$\Delta\delta$	T_K	$\log(n_{H_2})$	$\log(\sigma_{n_{H_2}})$		log(N)	$\log(\sigma(N))$	χ^2/ν
(′)	(′)	(K)	(cm^{-3})	(cm^{-3})	(cm^{-3})	(cm^{-2})	(cm^{-2})	
0.42	1.68	35.1	>6.0			13.7	0.04	0.6
0.84	1.68	23.7	>6.1			13.6	0.04	2.4
1.26	1.68	(23.7)	>6.2			13.3	0.04	3.3
−0.42	1.68	33.8	5.7	−0.3	+0.4	13.4	0.05	0.1
−0.84	1.68	42.9	5.3	−0.2	+0.2	13.4	0.05	0.3
−1.26	1.68	21.1	>6.2			13.4	0.04	4.1
−1.68	1.68	(24.8)	5.6	−0.3	+0.3	13.3	0.05	0.4
0.00	1.26	34.2	>5.9			13.6	0.04	0.5
0.42	1.26	33.8	>6.1			13.7	0.04	1.5
0.84	1.26	43.6	6.1	−0.6	+0.1	13.5	0.05	0.7
1.26	1.26	(43.6)	>5.8			13.1	0.04	2.1
1.68	1.26	(43.2)	5.7	−0.4	+0.8	12.7	0.06	0.2
−0.42	1.26	(35.7)	5.6	−0.3	+0.3	13.5	0.05	0.01
−0.84	1.26	(36.6)	5.8	−0.3	+0.5	13.4	0.05	0.7
−1.26	1.26	31.2	5.7	−0.2	+0.3	13.5	0.05	0.4
−1.68	1.26	32.2	5.5	−0.2	+0.2	13.4	0.05	0.3
−2.10	1.26	(34.4)	5.9	−0.4	+0.1	13.2	0.05	0.4
0.00	0.84	37.0	>5.7			13.8	0.04	2.6
0.42	0.84	51.3	>5.6			13.7	0.04	2.2
0.84	0.84	46.6	>5.7			13.3	0.05	3.1
−0.42	0.84	40.2	5.8	−0.5	+0.1	13.6	0.05	2.4
−0.84	0.84	40.2	5.7	−0.3	+0.6	13.5	0.05	1.0
−1.26	0.84	34.1	5.7	−0.3	+0.6	13.5	0.05	1.0
−1.68	0.84	(25.0)	6.2	−0.5	+0.1	13.4	0.05	1.2
0.00	0.42	36.0	>6.1			13.8	0.04	2.8
−0.42	0.42	34.0	>5.7			13.7	0.04	2.0
−1.26	0.42	33.7	6.3	−0.6	+0.1	13.4	0.05	0.5
−1.68	0.42	22.5	6.1	−0.6	+0.1	13.4	0.05	2.5
−2.10	0.42	(22.5)	5.8	−0.3	+0.6	13.2	0.05	1.4
0.00	0.00	59.9	>5.6			13.9	0.04	0.9
1.26	0.00	(46.0)	>5.8			13.0	0.04	0.6
−0.42	0.00	51.0	>5.5			13.8	0.04	2.1
−0.84	0.00	34.8	6.4	−0.7	+0.1	13.5	0.05	1.9

Table 3.2 (cont.)

$\Delta\alpha$	$\Delta\delta$	T_K	$\log(n_{H_2})$	$\log(\sigma_{n_{H_2}})$		$\log(N)$	$\log(\sigma(N))$	χ^2/ν
(′)	(′)	(K)	(cm^{-3})	(cm^{-3})	(cm^{-3})	(cm^{-2})	(cm^{-2})	
−1.68	0.00	(18.9)	>6.1			13.4	0.04	2.9
−2.10	0.00	22.4	>5.7			13.3	0.04	4.4
0.00	−0.42	30.3	>5.8			13.8	0.05	4.4
−0.42	−0.42	29.6	>6.2			13.7	0.04	1.5
−0.84	−0.42	25.2	>6.0			13.5	0.04	2.9
−1.26	−0.42	(25.2)	>5.9			13.4	0.04	2.3
−1.68	−0.42	(21.1)	>5.9			13.3	0.04	4.3
−2.10	−0.42	21.1	>5.8			13.4	0.04	2.2
0.00	−0.84	(32.0)	>5.9			13.7	0.04	1.6
−0.42	−0.84	44.7	>5.8			13.6	0.04	1.3
−0.84	−0.84	36.5	>6.0			13.3	0.04	1.0
−1.26	−0.84	(36.5)	5.8	−0.6	+0.1	13.1	0.05	1.3
−1.68	−0.84	(21.1)	>6.1			13.1	0.04	2.3
−2.10	−0.84	(21.1)	5.9	−0.6	+0.1	13.2	0.05	4.0
0.00	−1.26	(33.6)	>6.0			13.6	0.04	3.3
−0.42	−1.26	45.5	>5.8			13.7	0.04	1.0
−0.84	−1.26	31.7	>6.0			13.3	0.04	0.5
−1.68	−1.26	(31.7)	5.9	−0.4	+0.8	13.0	0.05	2.0
0.00	−1.68	29.2	>6.1			13.8	0.04	2.1
−0.42	−1.68	28.3	>6.2			13.8	0.04	1.9
−0.84	−1.68	(28.3)	>6.2			13.2	0.04	1.6
−1.68	−1.68	(28.3)	5.6	−0.3	+0.3	13.0	0.05	1.1
0.00	−2.10	30.0	>6.1			13.5	0.04	2.5
−1.26	−2.10	(29.8)	>5.7			12.7	0.05	2.1
0.00	−2.52	(30.0)	6.0	−0.5	+0.6	13.0	0.05	4.2
0.42	−2.52	(30.0)	6.1	−0.6	+0.1	12.8	0.05	1.2
0.84	−2.52	(30.0)	>5.6			12.5	0.06	2.3
−0.42	−2.52	(29.0)	>5.9			12.9	0.05	3.2
−0.84	−2.52	(29.0)	6.0	−0.4	+0.1	13.0	0.05	0.2
0.00	−2.94	(29.8)	>5.8			13.0	0.04	1.5
0.42	−2.94	(29.8)	>6.2			12.9	0.05	3.6
0.84	−2.94	(29.8)	5.8	−0.4	+0.7	12.7	0.05	0.2
0.00	−3.36	29.8	>5.7			13.1	0.04	2.2

Table 3.2 (cont.)

$\Delta\alpha$	$\Delta\delta$	T_K	$\log(n_{H_2})$	$\log(\sigma_{n_{H_2}})$	$\log(\sigma_{n_{H_2}})$	log(N)	$\log(\sigma(N))$	χ^2/ν
(′)	(′)	(K)	(cm^{-3})	(cm^{-3})	(cm^{-3})	(cm^{-2})	(cm^{-2})	
0.42	−3.36	(29.8)	>5.8			13.0	0.04	0.2
−0.42	−3.36	(29.8)	6.0	−0.5	+0.1	12.9	0.05	4.6
0.00	−3.78	(29.8)	5.9	−0.5	+0.1	13.1	0.05	4.9
0.42	−3.78	(29.8)	5.6	−0.4	+0.4	13.0	0.05	3.2
0.00	−4.20	(15.0)	>6.1			13.4	0.04	3.0
0.42	−4.20	(15.0)	>5.9			13.0	0.05	0.8
0.00	−4.62	20.7	6.1	−0.6	+0.1	13.4	0.05	3.1
0.42	−4.62	(20.7)	6.0	−0.5	+0.6	12.9	0.05	0.2
−0.42	−4.62	24.4	5.9	−0.4	+1.0	13.4	0.05	2.1
−0.84	−4.62	32.4	5.4	−0.3	+0.3	13.2	0.05	3.6
0.00	−5.04	(23.1)	5.7	−0.5	+0.6	13.2	0.05	4.2
0.42	−5.04	(23.1)	5.1	−0.3	+0.4	13.1	0.05	1.9
0.42	−5.04	(23.1)	5.1	−0.3	+0.4	13.1	0.05	1.9
−0.42	−5.04	26.7	5.6	−0.4	+0.4	13.4	0.05	3.0
−0.84	−6.30	(24.3)	>5.4			12.8	0.05	4.8

Table 3.3. M17 Densities[a]

$\Delta\alpha$	$\Delta\delta$	T_K	$\log(n_{H_2})$	$\log(\sigma_{n_{H_2}})$		$\log(N)$	$\log(\sigma(N))$	χ^2/ν
(′)	(′)	(K)	(cm^{-3})	(cm^{-3})	(cm^{-3})	(cm^{-2})	(cm^{-2})	
−0.84	1.26	(38.5)	5.9	−0.4	+0.1	12.9	0.06	1.2
−1.26	1.26	42.4	5.6	−0.3	+0.4	13.3	0.05	1.5
−1.68	1.26	48.7	5.9	−0.4	+0.1	13.1	0.06	3.0
−2.10	1.26	(31.0)	5.8	−0.3	+0.6	13.2	0.05	1.2
−2.52	1.26	24.9	>6.0			13.1	0.05	1.0
−2.94	1.26	(24.9)	6.0	−0.4	+0.1	13.2	0.05	1.8
−3.36	1.26	(24.9)	>5.9			13.0	0.05	1.7
−0.42	0.84	(37.3)	5.8	−0.3	+0.8	12.9	0.06	1.6
−0.84	0.84	37.3	>5.7			13.5	0.04	0.1
−1.26	0.84	51.7	5.8	−0.4	+0.1	13.6	0.05	0.1
−1.68	0.84	(46.8)	5.7	−0.3	+0.7	13.4	0.05	0.5
−2.52	0.84	26.0	>5.9			13.3	0.04	0.7
−2.94	0.84	(26.0)	6.2	−0.5	+0.1	13.2	0.05	0.7
−3.36	0.84	(26.0)	6.2	−0.7	+0.1	13.0	0.05	1.5
−1.26	0.42	37.2	>5.8			13.8	0.04	0.8
−1.68	0.42	(36.1)	6.4	−0.7	+0.1	13.5	0.05	0.6
−1.68	0.42	(36.1)	>5.7			13.5	0.04	0.6
−2.10	0.42	(27.9)	>5.9			13.4	0.04	0.1
−2.52	0.42	30.2	6.1	−0.5	+0.1	13.3	0.05	1.0
−2.94	0.42	(30.2)	>5.8			13.0	0.05	2.1
−3.36	0.42	(30.2)	6.0	−0.4	+0.1	13.0	0.06	1.0
−0.84	0.00	(32.0)	>6.1			13.5	0.04	1.9
−1.26	0.00	33.9	>6.0			13.7	0.04	1.1
−1.68	0.00	32.0	5.9	−0.4	+0.1	13.7	0.05	0.4
−2.10	0.00	26.5	6.0	−0.3	+0.8	13.6	0.05	0.1
−2.52	0.00	29.2	5.7	−0.3	+0.3	13.4	0.05	0.1
−3.36	0.00	(29.2)	5.9	−0.4	+0.6	13.0	0.05	0.2
−0.42	−0.42	28.6	5.9	−0.3	+0.8	12.9	0.06	1.6
−1.26	−0.42	34.6	>5.8			13.6	0.04	1.2
−2.10	−0.42	(27.4)	6.2	−0.6	+0.1	13.7	0.05	2.4
−2.52	−0.42	28.4	5.9	−0.4	+0.8	13.5	0.05	1.1

Table 3.3 (cont.)

$\Delta\alpha$	$\Delta\delta$	T_K	$\log(n_{H_2})$	$\log(\sigma_{n_{H_2}})$		log(N)	$\log(\sigma(N))$	χ^2/ν
(′)	(′)	(K)	(cm^{-3})	(cm^{-3})	(cm^{-3})	(cm^{-2})	(cm^{-2})	
−2.94	−0.42	(28.4)	5.6	−0.4	+0.4	13.4	0.05	3.0
−3.36	−0.42	(28.4)	5.8	−0.4	+0.6	13.1	0.06	1.9
−0.42	−0.84	(28.6)	6.1	−0.5	+0.1	13.0	0.06	3.6
−0.84	−0.84	(29.9)	>5.8			13.4	0.04	0.5
−1.26	−0.84	37.3	>5.8			13.4	0.04	1.2
−1.68	−0.84	(33.1)	6.0	−0.5	+0.1	13.6	0.05	1.7
−2.10	−0.84	29.9	6.1	−0.5	+0.1	13.6	0.05	2.1
−3.36	−0.84	(29.9)	5.7	−0.5	+0.6	13.1	0.05	3.8
−0.84	−1.26	(30.0)	>6.0			13.3	0.04	2.2
−1.26	−1.26	(37.3)	6.0	−0.5	+0.1	13.3	0.05	1.1
−1.68	−1.26	(30.0)	>5.8			13.3	0.04	1.9
−2.10	−1.26	(30.0)	5.8	−0.4	+0.7	13.5	0.05	3.0
−2.52	−1.26	(30.0)	5.7	−0.5	+0.6	13.3	0.05	3.9
−3.36	−1.26	(30.0)	6.0	−0.6	+0.1	12.9	0.06	3.6
0.00	−1.68	(30.0)	>5.8			12.8	0.05	1.7
−0.42	−1.68	(30.0)	>5.8			13.1	0.05	4.9
−0.84	−1.68	(30.0)	>5.9			13.3	0.04	4.3
−1.68	−1.68	(30.0)	5.5	−0.4	+0.3	13.5	0.05	3.6
−2.10	−1.68	(30.0)	5.5	−0.3	+0.3	13.6	0.05	1.3
−2.52	−1.68	(30.0)	5.5	−0.4	+0.3	13.4	0.05	3.7
−2.94	−1.68	(30.0)	5.0	−0.4	+0.5	13.3	0.05	4.3
−0.42	−2.10	(30.0)	>6.0			13.0	0.05	4.2
−1.26	−2.10	(30.0)	5.7	−0.4	+0.4	13.4	0.05	1.9
−1.68	−2.10	(30.0)	5.6	−0.5	+0.4	13.6	0.05	4.8
−1.68	−2.10	(30.0)	5.6	−0.5	+0.4	13.6	0.05	4.8

[a]offsets relative to $\alpha(1950) = 18^h17^m34.5^s$; $\delta(1950) = -16°13'24''$.

Table 3.4. Cepheus A Densities[a]

$\Delta\alpha$	$\Delta\delta$	T_K	$\log(n_{H_2})$	$\log(\sigma_{n_{H_2}})$		log(N)	$\log(\sigma(N))$	χ^2/ν
(′)	(′)	(K)	(cm^{-3})	(cm^{-3})	(cm^{-3})	(cm^{-2})	(cm^{-2})	
0.42	1.26	15.8	5.4	−0.3	+0.3	13.0	0.09	4.7
0.00	1.26	(20.7)	5.6	−0.3	+0.4	12.9	0.07	1.8
0.42	0.84	24.0	5.9	−0.3	+0.7	13.2	0.05	0.3
0.00	0.84	22.6	6.0	−0.4	+0.1	13.1	0.06	1.1
0.42	0.42	48.7	5.5	−0.3	+0.3	13.3	0.05	0.4
0.00	0.42	28.1	6.0	−0.3	+1.0	13.3	0.05	0.5
−0.42	0.42	(21.3)	>5.8			12.9	0.05	2.1
0.00	0.00	26.1	>6.3			13.4	0.04	2.4
−0.42	0.00	18.2	>6.2			13.3	0.04	2.9
0.42	−0.42	(22.4)	>6.1			13.3	0.04	3.5
0.00	−0.42	28.4	>6.1			13.3	0.04	3.0
−0.42	−0.42	34.1	>6.0			13.0	0.05	4.4
0.84	−0.84	20.0	5.9	−0.4	+0.8	13.0	0.06	2.7
0.42	−0.84	(19.5)	6.0	−0.4	+0.1	13.1	0.05	0.6
0.42	−0.84	(19.5)	6.0	−0.4	+0.1	13.1	0.05	0.6

[a]offsets relative to $\alpha(1950) = 22^h54^m19^s$; $\delta(1950) = 61°45'47''$.

convergence to $\chi^2 = 0.34$. The behavior of χ^2 with density suggests that for this particular line of sight only a lower limit to the density can be obtained.

The χ^2 behavior in the case of the last position shown in Figure 3.5 is a result of the choice of transitions we have used to model the excitation of HC_3N. The sensitivity to high densities in our study is set by the highest transition observed, the $J = 16 \rightarrow 15$ transition. Our calculations show that this transition (and also the lower transitions) is thermalized at $n_{H_2} > 5 \times 10^6$ cm^{-3}. Hence at densities approaching 5×10^6 cm^{-3}, the ratios of the line intensity are determined primarily by temperature and not by density and therefore we lose sensitivity to the hydrogen density. For the lines of sight that have this asymptotic dependence of χ^2 with density only a lower limit to the density can be set. In these cases observations of higher-J transitions are needed to bound the density.

The determination of errors from multi-dimensional χ^2 fitting usually utilizes a parabolic fit to the χ^2 hypersurface. The errors on the parameters are then determined by varying the free parameters separately about the minima measuring the increase in reduced χ^2 with the value of each parameter. An increase in the reduced χ^2 by one from its value at the minimum thus gives the range of acceptable values for the free parameters (Bevington and Robinson 1992). One assumption implicit in this method is that the parameters of the fit are independent of the other, which is valid in the case of optically thin emission. The maximum opacity determined as part of the intensity fits is 0.2, but values are typically < 0.1 for all 4 transitions. However, considering the possibility of beam filling factors less than unity, these opacities could be larger.

The method of estimating the errors also assumes that the χ^2 hypersurface is symmetric about the minimum, which in the case of a shallow asymmetric minimum is not valid. In order to determine valid errors on the data we have set the lower and upper limit to the error on the density determination for all fits, by

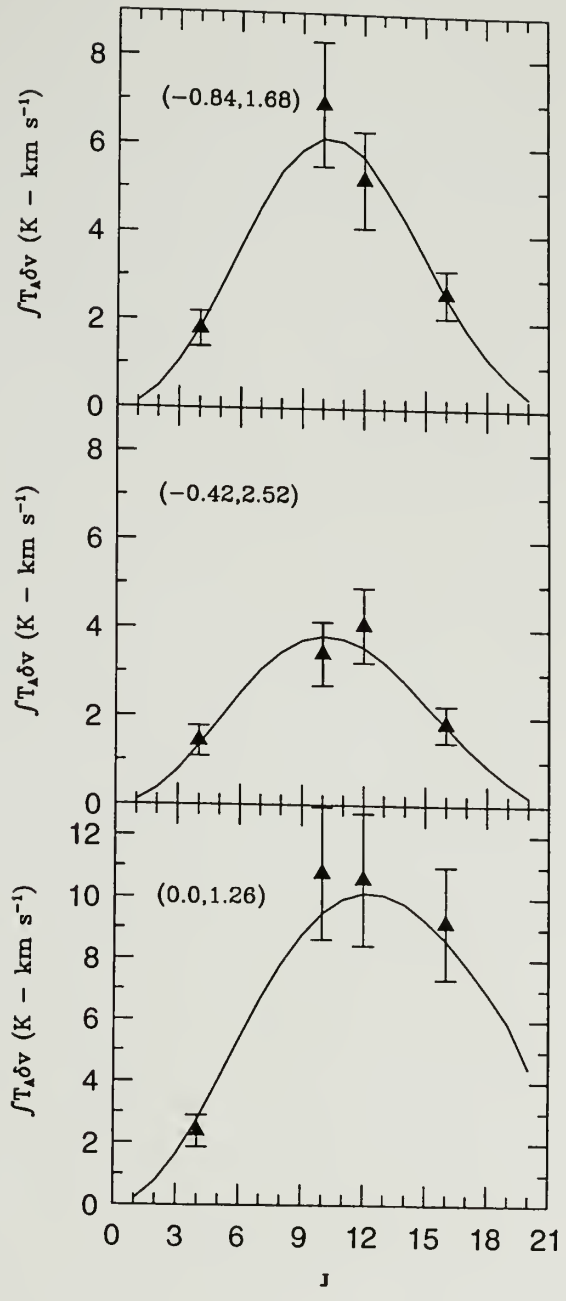

Figure 3.4. The observed integrated intensities as a function of J_{upper} of the transition along with the model fits are shown for three separate positions in Orion. The coordinate offset positions (relative to the central position listed in section 3.1) are listed in the top right hand corner of each panel.

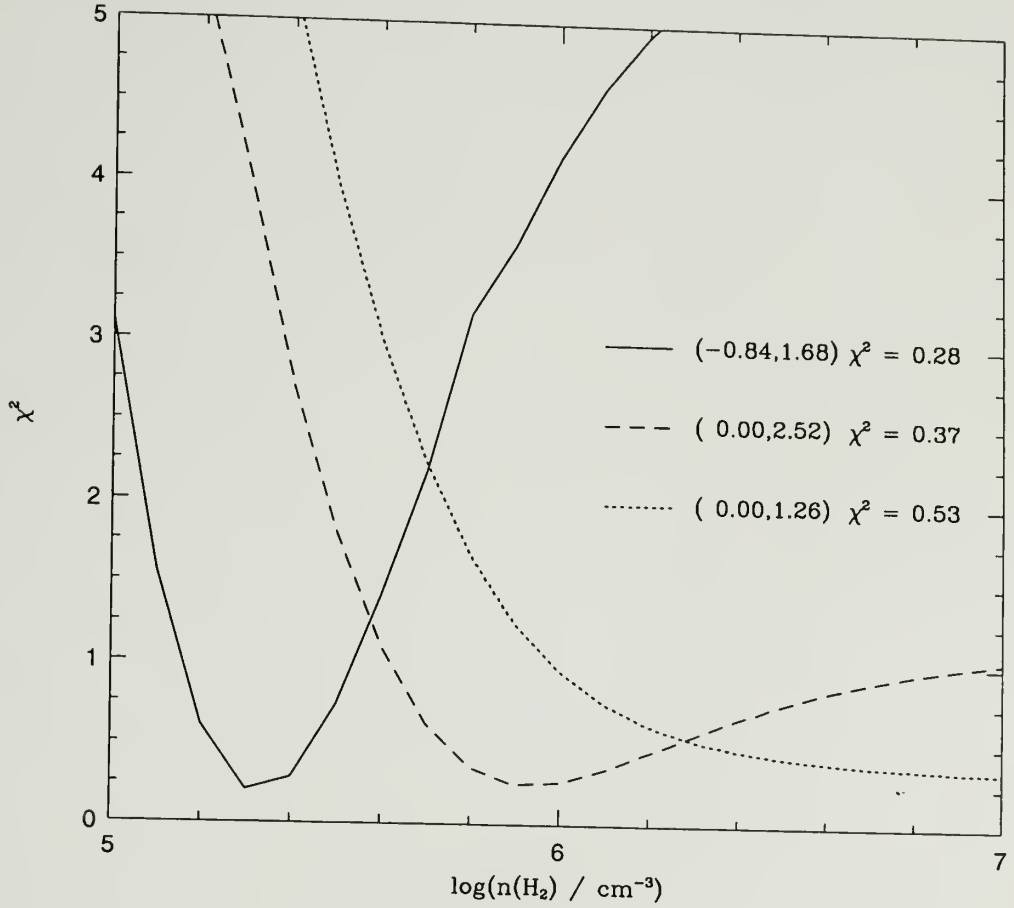

Figure 3.5. The variation of χ^2 with density for the three positions in Orion shown in Figure 4.

decreasing and then increasing the density until χ^2 increases by one in each direction. As an additional constraint we have only presented values with errors on the density, $\log[\sigma(n_{H_2})] < 1$.

In order to make an estimate of the lower limit to the densities for lines of sight without a minimum we have used the high density asymptotic value of χ^2 and lowered the density until the value of χ^2 increases by one. For example, for the position shown in the bottom panel of Figure 3.4 and in Figure 3.5, the high density limit $\chi^2 = 0.34$ and the corresponding lower limit to the density is determined at $\chi^2 = 1.34$ which corresponds to $n_{H_2} > 8 \times 10^5$ cm^{-3}.

3.4.3 Systematic Uncertainties

3.4.3.1 Effect of Temperature Model on the Analysis

The CH_3C_2H temperatures used here are typically lower than those adopted in the previous density studies. For example, the studies of M 17 by Snell et al (1984), Snell et al (1986), and Wang et al (1993) all adopt a single temperature of $T_K = 50$ K for the entire core. This value is greater than any of CH_3C_2H derived temperatures for M 17. The often-used temperature obtained from CO possibly applies only to the heated front surfaces of these cloud cores and not the temperature deep within the core (Chapter 2; Padman et al 1985). Thus we feel that the CH_3C_2H derived temperatures are more relevant for the dense gas, although they do have some uncertainty.

Because of this uncertainty, and to better compare with previous work, we have examined the effect of increasing the temperature on the χ^2 fits. The interdependence of temperature and density is shown in Figure 3.6. The temperature value of 34 K was used for the fit for the (0.0, 1.26) position presented in Table 3.2. As the temperature is increased the best fit density gradually shifts to lower densities. This is a feature consistently seen in the calculations which reflects the fact that higher temperatures require lower densities

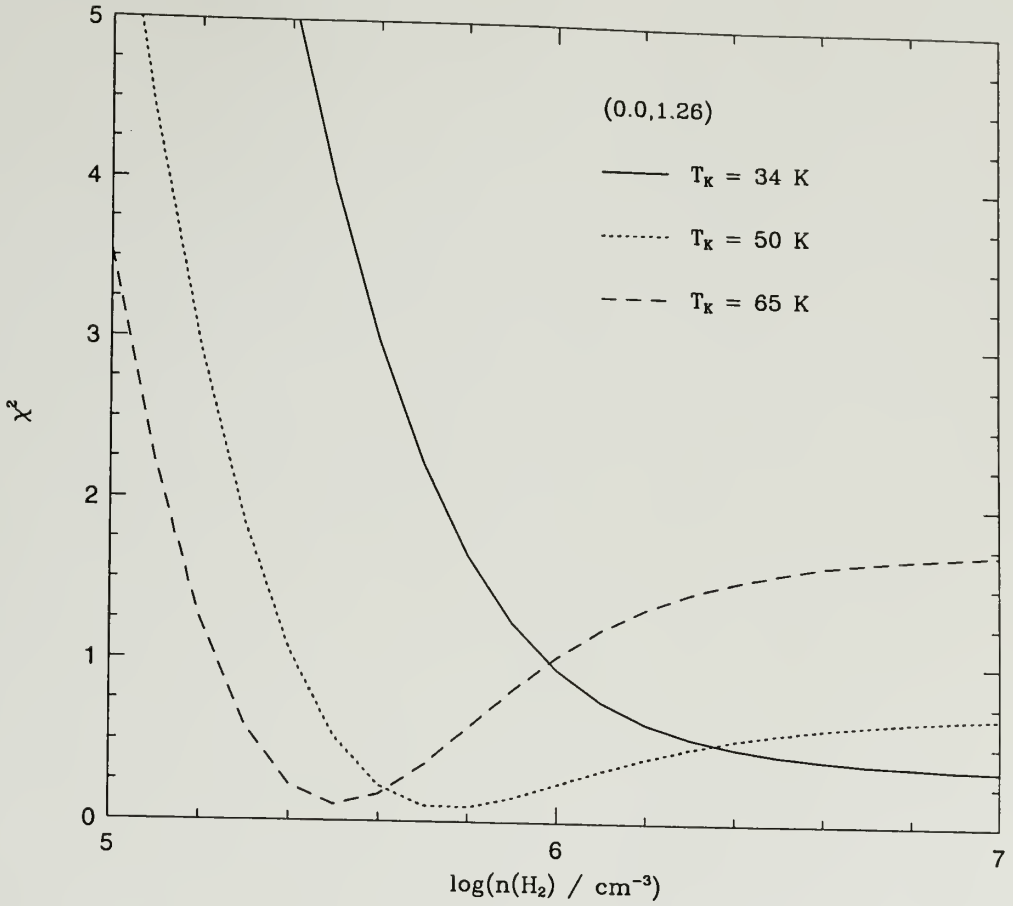

Figure 3.6. The variation of χ^2 as a function of density and temperature illustrating the interdependence of these two parameters when minimizing χ^2.

to populate the higher-J states. We have examined this dependence with several other positions and have found that increasing the temperature by a factor of two can lead to a reduction in the density by a factor of 5.

3.4.3.2 Line of Sight Density Gradients

A more significant complication that can arise in multitransitional studies is the possible presence of density gradients along the line of sight. Due to an

increase in the radiative decay rates with increasing J, higher densities are required to populate successively higher-J transitions. In the presence of a density gradient each transition may therefore be excited in different density regimes along the line of sight. This is particularly important given the evidence for a clumpy structure in GMC cores (Goldsmith 1995). If the clump to interclump density ratio is low, the lower rotational transitions may be produced in the interclump media while the emission from higher rotational transitions will come entirely from the dense clumps. Indeed this structure has been suggested to account for differences in the excitation of the CO molecule, with the lower-J transitions probing the interclump media and the higher-J transitions probing the hot clump edges (Meixner and Tielens 1993). Using high dipole moment molecules such as H_2CO, CS, or HC_3N certainly helps to alleviate this complexity by preferentially sampling only the densest regions along a given line of sight.

In this study we have fitted only a single density for each line of sight and, in general, the single density provides an adequate description of the observed line strengths (see section 3.4). Observations of the highest transition, the $J = 16 \rightarrow 15$, suggests that densities for most lines of sight are comparable to the critical density for this transition, $n_{cr} = 2.8 \times 10^6$ cm^{-3}. However, this analysis does not preclude the presence of low density material.

To determine the effect of low density material on our fit to the data, we have constructed a simple two component model by adding a column of lower density material to the solutions presented in Tables 3.2-3.4 and examined whether this added component produces a a better or worse fit to the data. For this purpose we have added a column of material at $n_{H_2} = 10^4$ cm^{-3}. Since the emission from HC_3N is optically thin, adding low density material will increase the strength of the $J = 4 \rightarrow 3$ transition ($n_{cr} = 4 \times 10^4$ cm^{-3}) relative to the other 3 transitions. Our analysis reveals that adding a column of molecular material $N(HC_3N) \sim 5 \times 10^{12}$

cm^{-3} at $n_{H_2} = 10^4$ cm^{-3} to the existing high density solution with $N(HC_3N) = 3 \times 10^{13}$ cm^{-2} does not appreciably change the fit to the data. However, if we add a column of low density gas with $N(HC_3N) = 1 \times 10^{13}$ cm^{-2}, then we no longer can obtain an acceptable fit to the $J = 4 \rightarrow 3$ data points. The temperature of the low density component is not critical because at these densities ($n_{H_2} = 10^4$ cm^{-3}) the emission from HC_3N is largely independent of the temperature.

The general result from our analysis is that while the observations of HC_3N imply that for all three sources the density is $> 3 \times 10^5$ cm^{-3}, they do not rule out the existence of low density material of moderate column density. In fact, almost any reasonable column density, with density substantially below 10^4 cm^{-3}, can be added without affecting the fit to our data.

3.5 Density Structure

3.5.1 Orion A

Reliable density determinations were made for 133 out of the 360 positions observed. These densities are superposed upon a map of the $C^{18}O$ $J = 1 \rightarrow 0$ integrated intensity from Ungerechts et al (1992) in Figure 3.7. The values in bold face are actual density determinations, while other values are lower limits. We again stress that the known hot core HC_3N emission was subtracted from the 9 positions surrounding IRc2. Thus, this density map represents the gas density of the quiescent ridge.

Along the ridge, the gas density, in general, is $> 3 \times 10^5$ cm^{-3}. Density determinations are confined, for the most part, to regions of strong $C^{18}O$ integrated intensity and therefore high column density. Many of the densities in Figure 3.7 are lower limits, and higher rotational transitions are needed in order to constrain the density. Rodriguez-Franco et al (1993) have mapped the $J = 24 \rightarrow 23$ transition of HC_3N in Orion, but their map is substantially smaller than ours. There is no evidence of HC_3N emission towards the molecular counterpart of the

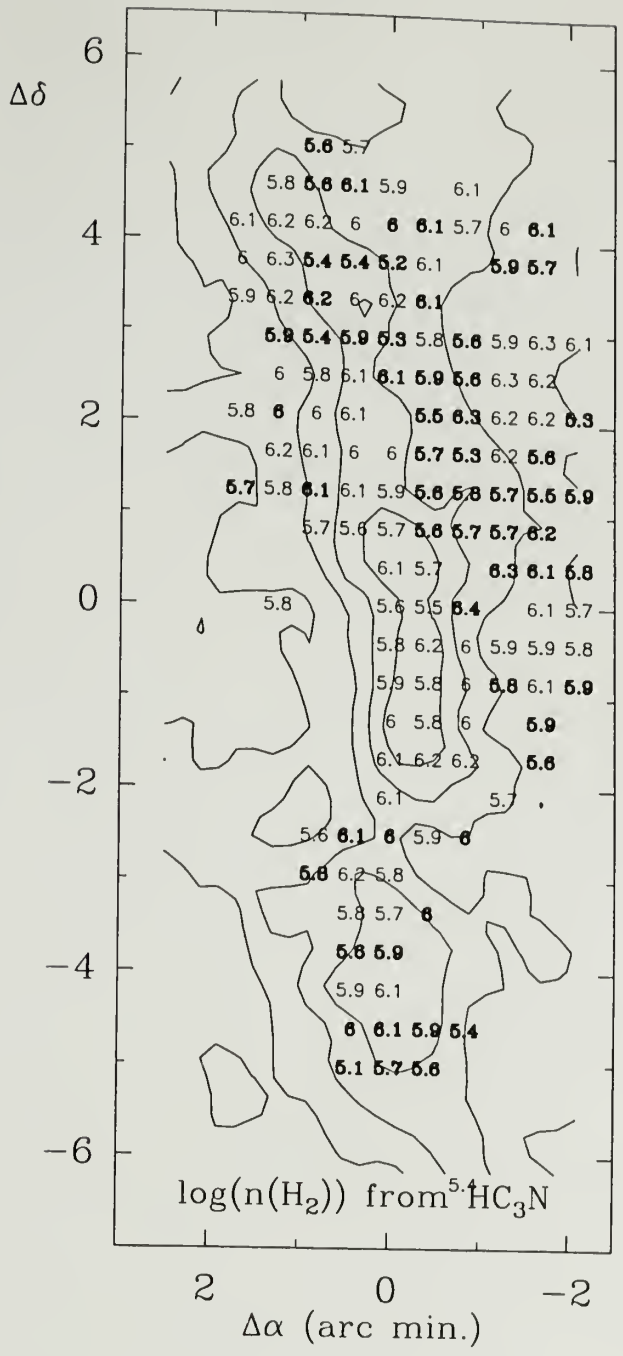

Figure 3.7. A map of the density of molecular hydrogen in Orion as determined from our model fits. The density values in bold face are actual determinations, while the other values are lower limits. The densities are overlaid on a $C^{18}O$ integrated intensity map from Ungerechts et al 1992 with contours at 2, 4, 6, and 8 K-km/s. The $C^{18}O$ integrated intensities are corrected for beam efficiency.

bright optical bar in Orion (see Figure 3.1), which was suggested by Rodriguez-Franco et al (1993) to be due to a drop in the HC_3N abundance.

One goal of this research is to examine whether the almost featureless density structure observed in several cloud cores by Snell et al (1984) and Mundy et al (1986) is also obtained when using an optically thin tracer and incorporating a temperature model for the dense gas in cores. An examination of the density structure, compared with the distributions of the total column density, shows that the peaks in column density do not appear as maxima in the gas density in agreement with the results of Snell et al (1984). It appears that the positions where our model fits could not determine an upper limit to the density cluster predominantly in the central portion of the ridge, suggesting that there may be a density enhancement there. However, the presence of many actual determinations scattered throughout the core, with both high and low column density, tends to argue against a density variation across the core. Thus, the density structure observed in the Orion A core, using an optically thin tracer with an improved temperature model for the source, shows no evidence of large scale variations in the density.

3.5.2 M 17

Figure 3.8 presents a map of the density in M 17. Like Orion these data show no evidence of large systematic variations in density. Densities in M 17 are typically $n_{H_2} \sim 10^6$ cm^{-3} and are quite similar to the values derived by Wang et al (1993) using CS. The corresponding column densities, which are listed in Table 3.3, span an order of magnitude with the greatest column densities towards the northern condensation where the HC_3N emission peaks. The fact that the highest densities do not occur at positions of peak column density is underscored by the fact that the density at the northern condensation is $n_{H_2} = 8 \times 10^5$ cm^{-3}, a value similar to that found at the lowest column density regions.

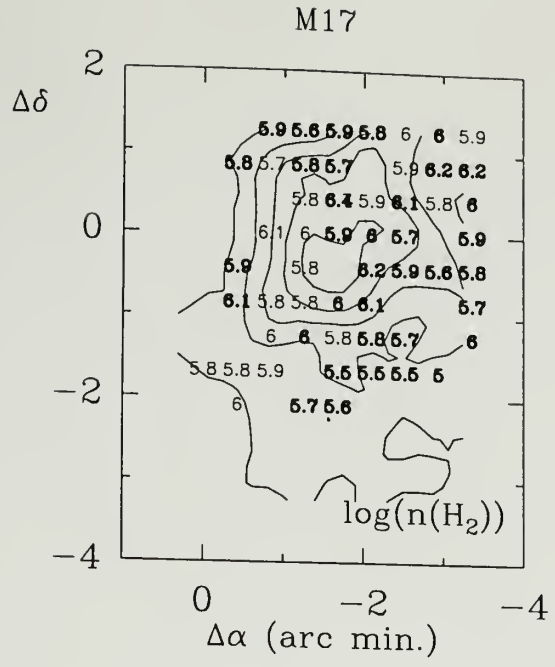

Figure 3.8. Same as in Figure 3.7 for M 17. The densities are overlaid on a $C^{18}O$ integrated intensity map from Goldsmith, Bergin, & Lis (1995) with contours at 4, 8, 12, 16, and 20 K-km/s. The $C^{18}O$ integrated intensities are corrected for beam efficiencies.

The positions where we have only lower limits to the density cluster predominantly on the eastern edge of the map near the column density maximum, while the lowest densities observed in M 17 appear in the northwestern corner of the map where the column density is lowest. This structure suggests that material near the interface with the H II region may be slightly denser than deeper in the core. However, this cannot be confirmed on this basis of these data since the density determinations near the interface are primarily lower limits. The higher resolution study by Wang et al (1993) found no evidence of these effects, although this study used only two transitions of CS to derive densities and assumed a uniform temperature for the core of $T_k = 50$ K.

We have investigated the effects on our density determinations of assuming a uniform temperature of 50 K, as adopted by both Snell et al (1984) and Wang et

al (1993). We find that using a constant temperature induces an artificial density gradient in the cloud, with densities being greater near the interface and decreasing with distance away from the H II region. This effect is simply understood by examining the temperature structure presented in Chapter 2. The gas temperature peaks near the interface where temperatures are ~50 K and decreases into the cloud to temperatures near 30 K. A uniform temperature of 50 K underestimates the densities in the central portion of the cloud (see section 3.4.3.2) while the density determinations near the interface, where the temperature is near 50 K, are unaffected. Therefore including an improved temperature model for M 17 lowers the density variation throughout the source.

3.5.3 Cepheus A

The density structure of Cepheus A is presented in Figure 3.9. Because of the weak HC_3N emission in Cepheus A we were able to derive densities in much fewer positions than in the other two sources. The density in Cepheus A ranges from $n_{H_2} = 10^{5.4}$ cm^{-3} to values $> 10^6$ cm^{-3}. Over this range the column density changes only by a factor of 3. In Cepheus A, as in Orion and M 17, the regions with the highest column density have only lower limits to the density. This systematic result, which has not been observed in previous density studies, is probably due to the fact that the temperatures from methyl acetylene are lower than the temperatures used in prior work (for Orion and M 17), requiring densities near the critical density of the highest transition we have observed to reproduce the observed emission.

The molecular emission morphology in Cepheus A has a very centrally condensed structure (see Figure 3.3), with the compact H II regions located close to the peak emission. With such a simple structure it is compelling to suggest that there may exist a simple density gradient increasing from the edge of the dense core to the center. Studies of dust emission (Colomé and Harvey 1993) have

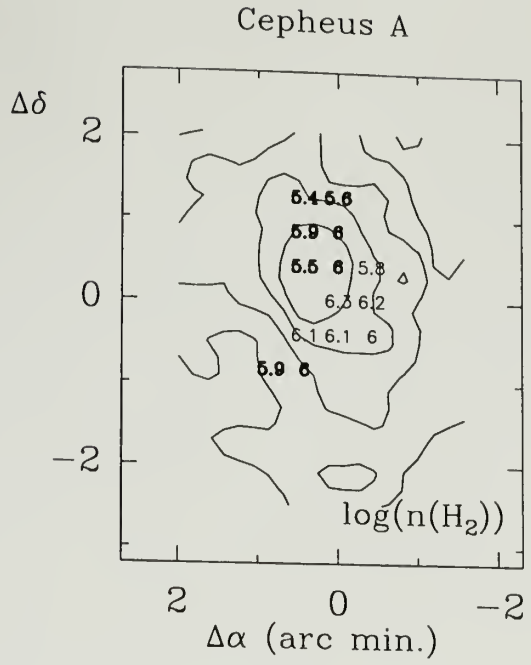

Figure 3.9. Same as in Figure 3.7 for Cepheus A. The densities are overlaid on a $C^{18}O$ integrated intensity map from Goldsmith, Bergin, & Lis (1995) with contours at 2, 4, 6, and 8 K-km/s. The $C^{18}O$ integrated intensities are corrected for beam efficiencies.

suggested such a centrally peaked density structure. However all of the HC_3N data are reasonably well fitted by a single density and these results show no evidence for a centrally peaked density structure. Observations of higher-J transitions of HC_3N would help in clarifying the issue of a density gradient.

3.6 Discussion

The results presented in the previous sections showed that for the three GMC cores studied the density does not change appreciably over the cloud core. Indeed, within the 3σ errors, the density determinations for all three clouds at almost any position can be considered the same. The lack of large scale structure in the density persists despite the use of an improved temperature model for each source and the use of an optically thin tracer. These results support the conclusions of

other studies (Snell et al 1984; Mundy et al 1986; Snell et al 1986; Wang et al 1993) that little density variation exists across GMC cores, in spite of the fact that the column density varies by over an order of magnitude over the same areas.

The lack of density variations led Snell et al (1984) to postulate that the cloud cores are composed of numerous small high density clumps that have a volume filling factor much less than unity, but each antenna beam encompasses many clumps. The volume filling factor decreases from the center of the cloud to the edge producing the observed variation in column density. This assertion has been supported by numerous other observations (cf. Goldsmith 1995).

Additional evidence for a clumpy structure can be obtained by examining the total gas column density. Table 3.5 presents the density of molecular hydrogen, and the column densities of HC_3N and $C^{18}O$ (taken from Goldsmith, Bergin, & Lis 1995) for a representative position in each cloud core. We also give estimates of the depth of each cloud, assuming that the depth of the cloud is equivalent to the half power width seen in the $C^{18}O$ emission. Using the $C^{18}O$ column density in Orion from Table 3.5 and the $C^{18}O$ abundance calculated by Frerking, Langer, and Wilson (1982) of $X(C^{18}O) = 1.7 \times 10^{-7}$, the H_2 column density is $N(H_2)$ $= 5 \times 10^{22}$ cm^{-3}. If we assume that this column to be filled by material at $n_{H_2} = 10^{5.9}$ cm^{-3}, the depth of the cloud is only 0.02 pc. Since the high density ridge has a width of $\sim$0.4 pc, the region would have to be extremely flattened along the line of sight, with a width to depth ratio of 20 to 1. Since the $C^{18}O$ column densities, densities, and size scales listed in Table 3.5 are quite similar for all three cores, M 17 and Cepheus A would also need to have very flattened geometries. The only plausible resolution of this dilemma is that the dense gas is filling only a small percentage of the cloud volume.

There have been several studies of the degree of clumping in molecular clouds. Many of these utilize observations of M 17 (Martin, Sanders, & Hull 1984; Greaves,

Table 3.5. Cloud Core Parameters

Cloud	$\Delta\alpha$	$\Delta\delta$	$\log[n_{H_2}]$	$\log[N(HC_3N)]$	$\log[N(C^{18}O)]^a$	L	f_c
	(′)	(′)	(cm^{-3})	(cm^{-2})	(cm^{-2})	(pc)	
Orion	-0.42	+2.94	$5.9^{+0.1}_{-0.4}$	13.6	15.9	∼0.4	0.05
M 17	-2.10	0.00	$6.0^{+0.8}_{-0.3}$	13.6	16.4	∼1.2	0.04
Cepheus A	0.00	0.46	$6.0^{+1.0}_{-0.3}$	13.3	16.1	∼0.4	0.06

[a] $C^{18}O$ column densities from Goldsmith, Bergin, & Lis (1995)

White, & Williams 1992; Hobson, Jenness, Padman, & Scott 1994; Stutzki & Gusten 1990) although others have targeted other clouds (Perault, Falgarone, & Puget 1985; Falgarone, Puget, and Perault 1992). These studies have examined both the spatial and velocity structure inherent in the molecular emission maps in order to empirically identify clumps of emission. The study of Stutzki & Gusten (1990) found > 100 clumps within the M 17 core, over a similar region to the maps shown in Figures 3.2 and 3.8, with a volume filling factor of 13% for the *dense* gas.

We can estimate the volume filling fraction from the data in Table 3.5 by assuming that the $C^{18}O$ column density is tracing the same dense component as HC_3N. Assuming that the total column density is dominated by the clumps then,

$$N_{H_2} = \frac{N^{18}}{X^{18}} = n_c L f_c, \qquad (3.1)$$

where N^{18} is the column density of $C^{18}O$, X^{18} the fractional abundance of $C^{18}O$, n_c is the density in the clumps, L is the line of sight depth of the cloud, and f_c is the clump volume filling fraction. We have used this expression with the $C^{18}O$ abundance of Frerking, Langer, & Wilson (1982) and the density and cloud depths given in Table 3.5 to estimate the volume filling factor for each cloud. These estimates are also listed in Table 3.5. The filling factors for each cloud are quite similar and suggest that the dense gas is filling only ∼5% of the cloud volume, which is consistent with the results of Stutzki & Gusten (1990).

If the clumps, with $n_{H_2} \sim 10^6$ cm^{-3}, fill only a small percentage of the volume then the density of the interclump medium must be below $\sim 10^4$ cm^{-3}, as densities

much higher than this are inconsistent with the fits to the HC_3N intensities (see Section 4.3.2). Similar results were found by Mundy et al (1986) in their multitransition study of $C^{34}S$. Thus, the HC_3N and $C^{34}S$ data imply a large clump to interclump density ratio of ~ 100. This large ratio is consistent with models to explain the observed C^+ emission which require a low density interclump medium (Stutzki & Gusten 1990; Howe et al 1991; Burton, Hollenbach, & Tielens 1990).

The above analysis assumes that the $C^{18}O$ emission is arising solely from the dense gas. Because of the low excitation requirements of $C^{18}O$, the interclump medium may, in fact, contribute to the $C^{18}O$ emission. We can use the above information to constrain the contribution of the interclump gas to the $C^{18}O$ emission. Assuming that the total column density of $C^{18}O$ is the sum of the column densities in the two components, the column density of $C^{18}O$ in the clumps, N_c^{18}, and the column density of $C^{18}O$ from the interclump medium, N_{ic}^{18},

$$N(C^{18}O) = N_c^{18} + N_{ic}^{18}. \tag{3.2}$$

This can also be expressed as:

$$N(C^{18}O) = n_c L X_c^{18} f_c + n_{ic} L X_{ic}^{18} (1 - f_c), \tag{3.3}$$

where n_c and X_c^{18} are the density and $C^{18}O$ fractional abundance in the clumps, and n_{ic} and X_{ic}^{18} are the density and fractional abundance of $C^{18}O$ in the interclump medium. If we assume equal abundances of $C^{18}O$ in clumps and in the interclump medium and use the derived limit on the clump to interclump ratio then Eqn (3) shows that the emission from $C^{18}O$ is dominated by clumps unless $f_c < 0.01$. Therefore, it is unlikely that the interclump medium is contributing substantially to the $C^{18}O$ emission, provided the estimated volume filling fractions are reasonably well determined. This result is consistent with the the good agreement between $C^{18}O$ and $C^{34}S$ clumping in M 17 (Stutzki & Gusten 1990).

This conclusion is strengthened, requiring even smaller clump filling factors, if the abundance of $C^{18}O$ in the interclump medium is lower than the $C^{18}O$ abundance in the dense clumps. There is some evidence that the $C^{18}O$ abundance may indeed be lower in the interclump material. Models of the clumpy photodissociation regions have shown that the interclump material is the limiting factor in determining the UV penetration (Meixner & Tielens 1993). The interclump gas will have enhanced photodissociation rates, possibly destroying the $C^{18}O$. The high density clumps, on the other hand, will absorb the UV radiation in the outer layers, allowing $C^{18}O$ to survive in the interior. Photodestruction of $C^{18}O$ is a more complicated process than for other molecules, such as HC_3N, because $C^{18}O$ (and CO) photodissociation is dominated by a line rather than a continuum process. Therefore these species are able to efficiently self-shield, which enables CO and its isotopes to survive in a region with a stronger radiation field than for other molecules. Since the efficiency of the self-shielding process is dependent on the abundance, it is possible for ^{12}CO, and its other isotope ^{13}CO, to exist in regions with little $C^{18}O$.

Some evidence for this stratification can be found by examining ^{12}CO J = 2 $\rightarrow$ 1 and $C^{18}O$ J = 2 $\rightarrow$ 1 emission in M 17 (Lada 1991; Stutzki & Gusten 1990). Comparison of the emission morphology reveals a region near the northern condensation devoid of $C^{18}O$ emission but characterized by strong CO emission (Meixner et al 1992). Meixner et al (1992) suggest that warm molecular material, traced by CO, is filling the material between clumps evident in the $C^{18}O$ emission. Other evidence can be found in the double isotope ratio, $^{13}CO/C^{18}O$, found in GMC cores. Taylor & Dickman (1989) demonstrated that in GMC cores this ratio exhibits a strong dependence on column density, with ratios much larger than the solar value towards lines of sight with small $C^{18}O$ column densities. Taylor and Dickman (1989) found that these variations could only be accounted for in a

clumped gas with fractionation and isotopic selective photodestruction raising the $^{13}CO/C^{18}O$ ratio. Fractionation will increase the abundance of ^{13}CO, while isotopic selective photodestruction lowers the $C^{18}O$ abundance. However, given the warm temperature of GMC cores, isotopic selective photodissociation will dominate over fractionation (Taylor 1989), thereby resulting in a lower $C^{18}O$ abundance on the edges of dense clumps and in the interclump medium.

3.7 Summary

We have observed the J = 4 → 3, J = 10 → 9, J = 12 → 11, and J = 16 → 15 transitions of HC_3N in the Orion A, M 17, and Cepheus A cloud cores. We have utilized the results of a previous study of the temperature structure of the dense gas in the same cloud cores with these data in order to obtain reliable measurements of the density of molecular hydrogen in giant molecular cloud cores. By using temperatures determined for the dense gas for each source, this study examined the density structure of molecular clouds in a more systematic and detailed fashion than in previous studies.

The multitransitional data were fit with a non-LTE model to derive the density of molecular hydrogen and the HC_3N column density. Densities were determined for 133 positions over a $4' \times 12'$ region in Orion, 55 positions over a $4' \times 5'$ area in M 17, and 14 positions within a $4' \times 5'$ region in Cepheus A. In spite of differences between the three clouds the density range for each core was found to be very similar, with densities between $n_{H_2} = 3 \times 10^5$ and 5×10^6 cm^{-3}. We find that in numerous instances, because of our choice of transitions, we were unable to determine the density, but instead were only able to establish lower limits to the density for these lines of sight.

The primary goal of this research is to examine whether the results of previous studies of the density structure of molecular cloud cores is reproduced by using both an optically thin tracer and incorporating a better temperature model for the

source. Our results, based on data that cover hundreds of positions within each core, are that changes in the density do not correlate with changes in total column density and that there is no evidence for a large scale variation in the hydrogen density of molecular cloud cores. These data therefore support the results of previous studies which have utilized other tracers and used a single temperature for the entire core. We have examined the effect on the density determinations by including a different model of the temperature structure of the core and found that variations in the temperature reduces the variation in density strengthening the conclusion that the density does not follow changes in column density.

Our data agree with a model in which molecular cloud cores are composed of numerous dense clumps which are smaller than the beam and fill a fraction of the cloud volume. An examination of the filling factors implied by an assumed cloud depth suggests that the dense gas is filling only $\sim$5% of the volume. The HC_3N emission is dominated by the dense, $n_{H_2} \sim 10^6$ cm^{-3}, clumps and to achieve consistency with the fits to the HC_3N data the density of the gas in the interclump medium must be $\lesssim 10^4$ cm^{-3}. This indicates that the clump to interclump density ratio is > 100. An examination of the implications of a high clump to interclump density contrast suggests that the emission from the low dipole moment molecule $C^{18}O$ is also dominated by the dense gas.

Chapter 4

Chemical Structure in the Orion A Molecular Core

4.1 Introduction

In this chapter we will discuss the chemical structure in the Orion A core. In particular we will present observations of the GMC chemical survey in Orion previously introduced in Section 1.1. These observations present the most detailed view of the chemical structure in any cloud core, over the largest area, to date. A brief discussion of the differences in the emission morphologies will lead into a presentation of the principal component analysis that was performed on these data (Ungerechts et al 1992). The principal component analysis is used to delineate areas where possible chemical differences may exist. Relative column densities are then determined for these separate positions to examine whether the differences are related to abundance gradients across the cloud or whether they are related to changes in the physical conditions which were discussed in the two previous chapters.

4.2 Observations

The Orion observations of the molecular transitions listed in Table 1.1 were carried out during the 1991 and 1992 observing seasons using the 15-element QUARRY focal plane array (Erickson et al 1992) mounted at the Cassegrain focus of the 14m FCRAO telescope. The two spectrometers used were both 32 channel filterbanks with resolutions of 250 kHz and 1 MHz. The corresponding velocity resolutions will vary with molecule (depending on the transition) and ranges from

0.65 - 0.88 km s^{-1} (250 kHz) and 2.6 - 3.5 km s^{-1} (1 MHz). All of the maps were placed on the same grid of $4.5' \times 12'$ (360 positions with $25''$ sampling) centered on the embedded Orion BN/KL complex at $\alpha(1950) = 5^h32^m46.8^s$, $\delta(1950) = -5°24'28''$. The observations were taken in single sideband mode and utilized position switching with the following reference position: $\alpha(1950) = 5^h27^m00^s$ and $\delta(1950) = -5°20'00''$. This position was examined and found to be free of ^{12}CO emission. The standard chopper wheel calibration method was used, placing all observations on the T_A^* scale.

The main beam efficiency then corrects for the coupling of a source which fills only the main beam of the antenna (Kutner and Ulich 1981). For a discussion of the applicability of the main beam efficiency for these observations see Section 2.2. Since most of the chemical analysis will be done with line ratios the absolute value of the calibration is unimportant.

The primary filterbank used in this study was one with 250 kHz resolution. However, due to the energetic events at and surrounding the Orion KL/BN position, the observed linewidths for some species are often greater than the total bandwidth of the 250 kHz filterbank ($\sim$ 25 km s^{-1}). For the following species: CO, ^{13}CO, SO, ^{34}SO, SO_2, and HC_3N the data from the 1 MHz filterbanks was used to replace the 250 kHz data for several (at least 9 positions) surrounding the central KL/BN position. This will provide more accurate integrated intensities for these species and therefore will lead to greater accuracy in determining column densities.

The resolution of the 14m telescope ($45'' - 60''$) is insufficient to resolve the hot core component which gives rise to some of the observed large linewidths. The size of the hot core measured from HC_3N is $\sim 11'' \times 7''$ (Masson & Mundy 1988), which is in close agreement with the H_2CO observations of Mangum et al (1993) of $\sim 11'' \times 9''$. With a small source size our observations of the hot core will suffer from the effects of beam dilution. This will only be a problem for those species

observed here which are present in abundance in the hot core, plateau, and compact ridge sources (^{12}CO, SO, ^{34}SO, SO_2, and HC_3N). For a discussion of the chemical stratification between these separate components see Blake et al (1987). Because of this effect we will concentrate solely on total integrated intensities for this position without separating out each component observed in the velocity profile as is commonly done. Any abundance determinations for the species mentioned above in the hot core or plateau will be lower limits. *It is important to note that the line profiles for most molecules suggest that their emission is tracing only the ridge component and therefore this survey is primarily concerned with changes in abundance in the "quiescent" molecular ridge.*

4.3 Morphological Differences

Figures 4.1 - 4.6 present the integrated intensity maps for all species listed in Table 1.1. The contour levels for each molecule and transition are listed in Table 4.1. These maps show that no single "morphology" or structure is applicable for the Orion A core. Some species, CO, SO, SO_2, CH_3OH, and HCO^+, show strong emission near the two star forming sites (KL/BN and 1.5′S), while other molecules, such as C_2H and N_2H^+, exhibit emission maxima at the radical-ion peak 3′ north of BN/KL. Still other species show almost flat morphologies (e.g. CN). These differences underscore the point presented by Goldsmith (1991) that our view of cloud structure can appear quite different depending on which tracer is being used. Whether the various morphologies observed in Figures 4.1 - 4.6 are related to true abundance variations remains to be seen and will be examined in Section 4.4.

4.3.1 Principal Component Analysis

In order to better quantify the morphological differences present in the maps a principal component (PC) analysis was performed on this data set by H.

Table 4.1. Contour levels for Figures 4.1 - 4.6

Species	Transition[a]	Levels (K km s^{-1})
CO		50 to 550 by 25
^{13}CO		5 to 55 by 5
$C^{18}O$		0.4 to 4.4 by 0.4
CS		5 to 50 by 5
$C^{34}S$		0.5 to 5.0 by 5
HCO^+		5 to 90 by 5
$H^{13}O^+$		0.3 to 2.4 by 0.3
N_2H^+		0.5 to 8.5 by 0.5
CN	$F = 3/2 \rightarrow 1/2$	1 to 5 by 1
	$F = 5/2 \rightarrow 3/2$	1 to 15 by 1
C_2H		0.5 to 4.5 by 0.5
SO	$J_K = 3_2 \rightarrow 2_1$	1 to 4 by 1; 10 to 120 by 10
	$J_K = 2_3 \rightarrow 1_2$	1 to 4 by 1; 10 to 120 by 10
	$J_K = 4_5 \rightarrow 4_4$	1 to 19 by 2
^{34}SO		1 to 4 by 0.5
HCN		10 to 80 by 10; 100 to 300 by 25
$H^{13}CN$		1, 2 to 26 by 2
HNC		2 to 20 by 2
$HN^{13}C$		0.2 to 0.8 by 0.2
CH_3OH		0.5 to 7.5 by 0.5
C_3H_2		0.2 to 1.2 by 0.2
HC_3N		0.5 to 5.0 by 0.5
CH_3C_2H		0.2 to 1.4 by 0.2
SO_2		0.5, 1.0, 5 to 55 by 10

[a] Transitions are only listed where necessary.

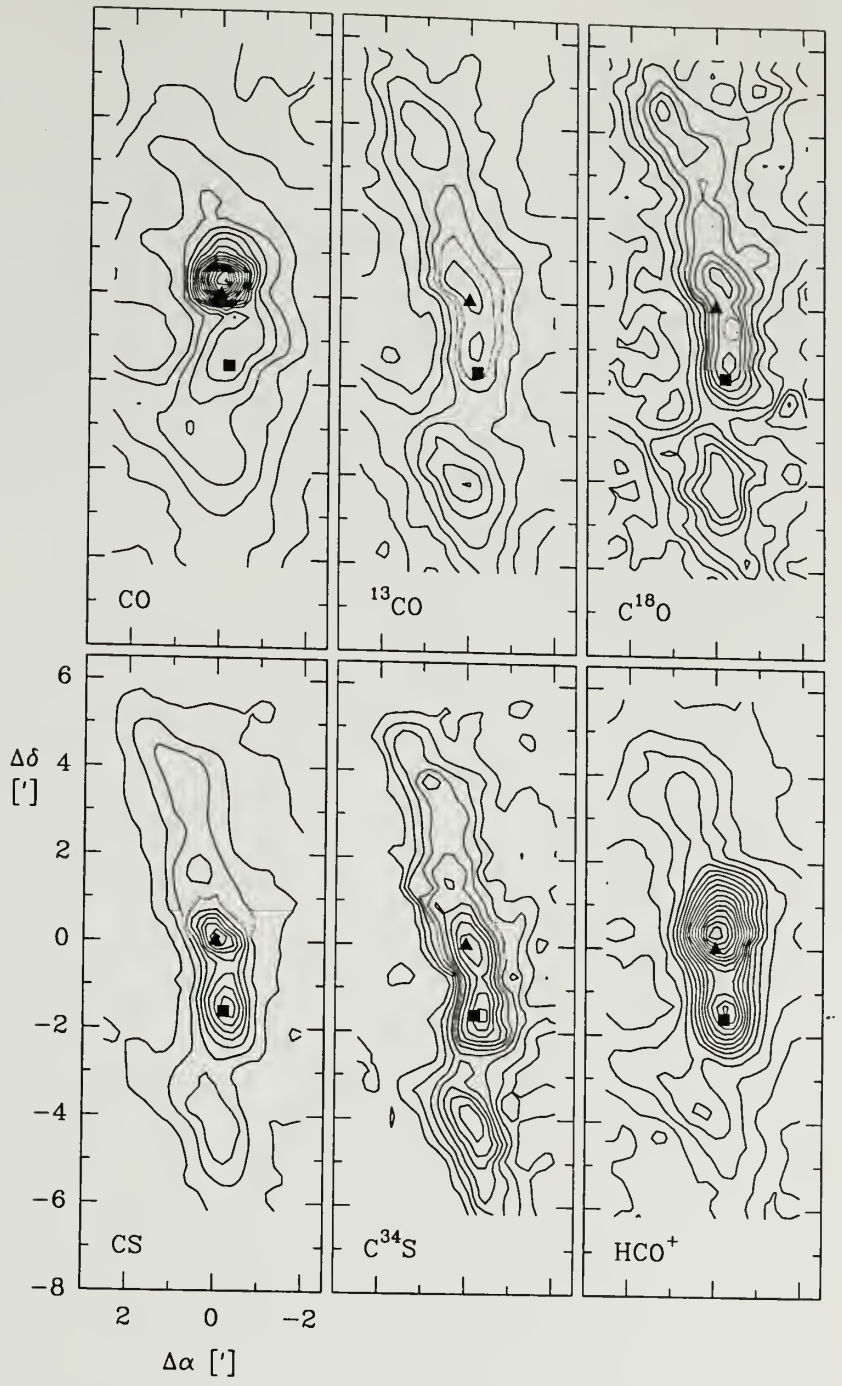

Figure 4.1. Integrated intensity distributions of CO, ^{13}CO, C^{18}O, CS, C^{34}S, and HCO$^+$ in Orion. The triangle denotes the position of BN/KL and the square is the position of the southern star forming site, Orion 1.5′S. The transitions are listed in Table 1.1 and the contour levels and spacing are listed in Table 4.1.

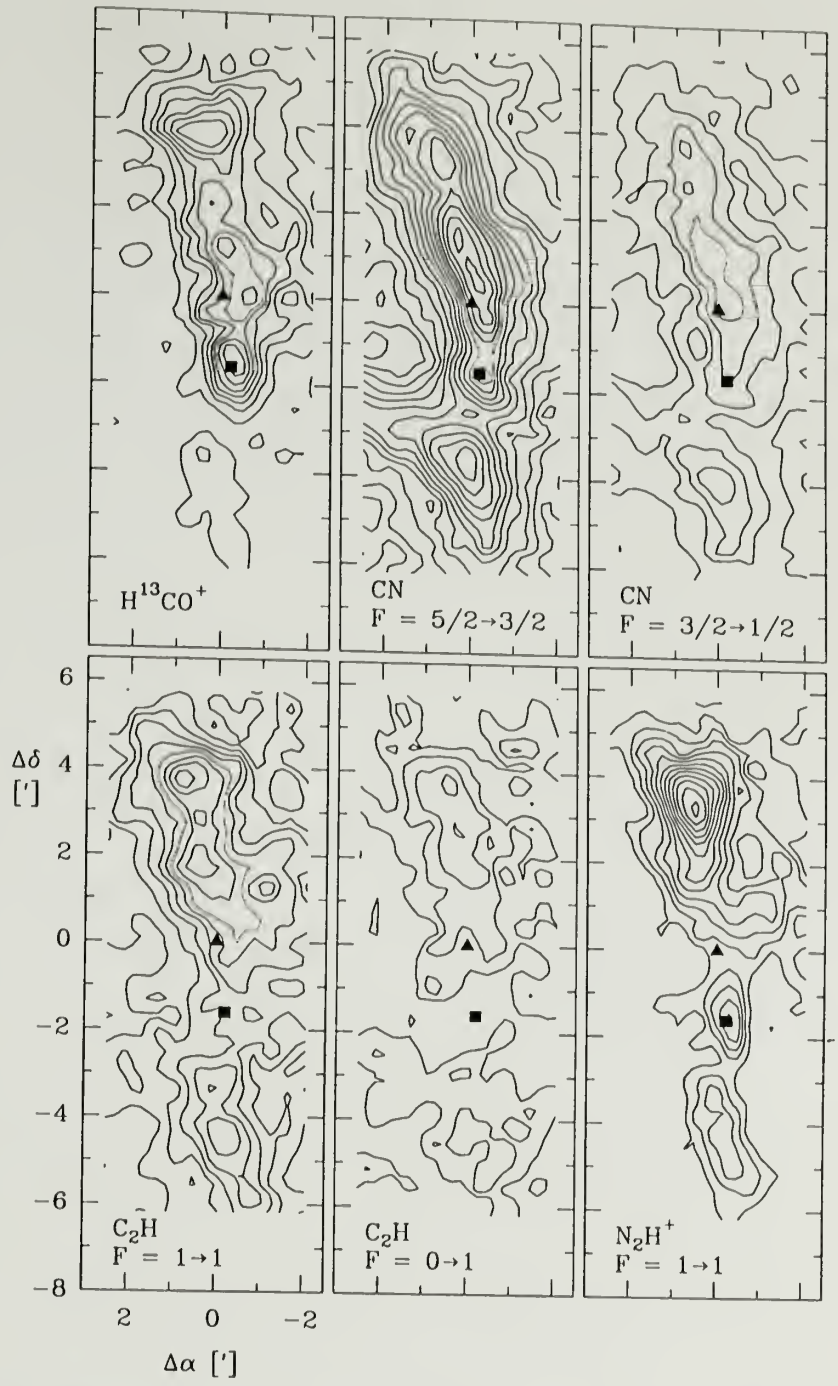

Figure 4.2. Integrated intensity distributions of $H^{13}CO^+$, CN $F = 5/2 \rightarrow 3/2$, $F = 3/2 \rightarrow 1/2$, C_2H $F = 1 \rightarrow 1$, $F = 0 \rightarrow 1$, and N_2H^+ $F = 1 \rightarrow 1$ in Orion. The triangle denotes the position of BN/KL and the square is the position of the southern star forming site, Orion 1.5′S. The transitions are listed in Table 1.1 and the contour levels and spacing are listed in Table 4.1.

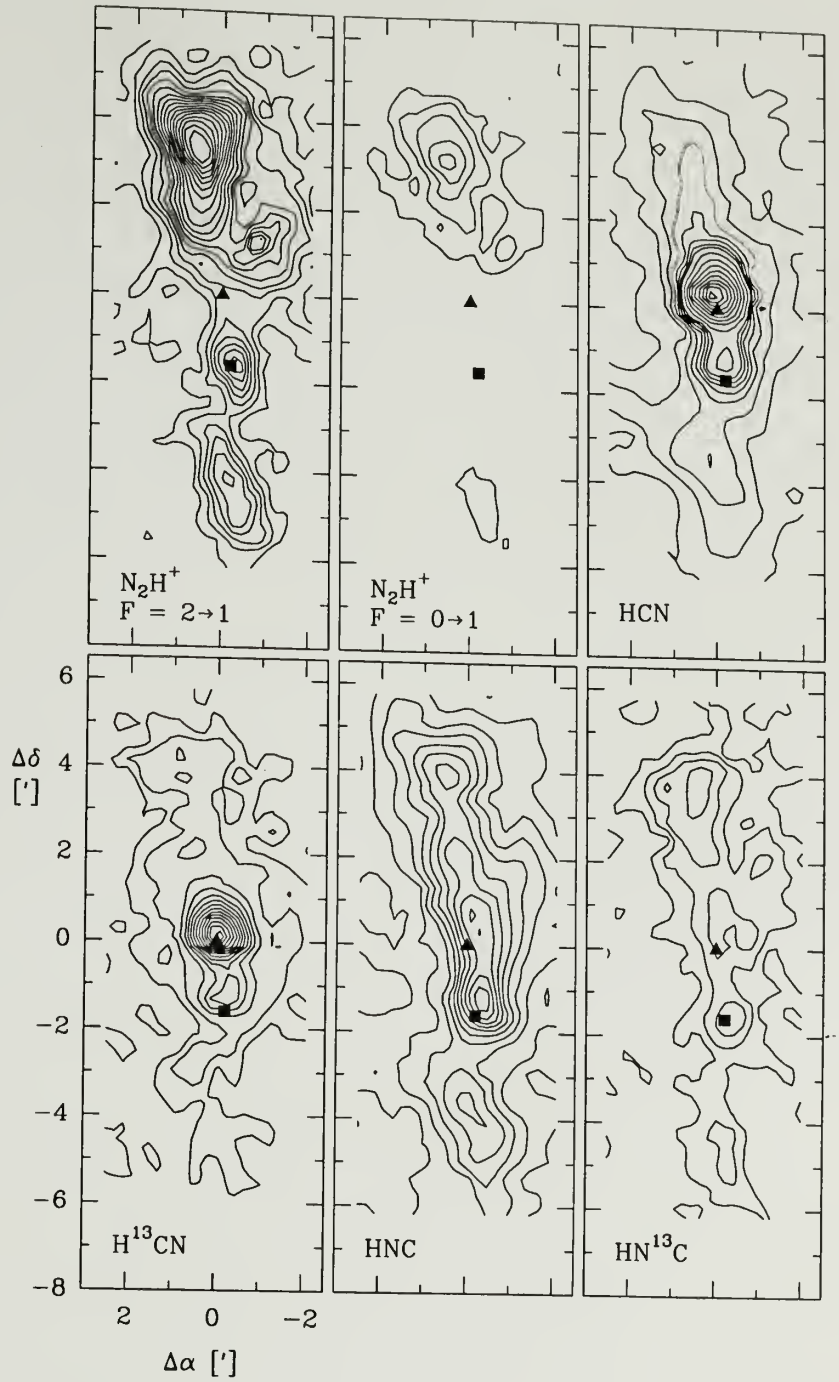

Figure 4.3. Integrated intensity distributions of N_2H^+ $F = 2 \rightarrow 1$, $F = 0 \rightarrow 1$, HCN, $H^{13}CN$, HNC, and $HN^{13}C$. in Orion. The triangle denotes the position of BN/KL and the square is the position of the southern star forming site, Orion 1.5′S. The transitions are listed in Table 1.1 and the contour levels and spacing are listed in Table 4.1.

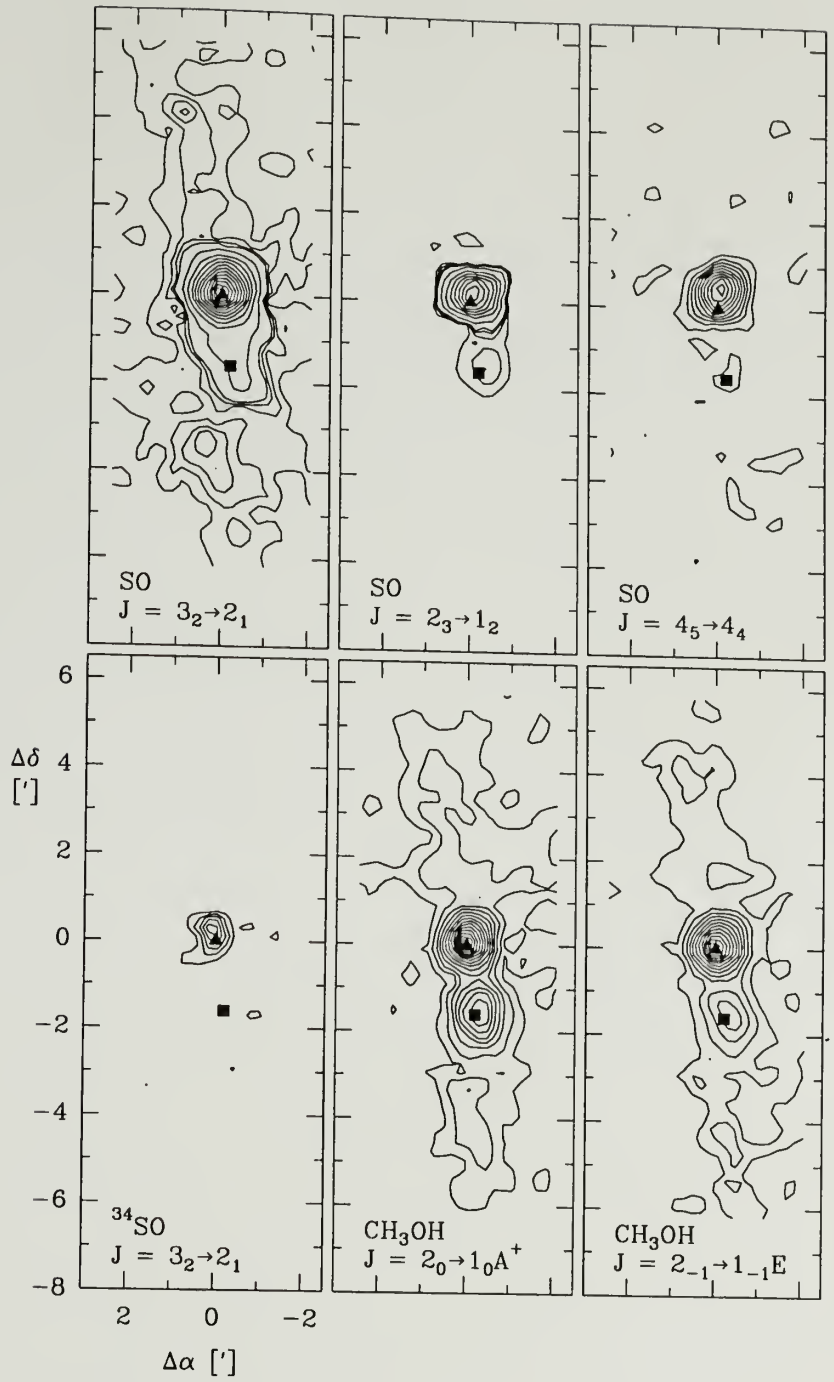

Figure 4.4. Integrated intensity distributions of SO $J = 3_2 \rightarrow 2_1$, $J = 2_3 \rightarrow 1_2$, $J = 4_5 \rightarrow 4_4$, ^{34}SO, CH_3OH $J = 2_0 \rightarrow 1_0A^+$, and CH_3OH $J = 2_{-1} \rightarrow 1_{-1}E$ in Orion. The triangle denotes the position of BN/KL and the square is the position of the southern star forming site, Orion 1.5′S. The transitions are listed in Table 1.1 and the contour levels and spacing are listed in Table 4.1.

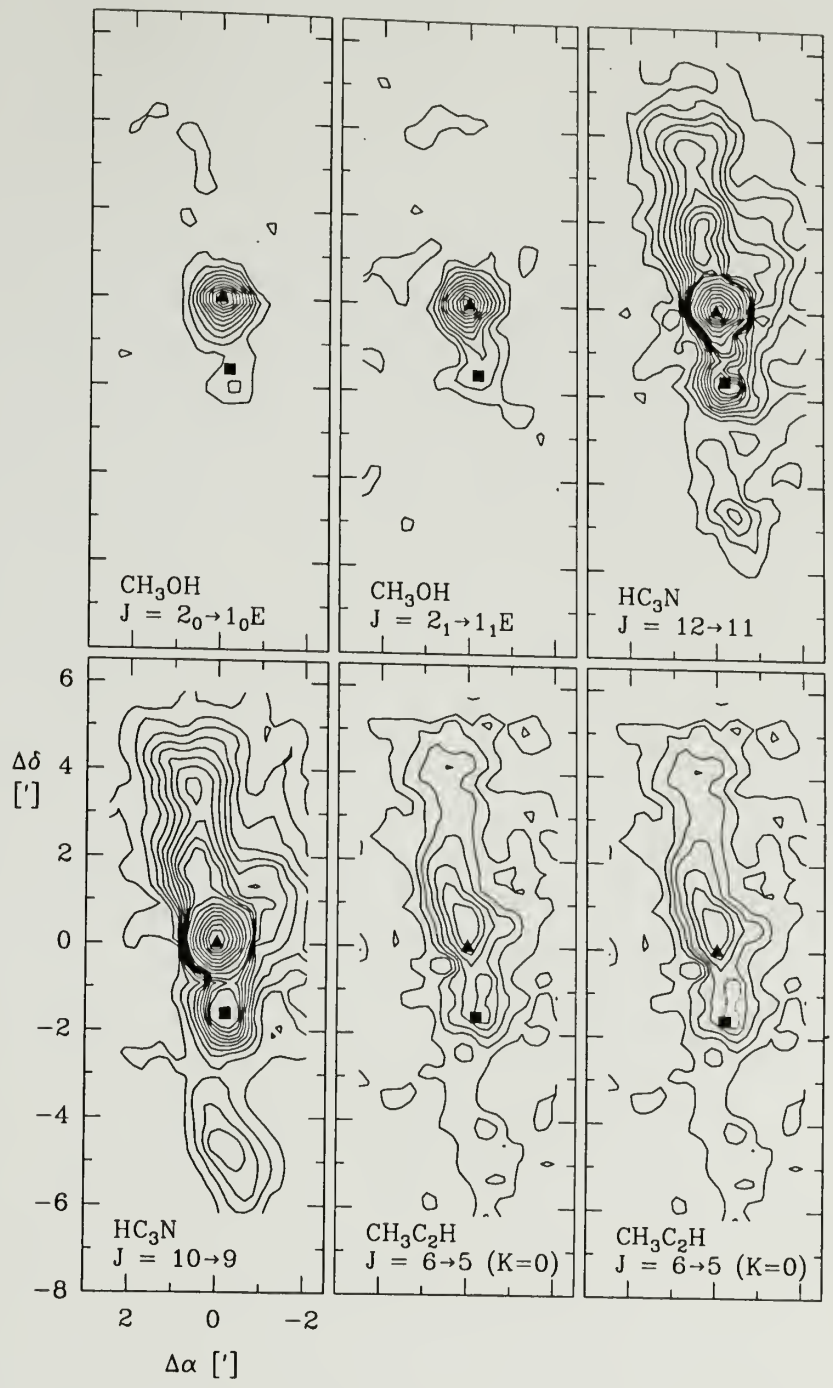

Figure 4.5. Integrated intensity distributions of CH_3OH $J = 2_0 \rightarrow 1_0E$, CH_3OH $J = 2_1 \rightarrow 1_1E$, HC_3N $J = 12 \rightarrow 11$, $J = 10 \rightarrow 9$, and CH_3C_2H $J = 6 \rightarrow 5(K = 0, 1)$ in Orion. The triangle denotes the position of BN/KL and the square is the position of the southern star forming site, Orion 1.5'S. The contour levels and spacing are listed in Table 4.1.

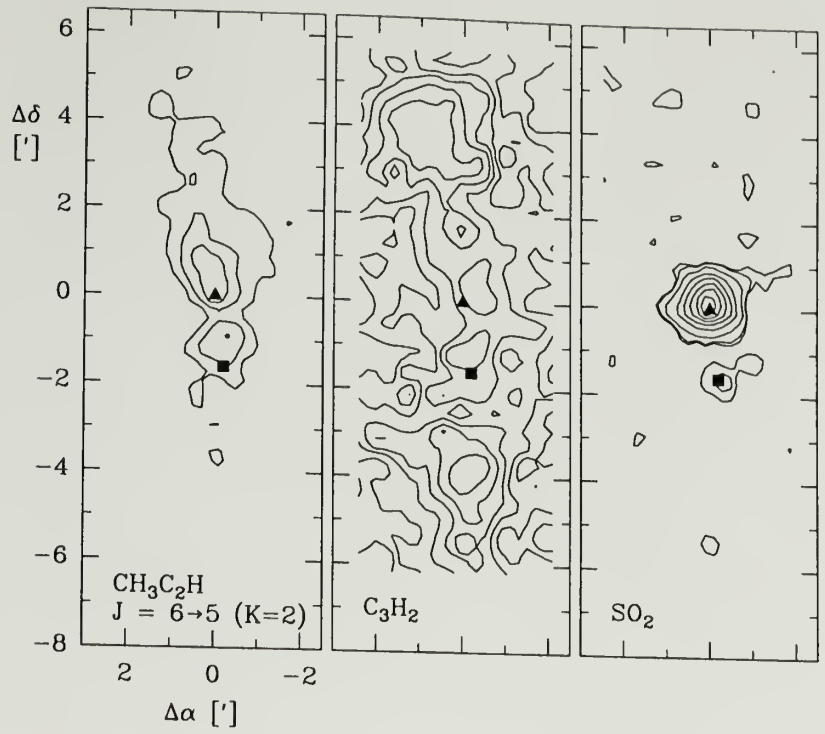

Figure 4.6. Integrated intensity distributions of CH_3C_2H $J = 6 \rightarrow 5(K = 2)$, C_3H_2, and SO_2 in Orion. The triangle denotes the position of BN/KL and the square is the position of the southern star forming site, Orion 1.5′S. The transitions are listed in Table 1.1 and the contour levels and spacing are listed in Table 4.1.

Ungerechts. For an excellent discussion of principal component analysis the reader is referred to Mittaz, Penston, & Snijders (1990). Here we provide only a brief outline of the method so that the reader will understand the uses of the technique as presented here. The main use of the analysis will be to identify a few positions that are representative of the morphologies that are seen in the various molecules for abundance determinations.

Principal component (PC) analysis is a useful technique for multivariable analyses, such as our survey, which involve maps of 33 transitions for 360 positions or essentially a space of 33 $\times$ 360 dimensions. The objective of the technique is to reduce the number of independent variables, or to ask whether we can explain *all* the variations observed in our data with fewer than 33 dimensions. Are the variations observed in Figures 4.1 - 4.6 unique in the sense that they have nothing in common or do some common factors exist, such that each observations (i.e. each molecular transition map) can be reconstructed by a linear combination of a small number of variables. The best example of this in astronomy is the HR diagram. While this diagram was not constructed with this technique, the fact that millions of stars show up on the main sequence, when their luminosities are plotted against their temperature, shows that each star has something in common and that the sample is not composed of millions of unique objects.

Common features exist in our data set and are easily observed in Figures 4.1 - 4.6. The observations of all 3 SO transitions show the same morphology. Molecules with optically thick emission: CO, HCO^+, and HCN also have similar distributions in their emission. Thus these data can certainly be reconstructed by fewer than 33 dimensions. The actual technique of PC analysis involves deconstructing the multivariate data set into a number of principal components. The first principal component (PC1) contains the most variance in the data. The second principal component (PC2) contains the most variance when the first component is removed

from the data. The remaining components are constructed in a similar manner. A more detailed discussion of this technique as applied to this survey is presented in Ungerechts et al (1992).

Each map of molecular emission can be reconstructed by a linear combination of the principal components, with each transition receiving different contributions in the reconstruction process from the separate components. This is best exemplified by examining the maps of the principal components that were created from the emission maps shown in Figures 4.1 - 4.6. The distribution of the principal components in Orion A is presented in Figure 4.7. Examining PC1, the distribution is similar to almost any of the molecules we have observed: a peak is seen near KL, Orion 1.5'S, and additional peaks are observed at the radical-ion position and the column density peak southwest of the Bar. This map has no negative contours because all molecules receive a positive contribution from PC1. PC2 has a negative feature at KL/BN and positive contours to the north and south. Thus this component is delimiting some of the differences seen in the data, where some molecules have peaks at the radical-ion position (e.g. N_2H^+), while others have strong emission only at BN/KL (e.g. SO, CH3OH). PC3 further differentiates the structure seen in the maps, and points out variations between the material far north (radical-ion peak) and south of BN/KL (the Bar).

The panels at the top show the amount of variance included in each component: PC1 contains 60% of the variance while PC2 has about 15% of the variance. Higher components >5 are all in the noise of the data. One conclusion from this analysis is that these data can be reconstructed from $\ll 33$ components (Ungerechts et al 1992). Another conclusion from Figure 4.7 is that, since every molecule receives a positive contribution, although varying in magnitude, from PC1, it is contributions of PC2 and PC3 that contain most of the variations

observed in the data. The first component therefore accounts for what all molecules have in common.

The mapping of the principal components back to the data is easy to understand by examining Figure 4.7. To consider this we will take CH_3OH and N_2H^+ as examples. The CH_3OH emission in Figure 4.5 exhibits a strong peak at BN/KL and weak emission north and south. The reconstruction of this distribution from the principal components can be obtained by subtracting some multiple of PC2 (and PC3) from PC1. This enhances the BN/KL peak while de-emphasizing the northern and southern peaks. The opposite is required for N_2H^+, N_2H^+ has a strong positive contribution from PC2 that removes the central peak and enhances the emission at the radical-ion position.

The principal components have therefore determined regions which may have different emission properties. These are: BN/KL which shows up strongly in all components and the southern star forming site (1.5′S) which is observed in PC1. The southern site also seems to be different from BN/KL in PC3. Other interesting features are the radical-ion peak and the peak observed 4′ due south of BN/KL. The characteristics of these positions are strongly contrasted to to the emission observed towards BN/KL in PC2, The last region of significance is the molecular Bar which is differentiated from the northern half of the ridge in PC3.

The importance of the PC analysis to this particular work is that the above discussion has suggested that each molecular map is not composed of 33×360 independent points. Instead they are all composed of a smaller number of components that are spatially represented in the maps of the principal components in Figure 4.7. Therefore we can use the PC analysis to isolate specific regions that are possibly physically and/or chemically different. This technique allows a further economization of the chemical analysis by allowing the computation of chemical properties for a small number of positions while still being able to examine all of

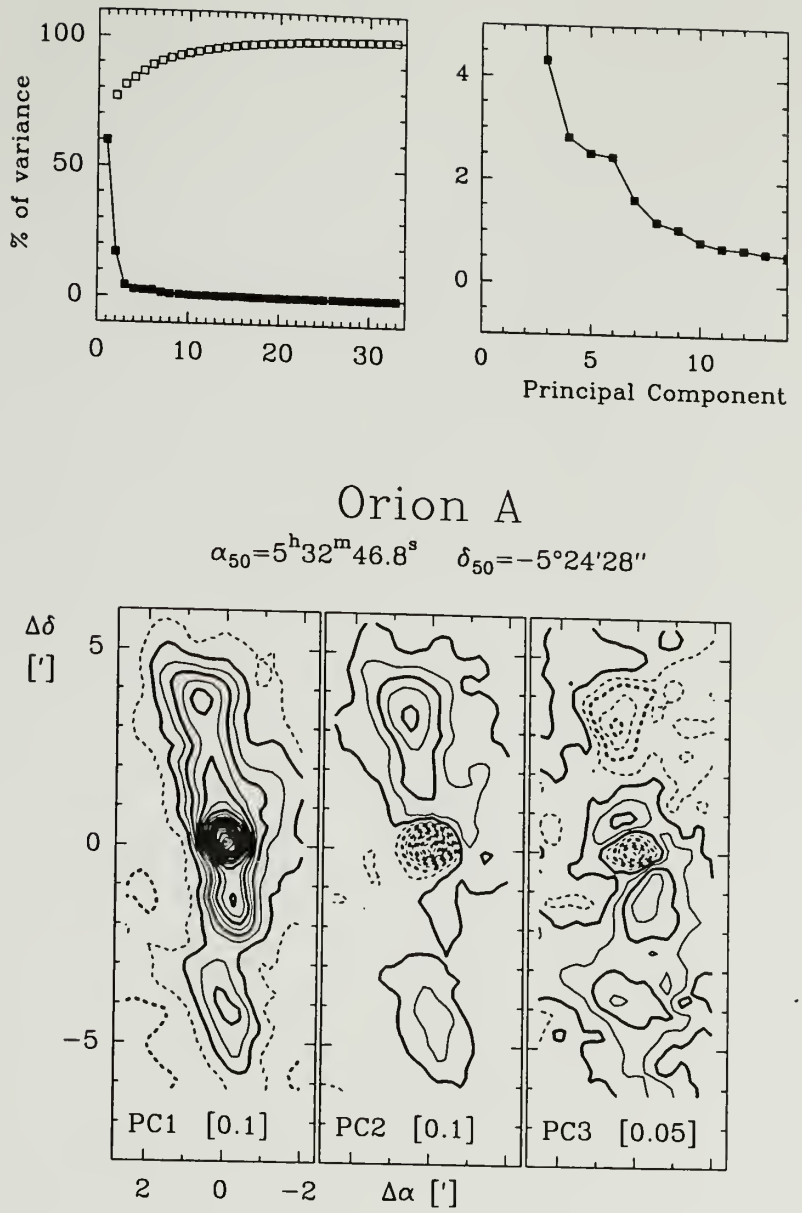

Figure 4.7. Principal components of the distribution of molecules in Orion A. Top panels: percentage contributed by each principal component to the total variance in the data (filled squares); cumulative percentage (open squares). Bottom panel: distribution of the first three principal components. The numbers in the brackets give the contour spacing and the dashed contours denote negative values (taken from Ungerechts et al 1992).

the variations observed in the data. For this purpose we have chosen 6 positions, these positions are listed in Table 4.2 along with the nomenclature that will be used to refer to each in the text. In the next section we will briefly discuss some of the previously known information on each region selected by the PC analysis.

4.3.2 Selected Representative Positions

Table 4.2 lists the positions that were selected on the basis of the PC analysis as being representative of the emission in the Orion A core. The first position, labeled RIP (for radical-ion peak) is $\sim 3'$ N of the star forming cores (and θ^1C). The RIP is characterized by sharp peaks in the emission of the ions N_2H^+ and $H^{13}CO^+$; and the radicals CN and C_2H. Because the radiation field towards the RIP is believed to be lower than the other 5 positions, the RIP *may* be least affected by photodissociation of any of the positions examined. The next position is only 1.2′N of the Orion KL/BN core and is labeled as the Ridge. This point is closer to the star forming cores and is useful to examine trends between the RIP and KL/BN. There is also a neutral carbon clump observed by White and Sandell (1995) that is spatially coincident with this position.

The third point is the well studied Orion KL/BN star forming core. This position has several velocity components along the line of sight that are typically distinguished by the characteristics of the velocity profile. Because the our poor velocity resolution (32 channels per pixel with resolution of 0.65-0.85 km s^{-1} per channel) and bandwidth ($21 - 27$ km s^{-1}) we have not attempted to separate them. Instead we treat emission as a single component. The sole exception is HC_3N. The HC_3N emission from the quiescent ridge component was isolated for the density study and we have used these results (see Chapter 3).

The next position, Orion 1.5′S, is the southern star forming site. This position is prominent in the maps of the dust continuum emission (Keene et al 1982). The star forming site is less luminous than Orion KL/BN but does show signs of star

Table 4.2. Orion Positions of Interest

$\Delta\alpha(')$	$\Delta\delta(')$	Label
+0.42	+3.36	RIP
+0.42	+1.26	Ridge
0.00	0.00	Orion KL
0.00	-1.26	Orion-1.5′S
-0.42	-4.62	Orion-4′S
+1.26	-2.97	Bar

formation activity (see McMullin et al 1992). Orion 4′S is a strong peak seen in the emission of several molecules, $C^{18}O$ for one, and has been isolated by the principal component analysis as having different emission characteristics than the two star forming regions.

The last position is the molecular counterpart to the bright optical Bar. This position is quite weak or non-existent in the emission of many molecules but shows up prominently in the emission of CN and CO. The Bar is illuminated by the hot O star θ^1C, and to a lesser extent θ^2A, which provide a local enhancement of the radiation field.

4.4 Determination of Total Column Densities

An objective of this study is to derive accurate relative column densities for all molecular species observed at several positions in Orion. In order to reduce complications due to radiative trapping we will only determine column densities for those species which we believe are optically thin. Although, as noted in Chapter 3, when clumps are taken into account even optically thin species may have moderate opacities. Table 4.3 lists the species which are nominally optically thin. The question of opacity for these species will be discussed later in the section. Computing abundances involves not only determining the column densities, but also attempting to understand whether the emission from the different molecules is probing the same layers of the cloud. We will examine this question first before discussing the method used to derive column densities.

Table 4.3. Thin Species

$C^{18}O$
$C^{34}S$
CN
C_2H
N_2H^+
HCO^+
$H^{13}CN$
$HN^{13}C$
SO
CH_3OH
CH_3C_2H
HC_3N

4.4.1 Averaging Spectra to Determine Principal Moments

One method to examine whether molecules are probing the same layer is to compare the principal moments (line center velocity and velocity linewidth) observed in the emission spectra for each molecule. If the line center velocity and the linewidth for each species are in agreement then it is reasonable to assume that the different molecules are probing the same layer of gas. We should note that while this is a reasonable assumption, it does not answer this question definitively.

To determine the line center velocity and linewidths for the 6 positions listed in Table 4.2 we have averaged several spectra surrounding each position. This will increase the signal to noise in each spectra, aiding in the fitting process, and will be particularly helpful for those species with weak emission (for example $HN^{13}C$). For every position, except for the Bar, spectra from the four nearest neighbors were averaged to the central position. This corresponds to a "cross" around the chosen point. Since the sampling interval was 25″, and the beam size is typically 50″, these positions are not independent of the other. Because the Bar was weak in many species we have decided to average 7 spectra along the Bar oriented in a NE to SW fashion. The positions used in the Bar average are listed in Table 4.4.

Table 4.4. Bar Positions

$\Delta\alpha(')$	$\Delta\delta(')$
0.42	-3.36
0.84	-3.36
0.84	-3.78
1.26	-2.94
1.26	-3.36
1.68	-2.94
2.10	-2.52

Figures 4.8 - 4.13 present the average spectra for the optically thin species at each of the six positions. Excluding Orion KL/BN, the emission profiles for each species, in general, look quite similar. The most notable difference is observed towards the Bar where HC_3N has weak emission centered $\sim 7-8$ km s^{-1} while other species such as CN and $C^{18}O$ have emission near 9-10 km s^{-1}. This is the first, and strongest (again excluding Orion KL/BN) indication line of sight stratification in the data. The molecules with emission centered near 10 km s^{-1} are probing the Bar itself while the other species are emitting from the background ridge cloud (see Tauber et al 1994). This difference will be taken into account when we compare molecular abundances at the Bar.

The spectra presented in Figures 4.8 - 4.13 are a simple way to look for differences in the emission profile. We have also looked for differences in the profiles in a more systematic and objective manner via the following procedure. The 360 spectra for each molecule were fitted with a gaussian to determine the line center velocity (V_{lsr}) and the full-width at half-maximum or linewidth (Δv). In the cases where more than one frequency component were observed (i.e. molecules with hyperfine structure and others) the spectra were fit with multicomponent gaussians with fixed separation and a single linewidth, which is the same, for each of the components.

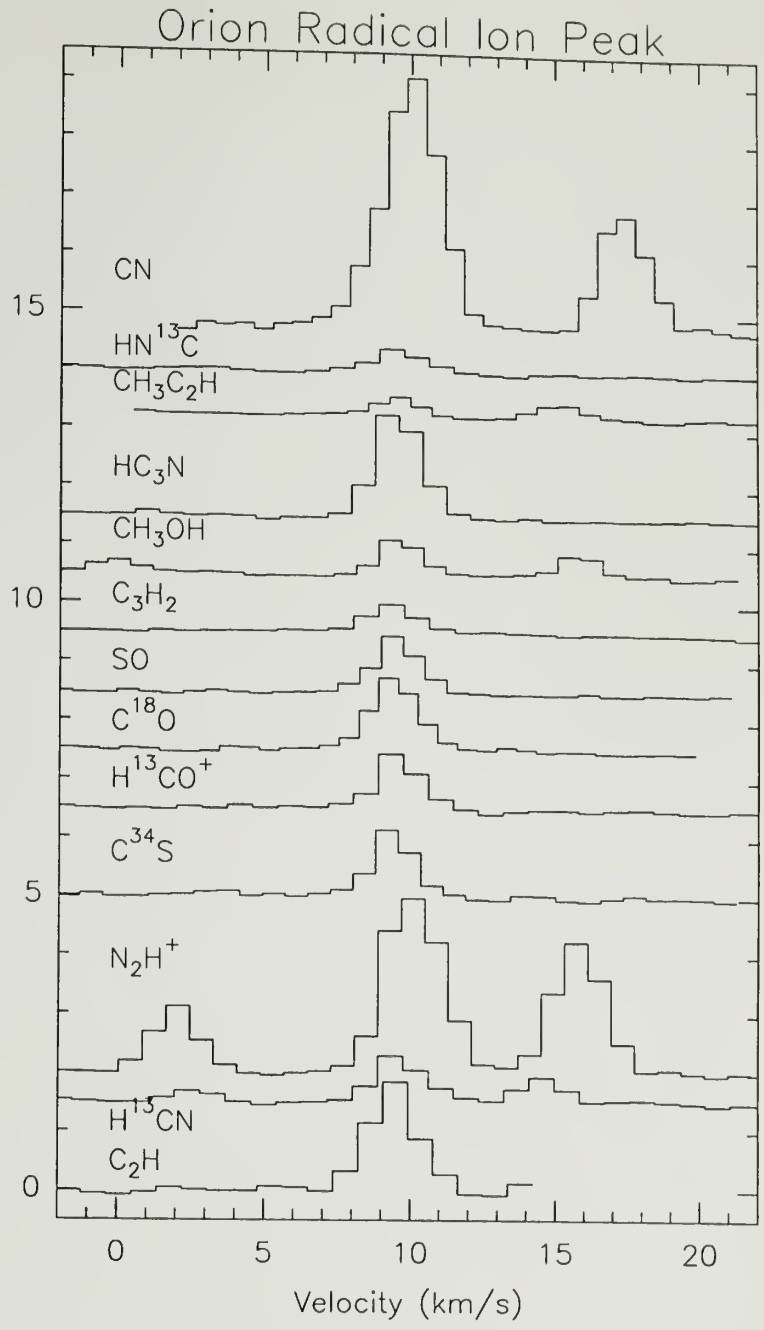

Figure 4.8. Spectra for the optically thin species towards the Radical-Ion peak.

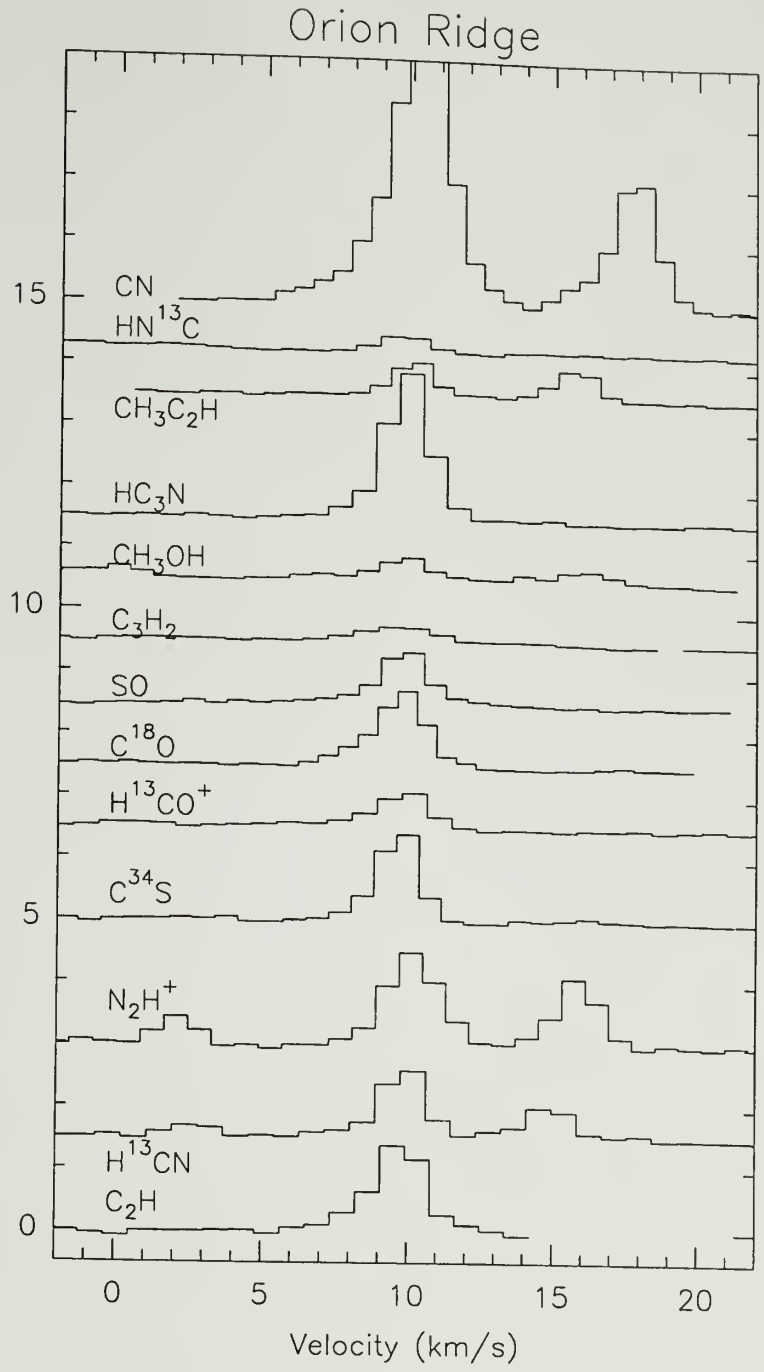

Figure 4.9. Spectra for the optically thin species towards the Ridge position.

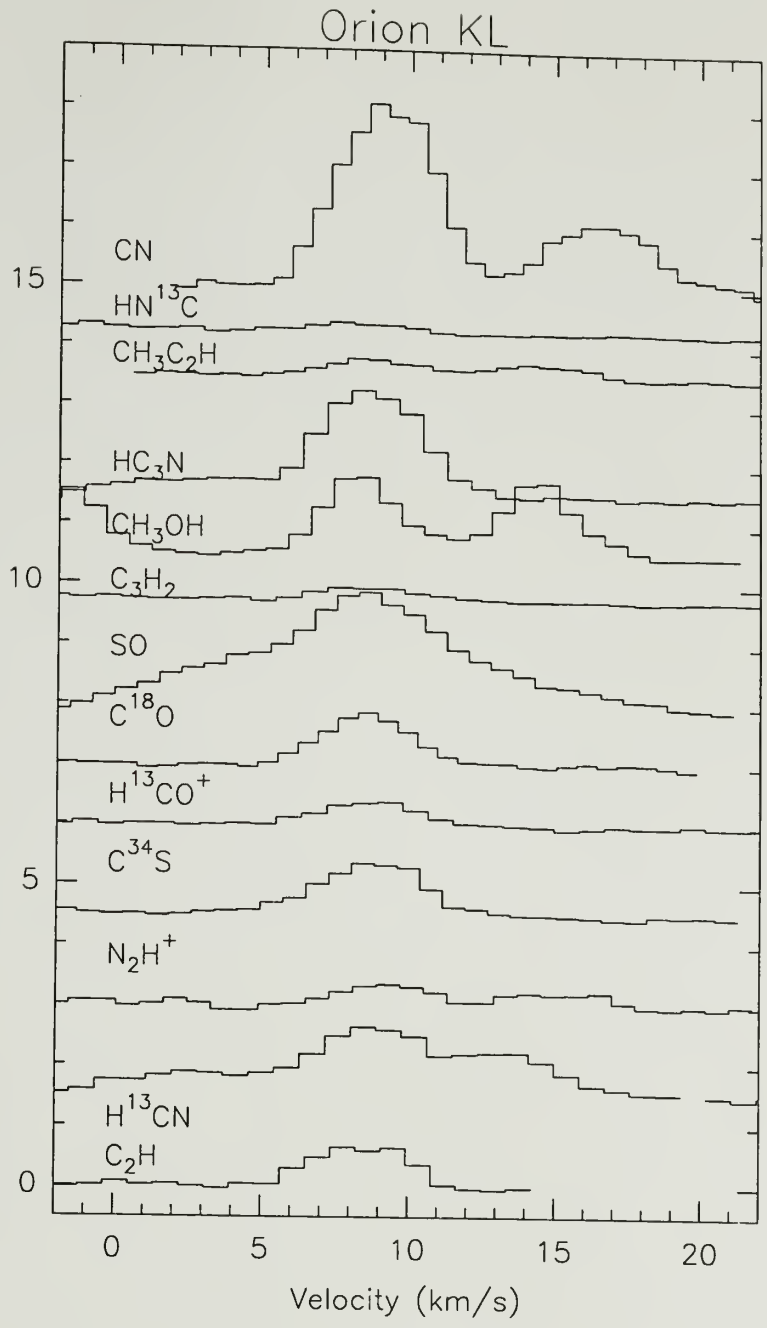

Figure 4.10. Spectra for the optically thin species towards the BN/KL core.

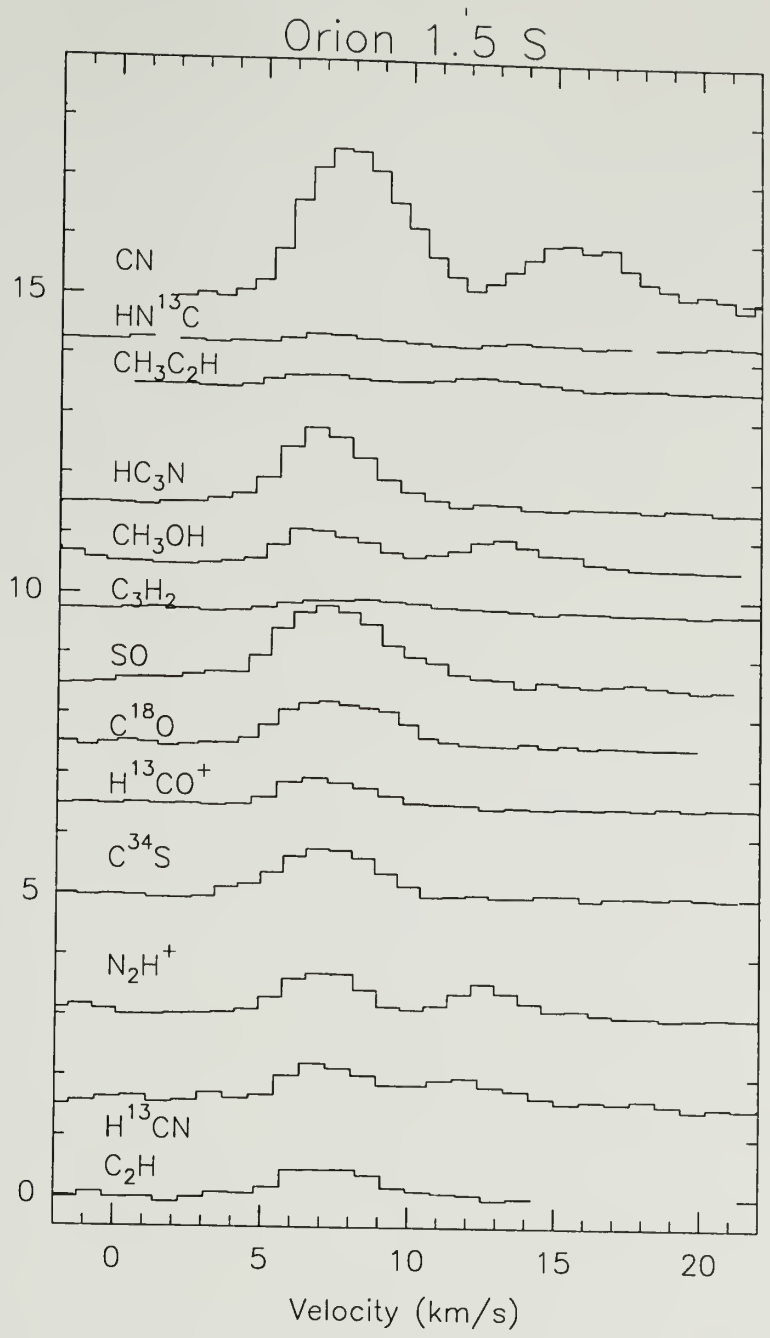

Figure 4.11. Spectra for the optically thin species towards Orion 1.5'S.

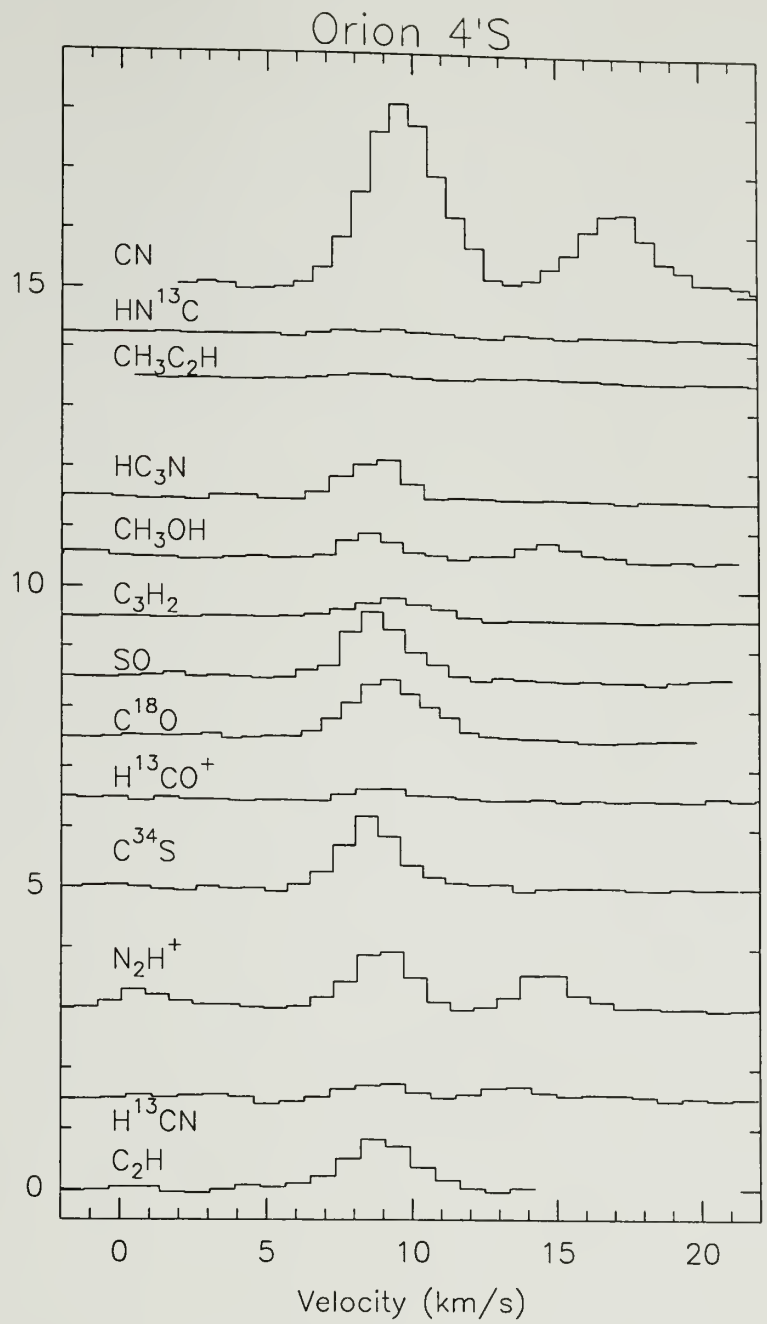

Figure 4.12. Spectra for the optically thin species towards 4′S peak.

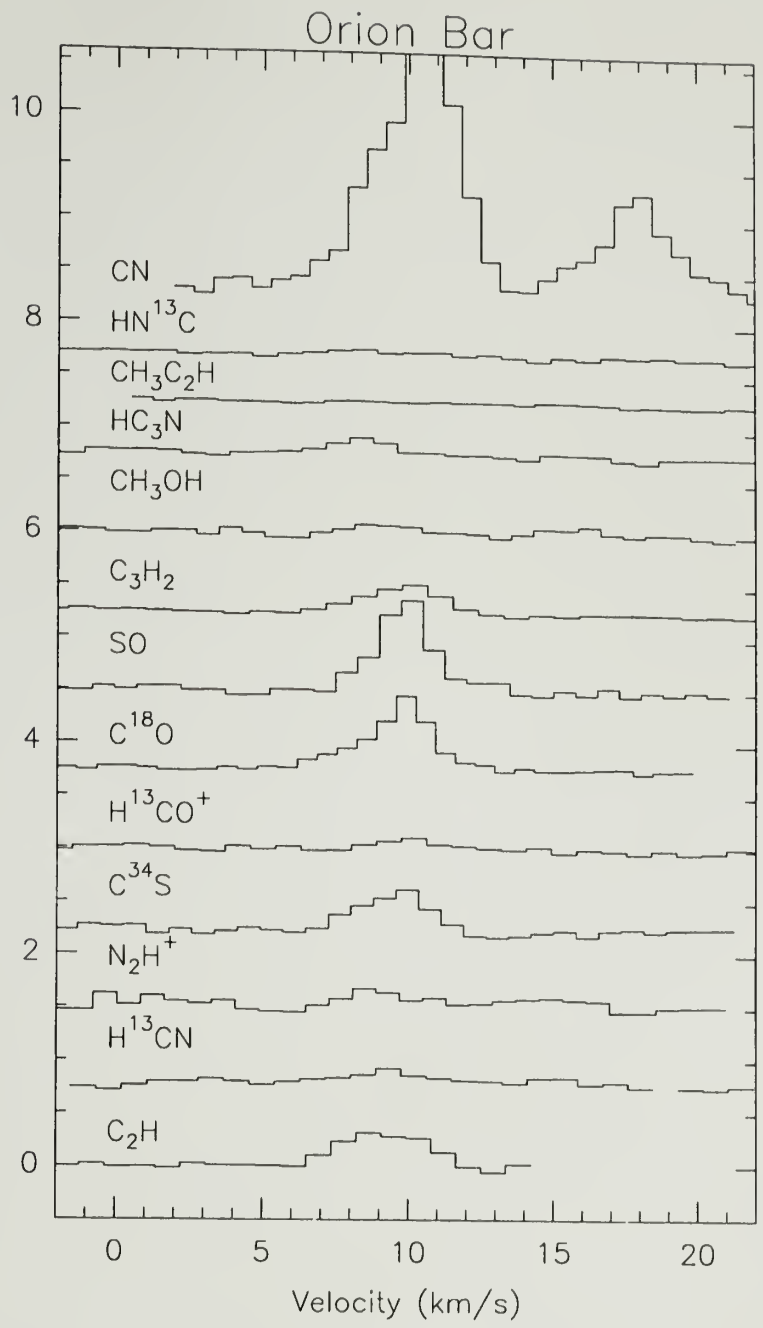

Figure 4.13. Spectra for the optically thin species towards Orion Bar.

Each line of sight is then described by a single average velocity and linewidth computed by averaging the velocities and linewidths of the optically thin molecules. These are defined as:

$$\overline{V}_j = \frac{\sum_{i=1}^{Nmol} V_{ij}}{Nmol} \tag{4.1}$$

and

$$\overline{\Delta v}_j = \frac{\sum_{i=1}^{Nmol} \Delta v_{ij}}{Nmol}. \tag{4.2}$$

Where the i subscript denotes the different molecules and j denotes the fact that each position possesses a separate average velocity, $Nmol$ is the number of optically thin species which are listed in Table 4.3. The lsr subscript on the velocity has been dropped. This average is used to compute χ^2 between the velocity of a given molecule and the average (over different lines of sight) in the following fashion:

$$\chi^2(V)_i = \frac{\sum_{j=1}^{360} (V_{ij} - \overline{V}_j)^2}{\sigma(V)_{ij}^2} \tag{4.3}$$

and

$$\chi^2(\Delta v)_i = \frac{\sum_{j=1}^{360} (\Delta v_{ij} - \overline{\Delta v}_j)^2}{\sigma(\Delta v)_{ij}^2}. \tag{4.4}$$

where $\sigma(V)$ and $\sigma(\Delta v)$ are the errors for the linewidths and velocities from the gaussian fits. The χ^2 computed in this fashion thus represents a measure of the total difference between the velocities and linewidths of a given molecule and all of the other molecules. Table 4.5 presents the χ^2 for each molecule. There is one additional factor that was utilized in this calculation. Typically the emission from each molecule is not detectable at all of the 360 positions over the map. For the positions with little or no emission, the gaussian fitting process typically fails to

Table 4.5. χ^2 Values

Species	$\chi^2(V)$	$\chi^2(\Delta v)$
CN	88.4	11.1
C_2H	15.2	3.1
$C^{34}S$	45.3	13.1
C_3H_2	17.1	13.1
CH_3C_2H	10.4	13.2
CH_3OH	18.4	22.7
$H^{13}CN$	5.7	18.0
$HN^{13}C$	14.0	3.0
SO	22.2	95.4
$C^{18}O$	39.2	14.1
HC_3N	34.9	6.4
N_2H^+	183.7	18.8
$H^{13}CO^+$	4.9	4.4

assign a fit to the spectrum. In order to take this into account χ^2 was not computed over all 360 positions, but only for those positions where the intensity of $C^{34}S$ was > 2.0 K. This will isolate only the densest part of the ridge. We examined using other species to set this "cutoff" and the results do not change appreciably.

We can immediately see from this table that the species that are present in the Orion hot core or plateau (with their larger linewidths) have the largest χ^2's in the linewidth column. These are SO, CH_3OH, and $H^{13}CN$. The other obvious result is the CN and N_2H^+ velocities have large deviations from the average. For these species this could be the result of several factors. Foremost among these is an incorrect frequency for the line. An examination of the difference between the CN velocity and the average velocity showed that the line center velocity for CN is typically greater than the average by a factor of $\sim$0.5 km s^{-1}. The line center frequency used for the CN N = 1 $\rightarrow$ 0; J = 3/2 $\rightarrow$ 1/2; F = 5/2 $\rightarrow$ 3/2 transition was $\nu = 115.49115$ GHz. The source for this frequency was from observational results by Turner and Gammon (1975). More recent laboratory measurements by Skatrud et al (1983) list the frequency as $\nu = 115.490943$ GHz which provides a

velocity correction of 0.547 km s^{-1}. This accounts for the observed differences between the CN velocities and the average.

The situation for N_2H^+ is more complicated. The frequency used for this transition was from the most recent laboratory results of Cazzoli et al (1985). The N_2H^+ ion has 7 hyperfine components in the $J = 1 \rightarrow 0$ transition. The laboratory reference resolved all of these components. We are centered on the strongest transition: the $F_1 = 2 \rightarrow 1$, $F = 3 \rightarrow 2$ component. In our study with the coarse velocity resolution and large linewidths associated with GMC cores we have resolved these 7 components into 3 components. The central component, seen in Figures 4.8 - 4.13, is a combination of three hyperfine components. Of these three components the frequency was centered on the middle component. An examination of the profiles in each of the figures reveals that the line centroid of emission for the central component of N_2H^+ appears to be at slightly higher velocities than other species.

This structure, with a slightly higher central velocity for the N_2H^+ line, could be observed if the emission from N_2H^+ is slightly optically thick. In this case of the central unresolved three hyperfine components, the component on the low frequency side will increase in intensity relative to the middle component, bringing the line to an "apparent" higher velocity (LTE ratio = 5:7:3, listed in order of increasing frequency). The difference in velocity between the low frequency component and the middle component is $\sim$0.9 km s^{-1} which is quite close to the observed shift. Thus we believe that the N_2H^+ velocity difference could be an effect of high optical depth and not due to any intrinsic difference in the velocity centroid. Higher resolution observations should be able to resolve the peaks of the different components and would be able to answer this question.

Outside of these glaring results, the χ^2 values in Table 4.5 show no apparent velocity differences. One molecule which might be expected to exhibit some

disagreement is $C^{18}O$. The ^{12}CO to HC_3N velocity comparison seen in Figure 2.14 shows that there exists a large difference between the CO velocities and the high dipole moment molecule HC_3N. However, the less abundant isotope of CO does not show such discrepancies in Table 4.5. The value of χ^2 for $C^{18}O$, for both velocities and linewidths, is a bit on the high side, but other species, such as $C^{34}S$ and HC_3N, have high values as well. Thus the result from this analysis is that there are no apparent differences between the velocities and linewidths between the different molecules, outside of the known variations near Orion KL/BN.

4.4.2 Method to Derive Relative Column Densities

With the assumption of optically thin emission and $T_{ex} \gg T_{bg}$, the column density in the upper state is directly related to the integrated intensity in K km s^{-1} via the following formula:

$$N_u = 10^5 \frac{8\pi k\nu^2}{hc^3 A_{ul}} \int T_R \Delta v \ \ (cm^{-2}) \tag{4.5}$$

Where ν is the frequency and A_{ul} is the spontaneous emission coefficient. The total column density is then simply related to the upper state column density by the faction in the upper state, f_u. To determine the fractional population assumptions must be made about the excitation. The typical assumption is that the molecular emission is in LTE at the local kinetic temperature. This raises the question as to what are the relevant temperatures for these lines of sight. We have decided to use the CH_3C_2H temperatures, presented in Chapter 2, for this purpose.

Ideally the average spectra in Figures 4.8 - 4.13 would be used to determine column densities. However each of the 5 positions that were used to create the average spectra had a separate (and independent) determinations of the kinetic temperature. Figure 2.8 shows the distribution of observed gas kinetic temperature in Orion. In this figure the 4 nearest neighbors to Orion KL/BN ($\Delta\alpha = 0.0$, $\Delta\delta =$

0.0; T_{gas} = 60 K) have a large spread in temperatures. We performed a weighted average of the temperatures around Orion KL/BN, using the 1σ errors from the determination and the "average" temperature would be 36 K. This is much lower than the temperature of 60 K observed towards this position. Using the average spectra will also not account for the changes in emission strength and central velocity which are quite sharp in some species towards the KL/BN position.

Because of these questions, and to account for possible changes in abundances from point to point, we have used the following method to determine column densities for each molecule. We once again use the central positions and its four nearest neighbors, but instead of averaging the emission we average the column density computed for each. Using the integrated intensities the column density in the upper state can be determine for each position on the cross. The only exception to this method is the Bar position which, because of its special characteristics, is dealt with in a separate fashion (see section 4.4.2.3).

The next step is to assume an excitation model and determine the total column density for each molecule (see discussion in the following section). The positions making the cross are then placed relative to a tracer of the total column density by dividing each position by the column density of $C^{18}O$. The relative column densities are averaged to form a single relative column density which is centered on the positions listed in Table 4.2. This method enables an examination to be made of the molecular column densities at each step in the process. If there exists significant point to point variations in abundances surrounding the central position this technique will enable a closer examination to be performed prior to forming an average relative column density.

One goal of this study is to determine reliable relative column densities. Since we have performed the study using a single telescope we have removed one of the largest contributions to the error that arises in comparisons between separate

molecular measurements: the telescopes' efficiency. As a matter of consistency and to minimize the risk of other errors being introduced we will examine the validity of some of the assumptions that are typically made in chemical studies. The primary method to determine abundances in chemical studies is to assume LTE to derive the total column density. This column density is divided by the column density of molecule that is a tracer of the H_2 column density, or normally $C^{18}O$. Before making these assumptions we will examine whether LTE is appropriate for the temperatures and densities observed in this study and examine the use of $C^{18}O$ as a tracer of the molecular hydrogen column density in *dense* regions.

4.4.2.1 The Validity of LTE

An examination of the LTE approximation for the determination of abundances is appropriate for this study because we have independent temperature and density information. Figure 2.8 presented a temperature map of the Orion ridge. In Figure 3.7 we present a map of the density of molecular hydrogen derived from 4 transitions of HC_3N. Figure 3.7 shows that the density for the Orion ridge (excluding the hot core which was removed from this data) is typically greater than 10^6 cm^{-3}. There is also no evidence for large-scale, systematic variations in the density. The lack of systematic variations throughout the cloud is believed to relate to unobserved structures within the beam which have a volume filling factor that is much less than unity. This situation is complex but, for the purpose of analysis, we can state that the density of the dense material is quite high, with a value that is typically $\sim 3 \times 10^6$ cm^{-3}.

To examine the validity of LTE approximation we used statistical equilibrium calculations to model the excitation of all of our molecules. As an example we will present the results for CS. The CS molecule has a high dipole moment ($\mu = 2.0$ D) with a critical density for the J = 2 $\rightarrow$ 1 transition of $n_{crit} \sim 5 \times 10^5$ cm^{-3}, which is similar (or less than) the critical density of many of the molecules listed in

Table 1.1. With this critical density and the densities typically observed towards the ridge it might seem reasonable to assume LTE. Figure 4.14 presents a comparison between the LTE results and statistical equilibrium calculations. This figure shows that for CS the assumption of LTE is not truly valid until densities > 10^7 cm^{-3}. Below this, even at the typical densities observed along the ridge (n(H_2) = 3×10^6 cm^{-3}), LTE will underestimate the population by as much as a factor of 1.6 for 50 K. LTE assumes that all levels, including the high-J levels, which have rapid radiative decay rates, are populated by a Boltzmann distribution. However, if the densities are not high enough to compete with the fast decay rates, the higher states will not be appreciably populated. Therefore the lower states will contain a greater fractional population than when in LTE.

LTE will thus underestimate the population for most of the species observed in our study. The amount of error introduced will vary between species, with larger values at higher temperatures. The only exceptions to this are $C^{18}O$, CH_3C_2H, and HC_3N. $C^{18}O$ has a low dipole moment and is actually predicted to be in LTE at the observed densities. While the emission from both CH_3C_2H ($E_{J=6_0}$ = 17 K) and HC_3N ($E_{J=10}$ = 24 K) come from energy levels that are not at the bottom of the ladder (which is typical for most of the species in this study).

We have therefore used statistical equilibrium (SE) calculations to determine total column densities. We have assumed, based on the results of Chapter 3, that the density does not vary across the ridge and is typically, n(H_2) = 3×10^6 cm^{-3}. For each molecule we have therefore run a grid of SE models at n(H_2) = 3×10^6 cm^{-3} and T_k = 5 to 60 K by 5 K and recorded the fraction population for the level in question. Table 4.6 lists the references for the cross-sections. We make no corrections for the difference between He and H_2 excitation. For the determination of the total column density we used the CH_3C_2H rotational temperature. A spline fit was used to interpolate between values within the temperature grid. The error

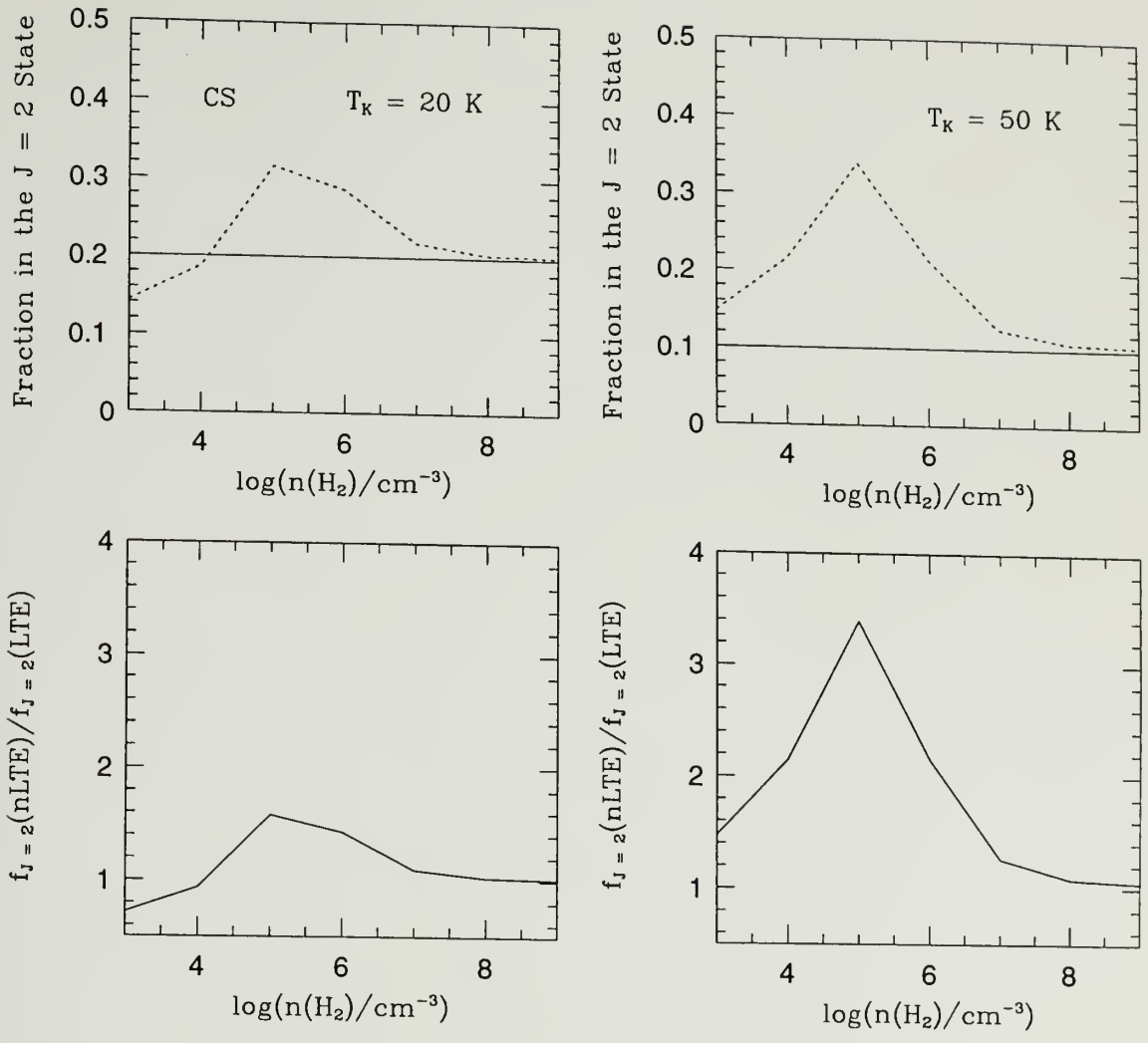

Figure 4.14. CS LTE (solid line) and non-LTE (dashed line) predictions for the population in the J = 2 state shown as a function of density and temperature.

Table 4.6. Collision Rate References

Species	Rates	Reference
$C^{18}O$	CO-paraH_2	Flower (1988)
$C^{34}S$	CS-He	Green & Chapman (1978)
$H^{13}CN$	HCN-He	Green & Thaddeus (1974)
$H^{13}NC$	HCN-He	Green & Thaddeus (1974)
CN	CO-paraH_2	Flower (1988)
C_2H	HCN-He	Green & Thaddeus (1974)
N_2H^+	N_2H^+-He	Green (1975)
HCO^+	N_2H^+-He	Green (1975)
HC_3N	HC_3N-He	Green & Chapman (1978)
SO	SO-H_2	Green (1994)
CH_3OH		see Menten et al (1985)
CH_3C_2H		Green (1986)

introduced by using a spline interpolation was found to be minimal.

4.4.2.2 Normalizing with the $C^{18}O$ Column Density

A good correlation has been found between $C^{18}O$ column densities and visual extinction (Frerking, Langer, and Wilson 1982; Lada et al 1994). Thus $C^{18}O$ is possibly one of the best tracers of H_2. Although $C^{18}O$ and A_V comparisons have not been made for GMCs like those studied here, nevertheless we will normalize the column densities by the $C^{18}O$ column density. The abundance relative to $C^{18}O$ can be converted to an abundance relative to H_2 by multiplying by the $C^{18}O$ fractional abundance of $X(C^{18}O) \sim 1.7 \times 10^{-7}$.

The chemistry of CO also helps in this regard. Of all molecules observed in interstellar space, including H_2, the formation of CO is perhaps the best understood. With many formation pathways, coupled with a low photodissociation rate due to self-shielding, the abundance of CO is not predicted to vary as a function of time (for $t > 10^5$ yr) or visual extinction. When abundances are defined relative to CO it can be reasonably assumed that any variations observed will be not be due to a change in the abundance of CO.

However, there is one complication that arises from the unusually low dipole moment of CO. The dipole moment of CO is only $\mu = 0.11$ D, which is a factor of $\sim$ 10-50 below that of other molecules observed. The low dipole moment translates to an extremely low critical density for excitation, $n_{crit} \sim 1000$ cm^{-3}. Therefore CO will be much more sensitive to all material along a line of sight, at both low and high densities. Whereas the emission from most of the other molecules in this study is expected arise predominantly from the high density component. In Chapter 3 we examined this question and suggest the $C^{18}O$ is dominated by the dense gas. *Therefore for consistency all our column densities are computed relative to $C^{18}O$. We define this term as the relative abundance.* We will discuss the consequences of this assumption in Chapter 6.

4.4.2.3 The Bar

As mentioned in Section 4.4.1, the Bar position was treated separately from the other 5 positions in determining the relative abundances. This was done for two reasons. First, many of the molecules show little or no emission towards the Bar. Examination of the spectra in Figure 4.13 shows the even averaging 7 positions along the Bar itself (see Table 4.4) does not reduce the noise enough to detect species such as CH_3C_2H, HC_3N, and $HN^{13}C$. The second reason follows from the first: because we did not observe any CH_3C_2H emission towards the Bar we do not have temperature information.

For the Bar position we have used the integrated intensities derived from the average spectra presented in Figure 4.13. The line center velocity from the emission profiles can be used to determine which species are actually arising from the Bar itself ($\sim$ 9-10 km s^{-1}) as opposed to the background cloud ($\sim$ 7-8 km s^{-1}). To estimate the temperature we have used the estimate of $T_k = 30$ K by Tauber et al (1994). This value was derived from ^{13}CO assuming that the emission was optically thick and is in agreement with models of the temperature structure in

dense photodissociation regions (Tauber et al 1994). For consistency with the other positions we will assume a density of $n(H_2) = 3 \times 10^6$ cm^{-3}. This value is consistent with other measurements in the literature (Hogerheijde et al 1995; Tauber et al 1994).

4.4.3 Relative Abundances for the Orion Ridge

Hereafter when we use the term relative abundance it refers to column densities relative to $C^{18}O$ and divided by the ratio of $^{16}O/^{18}O \simeq 500$. Table 4.7 presents the relative abundances for the Orion molecular ridge. The relative abundances of $H^{13}CO^+$, $H^{13}CN$, $HN^{13}C$ have been scaled by a factor of $^{12}C/^{13}C = 90$, while $C^{34}S$ has been multiplied by $^{32}S/^{34}S = 22.9$. We have also presented an average temperature and column density that can be ascribed to each position. Also listed in Table 4.7 are the relative abundances for these species in TMC-1 (Ohishi et al 1992) and the relative abundances for the extended ridge from Blake et al (1986). One of the more interesting points in this table is that the abundances at the RIP are somewhat similar to that observed in TMC-1. The abundances of HCO^+, HCN, N_2H^+, CH_3C_2H, CN, and C_2H are all within a factor of three to the observed TMC-1 abundances. However, the relative abundance of HC_3N is two orders of magnitude smaller than in TMC-1. Among the 6 positions in which relative abundances were computed the agreement with the TMC-1 relative abundances is certainly best for the RIP and the Ridge position.

Thus the earlier statement that the RIP is the closest to quiescent chemistry observed in Orion appears reasonably correct. Comparisons with the Blake et al (1987) study shows excellent agreement for almost any position. The only species with large differences are CN and CH_3C_2H for which Blake et al used temperatures much higher then presented here.

Table 4.7. Relative Abundances in Orion[a,b]

Species	RIP	Ridge	KL/BN	1.5′S	4′S	Bar	Blake[c]	TMC-1[d]
T_k[e]	28	40	45	32	24	30		
N(CO)[f]	4.4(18)	6.7(18)	8.4(18)	6.5(18)	4.3(18)	3.6(18)		
CS	1(-4)	1(-4)	2(-4)	1(-4)	2(-4)	8(-5)	5(-5)	1(-4)
CN	1(-4)	1(-4)	6(-5)	6(-5)	6(-5)	1(-4)	7(-5)	4(-4)
C_2H	4(-4)	3(-4)	2(-4)	2(-4)	3(-4)	2(-4)	1(-4)	9(-4)
HCO^+	7(-5)	5(-5)	5(-5)	5(-5)	1(-5)	1(-5)	5(-5)	1(-4)
N_2H^+	1(-5)	4(-6)	1(-6)	2(-6)	3(-6)	1(-6)		6(-6)
CH_3C_2H	4(-5)	6(-5)	6(-5)	4(-5)	2(-5)	<7(-6)	7(-5)	8(-5)
HC_3N	6(-6)	6(-6)	6(-6)	6(-6)	4(-6)	<1(-6)	3(-6)	8(-5)
SO	1(-5)	1(-5)	>1(-4)	4(-5)	2(-5)	8(-6)	<2(-5)	6(-5)
CH_3OH	9(-5)	8(-5)	>4(-4)	2(-4)	9(-5)	<2(-5)		3(-5)
HCN	2(-4)	2(-4)	>5(-4)	3(-4)	7(-5)	1(-4)	1(-4)	3(-4)
HNC	6(-5)	2(-5)	2(-5)	1(-5)	3(-5)	<2(-5)	1(-5)	3(-4)

[a] Column densities are relative to CO.

[b] Numbers are written in the form a(b) = a × 10^b.

[c] from Blake et al (1987) - Extended Ridge

[d] from Ohishi et al 1992

[e] Average temperature in K.

[f] Average CO column density computed from $C^{18}O$ assuming $^{16}O/^{18}O = 500$. Units are in cm^{-2}.

4.4.4 Error Analysis

Before examining what abundance variations exist along the Orion molecular ridge we will first determine what level of variation may be considered significant. Irvine, Goldsmith, and Hjalmarson (1987) presented molecular abundances for several cloud cores, including Orion and TMC-1. In their comparison of abundances they state that the abundances presented are only accurate to within an order of magnitude. This large error is the result of many factors but is predominantly due to questions of telescope efficiencies, molecular excitation, and opacity effects. This study has sought to minimize all of these various factors. We examine each separate factor in the following paragraphs.

4.4.4.1 Molecular Excitation: Density and Temperature

We will first examine the error introduced by assuming a constant density of $n(H_2) = 3 \times 10^6$ cm^{-3} for each position. Examining the CS excitation seen in Figure 4.14 , and assuming that it is typical of the other species, it can be seen that the fractional population is not changing appreciably at higher densities when the excitation is nearing LTE. Thus we will be introducing a larger error if the density along the line of sight is below $n(H_2) = 3 \times 10^6$ cm^{-3}. If the density is higher than the error will typically be lower. Allowing for a factor of 3 error on the density, the error introduced for CS will be $\sim$ 20-30%, if the density a factor of 3 below $n(H_2) = 3 \times 10^6$ cm^{-3}. The error will be $\sim$20% if the density is a factor of three greater. This difference is important since it is likely that the density for these positions is $> 3\times 10^6$ cm^{-3}, because for numerous positions in the cores we were only able to set a lower limit (see Chapter 3). Therefore the magnitude of the error introduced on the total column densities by the uncertainty in the density is typically $<$ 20-30%.

The statistical errors on the CH_3C_2H temperature measurements were quite small, since we presented only those values with errors less than 15 K. However, examination of the temperature structure in Figure 2.8 shows that there is significant variations in the temperature, even for neighboring positions. By using the averaging process outlined in Section 4 we certainly have minimized any contribution to the total error from the temperature. Assuming that the point to point variations in the temperature are representative of the error introduced by the temperature, we have computed the standard deviation of the mean when averaging the 5 "cross" positions. This was done and the error in the mean is $\sim$10%.

These conclusions rest on the assumption of a constant density and constant temperature cloud model. The errors will be greater in the presence of a density

and/or temperature gradient. The fact that most of the HC_3N emission and CH_3C_2H emission (by the correspondence of line center velocity and line widths) appear to be dominated by the high density material further suggests that these effects are not overly large (Chapter 3).

4.4.4.2 Antenna Efficiency

By using a single telescope we have minimized questions of efficiency. This leaves a residual question about the variation of the telescope efficiency across the 3mm band (86-115 GHz). Efficiency measurements by N. Patel during the 1992 observing season (which overlaps our measurements) give a beam efficiency of ~47% at 105 GHz and ~ 54% at both 95 and 86 GHz. Thus the variations in efficiency will introduce only small variations in the relative abundances.

Another systematic effect that could influence in the these calculations is differences in gain among the pixels. There is no guarantee that in choosing our positions that we are averaging over the same 5 pixels (with the same gain) each time. However this effect is quite small and we have also reduced any possible error by creating a final map for each species with an average of many smaller maps. These maps could have been taken with the dewar at the normal position of 90 degrees or possibly rotated 180 degrees, which will expose a different set of pixels to each position. While this error is truly hard to quantify, it is probably smaller than the other possible sources.

4.4.4.3 Random Errors

The previous paragraphs dealt primarily with systematic effects, which still leaves an examination of the random errors. This analysis is quantifiable by simply propagating the errors through from the 1σ error from the baseline. This error is very small, and will vary between each map. We will adopt a general error of ~10% which encompasses the actual error, even in cases of low signal to noise.

Thus the errors will be dominated mostly by the assumptions about the excitation, calibration, and opacity.

4.4.4.4 Optical Depth

To address questions of opacity we have examined only species that are thought to be optically thin. Of these, we assume that the emission from CH_3C_2H, HC_3N, $C^{34}S$, $HN^{13}C$, $H^{13}CO^+$ is optically thin. This assumption is strengthened because the spectra for these species (except HC_3N; $T_A^* < 3.0$ K) typically have $T_A^* < 1.0$ K, which is below the temperatures measured in Chapter 2 (typically ~30 K). Therefore, provided that filling factors are not extremely small, it is likely that the opacity from these lines is $\ll 1$.

For the other species, which have hyperfine structure or observations of a lesser abundant isotope, we can estimate the opacity. These are CN, C_2H, N_2H^+, $H^{13}CN$, CH_3OH, and SO. To estimate the opacity for the species with hyperfine structure (CN, C_2H, N_2H^+, and $H^{13}CN$) we have utilized the the routines from the CLASS package on the average spectra shown in Figures 4.8 - 4.13.

Table 4.8 presents the expected thin ratio for each species assuming the hyperfine components are in LTE, the observed ratio, and the optical depth in the main component. If the listed opacity is 0.1 it signifies that the line is optically thin; were an optical depth to be determined the true opacity is probably $\ll 0.1$. For C_2H derived optical depths are small except near KL where a moderate opacity of ~ 1 is observed. However an examination of the 1σ errors on the hyperfine ratios, when compared to the expected thin ratio, shows that the C_2H emission at KL/BN is consistent with optically thin emission. An examination of the hyperfine ratios for N_2H^+, CN, and $H^{13}CN$ also demonstrates that the emission from these species is consistent with the optically thin ratio. Thus this table suggests that these species do not suffer from large opacities, although the

Table 4.8. Optical Depths from Hf Structure

Hf Ratio	C_2H 2.5		$H^{13}CN$ 0.2:1.0:0.6	
Position	Ratio	τ_M	Ratio	τ_M
RIP	2.1±0.2	0.4	0.2±0.1:1.0:0.5±0.1	0.1
Ridge	2.4±0.1	0.1	0.2±0.1:1.0:0.5±0.1	0.1
KL/BN	2.1±0.1	1.3	0.4±0.5:1.0:0.6±0.5	0.6
1.5′S	3.0±0.2	0.2	0.2±0.2:1.0:0.7±0.2	0.6
4′S	1.8±0.1	0.6	0.3±0.2:1.0:0.8±0.1	1.0
Bar	1.5±0.1	3.6	0.5±0.1:1.0:1.0±0.1	1.1
Hf Ratio	CN 2.7		N_2H^+ 0.2:1.0:0.6	
Position	Ratio	τ_M	Ratio	τ_M
RIP	2.5±0.2	0.6	0.3±0.1:1.0:0.7±0.1	1.5
Ridge	2.8±0.3	0.1	0.2±0.1:1.0:0.7±0.1	0.7
KL/BN	2.6±0.3	0.2	0.1±0.1:1.0:0.7±0.1	0.3
1.5′S	2.5±0.2	0.3	0.2±0.1:1.0:0.7±0.1	0.3
4′S	2.5±0.2	0.3	0.3±0.1:1.0:0.7±0.1	0.4
Bar	2.7±0.2	0.1		

earlier comparison of N_2H^+ line center velocities with the average line of sight velocity has suggested that its emission may indeed be slightly optically thick.

Other molecules, SO and CH_3OH, may have optically thick emission at the KL/BN position. The study of methanol emission in Orion by Menten et al (1988) included observations of the isotopic variant $^{13}CH_3OH$. An isotopic ratio of ~20 is measured towards the KL/BN position, which implies that the CH_3OH emission is moderately optically thick. This may also be true for SO, where the abundance enhancements in the plateau may drive up the optical depth of the lines. However, as noted earlier, we are not properly resolving the hot core or the plateau, hence our abundance measurements for the species that have shown evidence of emission from any component outside of the ridge are already lower limits (see Blake et al 1987). It is likely, however, that the emission from both SO and CH_3OH in positions other than KL/BN is optically thin.

If the molecular emitting region is beam diluted (due to a low filling factor) then the opacities for SO and CH_3OH will only be lower limits. This would also effect other species, such as CH_3C_2H or $C^{34}S$, that we list as optically thin. One piece of evidence that the emission from these molecules may not be thick is the $CS/C^{34}S$ ratio. If the $C^{34}S$ emission is optically thick then the ratio would be close to one, which is not the case. $CS/C^{34}S$ at the radical-ion peak is $\sim$8, compared to the expected value in molecular clouds of $C^{32}S/C^{34}S \sim 15$. This analysis is only valid if both CS and $C^{34}S$ are tracing the same region with the same volume filling factor.

4.4.4.5 Estimated Error

In conclusion we estimate that the contribution from the many possible sources of error is between 40-50%, where the maximum contribution arises from the assumptions about the density. Therefore we believe that abundance variations less than a factor of two are marginal results. Especially considering this model of the cloud is one of uniform density and temperature, which the results presented in Chapters 2 and 3 do not support. The presence of clumps with separate filling factors between the gas traced by $C^{18}O$ and the high density tracers would also alter the relative abundances as discussed in Section 4.4.2.2, but this will affect all of the molecules abundances equally. Unless, of course, the filling factor of the dense gas varies significantly along the dense parts of the ridge. However the abundances determined with this study are certainly accurate to below an order of magnitude and probably to within factors of 2 - 4.

4.4.5 Abundance Variations

To examine whether the observed emission changes are reflective of true abundance variations across the ridge we present in Table 4.9 the relative abundances of each species normalized to the abundance at the RIP. One trend in

these data is the the decline of the relative abundances in the radicals and ions between the RIP and any other position. Although, as argued in the previous section, a change at or below a factor of two is not by itself a significant result. But the fact that the two highly reactive species, CN and C_2H show relative abundances declining from the colder regions to the warmer star forming cores is suggestive that the trend could be significant. The one species that stands out in this table is N_2H^+. The relative abundance of this ion decreases by an order of magnitude from the RIP to BN/KL. This large variation is certainly significant.

Because the decline in abundance for CN and C_2H is only a factor of 2, our results are in agreement with those of Greaves et al (1991) that the radical-ion peak is mostly a region that has enhanced emission characteristics due to excitation. The radical-ion peak may be more aptly named the N_2H^+ peak since this molecule shows the strongest evidence for abundance enhancements at the RIP.

Another trend seen in the data is the molecules that have large relative abundances at KL/BN as compared to the more quiescent RIP. These molecules are HCN, SO, and CH_3OH. Since these enhancements are well known it is perhaps more interesting to note that these species also have mild enhancements towards the southern star forming site 1.5′S.

The 4′S south position, which is a column density peak observed in many species has abundances that are are suppressed relative to the other positions. Since this position has a similar total column density and temperature as the RIP (see Table 4.7), it is somewhat surprising that this position stands out with lower relative column densities. This may suggest that another physical property of 4′S is different from the RIP, with the chief possibility being the radiation field. In addition, the molecular Bar has slightly lower relative abundances for many

species, C_2H, N_2H^+, CH_3C_2H, HC_3N, CH_3OH, and HCN. However the Bar does contain large amounts of both SO and HCO^+.

In conclusion, the Orion molecular ridge does not show much evidence for significant abundance variations. The radical-ion peak does stand out as having slightly greater abundances but to within a factor of 3 nearly all abundances are the same. This is excluding BN/KL and the Bar which both have very special properties. We note the abundance of the one species for which the hot core emission was removed, HC_3N, does not change at all. Therefore the ridge, in general, exhibits a fairly constant chemistry with most of the differences observed in molecular emission due to variations in excitation, primarily due to declining temperatures away from the star forming sites. However, it is important to state that some of the small abundance variations may indeed be real effects. In particular the 4′S position stands out as being possibly different in some fashion than the RIP and the Ridge. The large decline in N_2H^+ abundance also is intriguing. Observations of higher transitions of this molecular ion would be useful in examining whether this trend is indeed real.

One possible method to examine whether these trends are significant is to examine whether theoretical models that incorporate the changes in physical conditions along the ridge (e.g. temperature, radiation field) can account for the observed abundance variations. Current models, to the first order, can account for the effects of changing physical conditions. Whether the models can reproduce the observed abundances and variations will be discussed in Chapter 7.

Table 4.9. Abundances Relative to the RIP

Species	Ridge	KL/BN	1.5′S	4′S	Bar
CS	1.1	1.4	1.1	1.4	0.8
CN	1.0	0.6	0.6	0.6	1.0
C_2H	0.8	0.6	0.4	0.6	0.5
HCO^+	0.7	0.7	0.7	0.2	1.0
N_2H^+	0.4	0.1	0.2	0.3	0.1
CH_3C_2H	1.5	1.5	1.0	0.5	<0.2
HC_3N	1.0	0.9	1.0	1.4	<0.2
SO	1.0	>7.7	2.8	1.2	0.8
CH_3OH	0.9	>3.9	1.7	1.0	<0.2
HCN	1.2	>2.4	1.7	0.4	0.5
HNC	0.4	0.4	0.2	0.4	<0.3

Chapter 5

Chemical Structure in the M 17 and Cepheus A Cloud Cores

5.1 Introduction

In this chapter we discuss the chemical structure in the M 17 and Cepheus A cloud cores. For each core we first examine the principal differences in the emission between the various molecules. This will lead into an examination of whether the variations in emission are due to variations in abundance. The method used to derive column densities and relative abundances follows closely that for Orion discussed in the previous chapter. However, because the M 17 and Cepheus A maps are much smaller, we have not performed a principal component analysis as we did for Orion.

5.2 M17

5.2.1 Observations

The M 17 observations of the transitions listed in Table 1.1 (except for SO_2) were carried out during the 1991 and 1992 observing seasons using QUARRY. The details of the spectrometers used and corresponding velocity resolutions are given in section 4.2. For M 17 we have used only the data with a resolution of 250 kHz. The molecular emission maps all have the same grid of 120 points (10×12 spaced by $25''$) centered at $\alpha(1950) = 18^h17^m34.5^s$, $\delta(1950) = -16°13'24''$ and all observations were obtained by position switching to a reference position, free of ^{12}CO emission, at: $\alpha(1950) = 18^h17^m19^s$, $\delta(1950) = -16°30'00''$.

The chopper wheel calibrated antenna temperatures (T_A^*), were converted to radiation temperatures assuming a main beam efficiency of $\eta_{MB} = 0.45$ (see

Table 5.1. Contour levels for Figure 5.1

Species	Levels (K km s^{-1})
CO	20 to 200 by 20
^{13}CO	5 to 80 by 5.0
$C^{18}O$	1 to 10 by 1.0
CS	4 to 40 by 4.0
$C^{34}S$	0.5 to 7.0 by 0.5
SO	1 to 10 by 1
CH_3OH	0.7 to 7.0 by 0.7
C_2H	0.5 to 6 by 0.5
CN	2 to 20 by 2.0
HCN	5 to 45 by 5.0
$H^{13}CN$	0.5 to 5.0 by 0.5
HCO^+	5 to 45 by 5
$H^{13}O^+$	0.25 to 4.75 by 0.5
N_2H^+	1 to 11 by 1.0
HNC	4 to 24 by 4.0
$HN^{13}C$	0.2 to 1.6 by 0.2
HC_3N	0.7 to 6.3 by 0.7
CH_3C_2H	0.7 to 7.0 by 0.7
C_3H_2	0.5 to 2.5 by 0.25

section 4.2). As stated earlier, since the total column densities are placed relative to the $C^{18}O$ column density, the absolute value of the efficiency is unimportant for determining relative molecular abundances.

5.2.2 Morphological Differences

Figure 5.1 presents the maps of the integrated intensity for all molecular species included in the survey of M 17. The contour levels for each map are listed in Table 5.1. The emission from all of the molecules has a similar spatial extent, even in transitions arising from quite different energy states, such as HC_3N ($E_{J=12}/k = 34$ K) and $H^{13}CN$ ($E_{J=1}/k = 4.1$ K). In addition, the emission in all molecular species sharply cuts off in the northeast corner of the map where the H II region/molecular cloud interface is located.

There is one principal difference in the emission morphologies of the various molecular species. The emission of HC_3N and CH_3C_2H are strongly peaked at the

Figure 5.1. Integrated intensity maps for all of the survey molecules in M17. The transitions are listed in Table 1.1 and the contour levels and spacing are listed in Table 5.1.

position of the northern condensation, while most other molecules (eg. $C^{18}O$, $C^{34}S$, C_2H) peak further south. Some species, such as N_2H^+, have a second weaker emission peak even further to the south. These emission differences could simply be the result of a variation in temperature. The temperature of the dense gas in M 17, shown in Figure 2.11, reaches a maximum near the northern condensation and decreases south and west proceeding away from the H II region. The higher temperatures at the northern condensation will favor lines with greater excitation, such as CH_3C_2H and HC_3N, which are relatively more populated at higher temperatures. We will examine these questions in the following sections.

The M 17 maps exhibit considerably less structure than the Orion maps. However M 17 is more distant than Orion by a factor of four which will dilute any variations. For M 17 we have therefore chosen to derive abundances only for two positions: the northern condensation (-1.26,+0.84), labeled as NC, and the central condensation (-2.10, -0.84), denoted as CC. By determining abundances for these two positions we explore the main emission differences in M 17 and can use the edge-on geometry to examine possible abundance variations induced by the UV field.

5.2.3 Total Column Density Determinations

As in Orion we determine abundances for the nominally optically thin species listed in Table 4.3. However, because M 17 (2.2 kpc) is much more distant than Orion (450 kpc), spectra for different positions have not been averaged together. Instead, to compute total column densities, we use the integrated intensities derived from the spectra for the two positions. The signal to noise in the M 17 spectra is higher for most molecular transitions than those in Orion which aids this choice. Figures 5.2 - 5.3 show the spectra for the optically thin species and the principal moments derived from the profiles are listed in Table 5.2.

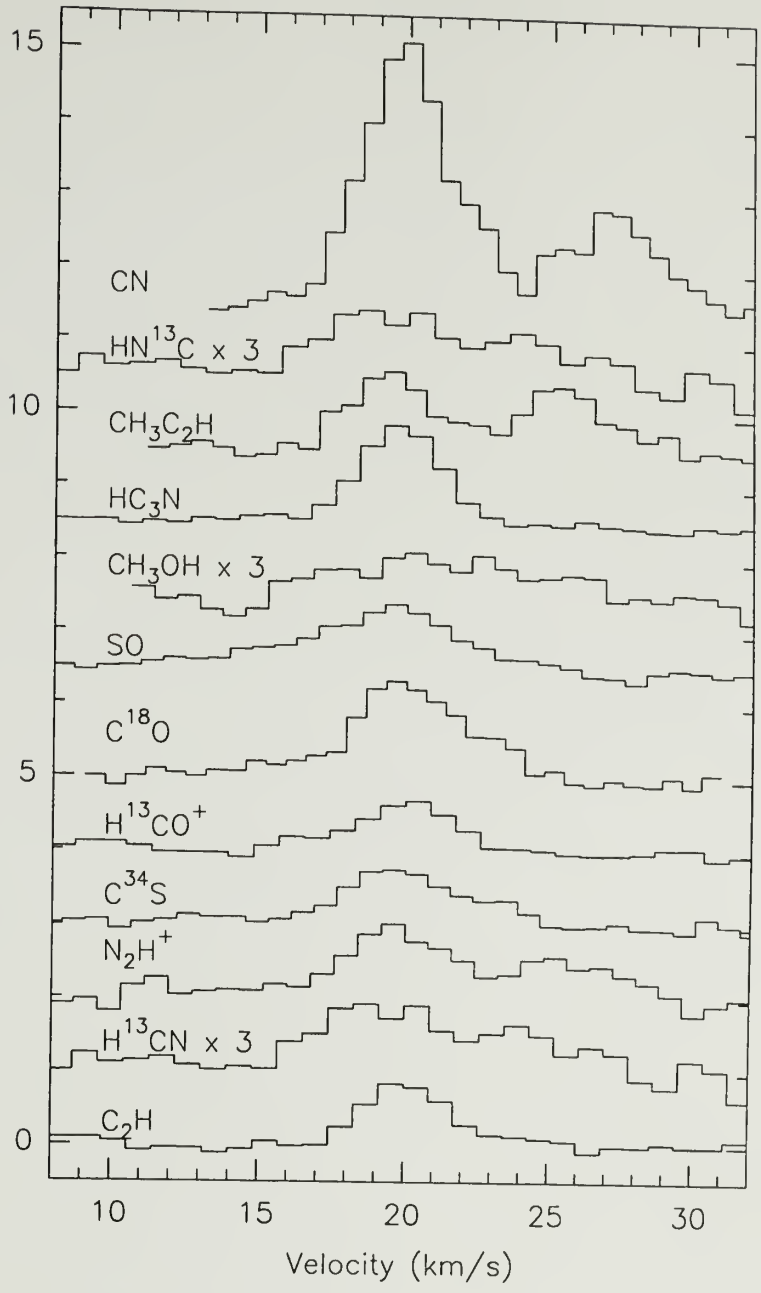

Figure 5.2. Spectra for the optically thin species towards the Northern Condensation. The intensities for $HN^{13}C$, CH_3OH, and $HN^{13}C$ have been multiplied by a factor of three.

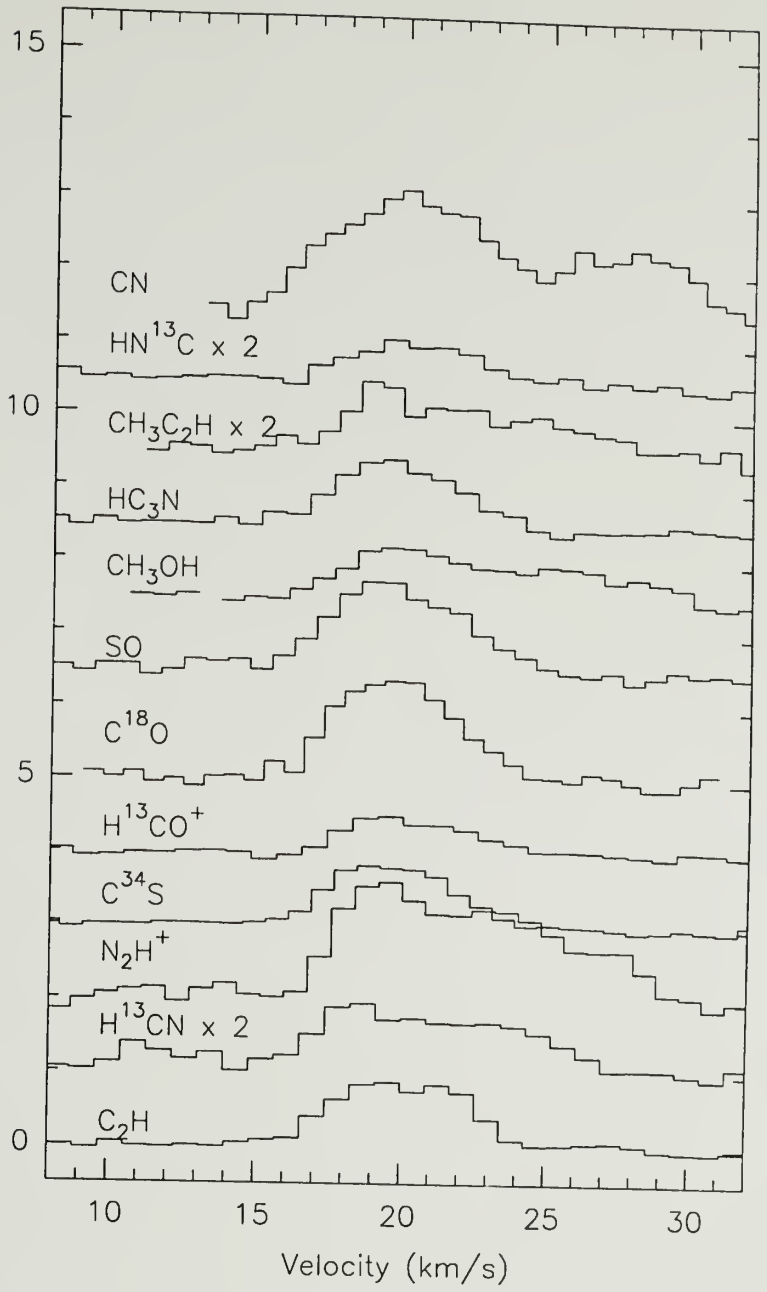

Figure 5.3. Spectra for the optically thin species towards the Central Condensation. The intensities for $HN^{13}C$, CH_3OH, and $HN^{13}C$ have been multiplied by a factor of two.

Table 5.2. Molecular Kinematics in M17[a]

	NC		CC	
Species	V_{lsr}	Δv	V_{lsr}	Δv
$C^{18}O$[b]	19.8± 0.1	2.9± 0.1	19.7± 0.1	4.7± 0.2
$C^{34}S$[b]	19.7± 0.1	4.0± 0.4	19.5± 0.1	4.8± 0.1
CN	19.9± 0.1	3.7± 0.1	20.0± 0.1	4.8± 0.2
C_2H	20.1± 0.1	3.2± 0.2	20.0± 0.1	5.1± 0.2
$H^{13}CO^+$	20.0± 0.1	4.2± 0.3	20.2± 0.1	5.0± 0.3
N_2H^+	19.7± 0.8	3.9± 0.8	19.9± 0.1	5.3± 0.2
CH_3C_2H	19.3± 0.1	3.2± 0.2	19.6± 0.2	4.5± 0.2
HC_3N	19.7± 0.1	3.2± 0.1	19.6± 0.1	4.7± 0.1
SO[b]	19.9± 0.2	3.1± 0.2	19.6± 0.1	4.7± 0.2
CH_3OH	19.7± 0.7	5.4± 0.5	20.0± 0.1	4.8± 0.1
$H^{13}CN$	18.9± 0.3	4.3± 0.5	18.9± 0.1	3.8± 0.3
$H^{13}NC$	19.7± 0.1	4.5± 0.3	20.1± 0.2	4.7± 0.2
Average[c]	19.8	3.4	19.7	4.8

[a]Velocities and linewidths are listed in km s^{-1}.

[b]Profile for the NC contained more than one component

[c]Weighted average computed from all molecules.

The spectra and the kinematic information listed in Table 5.2 can be used to examine whether the emission from each molecule is probing the same layer of gas in a manner similar to the analysis performed for the principal moments in Orion. The $C^{18}O$ and $C^{34}S$ profiles at the NC (see Figure 5.2) contain more than one velocity component; for these molecules we have tabulated values the velocity and line width of the stronger component. This component constitutes more than 75% of the total emission for these species. The line profiles for the CC are well fit by a single component. It is likely that there is substantial unresolved spatial and velocity structure in M 17 (eg. Stutzki and Gusten 1990), we will therefore only consider the total integrated intensity in both the NC and CC positions.

The velocities and linewidths of most molecules are constant, with the exception of CH_3C_2H and $H^{13}CN$. The CH_3C_2H emission deviates slightly from the average velocity at the northern condensation and the line center velocity of $H^{13}CN$ for both the NC and CC is also quite far from the average. However, the

Table 5.3. Optical Depths from HFS Ratio

	C_2H 2.5		$H^{13}CN$ 0.2:1.0:0.6	
	HFS Ratio	τ_M	HFS Ratio	τ_M
NC	4.1±0.2	0.1	0.2±0.1:1.0:0.6±0.1	0.3
CC	2.3±0.1	0.1	0.3±0.1:1.0:0.8±0.1	1.4
	CN 2.7		N_2H^+ 0.2:1.0:0.6	
	HFS Ratio	τ_M	HFS Ratio	τ_M
NC	2.5±0.1	0.1	0.3±0.1:1.0:0.6±0.1	0.7
CC	2.1±0.2	1.4	0.1±0.1:1.0:0.7±0.1	0.1

$H^{13}CN$ emission is very weak and the blending of the hyperfine components has made it difficult to make an accurate determination of the principal moments.

The above information suggests that most molecules are probing the same region along the line of sight. Another possibility that may separate molecular emission along the line of sight and effect velocities and velocity widths is if the emission is optically thick. To examine this question we have utilized the hyperfine structure of N_2H^+, CN, C_2H, and $H^{13}CN$ to estimate the opacity. Table 5.3 lists the opacities determined from the HFS ratio using the routines from the CLASS package. This table, at first glance, suggests that the some molecules have moderate optical depths. However, an examination of the 1σ errors on the hyperfine ratios, when compared to the expected thin ratio, demonstrates that the ratios of C_2H, N_2H^+, and $H^{13}CN$ are consistent with optically thin emission. The sole exception is the 3σ result for CN at the central condensation which is consistent with a moderate opacity ($\tau \simeq 1.4$). Thus for M17 we find no evidence for large opacities.

We therefore assume that the molecular emission is optically thin and use Equation 4.5 to derive upper state column densities. We have adopted $T_k = 50$ K for the northern condensation and $T_k = 30$ K for the CC, based on the temperatures derived for the dense gas in Chapter 2. The density in M 17 does not vary appreciably with position (Figure 3.8) therefore, we adopt a single value of $n(H_2) = 3 \times 10^6$ cm^{-3}. With these physical conditions and the excitation models outlined in Section 4.4.2, total column densities can be determined for each molecular species. Since the CN emission at the central condensation was determined to have moderate opacity, we corrected the optically thin column density using the following expression (Snell et al 1984),

$$N = N_{thin}\tau/(1 - e^{-\tau}) \tag{5.1}$$

where N_{thin} is the optically thin column density and τ is the opacity derived from the hyperfine structure in Table 5.3. The relative abundances are then derived by dividing by the $C^{18}O$ column density relative to CO, and then converted to a CO column density using an isotopic ratio. The column densities for isotopic species were scaled to the main isotope using the isotopic ratios listed in section 4.4.3.

5.2.4 Abundances Gradients in M17

Table 5.4 presents the relative abundances for the northern and central condensations, along with the temperatures and CO column densities. The first conclusion to be drawn from Table 5.4 is that, while the relative abundances at the two positions are quite similar, there is a general trend for lower relative abundances near the HII region interface (NC) and larger values farther away (CC). The sole exception to this trend is CH_3C_2H, which has a larger abundance at the northern condensation. CH_3C_2H also has the greatest abundance variation observed in M 17. It is somewhat surprising that the abundance of HC_3N does not

Table 5.4. Relative Abundances in M 17[a,b]

Species	NC	CC
T_k[c]	50	30
N(CO)[d]	2.0(19)	1.4(19)
CS	7(-5)	9(-5)
CN	3(-5)	7(-5)
C_2H	1(-4)	2(-4)
HCO^+	4(-5)	4(-5)
N_2H^+	2(-6)	4(-6)
CH_3C_2H	5(-5)	2(-5)
HC_3N	2(-6)	3(-6)
SO	1(-5)	2(-5)
CH_3OH	2(-5)	4(-5)
HCN	5(-5)	1(-4)
HNC	2(-5)	2(-5)

[a] Abundances are relative to CO

[b] a(-b) = a × 10^{-b}.

[c] Temperature in K.

[d] CO column density from $C^{18}O$ in cm^{-2}.

follow the trend observed for methyl acetylene, because the emission from HC_3N also strongly peaks at the NC.

Since the maximum change in relative abundances between the NC and the central condensation is a factor of 2.5 for CH_3C_2H, the principal conclusion from these observations is that there are no significant abundance variations in M 17. Indeed, within the estimated error of ~50% (section 4.4.3), the abundances do not vary at all. There is one general trend in the abundances which may be real; that all of the abundances in the CC (except CH_3C_2H), which is located further from the H II region, are typically greater than observed for the NC. For any single species this variation can not be considered significant, however that all species, except CH_3C_2H, follow the same variation argues that this trend is probably real and may indicate that the UV field is influencing the chemistry. Although this variation, with abundances greater at the CC than the NC, could be a result of a systematic error, such as a change in the density between these two positions.

5.3 Cepheus A

The Cepheus A observations were carried out during the 1991 and 1992 observing seasons using QUARRY. We have observed all transitions listed in Table 1.1, except for SO_2. The details of the spectrometers used and corresponding velocity resolutions are listed in section 4.2. Because of the moderate linewidths $\Delta v \sim 2$ km s^{-1}, we have used only the 250 kHz data. The maps are placed on the same grid of 120 points (10 × 12) spaced by 25″ centered on the FIR continuum peak (Moriarty-Schieven et al 1991) and the ultracompact H II region HW 2 at $\alpha(1950) = 22^h54^m19^s$ and $\delta(1950) = 62°45'47''$. All observations utilized position switching to a reference position at $\alpha(1950) = 22^h52^m03^s$ and $\delta(1950) = 62°37'05''$ which is free of ^{12}CO emission.

The observations are placed on the T_A^* scale, which was then scaled to the radiation temperature using a main beam efficiency of $\eta_{MB} = 0.45$ (see section 4.2). As stated earlier, since the total column densities are placed relative to the C^{18}O column density, the absolute value of this calibration is unimportant. Some of the maps that are presented in the following section have low signal to noise, in particular these are the transitions of C^{34}S, HN^{13}C, and perhaps C_3H_2. In spite of the poor quality of the data we will still use these maps in the analysis.

5.3.1 Morphological Differences

The integrated intensity maps for all survey molecules are shown in Figure 5.4, and the contour levels are listed in Table 5.5. The various emission morphologies in Cepheus A do not exhibit the complicated structure observed in Orion. All molecules show strong emission near the center of the map at the location of the embedded ultracompact H II region HW 2. A few molecules, such as SO and CH_3OH, deviate slightly from this structure having emission extended to the northeast and southwest. Other molecules (H^{13}CN and C^{34}S) appear to have some

Table 5.5. Contour levels for Figure 5.4

Species	Levels (K km s^{-1})
CO	20 to 100 by 10
^{13}CO	5 to 35 by 2.5
$C^{18}O$	0.5 to 5.5 by 0.5
CS	2 to 12 by 1.0
$C^{34}S$	0.4 to 1.6 by 0.2
SO	0.4 to 4.4 by 0.4
CH_3OH	0.4 to 4.4 by 0.4
C_2H	0.4 to 3.2 by 0.4
CN	0.5 to 4.0 by 0.5
HCN	1 to 12 by 1.0
$H^{13}CN$	0.2 to 1.8 by 0.2
HCO^+	1 to 11 by 1.0
$H^{13}O^+$	0.25 to 2.5 by 0.25
N_2H^+	0.5 to 4.5 by 0.5
HNC	1 to 14 by 1.0
$HN^{13}C$	0.5 to 1.3 by 0.2
HC_3N	0.4 to 3.2 by 0.4
CH_3C_2H	0.1 to 0.7 by 0.1
C_3H_2	0.3 to 0.1 by 0.2

additional structure but this may be due to the lower signal to noise in these maps. The N_2H^+ and CN integrated intensity maps are also quite similar to the NH_3 map of Gusten, Chini, & Neckel (1984) with fairly compact emission oriented in a NE-SW direction. However other nitrogen-bearing molecules, such as HC_3N, does not show a similar morphology, suggesting some differences in the nitrogen chemistry in the core.

The high-velocity outflow in Cepheus A is extended over nearly $\sim 1'$ and oriented in an east-west direction centered on HW 2 (Rodriguez et al 1980; Hayashi et al 1988). Since the SO and CH_3OH emission morphology is elongated in a northeast-southwest direction it is unlikely the emission from these species is related to the high-velocity flow. However, the low velocity flow in Cepheus A is much more extended, over $> 3'$, and oriented in a northeast-southwest fashion (Hayashi et al 1988). The low velocity outflow is believed to be a remnant outflow

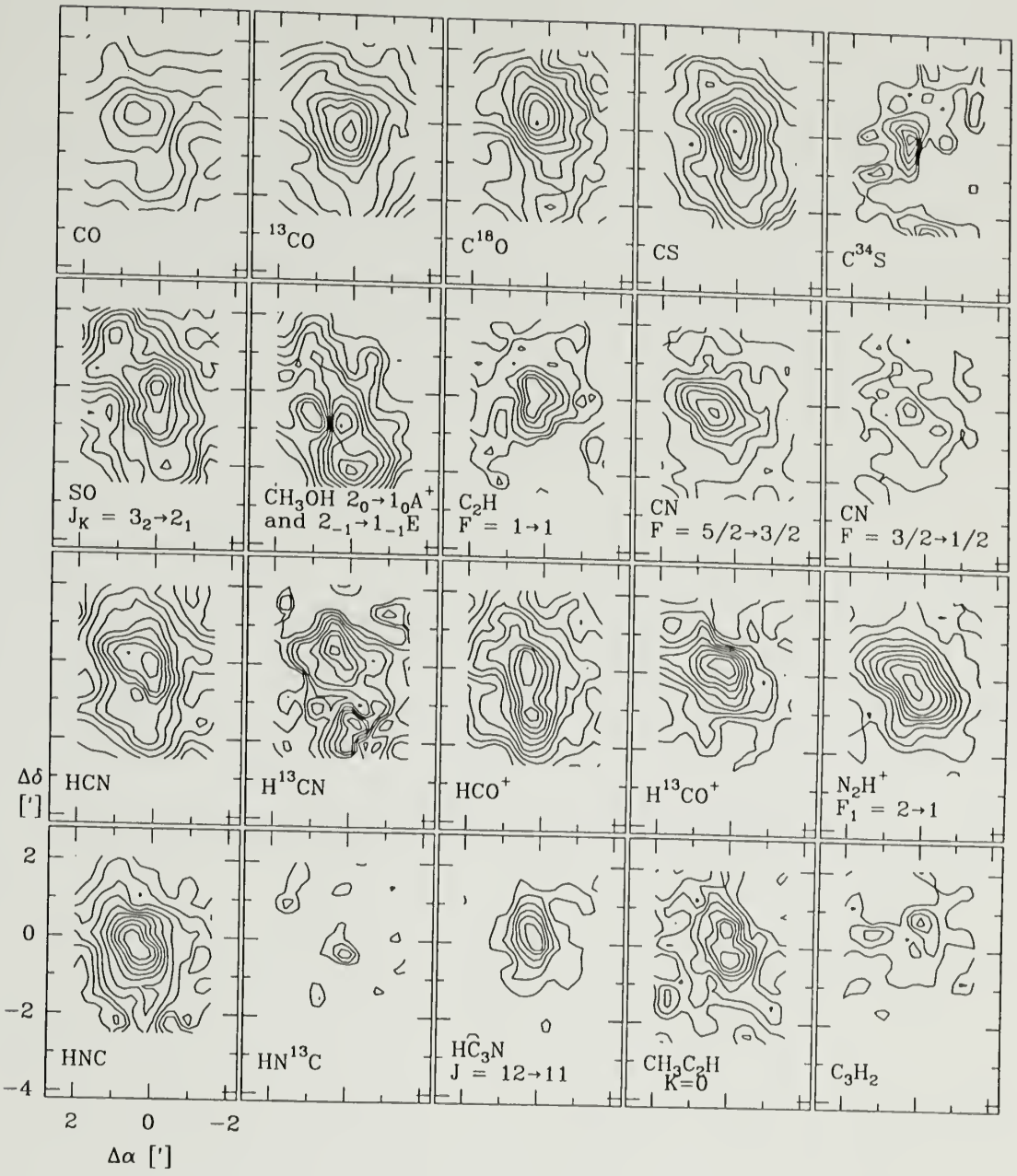

Figure 5.4. Integrated intensity maps for all of the survey molecules in Cepheus A. The transitions are listed in Table 1.1 and the contour levels and spacing are listed in Table 5.5.

that has lost its structure during its interaction with the surrounding quiescent gas, traced by HCN, NH_3, and CS (Staude & Elsasser 1993; Philips & Mampaso 1991). It is therefore possible that the morphology of the SO and CH_3OH emission indicates that these species are tracing the older flow, while other molecules (N_2H^+, $H^{13}CO^+$, C_2H, CN) are probing the quiescent gas. To properly examine this question the velocity structure in the various maps should be analyzed in detail, however this is beyond the scope of this study.

We can examine whether the outflow has altered the chemical evolution of the quiescent material in Cepheus A by comparing relative abundances northeast and south of the central peak. For this purpose we have chosen to compute relative abundances for $\Delta\alpha = 0.42$, $\Delta\delta = 0.42$, which we label Ceph-A N, and $\Delta\alpha = 0.0$, $\Delta\delta = -1.26$, which we refer to as Ceph-A S. While these positions do not directly correspond to emission maxima, they do enable an examination of possible abundance gradients induced by the large outflows in Cepheus A.

5.3.2 Total Column Density Determinations

To derive total column densities in Cepheus A we have utilized the method outlined in section 4.4 for Orion. We determine relative abundances only for optically thin species, listed in Table 4.3. We will examine the question of opacity in the following paragraphs. To determine the line center velocities and linewidths for these two positions we have averaged spectra in a 5 point "cross" pattern centered on each position (see section 4.4). These spectra are shown in Figures 5.5 - 5.6 and the kinematic information derived from the average spectra are listed in Table 5.6.

The spectra for Cepheus A, at both Ceph-A N and Ceph-A S, exhibit weaker emission than observed in either Orion or M 17. Although Ceph-A N is generally characterized by stronger emission than Ceph-A S. The velocities observed for these two positions indicates a systematic trend, with higher velocities evident

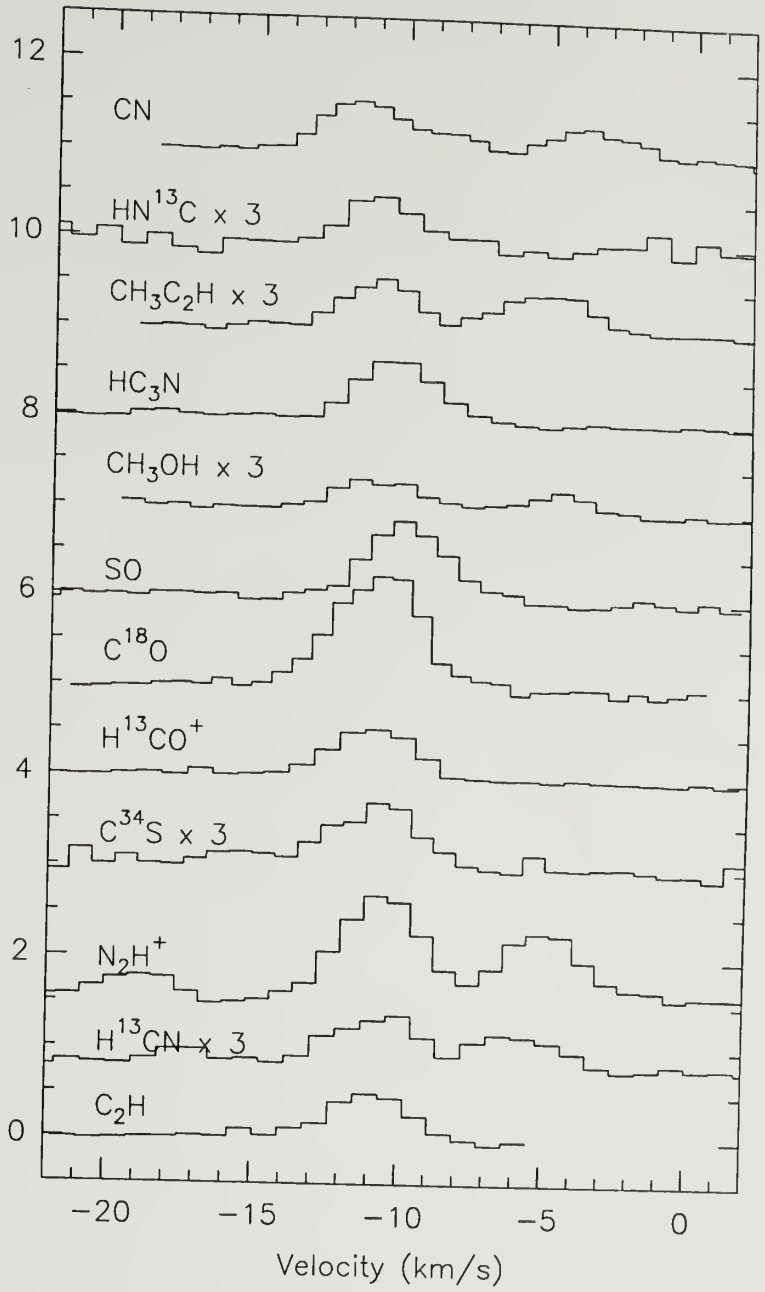

Figure 5.5. Spectra for the optically thin species towards the Ceph-A N (0.42, 0.42) position. The intensities for $HN^{13}C$, CH_3C_2H, CH_3OH, $C^{34}S$, and $HN^{13}C$ have been multiplied by a factor of three.

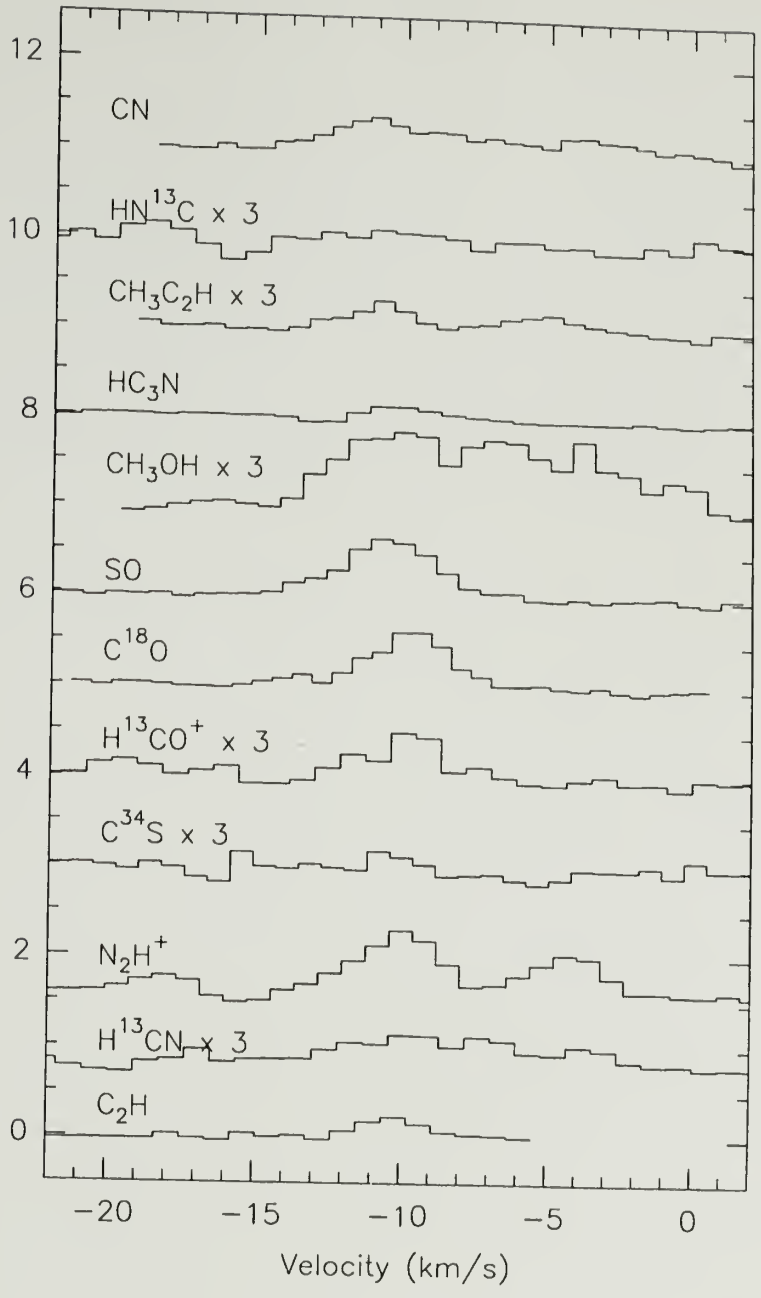

Figure 5.6. Spectra for the optically thin species towards the Ceph-A S (0.00, -1.26) position. The intensities for $HN^{13}C$, CH_3C_2H,CH_3OH, $H^{13}CO^+$, $C^{34}S$, and $HN^{13}C$ have been multiplied by a factor of three.

Table 5.6. Molecular Kinematic in Cepheus A[a]

	Ceph-A N		Ceph-A S	
Species	V_{lsr}	Δv	V_{lsr}	Δv
$C^{18}O$	-10.9± 0.1	3.5± 0.1	-9.8± 0.1	3.3± 0.1
$C^{34}S$	-10.9± 0.1	3.8± 0.5		
CN	-11.2± 0.1	3.4± 0.1	-10.7± 0.1	4.9± 0.1
C_2H	-10.9± 0.1	3.0± 0.1	-10.2± 0.1	2.7± 0.4
$H^{13}CO^+$	-11.0± 0.1	3.3± 0.1	-9.8± 0.2	2.9± 0.3
N_2H^+	-10.6± 0.1	2.9± 0.1	-10.0± 0.1	2.9± 0.1
CH_3C_2H	-11.0± 0.1	3.3± 0.1	-10.9± 0.1	3.1± 0.1
HC_3N	-10.4± 0.1	3.0± 0.1	-10.0± 0.2	2.7± 0.2
SO	-9.9± 0.1	3.2± 0.1	-10.5± 0.1	3.8± 0.1
CH_3OH	-10.9± 0.1	3.2± 0.1	-10.1± 0.2	5.6± 0.1
$H^{13}CN$	-10.7± 0.1	3.1± 0.1	-9.7± 0.2	5.0± 0.4
$H^{13}NC$[b]	-11.0± 0.2	2.5± 0.2		
Average[c]	-10.8	3.2	-10.3	3.9

[a] Velocities and linewidths are listed in km s^{-1}.

[b] $C^{34}S$ and $HN^{13}C$ emission too weak to determine moments of 1.5'S.

[c] Weighted average computed from all species listed

north of HW 2 and slightly lower velocities south of the compact H II regions. The total shift is not large, with the average velocity for Ceph-A N given by $< V_{lsr} >= -10.8$ km s^{-1}, compared to $< V_{lsr} >= -10.3$ km s^{-1} for Ceph-A S. The NH_3 study by Gusten et al (1984) found a systematic velocity shift of over 2 km s^{-1} along the major axis of the NH_3 emission (oriented similar to the N_2H^+ integrated intensity in Figure 5.5). The average velocity shift derived from other molecules is in the same direction as the gradient evident in the NH_3 observations. However, our velocity determinations are not over exactly the same region as the cut utilized by Gusten et al, nor is the gradient of a similar magnitude suggesting that these results are not probing the same material as NH_3.

Whether all molecules are probing the same layer is of considerable importance for our analysis of the chemistry. At Ceph-A N most molecules have velocities within 3σ of the mean, although SO, CN, and HC_3N deviate by 4σ or greater. The velocities for Ceph-A S show considerably more scatter, which may in part be due

to weak emission and low velocity resolution (0.6 - 0.8 km s^{-1}). Indeed, at Ceph-A S, the emission for $C^{34}S$ and $HN^{13}C$ was too weak to obtain a useful fit to the spectrum. The linewidths for both positions are quite similar, although the southern position has slightly larger line widths.

One intriguing observation is that line center velocity for SO seems to be significantly below the average velocity at Ceph-A N, and shifts to a velocity slightly above the mean to the south. This can be seen in the spectra presented in Figures 5.5 and 5.6 where the SO profile peaks at higher velocities than $C^{18}O$ at Ceph-A N, the peak velocity shifts to lower velocities at Ceph-A S. This gradient is interesting because the low velocity blueshifted component is centered near the Ceph-A N position, while the red shifted gas is $\sim$1′S from our map center (Hayashi et al 1988). Therefore we conclude that the SO emission could be tracing the low velocity bipolar flow. None of the other species, including CH_3OH which has a similar emission morphology to SO, exhibits similar velocity structure. Again a detailed examination of the velocity structure of these data is warranted.

The result from the kinematic analysis is that most molecules seem to be tracing the same quiescent gas towards Ceph-A N. While for the southern position the results are more ambiguous. SO is the only molecule which may be tracing different material, and this molecule may be probing the low velocity outflow.

We must also examine, as best as we can, whether the emission from the different species is optically thin. Table 5.7 lists the optical depths derived from the hyperfine ratios of CN, C_2H, N_2H^+, and $H^{13}CN$. As in M 17, the ratios for C_2H, N_2H^+, and $H^{13}CN$ are, within the errors, consistent with optically thin emission. However, the ratios determined for cyanogen (CN) diverge significantly ($>3\sigma$) from the thin ratio and is possibly optically thick.

Table 5.7. Optical Depths from HFS Ratio

	C_2H 2.5		$H^{13}CN$ 0.2:1.0:0.6	
	HFS Ratio	τ_M	HFS Ratio	τ_M
1′N	2.5±0.3	0.1	0.3±0.1:1.0:0.7±0.1	1.0
1.5′S	2.6±0.9	0.1	0.2±0.1:1.0:0.6±0.1	0.2
	CN 2.7		N_2H^+ 0.2:1.0:0.6	
	HFS Ratio	τ_M	HFS Ratio	τ_M
Ceph-A N	1.8±0.1	1.6	0.2±0.2:1.0:0.7±0.1	0.4
Ceph-A S	1.8±0.2	1.5	0.2±0.1:1.0:0.6±0.1	0.1

To determine upper state column densities we have used Eqn. 4.5, which assumes optically thin emission. Since Cepheus A is not as distant as M 17 (d $\sim$ 720 pc), we use the averaging method presented in section 4.4.2 for Orion to derive relative abundances. We have adopted the kinetic temperatures determined by CH_3C_2H and a density of $n(H_2)$ equal to 3×10^6 cm^{-3} for both positions, based on the HC_3N measurements in Chapter 3. Because of the lower intensity of the CH_3C_2H emission in Cepheus A, we have fewer temperature determinations that for Orion or M 17. In cases where a position lacked a temperature determination we have used a weighted average of the temperature from the nearest neighbors. For CN we have corrected the total column densities for the effects of opacity using Eqn. 5.1 and the optical depths listed in Table 5.7. The correction to the total column density for optically thick emission, with an opacity $\tau \sim$1.5, is only a factor of 2.

5.3.3 Abundance Gradients in Cepheus A

The relative abundances in Cepheus A, along with an average temperature and CO column density for each position, are presented in Table 5.8. The main conclusion from this table is that there are no significant abundance variations within the Cepheus A cloud core. Although the estimated error is near a factor of two, we may be able to identify some *possible* small trends. These variations are

Table 5.8. Relative Abundances in Cepheus A[a,b]

Species	1′N	1.5′S
T_k[c]	30	20
N(CO)[d]	8.0(18)	3.4(18)
CS	3(-5)	2(-5)
CN	2(-5)	4(-5)
C_2H	1(-4)	7(-5)
HCO^+	4(-5)	2(-5)
N_2H^+	3(-6)	3(-6)
CH_3C_2H	2(-5)	2(-5)
HC_3N	2(-6)	1(-6)
SO	1(-5)	2(-5)
CH_3OH	5(-5)	1(-4)
HCN	5(-5)	9(-5)
HNC	2(-5)	2(-5)

[a] Abundances are relative to CO

[b] a(-b) = a × 10^{-b}.

[c] Temperature in K.

[d] CO column density from $C^{18}O$ in cm^{-2}.

not significant for a single species but may be significant if several species follow the same variation in abundance. The first trend is in SO, which has a different kinematic signature from other molecules, and has a small abundance variation. The abundance variation observed for SO, with a slightly greater abundance to the south, is mirrored by CH_3OH, $H^{13}CN$, and CN. Since the kinematic information for SO hints that this molecule is tracing the low velocity outflow this abundance gradient may be related in some fashion to the outflow. This is supported by the observations in Orion where each of these species, SO, CH_3OH, and HCN (except CN) is associated with the energetic events at Orion KL/BN. None of the other species that are observed only in the quiescent ridge in Orion (eg. CH_3C_2H, C_2H), except CN, follow the variation observed for SO in Cepheus A.

Other species show an opposing gradient, with greater abundances towards Ceph-A N (C_2H, HCO^+, HC_3N), while and the abundances of CH_3C_2H, N_2H^+, and HNC do not vary appreciably. Therefore one scenario for Cepheus A is that

the gradient observed for these species, with larger abundances at Ceph-A N, is following the evolution of the quiescent cloud. The abundance of SO, CH_3OH, and HCN may have been altered by the outflow phase, which resulted in the different abundance gradient.

5.3.4 Chemical Abundances in GMC Cores

An examination of the chemistry in each core enables a few general statements to be made about the chemical evolution in GMC cores.

1) Outside of KL/BN in Orion, chemical abundances in GMC cores typically only vary by factors of a few.

2) Within each core, some of the emission variations for the quiescent gas do trace variations in abundance (eg. N_2H^+ in Orion, CH_3C_2H in M 17, SO in Cepheus A). However, some of the abundance gradients are the result of variations in the physical conditions, such as HC_3N in M 17. Therefore careful accounting of the physical conditions is necessary when computing chemical abundances.

3) The largest abundance variation observed is for N_2H^+ in Orion which shows an order of magnitude difference between the RIP and KL/BN positions.

4) The most significant abundance variation within a single cloud is observed in Orion between the northern radical-ion peak relative to both 4'S and the Bar.

5) M 17 and Cepheus A do exhibit some abundance variations which may be related to physical features (eg. UV field in M 17 ; outflows in Cepheus A). These variations are not large and are within the estimated error of 50%.

These conclusions are limited to examining abundance variations within a single cloud. We can also compare abundances among GMC cores a this is presented in Table 5.9. In this table, for consistency with the comparison in Orion, we have divided all relative abundances by the relative abundances observed for the RIP. One conclusion that can drawn from this table is that the relative

abundances in M 17 and Cepheus A are quite similar. Because of the complexities of the chemistry along the Orion ridge (eg. KL/BN and the Bar) this comparison is not as easily extended to include Orion. If we exclude KL/BN and the Bar, due to their special characteristics, the abundances in Orion are also similar to M 17 and Cepheus A, although the Orion abundances are typically greater. The relative abundances of CS, HCO^+, CH_3C_2H, and HNC are the same (to within a factor of 4) for any position in Orion, M 17, or Cepheus A. These molecules may therefore be marked as *the* tracers of quiescent material in GMC cores. However some molecules exhibit large differences, in particular CS and C_2H, which are a seven to ten times more abundant in Orion than in Cepheus A or M 17.

These differences are outweighed by the general agreement. The position in Orion that is has the greatest agreement with the other cores is the quiescent Ridge position. At this position, 8 out of 12 molecules have relative abundances that are within a factor of three of the M 17 and Cepheus A abundances. Other positions in Orion come close to this agreement, such as the 4′S peak, where 9 molecules are within a factor of 4 of the M 17 and Cepheus A abundances. This points to a general conclusion that the chemical evolution of GMC cores is not markedly different. There are positions that stand out with specific characteristics, such as the Bar or KL/BN, but these positions are remarkable in many other observations. This does not mean that the chemistry in each core is exactly the same. The relative abundances observed in Orion, at the RIP for example, are typically greater than in either M 17 or Cepheus A. Rather, the general agreement of relative abundances, to within factors of 3-4, argues that the chemistry active in each core is not unique and that the chemical processes occurring in the different GMC cores are relatively similar.

Table 5.9. Abundances in GMC Cores relative to the RIP

	Orion A					M 17		Ceph-A	
Species	Ridge	KL/BN	1.5′S	4′S	Bar	NC	CC	N	S
CS	1.1	1.4	1.1	1.4	0.8	0.7	0.9	0.3	0.2
CN	1.0	0.6	0.6	0.6	1.0	0.3	0.7	0.2	0.4
C_2H	0.8	0.6	0.4	0.6	0.5	0.3	0.5	0.3	0.2
HCO^+	0.7	0.7	0.7	0.2	1.0	0.6	0.6	0.6	0.4
N_2H^+	0.4	0.1	0.2	0.3	0.1	0.2	0.4	0.3	0.3
CH_3C_2H	1.5	1.5	1.0	0.5	<0.2	1.2	0.5	0.5	0.5
HC_3N	1.0	0.9	1.0	1.4	<0.2	0.3	0.5	0.3	0.2
SO	1.0	>7.7	2.8	1.2	0.8	1.0	2.0	1.0	2.0
CH_3OH	0.9	>3.9	1.7	1.0	<0.2	0.2	0.4	0.6	1.1
HCN	1.2	>2.4	1.7	0.4	0.5	0.3	0.5	0.3	0.5
HNC	0.4	0.4	0.2	0.4	<0.3	0.3	0.3	0.3	0.3

Chapter 6

Theoretical Models of Chemistry Applied to the Radical-Ion Peak

6.1 Introduction

Theoretical models of the chemical evolution of molecular clouds have been fairly successful in predicting the observed abundances of many species (cf. Prasad & Huntress 1980a,b; Graedel, Langer, & Frerking 1982; Leung, Herbst, & Huebner 1984; Millar and Freeman 1984; Brown & Rice 1986a,b; Herbst & Leung 1989; Langer & Graedel 1989). These models range in complexity from modeling only the "steady state" or equilibrium abundances, to others solving the so-called "pseudo-time dependent" chemistry, to even more involved approaches. The various models have also examined different aspects of chemical interactions. For example, Tielens and Hollenbach (1985) examined the chemistry of a small set of simple species in photon dominated regions, while Leung, Herbst, and Huebner (1985) examined the formation of complex molecules in dense well shielded regions. One common factor in all gas-phase models is the dominance of ion-molecule reactions in controlling the chemical formation and destruction pathways. Although the importance of certain classes of neutral-neutral reactions has increased in recent years, due to low temperature laboratory measurements (Sim et al 1992; 1993; 1994a,b), ion-molecule reactions are still believed to dominate the formation paths of most molecular species (Bettens, Lee, & Herbst 1995).

These models have built upon advances in both theoretical and experimental determinations of reaction rates, as well as on improved understanding of physical processes occurring in molecular clouds, such as shocks. One problem inherent in

comparing such models with observations is that not only are the models uncertain in some respects, due to unknown reaction rates, but the abundances are uncertain as well. As mentioned in section 4.4.4 chemical abundances are often uncertain by up to an order of magnitude. We believe the relative abundances computed for Orion, M 17, and Cepheus A presented in Chapters 4 and 5 are accurate to a factor of $\sim$2 and thus this investigation will place better constraints upon chemical models. Perhaps more importantly this study has made independent estimates of the density and temperature in molecular clouds which can be used as inputs for the chemical models. These parameters are required for chemical modeling because the density and temperature respectively govern the frequency and rate of reactions. A detailed coupling between observations and theoretical modeling has not been attempted previously since modeling efforts normally have been undertaken independent of observational work.

Besides the gas-phase chemistry, another prominent area of current chemical research is modeling the interactions of molecules with grain surfaces, sometimes including reactions on the grain mantles. The inclusion of grain processes into chemical networks is important because at typical cloud densities, $n(H_2) > 10^5$ cm^{-3}, the timescale for molecular depletion is comparable, or less than, expected cloud ages (cf. Iglesias 1977). This suggests that an efficient mechanism must exist to return species back into the gas-phase. However, the desorption mechanism, and the reactivity of interstellar grain mantles, are subjects matter of current debate (Williams 1993). The present work will adopt the approach of comparing the observations solely to a gas-phase chemical network. If gas-phase reactions are unable to reproduce the observations then we will examine whether grains could provide an active or supporting role in the chemical interactions. To examine this, we can make use of the literature and an examination of gas-phase chemistry including grain surface molecular depletion and desorption published in Bergin,

Langer, & Goldsmith 1995. This work, treated in Appendix B, used a restricted network which enables an examination of the general principles but does not allow for a direct comparison with these observations.

Two separate approaches will be used to model the chemistry. First, we will model the chemistry only in the dense well shielded interior of the cloud. This is the normal method in which chemical models are calculated and compared to observations. This will present the model in a clear fashion and will allow it to be compared directly to previous modeling efforts. However, a well shielded chemical model may not be applicable to these cores because of the proximity of massive star formation sites. As mentioned earlier in Chapter 2, and discussed in detail in Chapter 3, current observational evidence suggests that giant molecular cloud cores have a clumpy structure. This structure allows greater penetration of the ultraviolet (UV) photons from the newly formed massive stars.

The general picture of giant molecular clouds that is emerging is one numerous dense clumps embedded in a tenuous interclump medium (cf. Goldsmith 1995). The irregular structure allows for greater penetration of UV photons, such that the edge of each of clump is in itself a dense photodissociation region. To better account for possible chemical changes induced by an enhanced UV field we have constructed a one-dimensional (1-D) model, which includes an enhanced UV field. In this model we integrate the contribution of the molecular abundances as a function of cloud depth to produce a total column density that can be compared directly with the observations. In such a 1-D cloud model the depth is fixed by the observed $C^{18}O$ column density. This model does not directly address the clumpy structure of clouds but instead allows for an examination of the effects of the UV field on chemical abundances as a function of depth. We will also examine the effects of varying the cloud depth and thereby can approximate the effects of having small clumps that allow greater UV penetration. A common practice in

chemical studies of molecular clouds is to place all column densities relative to the abundance of H_2. For this study we have divided all column densities by the CO column density. We will refer to all column densities relative to CO as "relative abundances". In some instances when we are presenting general results we will present abundances relative to H_2, these will be referred to as "abundances".

6.2 The Chemical Model

We have used the reaction network compiled by by Millar et al (1991). This network includes the formation of complex molecules, photodissociation of molecules, and the enhanced reactions rates of ions with high dipole moment molecules. The gas-phase reaction network consists of the major formation and destruction pathways for carbon-, oxygen-, nitrogen-, and sulfur-bearing species, including all of the molecules encompassed by this study. The entire reaction set links 389 species through a network of more than 3000 reactions. Below we outline some of the basic aspects of the chemical reaction network.

Since we are modeling regions that are exposed to enhanced ultraviolet (UV) radiation fields, the chemical reaction scheme accounts for the photodissociation and photoionization of molecules. We have used rates for CO photodissociation presented in van Dishoeck & Black (1988) which include an approximation for CO self-shielding. The transition from atomic to molecular form for most molecular species occurs much deeper in the cloud than that for H to H_2. Therefore we have not included the effects of H_2 self-shielding. In our model the molecular hydrogen density remains constant in time. The main destruction process for H_2 is cosmic ray ionization and the main formation path is immediate H_2 formation when a hydrogen atom sticks to a grain. It should be kept in mind, however, that for very small values of visual extinction (< 0.25 - 0.5 mag) the amount of H_2 will be overestimated.

Table 6.1. Initial Elemental Abundances[a]

Element	Abundance (Relative to H_2)
C^+	1.46(-4)
N	4.28(-5)
O	3.52(-4)
S^+	4.0(-8)
Si^+	4.0(-8)
Mg^+	6.0(-9)
Fe^+	6.0(-9)
Na^+	4.0(-9)
P^+	6.0(-9)

[a]Numbers are written in the form a(-b) = a × 10^{-b}.

The coupled differential equations governing the gas-grain chemical evolution are solved using a variant of the Gear (1971) algorithm, the code used is called LSODE (Hindmarsh 1980). This code, which is a linear implicit multistep method, utilizes variable time step and error control techniques to preserve numerical accuracy during the integration. The adjustable variables for a given calculation are the space density of *molecular* hydrogen, n(H_2), the factor by which the external UV radiation is enhanced above the normal interstellar radiation field (ISRF), χ, the gas temperature, T_{gas}, and the visual extinction to the center of the cloud, A_v. τ_V is the visual extinction proceeding from edge to center such that $\tau_V^{max} = A_V$.

For the initial conditions, presented in Table 6.1, we use depleted elemental abundances based for the most part on observations in the diffuse cloud towards ζ Ophiuchi (Savage, Cardelli, and Sofia 1992, see also Graedel et al 1982). The abundance of the helium ion was fixed by balancing the major formation and destruction paths at t = 0 (see Graedel, Langer, & Frerking 1982). The carbon, sulfur, silicon, and iron are assumed to be initially all in ionized form while oxygen and nitrogen are neutral.

This type of time dependent chemical model, with these initial conditions, is often labeled a "pseudo-time dependent" calculation. The assumption is that the

initial cloud starts out in a diffuse state, with all the atoms singly ionized (provided the ionization potential is < 13.6 eV) and then undergoes instantaneous collapse, at t = 0, to higher density. The chemical clock is started at t = 0 and the molecular abundances evolve under fixed physical conditions. In this fashion the model assumes a sudden "collapse", but does not model the dynamics of the event itself. This approximation may seem, at first glance, to be rather unphysical, but the timescale of chemical interactions is governed primarily by the density. Therefore, the chemical evolution in the diffuse state will occur at a much slower rate then in the dense state. Thus, the term "time" in pseudo-time dependent model becomes more realistic.

In general, times in chemical models have been broken up into three separate timescales: early times, $10^5 < t < 10^6$ yrs, intermediate times, $10^6 < t < 10^7$ yr, and steady state, $t > 10^7$ yrs. These models have shown that complex molecules actually peak at early times, $t \sim 10^5$ yr, when the atomic carbon abundance is higher, and decline before the onset of equilibrium (Herbst 1983). Since our study has included several complex species in our observations, such as CH_3C_2H, the inclusion of time dependence in the chemical calculations is critical. Moreover, the sources observed for this project are regions of high mass star formation with associated outflows, such as the plateau region in Orion or the high velocity flows in Cepheus A. These dynamical events may inhibit the attainment of chemical equilibrium and require an examination of the time dependence involved in the chemical evolution.

6.3 Chemical Model for the RIP

We will first apply the chemical model to the radical-ion peak (RIP) in Orion because this position has been shown (see Section 4.4.3) to be the closest to quiescent chemical evolution by comparison to dark cloud cores. For the physical conditions we have adopted $n(H_2) = 10^6$ cm^{-3} and $T_k = 25$ K. The density and

temperatures were chosen based on the results of Chapters 2 and 3. We have computed abundances for a depth of $\tau_V = 20.0$ mag. At this cloud depth the rates for photodissociation are negligible, even for the enhanced radiation fields observed in Orion.

The time evolution of the abundances for all molecules surveyed and other important species is presented in Figures 6.1 - Figures 6.3. The general features of the evolution is in agreement with previous theoretical models (Leung, Herbst, & Huebner 1985; Herbst & Leung 1989; Langer & Graedel 1989). The ionized carbon recombines quickly, in $\simeq$1000 yrs, to form C. The neutral carbon takes slightly longer to be processed into CO, with this species becoming the dominant carbon reservoir by t = 10^4 yr. The abundance of neutral carbon shows a sharp decline at t $\sim$ 10^4 yr, which is related to, but not entirely dominated by, the formation of O_2, a major destroyer of C through the reaction C + O_2 $\rightarrow$ CO + O. It is at these early times, where the neutral carbon abundance reaches a maximum, that the peak abundances are seen for many of the species included in our study. These are CN, HCN, HNC, C_2H, HC_3N, CH_3OH, CH_3C_2H, and also CS. Only SO, HCO^+, and N_2H^+ have abundances that are greater at equilibrium than at this early time.

The results of this model and a comparison to the relative abundances measured in the RIP are presented in Table 6.2. We have also included a measurement relative atomic C abundance from White & Sandell (1995). This ratio is important as a measure of the amount of carbon available in the gas-phase. It should be stressed that the observed C/CO ratio listed in this table *may* be tracing only the interclump medium. The interclump medium is expected to have more neutral carbon than in dense clumps because of enhanced photodestruction of CO (Meixner and Tielens 1993). Therefore this ratio should be viewed as an upper limit.

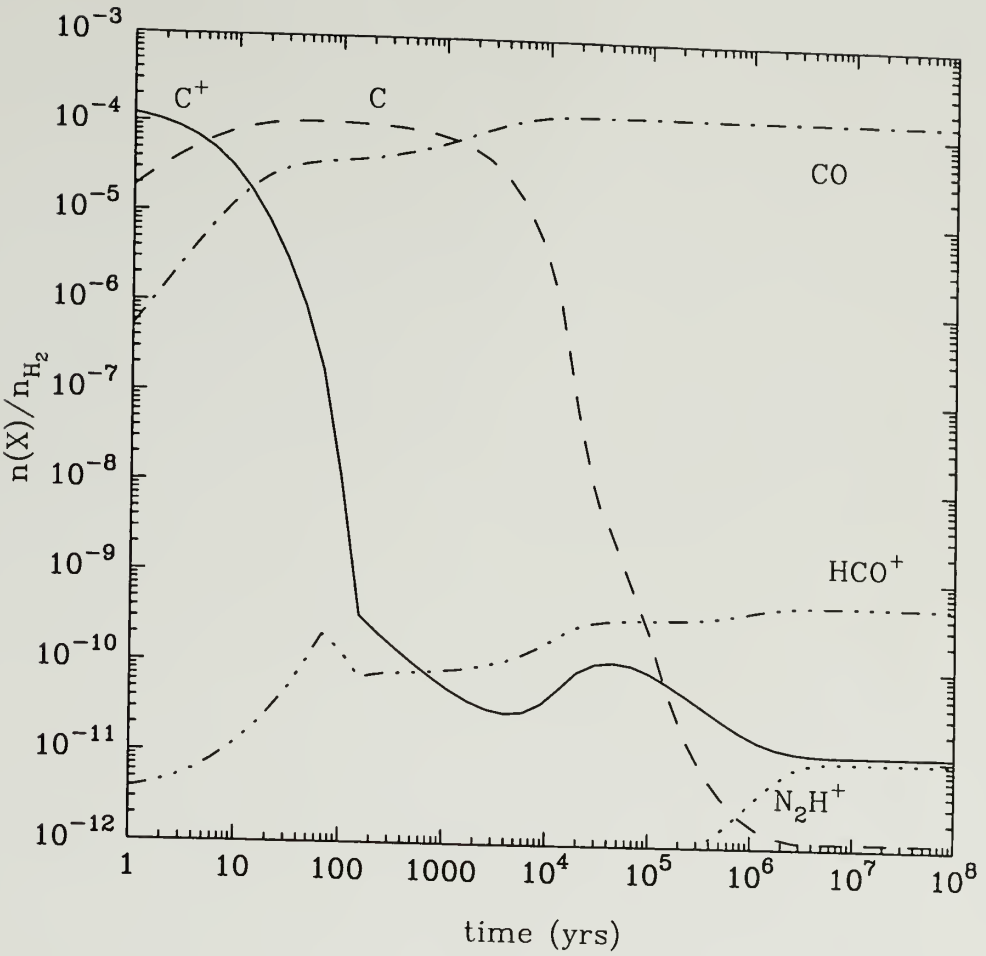

Figure 6.1. Time evolution for the major carbon reservoirs and trace species at τ_V = 20.0 mag.

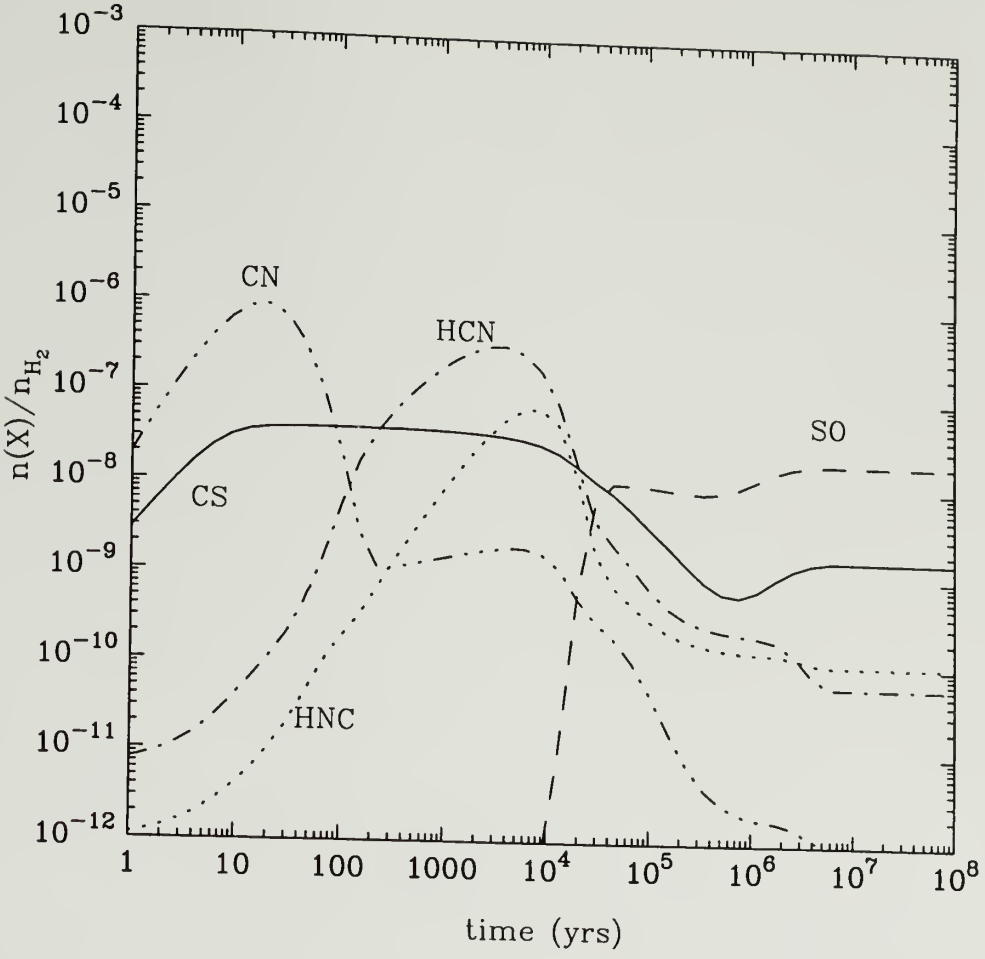

Figure 6.2. Time evolution for selected trace species at $\tau_V = 20.0$ mag.

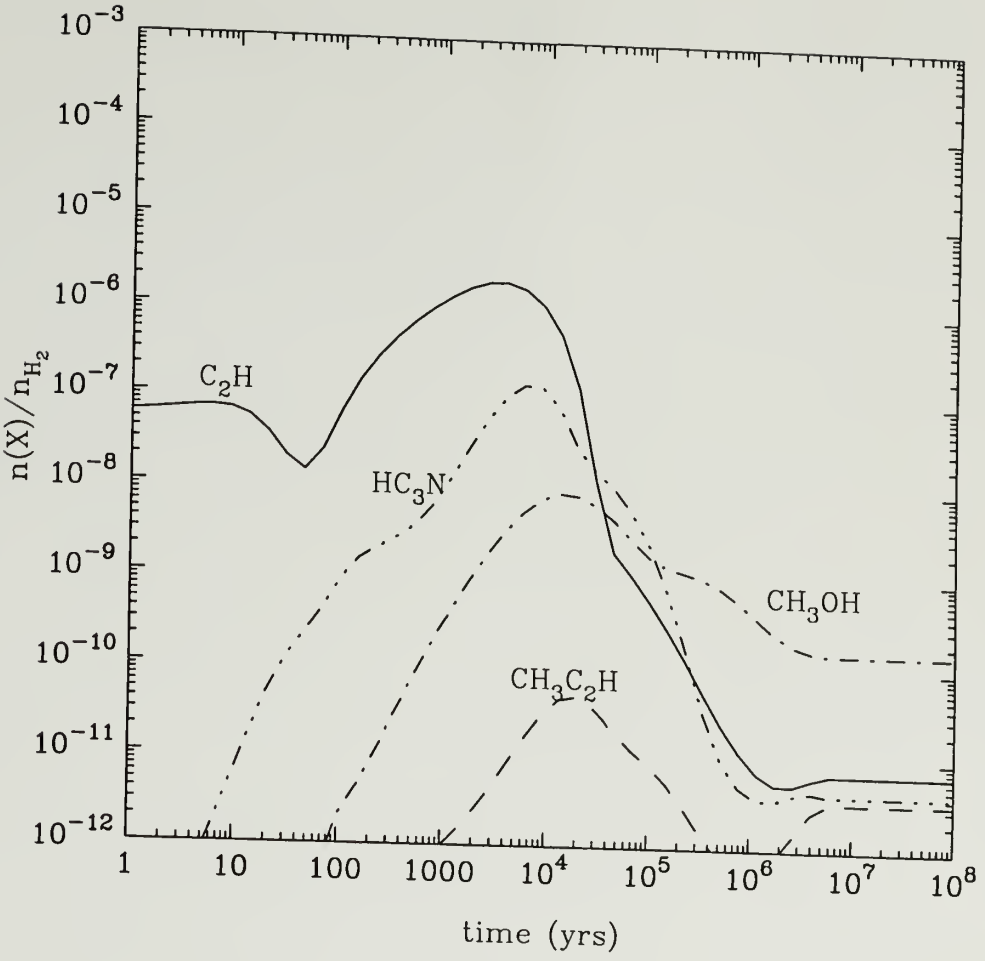

Figure 6.3. Time evolution for selected trace species at $\tau_V = 20.0$ mag.

Table 6.2. Relative Abundance Calculated for Well Shielded Dense Core[a,b]

	Calculated				Observed
Species	$t = 10^4$ yr	$t = 10^5$ yr	$t = 10^6$ yr	$t = 10^7$ yr	RIP
CS	2(-4)	2(-5)	5(-6)	1(-5)	1(-4)
CN	8(-6)	3(-7)	1(-8)	7(-9)	1(-4)
C_2H	4(-3)	4(-6)	5(-8)	5(-8)	4(-4)
HCO^+	1(-6)	2(-6)	3(-6)	4(-6)	7(-5)
N_2H^+	2(-9)	4(-9)	3(-8)	6(-8)	1(-5)
CH_3C_2H	3(-7)	6(-8)	4(-9)	2(-8)	4(-5)
HC_3N	5(-4)	2(-5)	2(-8)	3(-8)	6(-6)
SO	8(-8)	7(-5)	9(-5)	1(-4)	1(-5)
CH_3OH	6(-4)	1(-5)	3(-6)	1(-6)	9(-5)
HCN	6(-4)	5(-6)	1(-6)	4(-7)	2(-4)
HNC	3(-4)	2(-6)	1(-6)	2(-7)	6(-5)
C	8(-3)	2(-6)	1(-8)	1(-9)	0.05[c]

[a]Numbers are written in the form a(-b) = a $\times$ 10^{-b}.

[b]Abundances are relative to CO

[c]from White & Sandell 1995

The most striking conclusion from the table is that at only at very early times $t \sim 10^4$ yrs are the abundances even close to the observed values. An this time CS, HCO^+, and HCN are in reasonable agreement, however the model produces an order of magnitude more C_2H and nearly two orders of magnitude more HC_3N. The theoretical model also underproduces, by two orders of magnitude, the relative abundances of CN, CH_3C_2H, and N_2H^+, and SO. Therefore model of well shielded regions with physical conditions directly determined from observations can only match the abundances of 3 out of 12 species, at extremely short times, which suggests that something is drastically wrong with the model.

We examine the effect of density on the chemical evolution in Table 6.3. The relative abundances are presented at 10^5 yr because the abundances for most species are greatest at early times suggesting that short timescales are more appropriate. One trend observed in this table is that the molecules, HCN, HNC, CH_3OH, HC_3N, CH_3C_2H, and C_2H all have relative abundances that are more than an order of magnitude higher at $n(H_2) = 10^4$ cm^{-3} than at $n(H_2) = 10^6$

Table 6.3. Relative Abundances (relative to CO) Calculated for Well Shielded Dense Core at Various Densities[a,b]

	Calculated				Observed
	This Work			HL[c]	
Species	1x10^4 cm^{-3}	1x10^5 cm^{-3}	1x10^6 cm^{-3}	1x10^4 cm^{-3}	RIP
CS	9(-5)	4(-5)	2(-5)	1(-4)	1(-4)
CN	3(-4)	9(-6)	3(-7)	1(-3)	1(-4)
C_2H	2(-3)	5(-5)	4(-6)	9(-4)	4(-4)
HCO^+	6(-5)	1(-5)	2(-6)	6(-5)	7(-5)
N_2H^+	2(-7)	3(-8)	4(-9)	2(-8)	1(-5)
CH_3C_2H	9(-6)	2(-6)	6(-8)	6(-6)	4(-5)
HC_3N	2(-4)	5(-5)	2(-5)	6(-5)	6(-6)
SO	3(-7)	1(-5)	7(-5)	2(-5)	1(-5)
CH_3OH	3(-3)	3(-4)	1(-5)	3(-5)	9(-5)
HCN	3(-4)	2(-5)	5(-6)	2(-3)	2(-4)
HNC	2(-4)	9(-6)	2(-6)	1(-3)	6(-5)
C	0.45	5(-4)	2(-6)	0.67	0.05[d]

[a]Numbers are written in the form a(-b) = a × 10^{-b}.

[b]Abundances are relative to CO and presented at 10^5 yr

[c]Herbst & Leung 1989; T_K = 10 K

[d]from White & Sandell 1995

cm^{-3}. The relative abundances of the molecular ions HCO^+ and N_2H^+ show the same trend but with somewhat smaller increases. Comparing these relative abundances with the observations it appears that a density of n(H_2) = 10^4 cm^{-3}, and early times, provides the best match to the observations. However, this density is certainly inappropriate for the Orion ridge, or for that matter, M17 or Cepheus A. All evidence from multitransitional studies of high dipole moment molecules, such as that presented in Chapter 3, suggests the dense regions in GMC cores have H_2 densities at least > 10^5 cm^{-3}.

The dependence of molecular abundances with density is due to two related factors. First, molecular complexity is governed by the abundance of the H_3^+ ion (Graedel, Langer, & Frerking 1982). For example, hydrocarbons and other complex species are initiated through the C + H_3^+ → CH^+ + H_2 reaction (Herbst and Leung 1989). The abundance of H_3^+ also has a weak inverse power law

dependence on the density. A large abundance of the precursor ion will therefore lead to higher abundances for the dependent species, such as HCO^+.

The changing density also has an effect on chemical timescales since the reactions will be more frequent at higher densities. This is illustrated in Figure 6.4 where we show the time dependence of C^+, C and CO. The C^+ and CO time dependence are shown only at a density of $n(H_2) = 10^5$ cm^{-3}, while the evolution of the neutral carbon abundance is presented for three densities $n(H_2) = 10^5$, 10^6, and 10^7 cm^{-3}.

In this figure the sharp decline in the carbon abundance occurs at progressively earlier times as the density is increased. *The time difference is quite important since most complex molecules form when the C/CO ratio is close to one* (Leung, Herbst, & Huebner 1984). Although the actual peak of the complex molecule abundances occurs slightly later in time. Thus, the decline in relative abundance with density of CH_3C_2H, HC_3N, C_2H, HCN, and HNC is partially due to the peak abundances of these species occurring at times prior to $t = 10^5$ yr. Instead, examining Figures 6.1 - Figures 6.3, at $n(H_2) = 10^6$ cm^{-3}, the peak complex molecule abundances will occur at a few thousand years and not at 10^5 yr.

Thus knowledge of the density is necessary to set the timescales for chemical interactions. Because of this dependence whenever we refer to a time in the text we will also list the density used in the calculation. This is the first and a significant result of the comparison between theory and observations. Using the densities directly determined though observations and comparing the chemical theory with observations finds the greatest agreement at extremely early times and indicates that chemical timescales determined for the RIP are very short, $t < 10^4$ yrs. This conclusion will be examined more closely in the following sections. However, this model may be inappropriate for GMC cores because we have not accounted for the enhanced radiation field due to newly formed stars.

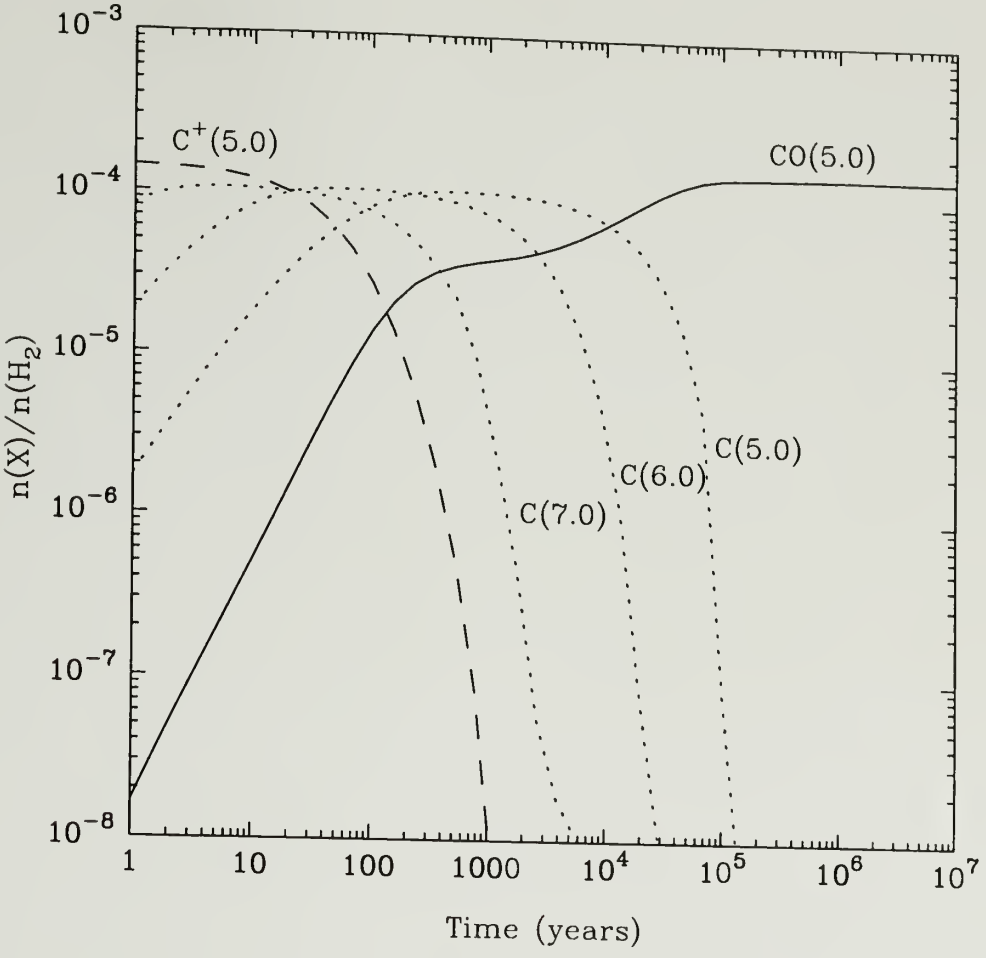

Figure 6.4. Time evolution of C^+, C, and CO abundances (abundances are relative to H_2) at $\tau_V = 20.0$ mag. The numbers in parenthesis are log[n(H_2)], the density of the model.

6.3.1 Comparison with Previous Theoretical Models

Before introducing the more complicated one dimensional model, we will first compare our theoretical and observational results with previous modeling efforts. This comparison is shown in Table 6.3. For this purpose we have chosen the work of Herbst, & Leung (1989; hereafter HL). HL was chosen because their model includes all of the molecules observed and is from a different reaction network. HL only present their results at $n(H_2) = 1 \times 10^4$ cm^{-3}. This discussion is complicated due to differing assumptions on initial conditions and reactions, but the comparison is useful to examine these results in light of previous work.

The relative abundances of CS, HCO^+,CH_3C_2H, CN, and C_2H are different by no more than a factor of three, while the relative abundances of HCN, HNC, and N_2H^+ agree to within an order of magnitude. But our model produces two orders of magnitude more CH_3OH, while HL predicts two orders of magnitude more SO. It is worth noting that these differences occur in spite of the fact that the ionization fraction and the relative abundance of the key H_3^+ ion are virtually identical between the two models.

The agreement between the relative abundance of electrons and H_3^+ suggests that the disparity between the two networks is not due to any difference in the initial conditions or the cosmic ray ionization rate, since the metal ions control the ionization fraction and cosmic rays control the abundance of H_3^+. Instead, these differences are probably the result of different pathways for the formation and destruction of the various molecular species. Millar, Leung, and Herbst (1987) have made a detailed comparison between the networks compiled by Millar and co-workers and that compiled by Herbst and Leung. This study found that the differences between the two networks was due to a philosophical disagreement on which reactions are more likely to proceed under interstellar conditions. It is likely the differences have narrowed in recent years as more reactions have been

measured in the lab and the theory improved. That order of magnitude differences still exist emphasizes the fact that chemical modeling, mostly for complex species, is still a very fluid field subject to continuous change and revision which can result in large changes in predicted abundances. We will address the consequences of this in the following sections.

In spite of these uncertainties one facet of the complex molecular chemistry that is unlikely to change is the requirement that neutral carbon exist in abundance to form these species. Chemical reactions, for simple molecules such as CO where the chemistry is well determined, consistently lead to the formation of extremely stable species that are "end points" in the chemical evolution. For gas-phase chemistry these are CO (carbon and oxygen), O_2(oxygen), N and N_2(nitrogen). Because these species are so stable at equilibrium they will be the major reservoirs of reactive atomic species and leave only trace amounts to form other molecules. Therefore either some mechanism must be found to continuously destroy these species or early times prior to the formation of stable molecule must be invoked.

6.4 Chemical Model Including Enhanced Radiation Field

6.4.1 One-Dimensional Model

To account for possible line of sight differences in the chemistry we have constructed a one dimensional cloud model by running a pseudo-time dependent calculation to times up to 10^7 yr with fixed physical conditions for a given visual extinction, defining a "zone". The visual extinction was then incremented from the cloud edge ($\tau_V = 0.0$ mag) up to some maximum value, normally $A_V \sim 15$ - 20 mag, defining a set of zones. A typical run had 40 zones between $\tau_V \sim 0.0 - 20.0$ mag. Each zone was independent of other zones except for the calculation of total CO and H_2 column densities required for the CO self-shielding photorate. In this fashion the physical conditions, density and temperature, can vary with depth or

be held constant for a "uniform" cloud model. For this work the physical conditions were held to constant values at each cloud depth. The model therefore enables an examination of the the effects of time and depth on the chemistry explicitly and simultaneously.

The chemical abundances are computed by integrating the contribution from each molecule in each zone up to some depth limit (assuming $N(H_2) = 10^{21} A_v$). This creates a computed column density for each species. We have fixed the cloud depth by using the column density of $C^{18}O$, converted to the CO column density using an isotopic ratio of $^{16}O/^{18}O = 500$. The predicted column density for each molecule is then divided by the CO column density enabling a direct comparison to be made with the observations.

One further modification was performed. Real molecular clouds have two sides, for example in Orion the H II region is on the front of the cloud, therefore one side of the cloud is receiving an enhanced photon flux ($\chi > 1$), while the other side of the cloud, the back side, is only impinged by the ISRF ($\chi \sim 1$). In order to account for this we have divided the CO column density by two and computed two separate models: one with an enhanced ultra-violet field ($\chi > 1$) and the other with the IRSF ($\chi = 1$). The predicted column densities for each molecule from the separate models were added together to produce a single set of total column densities. The column densities are divided by the total CO column density to create a model with an enhanced UV field only on one side of the cloud.

6.4.2 Comparison with Observations

We will once again compare our results first to the RIP in Orion. The physical conditions used for this model are $n(H_2) = 10^5$ cm^{-3}, $T_k = 25$ K, and $N(CO) = 4.4 \times 10^{18}$ cm^{-3}.

For simplicity in modeling, we have lowered the density by a factor of ten. This brings the timescales for complex molecule formation in line with the

previous chemical work ($\sim 10^5$ yr). *However, as outlined in the previous section, the chemical age can be lowered by about an order of magnitude to bring them in line with the results at $n(H_2) = 10^6$ cm^{-3} (see Figure 6.4). Because the chemical evolution is a non-linear process this does not mean that the abundances at this lower density will be equivalent to the results at $n(H_2) = 10^6$ cm^{-3}. However, the differences are not large enough to change our results.*

It is also necessary to make an estimate of the UV field enhancement towards the radical-ion peak. Theoretical models of dense clumpy photodissociation regions have shown the that flux from ionized carbon can be related to the UV field enhancement factor (Burton, Hollenbach, & Tielens 1991). We have estimated an enhancement factor of $\chi = 10^3$ from the intensity of the C^+ emission at the RIP taken from the C^+ map of Stacey et al (1993) and the theoretical models of Burton, Hollenbach, and Tielens (1991). This estimate is uncertain but should provide some measure of the ultraviolet field which is certainly lower at the radical-ion peak than further south near the ionized bar, where the enhancement factor has been estimated to be $\chi \sim 10^5$ (Tielens & Hollenbach 1985b).

To emphasize why the 1-D model is more appropriate for dense regions exposed to an enhanced UV field, Figures 6.5 and 6.6 present the abundance profiles for the survey species at t = 10^5 yr for both sides of the cloud, one impinged by an enhanced flux of UV photons (Figures 6.5) and the other bathed by the ISRF (Figure 6.6). These profiles were created using the physical conditions for the RIP.

Comparing the abundance profiles the most notable feature is the enhancement of the primary carbon species: C^+, C, and CO at the cloud edge. With a large UV field significant amounts of ionized and neutral carbon are observed deep into the cloud due to CO photodissociation. For example, the fractional abundance of neutral carbon is above $\sim 10^{-9}$ until $\tau_V > 6$ mag in the model with $\chi = 10^3$, but, for $\chi = 1$ the abundance of C falls below $\sim 10^{-9}$ at $\tau_V \sim$

3 mag. The inclusion of clumps into the model shown here will further increase the abundances of C^+ and C.

These figures illustrate the importance of integrating the cloud model, and including the cloud surfaces, when comparing model results with data from giant molecular cloud cores. The significance of this structure on the edges of dense clumps was recognized several years ago as providing a possible solution for the high abundance of neutral carbon in interstellar clouds (Tielens and Hollenbach 1985a). While the import of cloud structure for neutral carbon has been recognized, the depth dependence for the chemistry of other species has rarely been examined. Vialla (1986) computed abundances as a function of cloud depth, but this was for an equilibrium chemical model which does not include complex species.

Upon examination, the abundance profiles, in general, show similar structure. For most molecules the abundances are suppressed at low τ_V, due to photodestruction, and increase as the radiation field is attenuated; the abundances are suppressed to higher τ_V on the $\chi = 10^3$ side (Figure 6.5), than the side with $\chi = 1$ (Figure 6.6). The two notable exceptions to this trend are C_2H and CN. The abundance of C_2H is *greater* at very low extinctions in spite of the high photodestruction rates. The CN radical, on the other hand, has a dependence that is fairly constant with depth. A small peak in the CN abundance is observed at τ_V = 1.5 mag where the abundances of most other species is suppressed due to photodestruction for the $\chi = 10^3$ side. CN and C_2H are present at low τ_V because they have formation pathways linked to ionized and atomic carbon. For a discussion of the formation pathways at low extinction for these species see Appendix B3 in Bergin, Langer, and Goldsmith (1995).

A comparison between the 1-D model of the RIP at different times and the observations is presented in Table 6.4. Reasonable agreement is found for CS, SO, and CH_3OH, and early time 1-D models. However, in spite of the reasonable

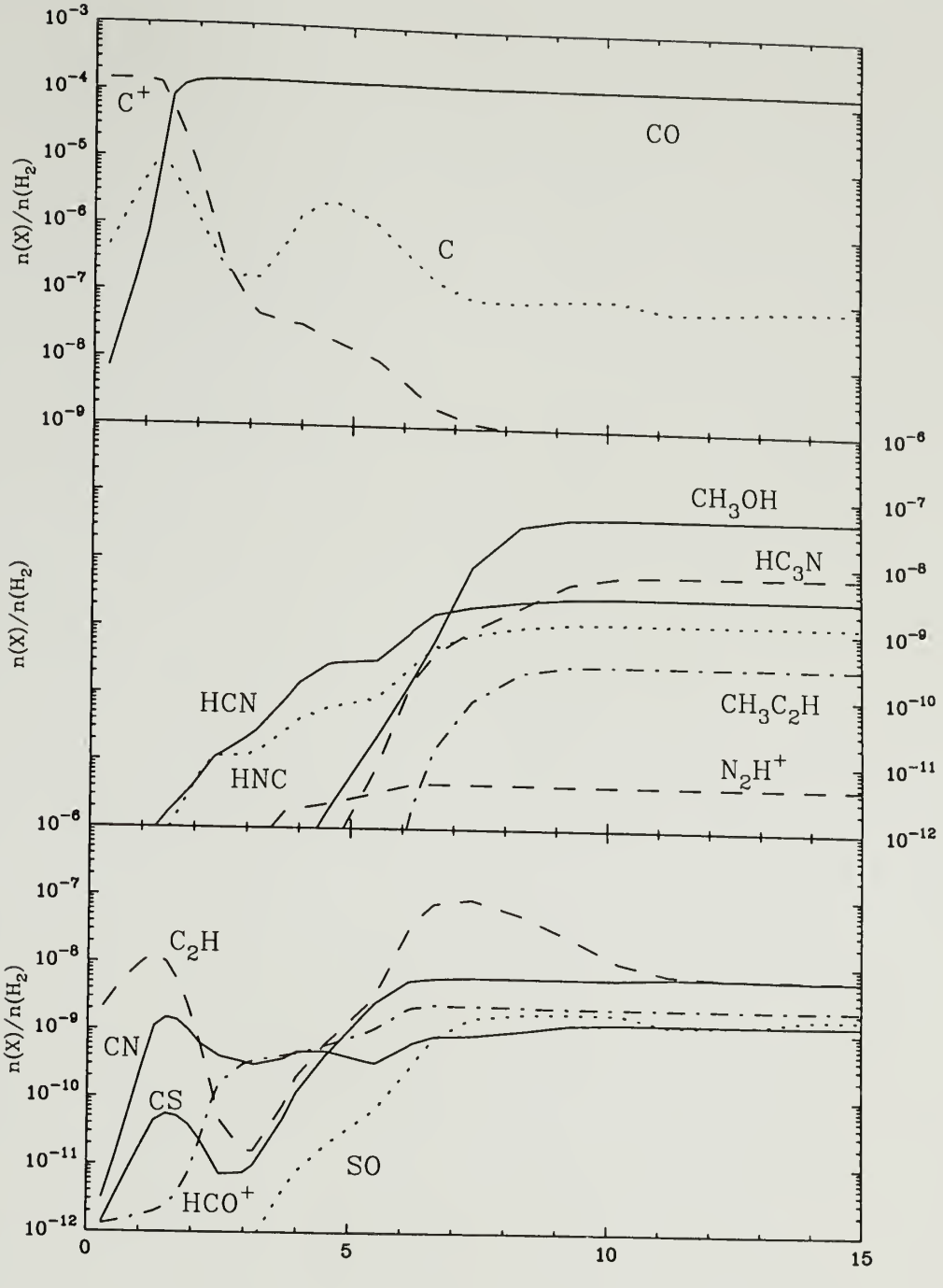

Figure 6.5. Profile of gas-phase abundances (abundances relative to H_2) against depth for all of the observed molecules. The physical conditions are for the radical-ion peak model: $n(H_2) = 10^5$ cm^{-3}, $T_k = 25$ K, and $\chi = 10^3$. The profiles are presented for t = 10^5 yr.

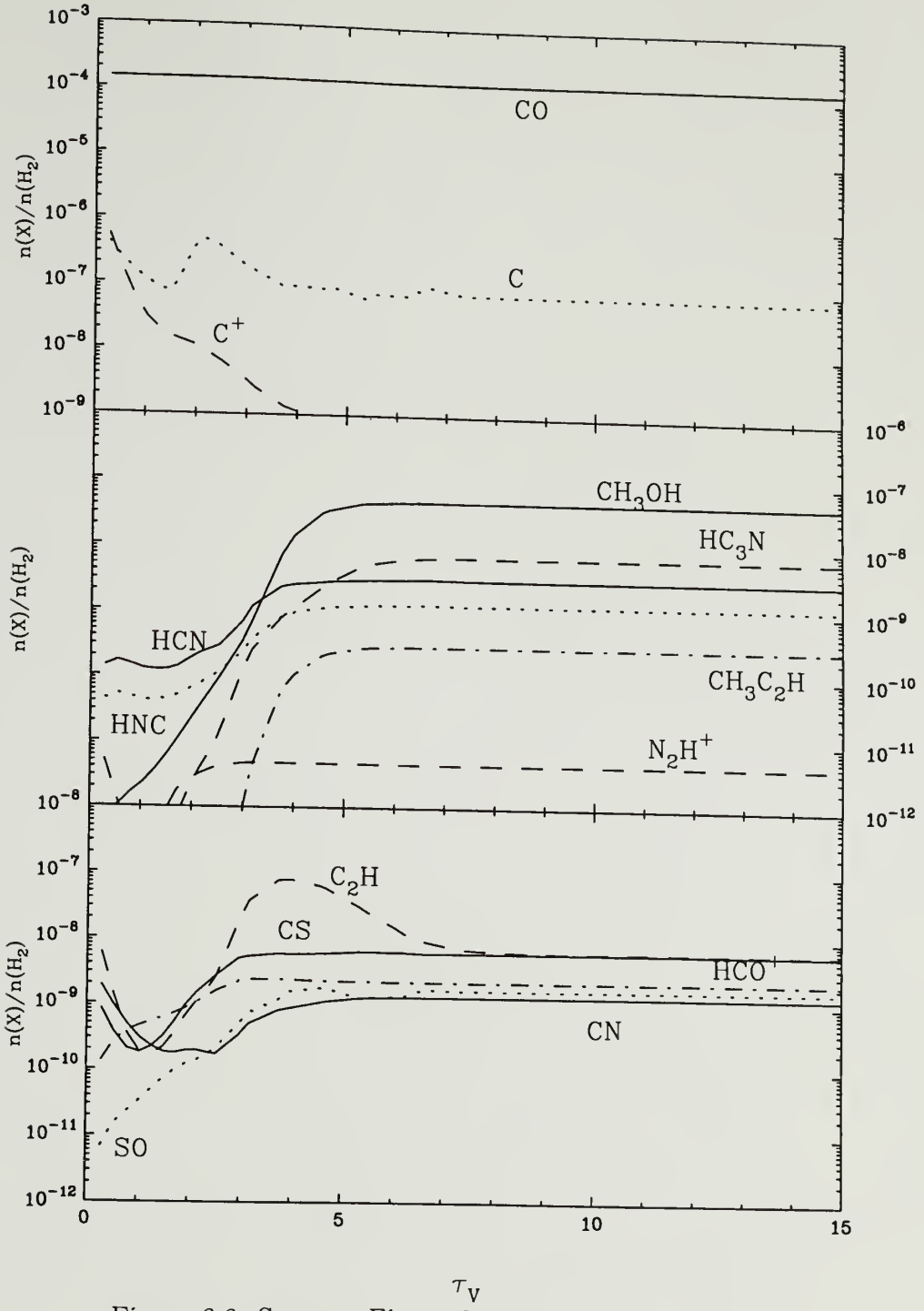

Figure 6.6. Same as Figure 6.5 except $\chi = 1.0$.

correspondence between theory and observations for a few molecules, the theoretical predictions for many more species do not match the relative abundances determined towards the RIP at any time. The early time relative abundances of HCN and HNC in the 1-D model are both a factor of ~10 below the observations, while CH_3C_2H, CN, and N_2H^+ have abundances in the 1-D model that are more than an order of magnitude below the observations.

These differences are highlighted by the extremely low C/CO ratio predicted by the theory. At all times the C/CO ratio is smaller than observed by a factor of ~25. The 1-D model, however, is more successful than the single zone model at τ_V = 20 mag, where the discrepancy is a factor of 100. As mentioned in Section 6.3, the neutral carbon observations may not be probing directly the amount of carbon in the dense gas. However, a factor of 25-100 is a significant difference and indicates problems or limitations of the model. The more complicated 1-D model, including line of sight variations in abundances, still cannot account for the relative abundances derived for the radical-ion peak in Orion. An additional mechanism is required to provide the extra neutral carbon to form both complex species and some simple species, such as HCN and HNC. Thus, these observations support the well documented "carbon problem" in dense molecular clouds (Philips & Huggins 1981; Graedel, Langer, & Frerking 1982; Herbst 1983; Leung, Herbst, & Huebner 1985; Langer & Graedel 1989).

6.4.3 Effect of Clumps

One possible solution for the carbon problem is that the clumpy structure of the cloud could increase the surface to volume ratio, and thus effectively enhance dissociation of CO to provide the required neutral carbon. This has been suggested as the solution to the large abundance of atomic C deep in GMC cores (Tielens & Hollenbach 1985). While it is likely that this mechanism can produce enough atomic carbon to match observations, the effect on more complex

Table 6.4. Relative Abundance (relative to CO) Comparison for the One-Dimensional Model[a,b]

	1-D Model					Observed
Species	τ_v=20[c]	t=1x10^{5}yr	t=3x10^{5}yr	t=1x10^{6}yr	t=3x10^{6}yr	RIP
CS	4(-5)	4(-5)	3(-5)	2(-5)	2(-5)	1(-4)
CN	9(-6)	8(-6)	2(-6)	1(-6)	1(-6)	1(-4)
C_2H	5(-5)	1(-4)	2(-5)	8(-6)	7(-6)	4(-4)
HCO^+	1(-5)	1(-5)	1(-5)	2(-5)	2(-5)	7(-5)
N_2H^+	3(-8)	3(-8)	3(-8)	2(-7)	4(-7)	1(-5)
CH_3C_2H	2(-6)	1(-6)	3(-7)	2(-8)	1(-8)	4(-5)
HC_3N	5(-5)	3(-5)	2(-6)	1(-7)	5(-8)	6(-6)
SO	1(-5)	9(-6)	1(-4)	1(-4)	1(-4)	1(-5)
CH_3OH	3(-4)	2(-4)	1(-5)	3(-6)	2(-6)	9(-5)
HCN	2(-5)	2(-5)	3(-6)	1(-6)	1(-6)	2(-4)
HNC	9(-6)	6(-6)	2(-6)	1(-6)	2(-6)	6(-5)
C	5(-4)	3(-3)	2(-3)	2(-3)	2(-3)	0.05[d]

[a]Numbers are written in the form a(-b) = a $\times$ 10^{-b}.

[b]n(H_2)=10^5 cm^{-3}; T_k=25 K; χ = 1000; A_v=31

[c]Well shielded single zone model where photoprocesses are negligible

[d]from White & Sandell 1995

molecules has not been studied. We have used the one-dimensional uniform density and temperature model presented in the previous section to investigate this effect. In the one-dimensional model the depth of the cloud is fixed by the $C^{18}O$ column density. In a clumpy cloud model this column density is the result of the superposition of numerous clumps, with N_{clump} (column density of a clump) $\ll$ N_{total}, along the line of sight. Therefore, by progressively lowering the cloud depth and computing column densities, we can mirror the effects of progressively smaller clumps. If the abundances of any molecule is enhanced at low τ_V, because of the high abundance of neutral carbon, then the abundance relative to CO will get larger since self-shielding will maintain the a fairly constant abundance of CO with depth. Of course, for very small cloud depths and large radiation fields, the abundance of CO is also reduced but, for these depths the photodestruction rates are high enough to suppress the formation of most molecules.

The clump model was constructed using the 1-D model of the previous section and the dependence of abundance with clump size is shown in Figure 6.7. The relative abundances of each species were normalized to its abundance at $A_V = 15$ where the photo-rates are negligible. We define this term as the abundance ratio. A value of log(abundance ratio) = 0 implies the abundance of the given molecule or atom is the same as for $\tau_V = 15$ mag, while if log(abundance ratio) > 0, then the abundance for that species is enhanced above the value in the well shielded interior of the clump.

The observed distribution of abundance ratio with clump size is rather complicated, but we can isolate 3 different types of behavior. The first is the species which have large abundance enhancements when the 1-D depth is small, these are $C^+$and C. This behavior is simply understood as the direct result of CO photodissociation, which will have a preferentially larger effect for smaller clump sizes. A different dependence is observed for HCN, CS, HC_3N, and HCO^+. The abundances of these species are greatly reduced for small clumps and then gradually increase to their well shielded value as the radiation field is attenuated. The other survey species are not shown in this figure, but have a similar dependence as HCN, CS, HCO^+, and HC_3N.

The final behavior is exhibited by CN and C_2H. The CN abundance remains close to the value in the cloud interior, almost independent of the clump size, while the C_2H abundance is enhanced by a factor of ~1.5 for moderate sized clumps with A_V = 8-10. Since these species can form nearly directly from C^+ and C they are enhanced in the photodestruction region.

This difference suggests that these species may be good tracers of the UV field in dense regions. Fuente et al (1993) suggested that the CN/HCN ratio would be a good tracer of UV fields. Figure 6.7 illustrates that this ratio is indeed dependent on the UV field. For regions with greater penetration the HCN abundance is

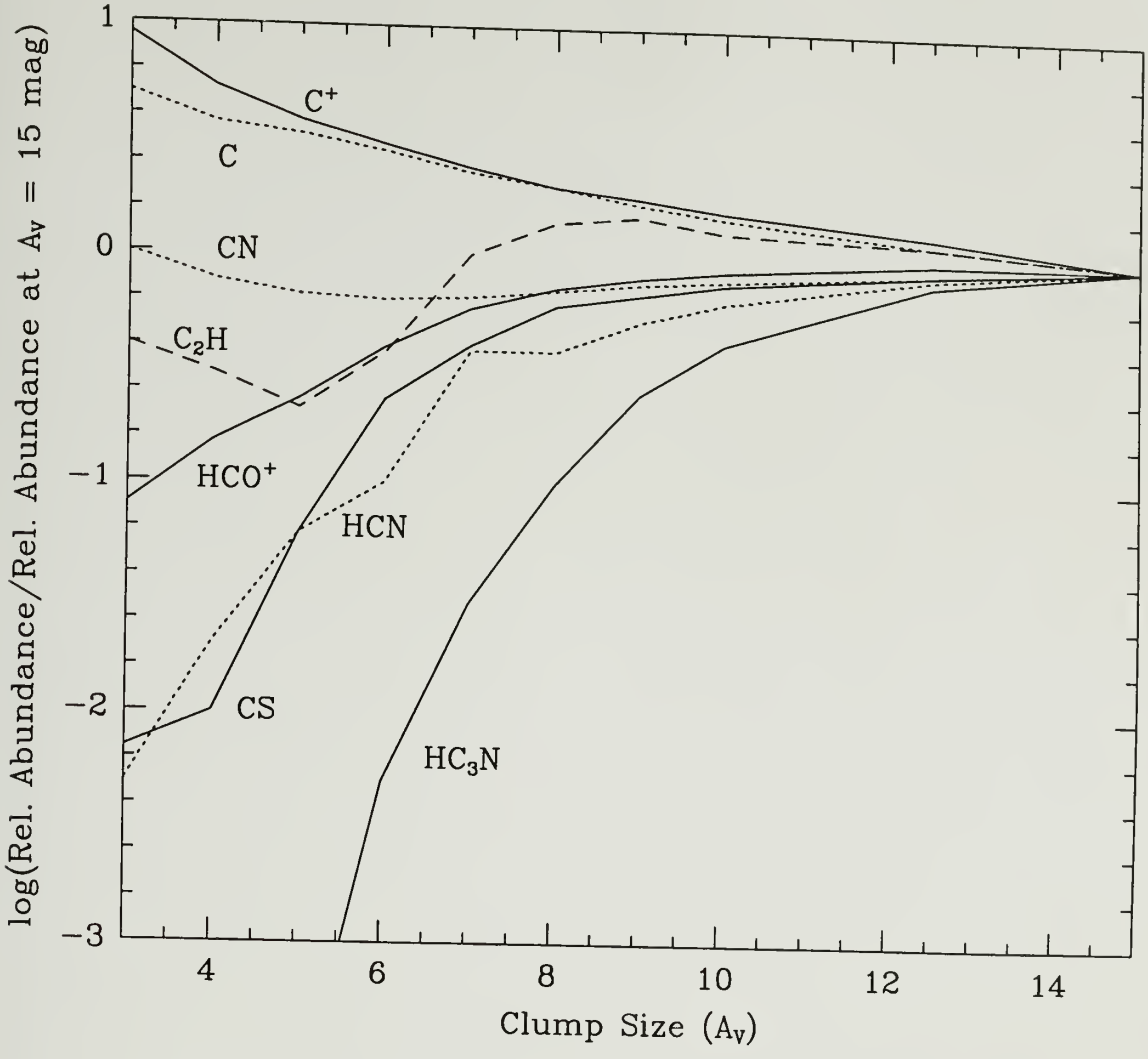

Figure 6.7. Plot of the logarithm of the relative abundance for a clump of variable size divided by the relative abundance from a clump with a depth of $A_V = 15$ mag.

greatly reduced, while the abundance of CN stays almost constant. Fuente et al (1993) also hypothesized that C_2H may be a good tracer of the UV field as well. This is in agreement with our results because C_2H is the only molecule that actually has an abundance enhancement, albeit a small one, in less shielded regions. These effects should be greater for larger UV fields. However, if the temperatures are much higher at the edges of clumps where the UV field is unattenuated then the rates for the neutral-neutral destruction reactions could begin to compete with the enhanced production rates and decrease these effects. Detailed modeling including a temperature gradient would be useful in this regard.

Outside of CN and C_2H, the chemistry of most molecules is still dominated by photodissociation. It is not until the UV field has been significantly attenuated that other species, such as HCN and CS form in abundance, and at these depths the abundance of carbon is not high enough to make a difference in their production rates. Therefore, although the clumpy model can produce the observed amounts of atomic and ionized carbon, clumps cannot explain the large abundances of most molecules, in fact a clumpy model makes it more difficult for the theory to be reconciled with the observations. A method must be found to raise the amount of neutral carbon to produce other species deep inside the clumps.

6.4.4 Effect of C/O Ratio on Chemical Evolution

Over the past decade chemical models have used the carbon to oxygen ratio, measured along lines-of-sight towards diffuse clouds, of C/O $\sim$ 0.4. With this constraint, chemical studies have been unable to reproduce the observed amount of neutral carbon and complex molecules in giant molecular clouds cores (Leung, Herbst, & Huebner 1985).

The cosmic C/O ratio of 0.4 is unable to produce complex carbon bearing species because it allows most of the carbon to be locked up into the stable CO molecule by 3×10^5 yr at $n(H_2) = 10^5$ cm^{-3}. With a large fraction of the carbon

locked up into molecular form this leaves a significant reservoir of atomic oxygen available to react in the gas phase. The excess oxygen will quickly form simple molecules (OH, H_2O, O_2) and deplete the remaining atomic and ionized carbon through reactions of carbon with these species, such as

$$C^+ + OH \rightarrow HCO^+, \tag{6.1}$$

$$C^+ + H_2O \rightarrow HCO^+ + H \tag{6.2}$$

and,

$$C + O_2 \rightarrow CO + O. \tag{6.3}$$

These few reactions are illustrative of the difficulty in maintaining atomic (and ionized) carbon at times $> 10^5$ yr, because significant amounts of oxygen in the gas phase will result in the production of O_2, OH, and H_2O at these times.

A plausible solution to increase the amount of carbon in the gas-phase is to raise the C/O ratio, which will lower the depletion paths from atomic and ionized carbon and allow for both C and CO to co-exist over a wide range of densities (cf. Langer et al 1984). Indeed the 1.3mm survey of Orion KL/BN by Blake et al (1987; hereafter BSGP) found that in order to match the theory with the abundances observed for the quiescent ridge in Orion a C/O ratio > 0.4 was necessary. A greater C/O ratio has also been suggested as the reason for the non-detection of the $^{16}O^{18}O$ isotope in TMC2, L134N, and B335 (Fuente et al 1993). Some evidence for a C/O ratio ~ 0.8 has been found from the atomic oxygen abundances derived from spectral lines of stars in the Orion association by Cuhna and Lambert (1992).

To achieve these ratios either the initial abundance of either carbon or oxygen must be non-cosmic, as inferred by Cuhna and Lambert (1992) or some mechanism

must exist that preferentially depletes the oxygen from the gas phase relative to the carbon. One possibility, put forward by BSGP, Swade (1989), and Fuente et al (1993), was for carbon and oxygen atoms to stick to grain surfaces with equal probability. Surface H-atom reduction on the mantle will quickly process these atoms to the saturated form (H_2O, and CH_4). H_2O will be strongly bound to the grain mantles while the polar CH_4 molecule will rapidly desorb from the surface placing the carbon back into the gas phase. There exists some recent observational evidence that the C/O ratio may be altered by some selective depletion mechanism. Current observations of the absorption profile of CO ice suggests that the surface CO is embedded in mantles of two distinct compositions. One component exhibits a weak, broad spectral feature (Sandford et al 1988); this is presumed to be CO embedded in a mantle dominated by polar molecules, probably H_2O. The other spectral feature is a narrow, stronger component superposed on the broad feature. The origin of this component is inferred to be CO ice in a matrix dominated by nonpolar species, possibly N_2, O_2, and CO_2 (Tielens et al 1991). The two grain mantle components could reflect differences in the grain mantle constituents along the line of sight, or gas-phase abundance differences at the time of mantle formation.

In Appendix B we present a model of the gas-phase chemistry in dense interstellar clouds including grain surface molecular depletion and desorption. This study found that the binding in the non-polar mantle could be considerably less than in the H_2O dominated mantle. Therefore the non-polar mantle could be in constant equilibrium with the gas phase, putting CO, and possibly CO_2 and CH_4, back into the gas phase, while the water remains locked on the grain surface. Whittet (1993) finds and abundance (relative to H_2) of water frozen on grain surfaces from observations along lines of sight towards field stars in Taurus to be $\sim 8.6 \times 10^{-5}$, which is a significant fraction of the available oxygen. If the H_2O

formed on the grain surface during the collapse of a diffuse region to a dense core then this would lower the initial oxygen abundance during the crucial period prior to steady state. If we assume that the observed abundance of water ice reduces the initial oxygen abundance then the C/O ratio would be ~0.6. Depletion is also strongly dependent on the density suggesting that the C/O ratio could be even higher than 0.6 given the fact that GMC cores are at least an order of magnitude denser than their dark cloud counterparts (Schloerb et al 1983; Chapter 3).

Motivated by these observations we have examined the effect of different C/O ratios on the chemistry of the RIP. For these models we have used the 1-D zone model with the same initial conditions as in the previous two sections. Figures 6.8 - Figures 6.10 present these results. We have modeled the effects of three different initial C/O ratios, the cosmic ratio of 0.4, and two depleted oxygen values of C/O = 0.6 and C/O = 1.0. The relative abundances of all the molecular species are shown in these figures as a function of time and the initial C/O ratio. The solid lines in the figures is the relative abundance measured at the radical-ion peak. The dashed lines are a factor of three above and below the measurement and represent the range in which reasonable agreement is made between the theory and the observations.

These figures illustrate the results outlined in Section 6.4.4 , that for a C/O ratio of 0.4, even early times, when the atomic carbon abundance is greater, cannot reproduce the observations. Raising the C/O ratio to 0.6 does alleviate some of the differences, but a large disparity between theory and observations still exists for CH_3C_2H, N_2H^+, and C, and to a lesser extent for HCO^+, HCN, and HNC. It is clear that a C/O ratio of 1.0 provides the most reasonable match to the observations. A C/O ratio of 1.0 brings 9 out of 12 species into agreement with the RIP relative abundances. This ratio also allows the abundances for these species to be reproduced at later times $\sim 10^6$ yr for $n(H_2) = 10^5$ cm^{-3}. *The agreement at*

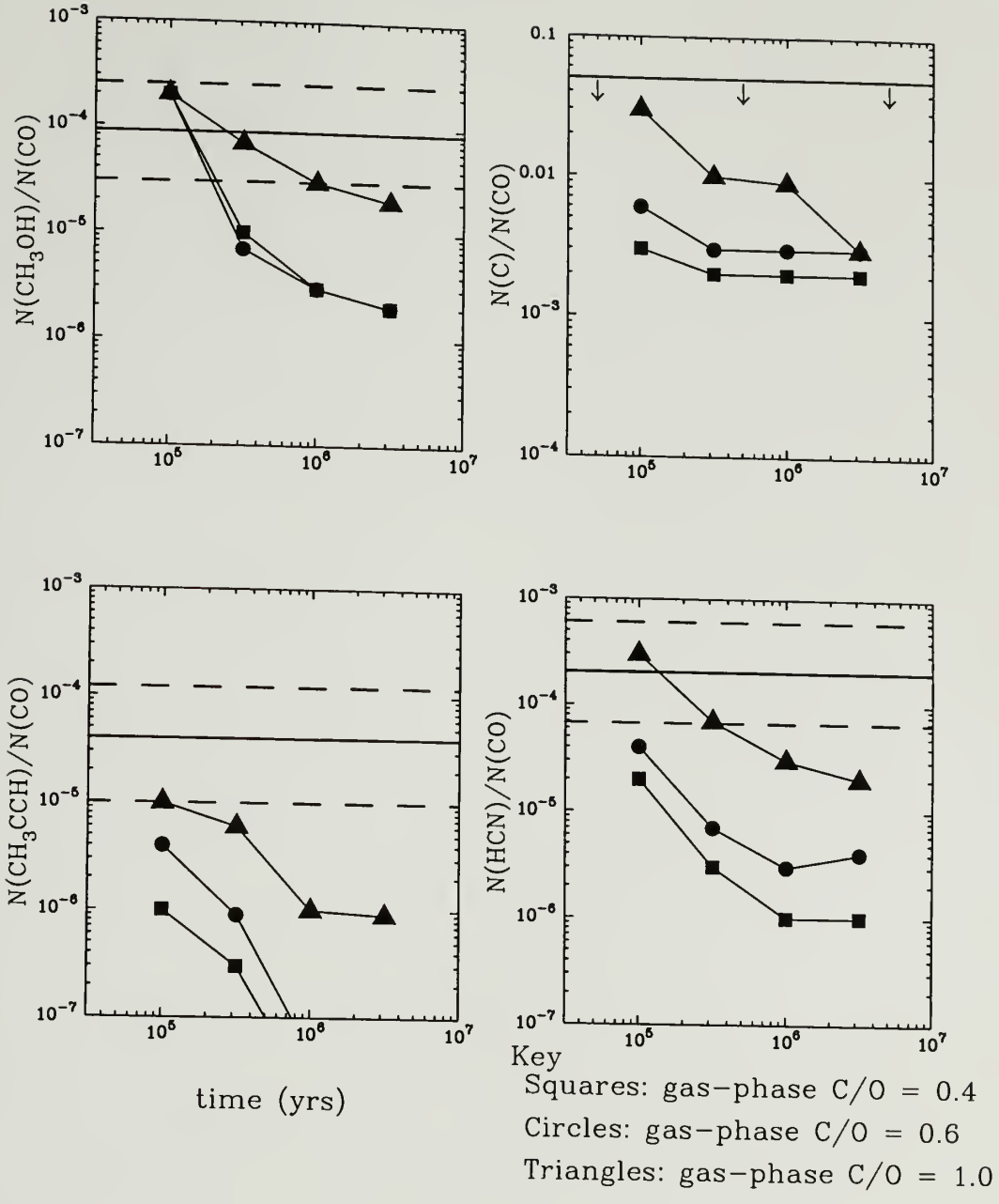

Figure 6.8. Panels showing the relative abundances of CH_3OH, C, CH_3C_2H, and HCN as a function of time and the initial gas-phase C/O ratio for the 1-D RIP model. The solid line denotes the observed relative abundance observed towards the RIP, while the dashed lines are a factor of three above and below the observations denoting a reasonable estimate of the error. The arrows below the solid line in the neutral carbon panel suggest that the observed value is an upper limit.

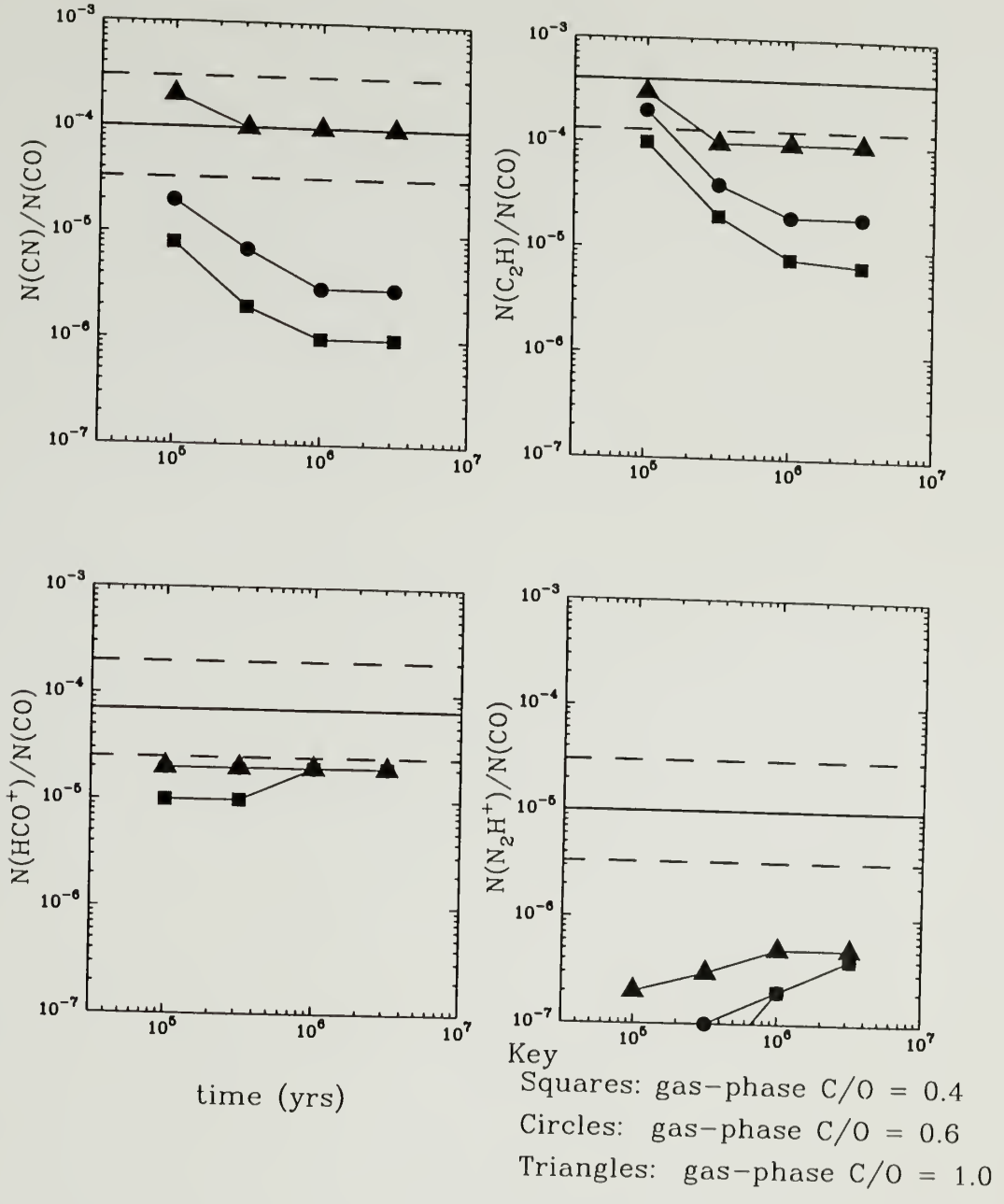

Figure 6.9. Panels showing the relative abundances of the radicals and ions, CN, C_2H, HCO^+, and N_2H^+ as a function of time and the initial gas-phase C/O ratio for the 1-D RIP model. The solid line denotes the observed relative abundance observed towards the RIP, while the dashed lines are a factor of three above and below the observations denoting a reasonable estimate of the error.

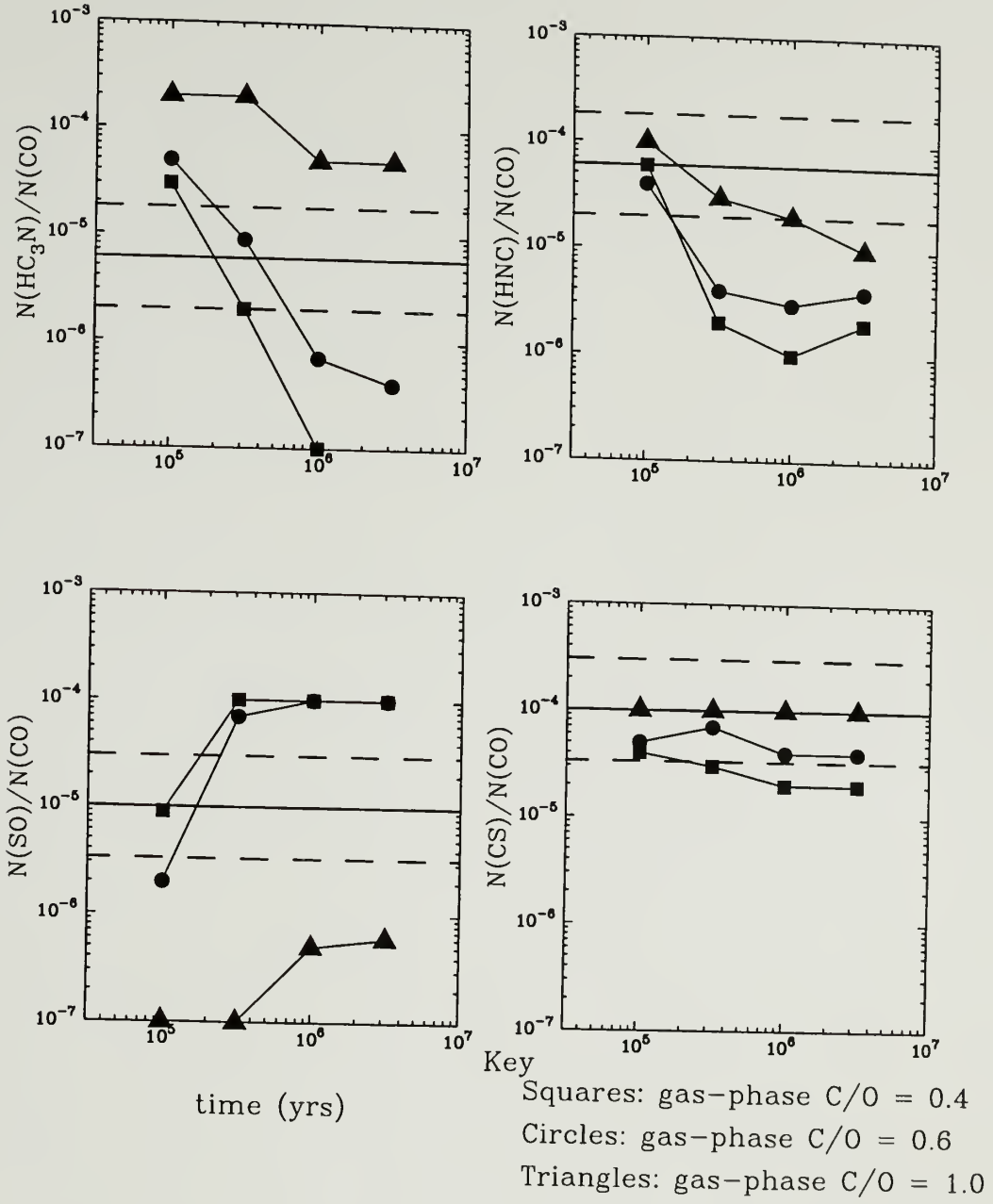

Figure 6.10. Panels showing the relative abundances of HC_3N, HNC, SO, and CS as a function of time and the initial gas-phase C/O ratio for the 1-D RIP model. The solid line denotes the observed relative abundance observed towards the RIP, while the dashed lines are a factor of three above and below the observations denoting a reasonable estimate of the error.

later times is important because at greater densities the timescales are even shorter (see Section 6.3). The only species that are not in agreement for C/O = 1 are N_2H^+, HC_3N, and SO.

Of these the sharp drop in the relative abundance of SO with the C/O ratio is perhaps the most notable. This is in marked contrast to the other sulfur-bearing molecule, CS, which shows almost no dependence with time or C/O ratio. The disparate behavior of the two major sulfur-bearing molecules suggests that the CS/SO ratio may be a good probe of the C/O ratio in molecular clouds. Indeed this ratio has been used before by Swade (1989) to provide an estimate of the amount of oxygen in L134N. Figure 6.11 presents the dependence of this ratio as a function of time and the initial carbon to oxygen ratio. The observed dependence is quite striking, the CS/SO ratio is extremely sensitive to amount of carbon and oxygen, but for a given C/O ratio two solutions exist, for early times ($t = 10^5$ yr) and at times $t \gtrsim 3 \times 10^5$ yr. The dichotomy between the early time results and later times suggests that other observations, of a molecule sensitive to time evolution, are required to discriminate between the two possible solutions. This sensitivity of the CS/SO ratio to both time and to the higher C/O ratios is primarily due to a drop in the formation rate of SO, through a reaction of atomic sulfur with OH. For high C/O ratios, the excess carbon rapidly destroys OH (forming CO) and therefore produces less SO. We outline the mechanisms for this dependence in greater detail in the Appendix.

We can examine Figures 6.8 - 6.10 to see which C/O ratio is most appropriate for these observations. The observed CS/SO ratio of 10 has two possible solutions, C/O $\sim$ 0.5 at 10^5 yr, and C/O $\sim$ 0.8 at later times. Of these two the best fit to the other molecules occurs for C/O $\sim$ 0.8 and $\sim 10^6$ yrs, because the lower C/O ratio of 0.6 clearly cannot reproduce the observed relative abundances for most other molecules. A C/O ratio of 0.8 will also bring the abundance of HC_3N into

agreement with the observations. A C/O ratio slightly less than unity will decrease the agreement with other species, such as CH_3C_2H, which does not agree well at later times, but it represents a reasonable trade-off to increasing agreement with a simple sulfur-bearing molecule, such as SO, whose chemistry is better understood.

The relative abundance of N_2H^+ presents the largest discrepancy between the theory and observations, and is not extremely sensitive to the C/O ratio. Previous examinations of chemistry in the Orion ridge have found similar problems in creating N_2H^+ (cf. Brown & Rice 1986a). It is possible that, because the nitrogen chemistry is not as understood as the carbon and oxygen chemistry (McGonagle 1995), there are unknown activation barriers or formation pathways for this molecule, perhaps linking its chemistry to NH_3.

6.5 Conclusion

In this Chapter we constructed two different chemical models for the radical-ion peak in Orion. The first model, for a dense well shielded core, was unable to reproduce the observed relative abundances for most species. This disagreement occurred in spite of the fact that the density and temperature used for the model were taken directly from the observations presented in Chapters 2 and 3. Indeed, using a density of $n(H_2) = 10^6$ the timescale implied by the chemistry is incredibly short, $t < 10^4$ yr.

A more complicated 1-D model that integrated the abundances of the different molecules as a function of cloud depth in the presence of an external enhanced radiation field, thereby incorporating line-of-sight effects into the chemistry. This model demonstrated that the inclusion of line of sight effects will not reconcile the theory with observations, a greater amount of neutral carbon is required in the cloud interior.

Two mechanisms to raise the amount of neutral carbon in the chemistry were discussed. The first invokes the presence of a clumpy medium, in which each

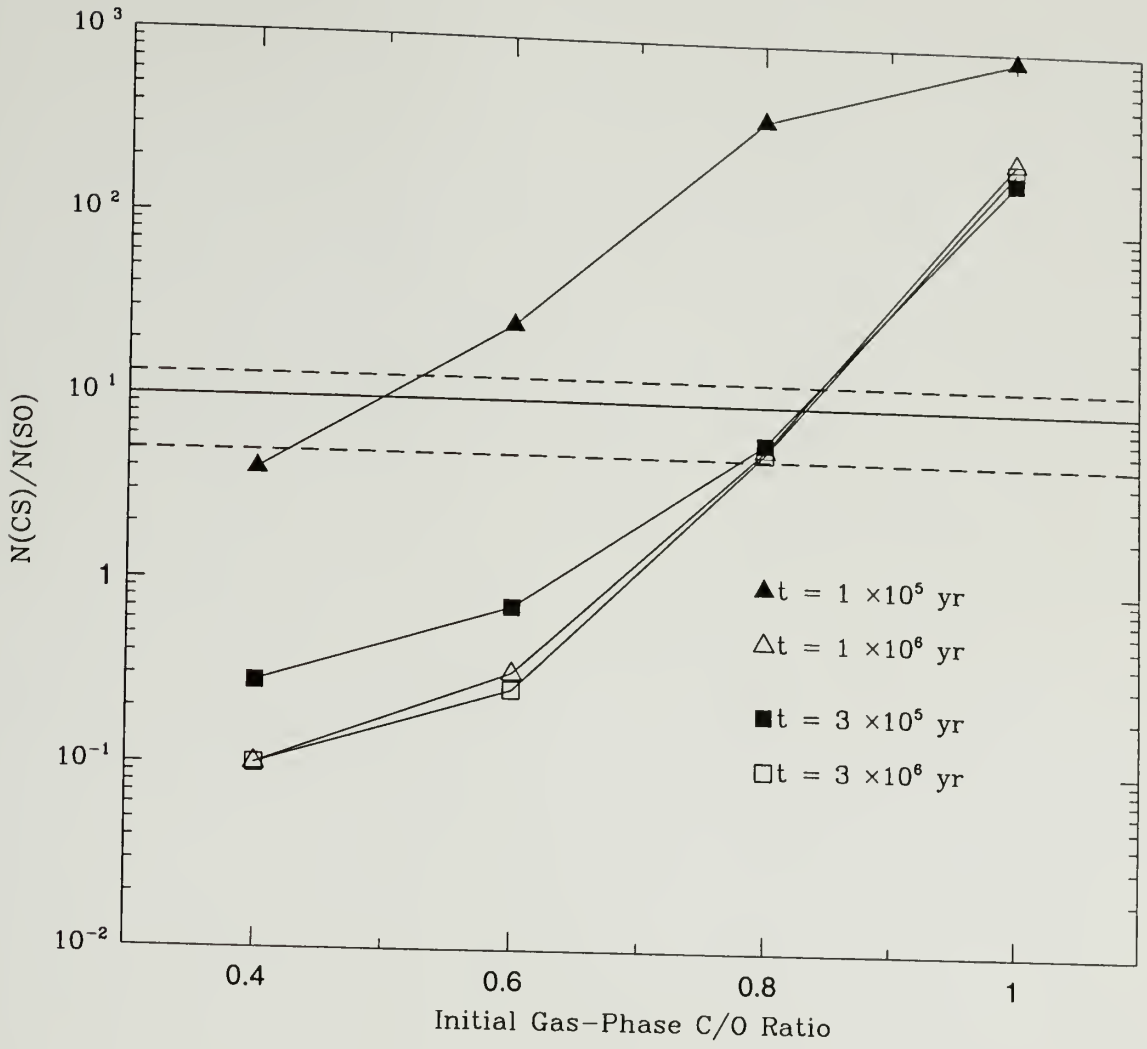

Figure 6.11. Predicted N(CS)/N(SO) ratio at a function of the initial C/O ratio. The solid line denotes the observed value towards the Orion radical-ion peak while the dashed lines are a factor of 3 above and below denoting a reasonable error limit.

clump is itself a dense PDR. This mechanism, which explains the observed extent of C^+ and C emission, was found to lower the abundances of most other molecules making it more difficult for the theory to match the observations. This model does not rule out the existence of clumps and only suggests that a more consistent model of GMC cores must be constructed that includes the various observations.

The second model examined C/O ratios larger than measured in diffuse clouds (C/O = 0.4). These models showed a C/O $\sim$ 0.8 provides a good fit between the theory and the observations. Not only does this model reproduce the observed abundances but it also allows for agreement to occur at later times, t $\sim 10^6$ yr (for $n(H_2) = 10^5$ cm^{-3}). This is important since chemical timescales are dependent on the density and for the measured density (Chapter 3) of $n(H_2) \sim 10^6$ cm^{-3} the chemical age is t $\sim 10^5$ yr. Two possible solutions to lower the abundance of oxygen were suggested. The first that the Orion region has a greater intrinsic C/O ratio, which is greater than the cosmic value. The second mechanism, first suggested by Blake et al (1987) involves selective depletion of oxygen relative to the carbon when the dense gas is forming from diffuse material. In the next chapter we will examine whether these conclusions are unique to the radical-ion peak or whether they represent a general property of the chemistry in GMC cores. We will also discuss other possible mechanisms to alter the C/O ratio and the relevance of grain chemistry on these results.

Chapter 7

The Chemical Evolution of GMC Cores

In the previous chapter we examined the chemistry of the Orion radical-ion peak (RIP) position and found that the chemical evolution there could be explained by a combination of (1) choosing a characteristic early time and (2) raising the initial C/O ratio. In this section we will examine whether these conclusions are specific to the RIP or whether they represent a general property of the chemistry in giant molecular cloud cores. First we will examine whether the conclusions apply to other positions in Orion, and then we will apply models of chemical evolution to M 17 and Cepheus A.

7.1 Orion

In addition to the RIP we have determined abundances for several other positions in Orion. Instead of examining the chemistry in detail for each point, we will compare the model to those positions with the most extreme physical properties in comparison to the radical-ion peak. For this purpose we have chosen Orion KL/BN and 4′S,

We will first examine the chemistry observed towards KL/BN. Given the impact of the star formation on the abundances of SO, CH_3OH, HCN, and HC_3N (Blake et al 1987), it is certain that the chemical evolution towards this position is different from that at the RIP. However we note the other species in our survey are not as greatly affected by the star formation (see Table 4.7). Outside of the chemical abundances other differences are worth noting. First the temperature of the *quiescent gas* is greater at KL/BN ($T_k \sim 45$ K) than at the RIP ($T_k \sim 28$ K) and, given the close proximity of the Trapezium stars to KL/BN line of sight, the

star forming core is certainly exposed to a larger UV field. With these two facts we will examine whether the different physical properties observed at KL/BN will change the chemical evolution.

We have created a 1-D model for the Orion KL/BN line-of-sight which has $n(H_2) = 10^5$ cm^{-3}, $T_k = 50$ K, $\chi = 10^5$ on the front side of the cloud, $\chi = 1$ on the back side of the cloud, and $N(CO) = 8.5 \times 10^{18}$ cm^{-2}. Figures 7.1 - 7.3 present the relative abundances for the KL/BN model compared with the observations.

These figures show that the same general conclusion obtained for the RIP applies to KL/BN. The relative abundances of simple carbon-bearing species C_2H, CN, and HNC, which are only present in the quiescent ridge component and not the hot core or plateau (BSGP), require both t $\sim 10^6$ yrs **and** C/O >0.4. As observed for the RIP, the relative abundance of HC_3N does not agree well with observations when C/O = 1. We cannot predict the possible C/O ratio for this position because of SO is tracing a different component (the plateau) than CS (quiescent ridge) along this line of sight (see SO and $C^{34}S$ spectra in Figure 4.10). However, the agreement between the calculated abundances and the observed abundances is certainly closest for C/O $\sim 0.6 - 1.0$.

Thus, we see that modeling a position with more extreme conditions than the radical ion peak still produces the same basic result. This suggests that the chemical evolution along the Orion *ridge* may be relatively unchanged. In fact, excluding the two star forming sites, the CS/SO ratio is a constant value of 10 for every position, thus the C/O ratio is not varying. At the star forming sites high temperatures near the protostars may be evaporating species off of grain mantles and/or overcoming energy barriers for some reactions which will produce deviations from the CS/SO relationship presented in Figure 6.11. At these positions it is also possible that water molecules are desorbing from dust mantles, thereby replenishing the "lost" oxygen. However, these effects may not be

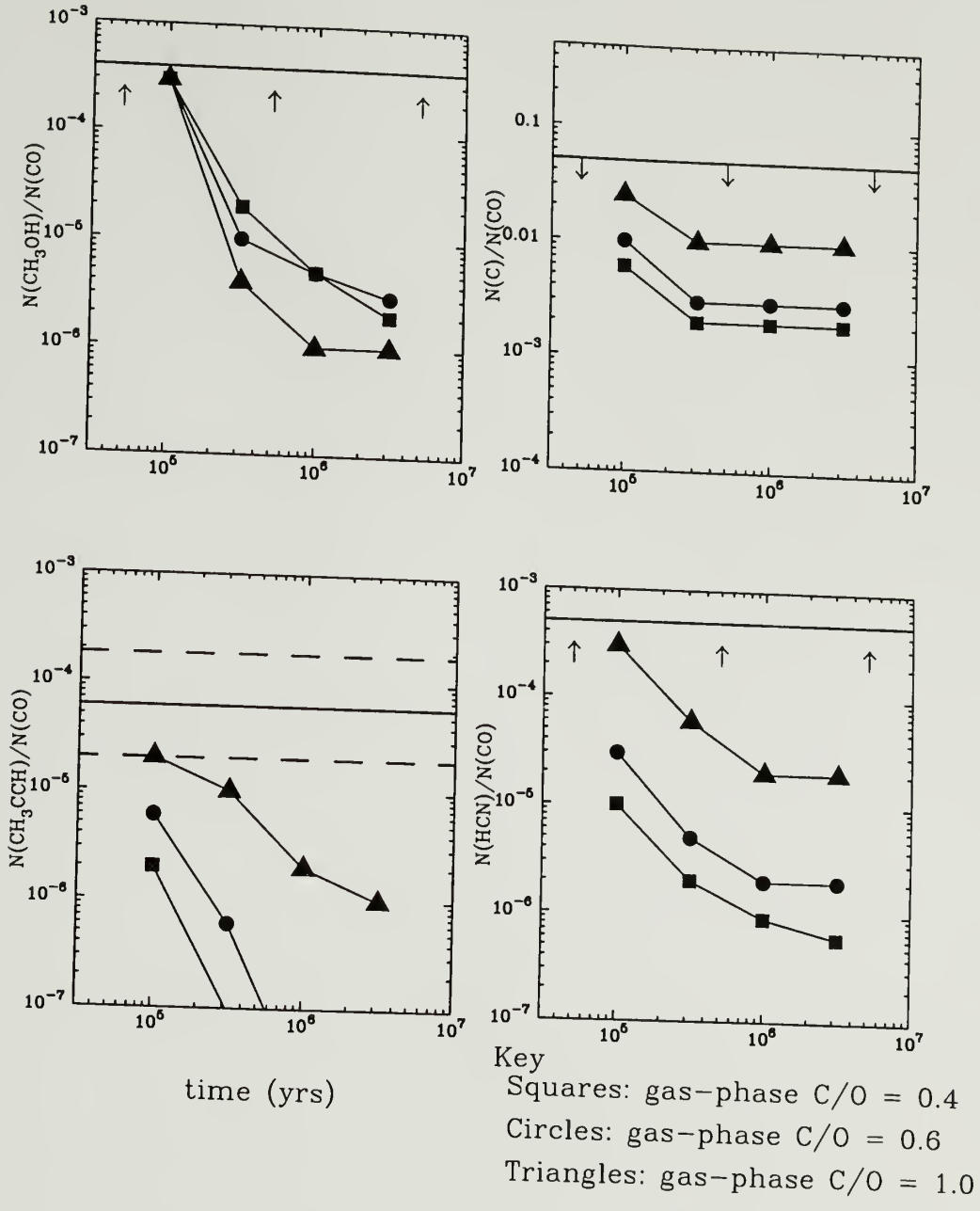

Figure 7.1. Panels showing the relative abundances of CH_3OH, C, CH_3C_2H, and HCN as a function of time and initial gas-phase C/O ratio. The solid line denotes the observed value at the Orion KL/BN position, while the dashed lines are a factor of three above and below the observations denoting a reasonable estimate of the error. The arrows below the solid line in the neutral carbon panel mark the observed value as an upper limit (see Chapter 4), while the arrows in the CH_3OH and HCN panels mark the abundances as lower limits.

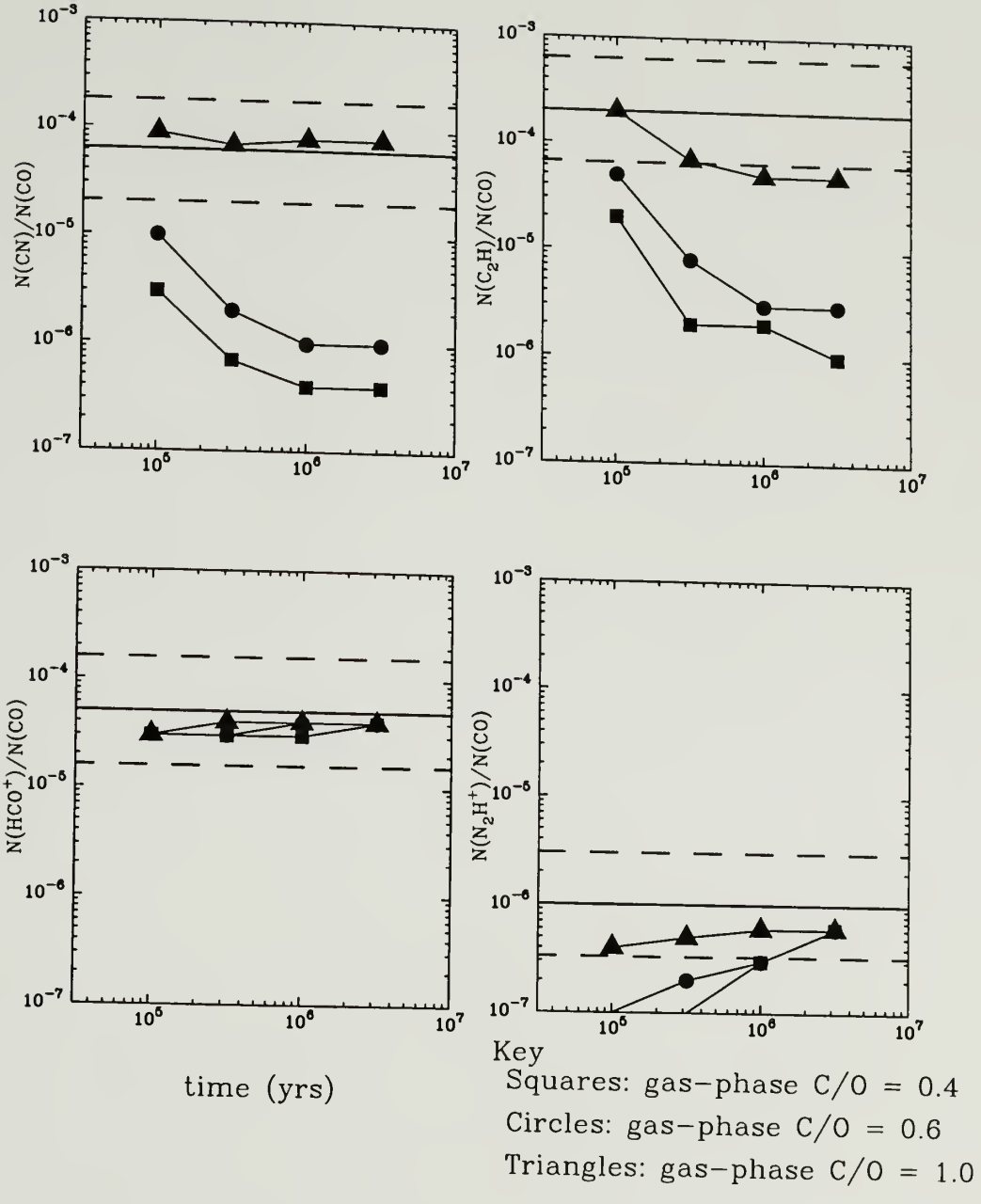

Figure 7.2. Panels showing the relative abundances of the radicals and ions, CN, C_2H, HCO^+, and N_2H^+ as a function of time and initial gas-phase C/O ratio. The solid line denotes the observed value at the Orion KL/BN position, while the dashed lines are a factor of three above and below the observations denoting a reasonable estimate of the error.

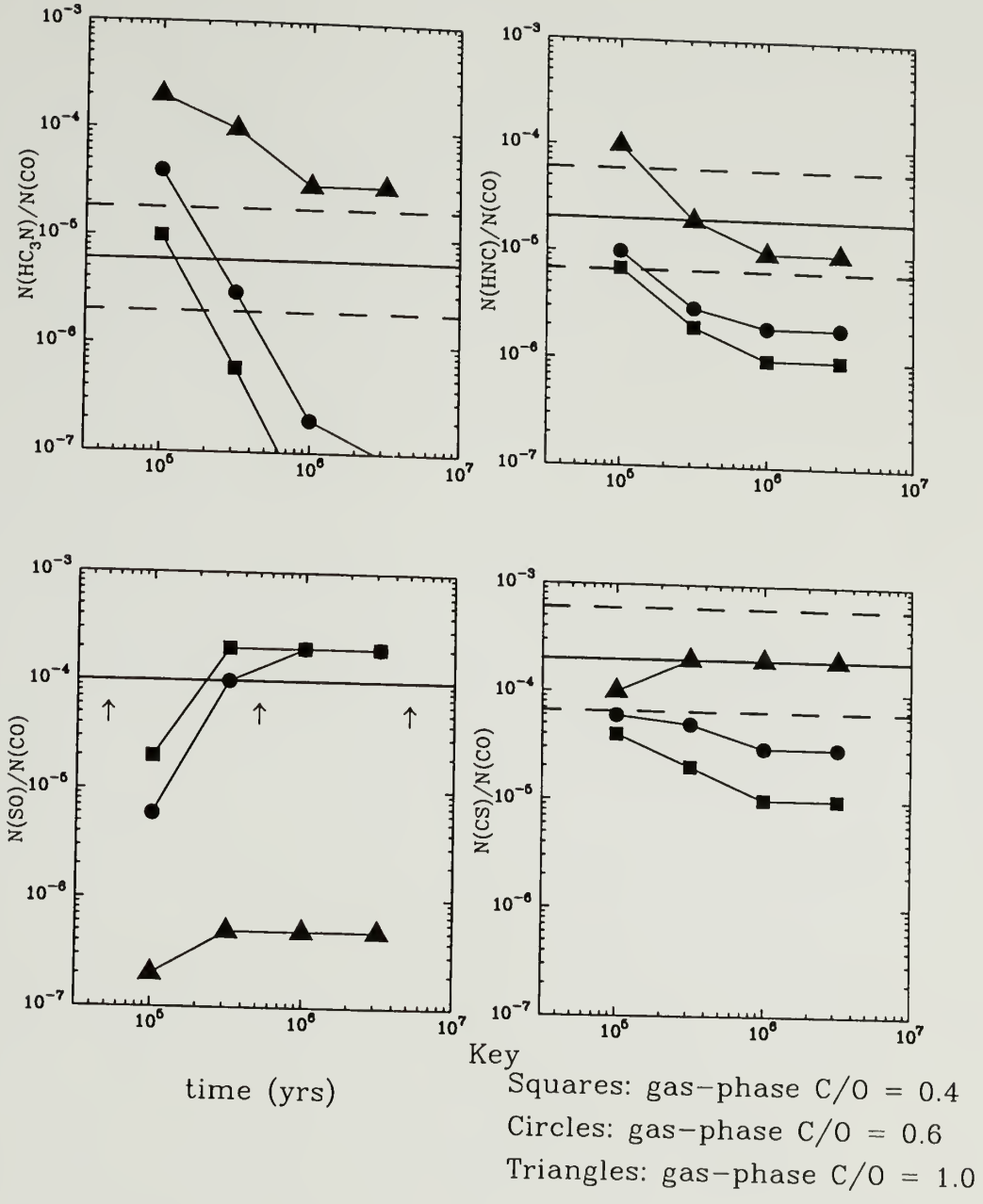

Figure 7.3. Panels showing the relative abundances of HC_3N, HNC, SO, and CS as a function of time and initial gas-phase C/O ratio. The solid line denotes the observed value at the Orion KL/BN position, while the dashed lines are a factor of three above and below the observations denoting a reasonable estimate of the error. The arrows in the panel for SO marks the abundance as a lower limit.

apparent for the extended ridge material because the impact of the star formation is not as extreme as it is closer to the embedded protostars.

The other two positions that may be chemically distinct from other positions along the ridge are 4′S and the Bar. The relative abundances for these positions, listed in Table 4.7, are typically lower than observed for the more quiescent RIP. In particular, the relative abundances of the molecular ions HCO^+ and N_2H^+ towards 4′S and the Bar are both factors of 3-10 lower than seen for the RIP, while CH_3C_2H, HC_3N, CH_3OH, and HNC are not observed at all towards the Bar.

The differences between 4′S and the RIP are particularly intriguing since both have similar $C^{18}O$ column densities and kinetic temperatures (see Table 4.7). The principal difference between the two positions is a larger radiation field observed along the Bar. The radiation field enhancement presumably extends at some level to the 4′S position, which is located on the southeastern edge of the bar. The radiation field for the Bar has been estimated to be enhanced by a factor of 10^5 above the ISRF (Tielens and Hollenbach 1985b). We will assume that this value also applies to 4′S. Therefore the radiation field for 4′S is two orders of magnitude greater than the radiation field estimated for the RIP. It is possible that the relative abundance differences between the RIP and 4′S are due to the larger radiation field. However, the KL/BN 1-D model presented in the preceding paragraphs included a radiation field of $\chi = 10^5$ and the enhanced radiation field of this model does not reduce the relative abundances of species such as HCO^+ or HCN. For example at early times the relative abundance of HCO^+ (using C/O = 0.6) for the RIP model ($\chi = 10^3$) is $N(HCO^+)/N(CO) = 1 \times 10^{-5}$, while the 1-D model for KL/BN, with $\chi = 10^5$, predicts the abundance should increase to $N(HCO^+)/N(CO) = 3 \times 10^{-5}$. This increase is in the opposite direction from the abundance gradient that is observed for HCO^+ (Table 4.7). A variation in the C/O ratio is also ruled out because the CS/SO ratio = 10 for the RIP, 4′S (and

the Bar). A more likely solution is a greater penetration depth for UV photons due to a lower filling factor for the dense gas.

Recently there has been a series of high resolution observations of C I, CO, and other species towards the Bar, sometimes including the 4′S position (Tauber et al 1995; Hogerheijde, Jansen, & van Dishoeck 1995). A comparison of C I intensities and ^{13}CO intensities by Tauber et al (1995) showed that for the Bar (including 4′S) the carbon and ^{13}CO intensities are linearly correlated. However, the extended ridge material observed north of the Bar near 1.5′S shows a different dependence. At Orion 1.5′S the C I/^{13}CO ratio is typical of that observed in dense regions (Keene 1994).

The linear correlation of C I and ^{13}CO observed towards the Bar and 4′S suggests that these regions are being penetrated by a greater amount of UV flux, which dissociates CO and creates the atomic carbon deep within the PDR. Since total column densities for 4′S and the RIP are similar, a plausible solution for the relative abundance differences between the RIP and 4′S is that the filling factor of the dense gas is smaller towards 4′S. This reduction will have two effects. First, it will lower the computed abundances of most species, because of lower beam filling factors. Second, based on the theoretical calculations presented in Figure 6.7, it will allow greater penetration of UV photons, thereby increasing the photodestruction rate and lowering molecular abundances. The additional UV photons will also photo-ionize molecules and atoms, leading to increased abundances of electrons that can reduce the abundances of HCO^+ and N_2H^+. However, these conclusions should be tested with a more realistic model and observations at higher angular resolution than presented here.

Excluding the Bar and the associated southern column density peak, the relative abundances and physical conditions for the other positions in Orion are similar. Therefore, we conclude that the chemical evolution for the extended ridge

is best described by t $\sim 10^6$ yr (for $n(H_2) = 10^5$ cm^{-3}) and C/O $\sim$0.8. We will examine the abundance variations in Orion and their relation to physical variables in section 7.5.

7.2 M 17

For M 17 we have chemical information for only two positions, the northern condensation (NC), which has greater temperatures and a high UV field making this position comparable to BN/KL, and the central condensation (CC), which has physical properties more similar to the radical-ion peak in Orion. We have chosen to model the northern condensation using the model introduced for BN/KL in the previous section. Although the geometry of M 17 is different than that of Orion, this model should be appropriate for the NC because the emission from the H II region overlaps the molecular material near the northern condensation.

The results of this model, shown in Figures 7.4 - 7.6, demonstrate that C/O $\sim$ 0.8 and times between 3×10^5 and 10^6 yrs provides the best agreement. Therefore the evolution observed in M 17 is similar to that observed in Orion. The relative abundances for the NC are quite similar to that of the CC, suggesting that the chemistry at these two positions is not appreciably different. Direct comparison between the theory and the relative abundances observed for the central condensation shows similar results. The CS/SO ratio for the CC is slightly lower than the NC, $\sim$4.5 instead of 7, but examining Figure 6.11 this will not change the predicted C/O ratio by a large amount. Therefore the chemical evolution observed in M 17 is similar to that found for the quiescent ridge in Orion.

7.3 Cepheus A

In Cepheus A we have determined abundances in two positions, Ceph-A N and Ceph-A S. The physical conditions for the two positions are quite similar, with the temperature of the Ceph-A N position ($T_k \sim 30$ K) only slightly greater than that

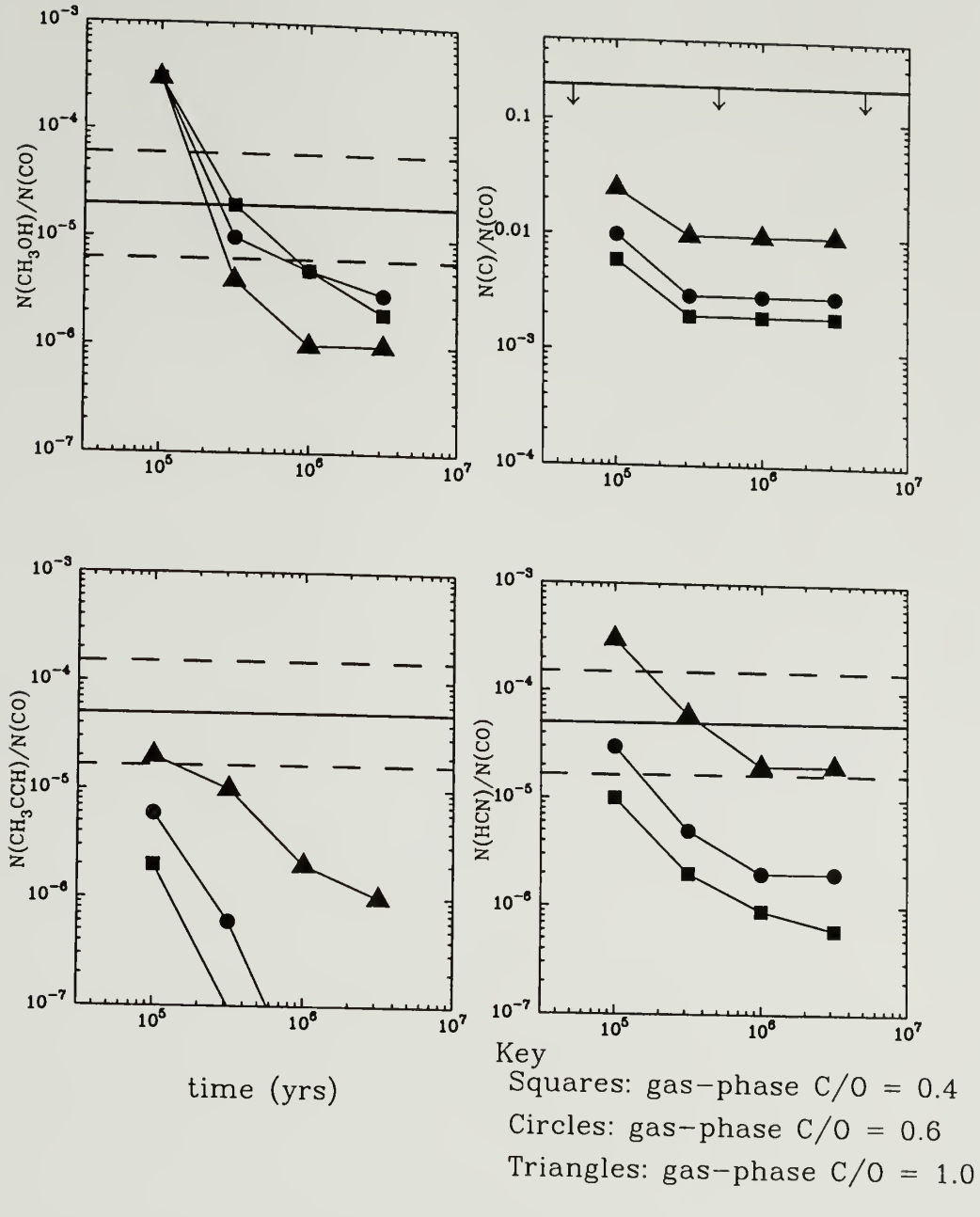

Figure 7.4. Panels showing the relative abundances of CH_3OH, C, CH_3C_2H, and HCN as a function of time and initial C/O ratio. The solid line denotes the observed value at the M 17 NC position, while the dashed lines are a factor of three above and below the observations denoting a reasonable estimate of the error. The arrows below the solid line in the neutral carbon panel suggest that the observed value is an upper limit.

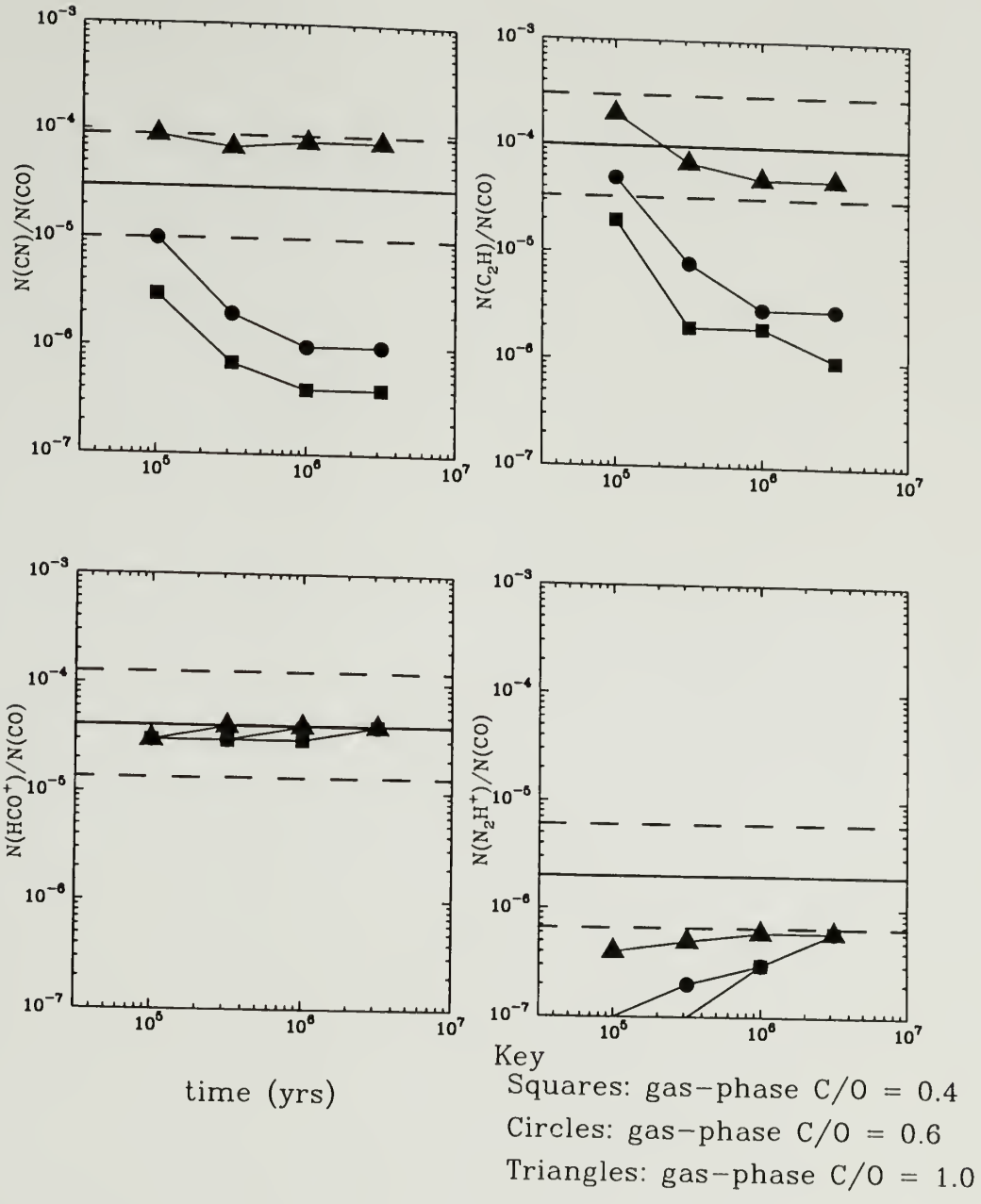

Figure 7.5. Panels showing the relative abundances of the radicals and ions, CN, C_2H, HCO^+, and N_2H^+ as a function of time and initial C/O ratio. The solid line denotes the observed value at the M 17 NC position, while the dashed lines are a factor of three above and below the observations denoting a reasonable estimate of the error.

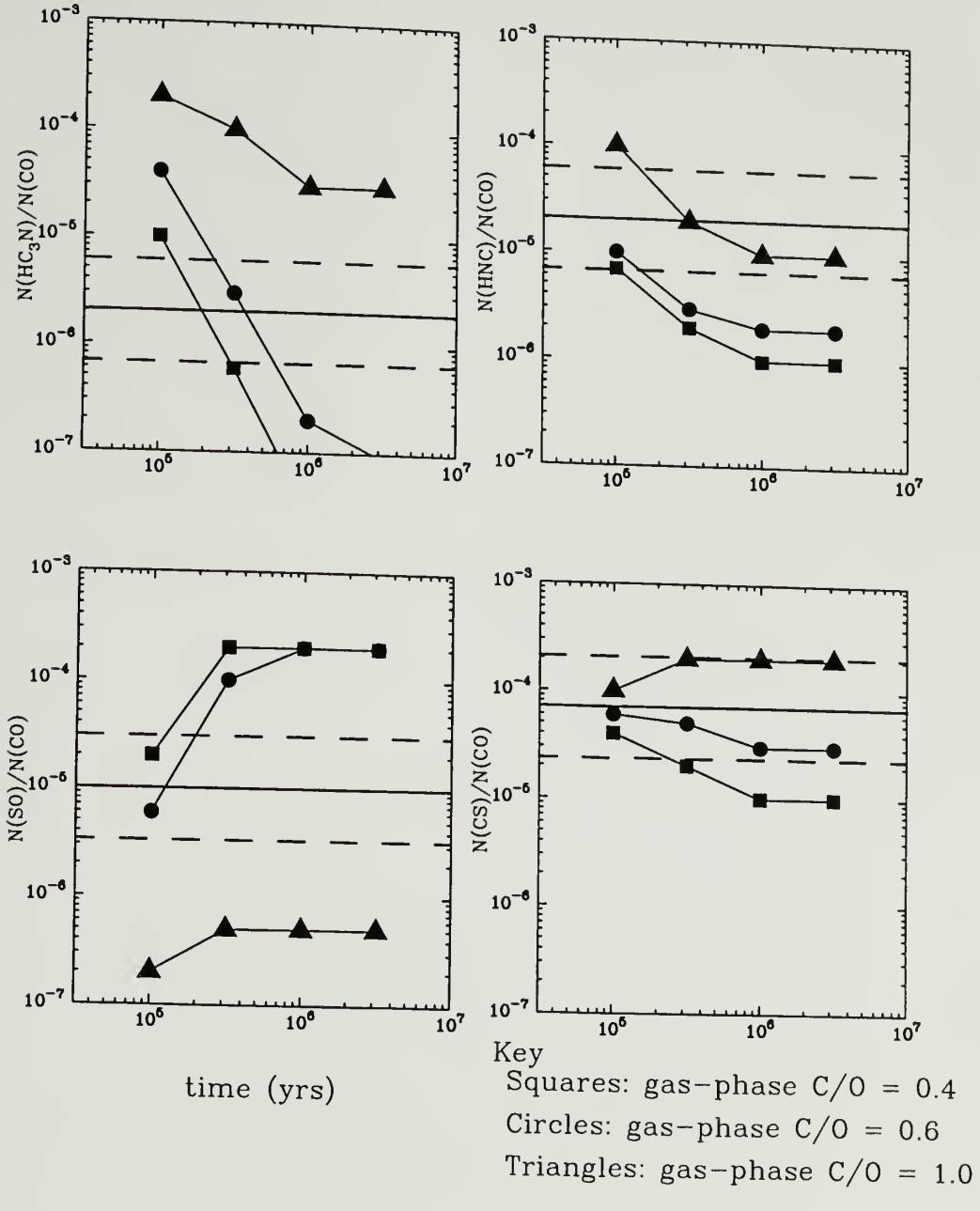

Figure 7.6. Panels showing the relative abundances of HC_3N, HNC, SO, and CS as a function of time and initial C/O ratio. The solid line denotes the observed value at the M 17 NC position, while the dashed lines are a factor of three above and below the observations denoting a reasonable estimate of the error.

observed for Ceph-A S ($T_k \sim 20$ K). We have chosen to model the Ceph-A S position using the model introduced for the RIP in Chapter 6, because this position (Ceph-A S) has a similar temperature and CO column density as the RIP. Figures 7.7 - 7.9 presents the 1-D model compared to the Cepheus A observations at the Ceph-A S position. There are no published measurements of the C/CO ratio in Cepheus A, so we are therefore unable to present a comparison for this key ratio and the theory. Since the relative abundances and physical conditions for Ceph-A S and Ceph-A N are similar to within a factor of two, the comparison between theoretical abundances and observed abundances for Ceph-A S is applicable to the Ceph-A N position as well.

In general, the relative abundances of species observed towards Ceph-A S are lower than observed towards the Orion RIP. Thus better agreement is found with theory, since in general, the model was under-producing most carbon-bearing molecules. Despite the improved agreement with theory the abundances of HCN, CN, HNC, and CH_3C_2H are still inadequate for a C/O ratio of 0.4. For these species, a C/O ratio between 0.5 and 0.6 provides the best agreement, although for CH_3OH and HC_3N agreement is best for the normal C/O ratio. The CS/SO ratio in Cepheus A is much smaller than Orion, varying from $1 - 3$ between the two positions (Table 5.9) predicting a lower C/O ratio of ~ 0.6. This is consistent with the earlier statement for HCN, CN, HNC, and CH_3C_2H and provides additional evidence that the CS/SO ratio may a useful tracer of the carbon and oxygen content of clouds. The abundances in Cepheus A also appear to be in agreement for times between 3×10^5 and 10^6 yrs, which is in agreement with the Orion and M 17 results.

In spite of the differences between Cepheus A, Orion, and M 17 one general conclusion can be drawn. *The best agreement between theory and observations is for $t \sim 10^6$ yr (for $n(H_2) = 10^5$ cm^{-3}) and C/O > 0.4. We have used a density of*

$n(H_2) = 10^5$ cm^{-3} for the chemical models, this value is an order of magnitude below the densities measured in these cores of $n(H_2) \sim 10^6$ cm^{-3}. In Chapter 6 we found that at higher densities, $n(H_2) = 10^6$ cm^{-3}, chemical timescales are shorter and therefore the implied chemical ages are $\sim 10^5$ yr. Thus the chemistry of GMC cores appears to the fairly consistent, with the common feature for all cores being the under-abundance of neutral carbon, and carbon bearing species, for models using the cosmic carbon to oxygen ratio.

7.4 Grain Chemistry and Other Possibilities

7.4.1 Grain Chemistry

For the RIP model and for the models presented in previous sections grain depletion was invoked a a possible mechanism to lower the initial oxygen relative to the carbon in the gas phase. The depletion mechanism may only be active during the collapse of the diffuse cloud to a denser state. This mechanism is supported by the observations of two grain mantle components, provided the components are the result of the temporal evolution of the grain mantle, with the polar mantle accreting earlier and the non-polar mantle, possibly dominated by CO, accreting at a later time. Therefore during the early stages of core evolution the C/O ratio will be altered by the formation of H_2O in the polar mantle. However, the presence of another major reservoir of carbon existing on grain mantles, such as CO_2, cannot be ruled out at present and confirmation awaits observations by the Infrared Space Observatory.

To examine the influence of grains on the chemistry we have modeled gas-phase chemical evolution including the effects of grain depletion and desorption in regions exposed to enhanced UV flux (Bergin, Langer, & Goldsmith 1995). This work, treated in Appendix B, used a restricted network which enables an examination of the general principles but does not allow for a direct comparison with these observations. As shown in the appendix depletion is highly sensitive to

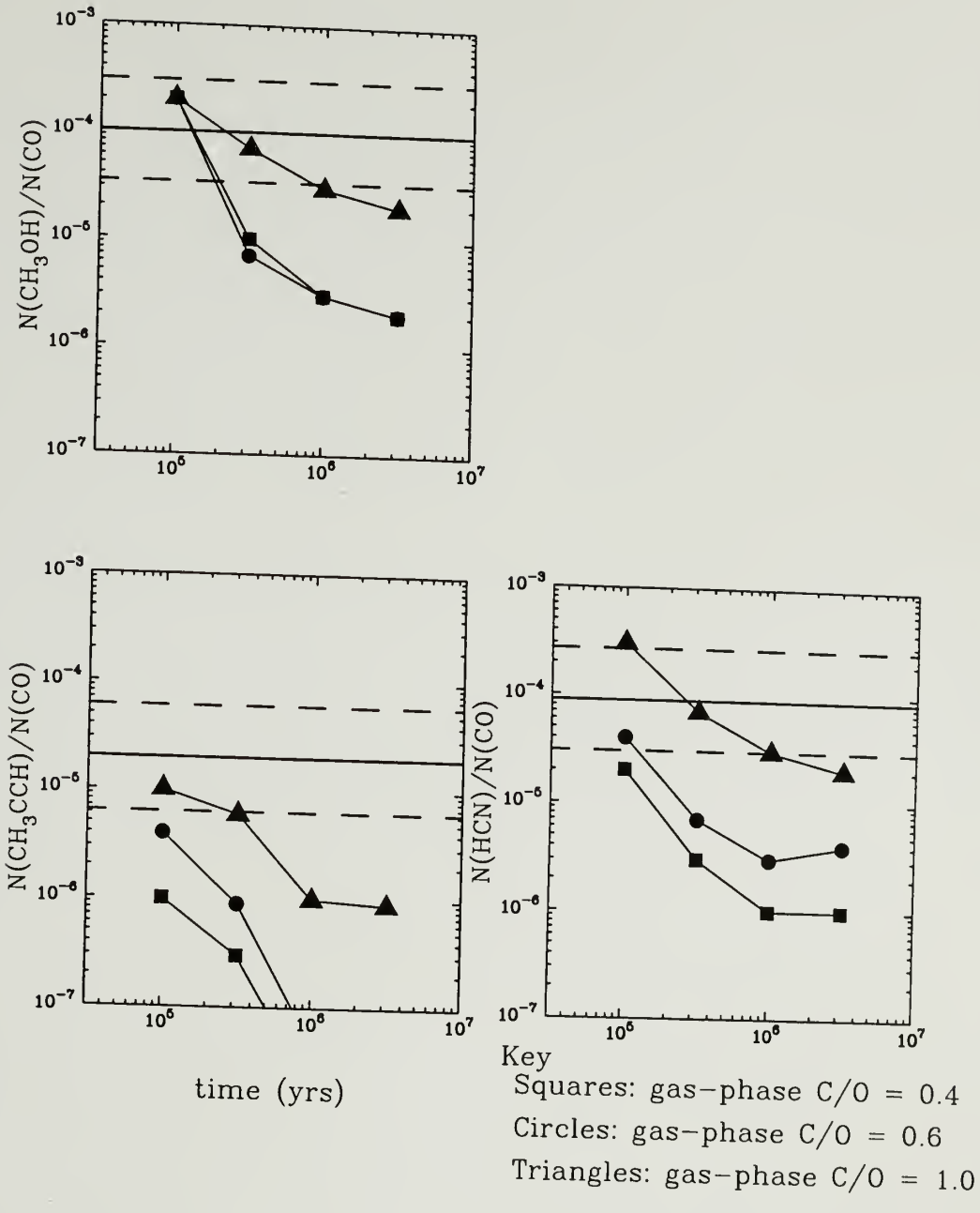

Figure 7.7. Panels showing the relative abundances of CH_3OH, C, CH_3C_2H, and HCN as a function of time and initial C/O ratio. The solid line denotes the observed value at the Cepheus A S position, while the dashed lines are a factor of three above and below the observations denoting a reasonable estimate of the error.

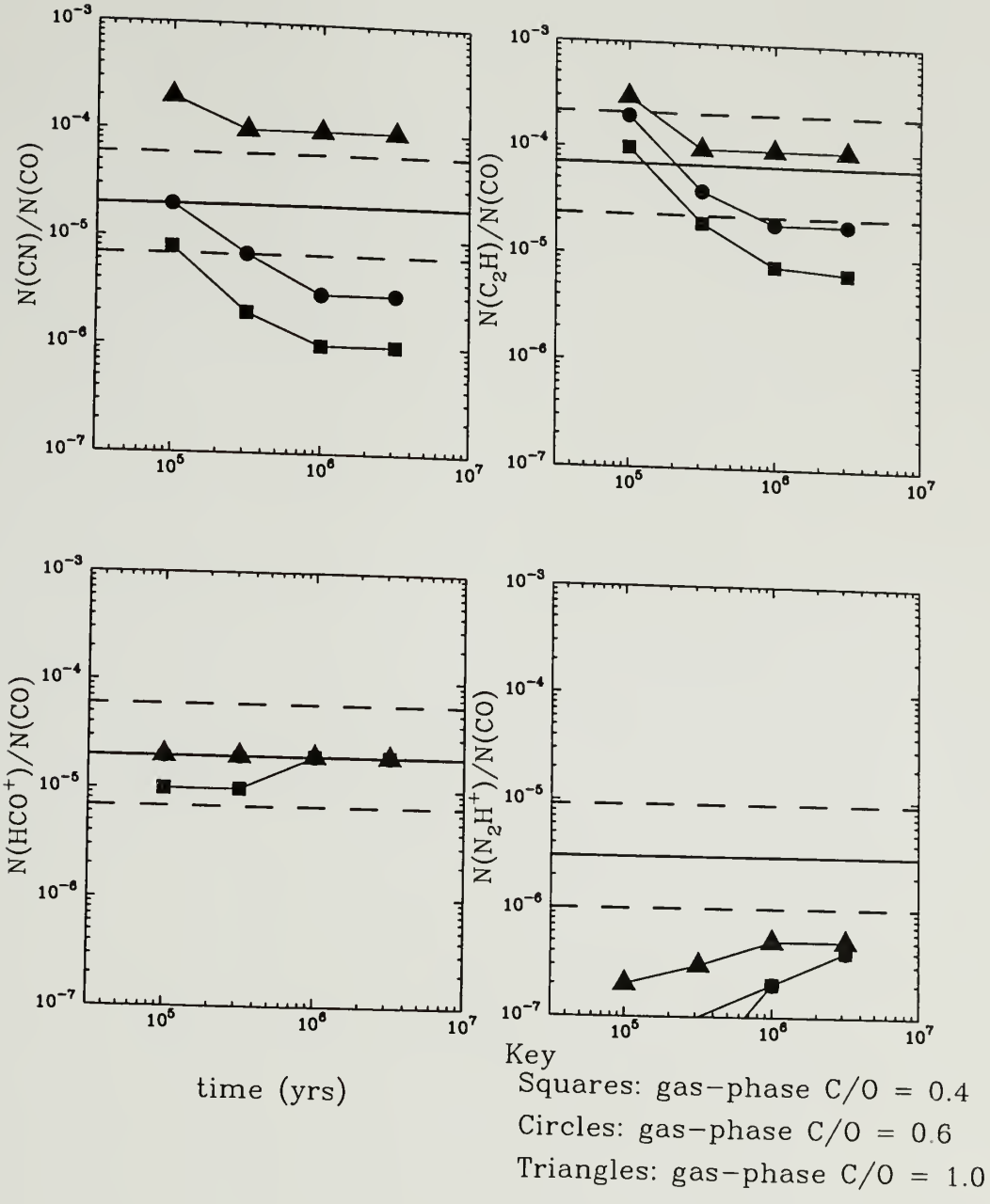

Figure 7.8. Panels showing the relative abundances of the radicals and ions, CN, C_2H, HCO^+, and N_2H^+ as a function of time and initial C/O ratio. The solid line denotes the observed value at Cepheus A S position, while the dashed lines are a factor of three above and below the observations denoting a reasonable estimate of the error.

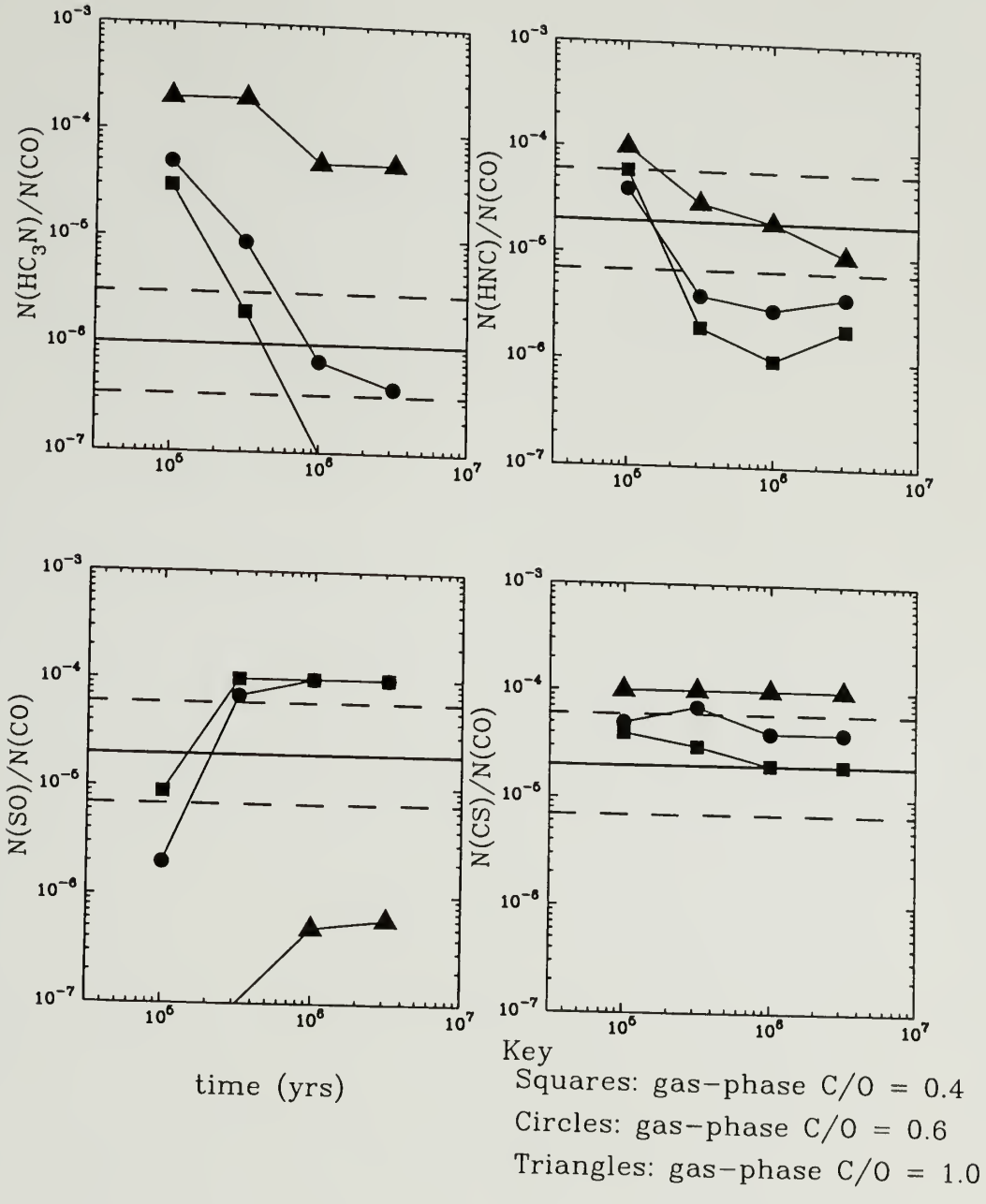

Figure 7.9. Panels showing the relative abundances of HC_3N, HNC, SO, and CS as a function of time and initial C/O ratio. The solid line denotes the observed value at the Cepheus A S position, while the dashed lines are a factor of three above and below the observations denoting a reasonable estimate of the error.

numerous factors including the density, temperature, and the evolutionary state. This study found that for $n(H_2) = 10^4$ cm^{-3} significant amounts of simple species, such as CO, CN, HCN, can be maintained in the gas phase, even at times much greater than the depletion timescale ($\tau_{dep} \sim 10^6$ yrs). However, at the densities typical of GMC cores, $n(H_2) \sim 10^6$ cm^{-3}, the depletion timescale is shorter, $\tau_{dep} \sim 10^3$ yrs, and most molecules observed in this study (eg. HCN, CN, CO) are predicted to reside on grain surfaces and should not be present at all in the gas phase. For example in Figure B.3 we have presented depletion as a function of density and found that at $n(H_2) = 10^5$ cm^{-3} the abundances of CO, CN, and HCN in the gas phase would be significantly reduced.

The mechanisms to remove species from grain surfaces are a matter of debate (Williams 1993), in our work we suggest two possible solutions to remove species from the mantles and allow for an active gas phase chemistry. First, depletion is highly sensitive to the dust temperature, if dust temperatures in GMC cores are > 30 K thermal evaporation could be sufficient to remove all molecules except for the most tightly bound (eg. H_2O). Another important possibility, given the evidence for CO ice (Whittet 1993), is that if interstellar grains consisted of an outer layer of CO ice, then the binding energies for many species to the grain mantles would be reduced, and a significant portion of material may be maintained in the gas phase, possibly through cosmic ray desorption. This mechanism could be very efficient, even at high densities, because the timescale for CO to deplete on a grain mantle is small, and therefore the grains could be coated with a layer of CO ice within a short amount of time.

Another possibility that should be considered is that molecules in the grain mantle are being processed into more complex species through reactions on the grain surfaces. In our examination of gas-phase chemistry including grain surface molecular depletion and desorption we found that gas-phase chemistry could not

account for the observed amount of water ice on grain surfaces along lines of sight to field stars in Taurus. This result is in agreement with the assertions of Jones & Williams (1984) who argue that the water ice observed in Taurus is the result of *H_2O formation on grain surfaces.* Therefore grain surface reactions are forming at least two (H_2O and H_2) species on grain surfaces (Hollenbach & Salpeter 1970; Jones & Williams 1984). Grain surface reactions also appear to play a role in Orion, where the large abundances of methanol and other more complex molecules in the hot core are believed to be the result of relatively recent evaporation of these species which were formed on grain surfaces (BSGP; Brown, Charnley, & Millar 1988; Millar, Herbst, & Charnley 1991).

There is some evidence that in quiescent regions grains surface reactions are not playing a dominant role in the formation of some species. Recent observations, using proto-stars to provide background continuum (Grim et al 1991; Allamandola et al 1992), have confirmed the existence of solid methanol on grain surfaces. Searches for CH_3OH ice along lines of sight towards background sources in Taurus have found no evidence for methanol ice features (Smith, Sellgren, & Brooke 1994; Chiar et al 1994). These results suggest that the production of methanol may not occur at all times on grain surfaces. Instead, its production may occur only in conjunction with energetic events such as UV processing of water ice on grain mantles close to the protostars, or when methanol is released from heated water ice in a phase transition to a clathrate structure (Sandford & Allamandola 1993). Thus grains may not be as active in quiescent gas as has been previously thought (cf. Hasagawa, Herbst, & Leung 1991).

However, we cannot rule out grain surface reactions in the formation of most species. The mere observation of CO, H_2O, H_2CO, and CH_3OH ices demonstrates that the effects of grains on chemical evolution should not be ignored. But the mechanism that can consistently remove molecules from grain mantles, especially

in dense regions, as outlined earlier is still a matter of debate (Bergin, Langer, & Goldsmith 1995; Willacy & Williams 1994, Schutte & Greenberg 1991) and since the abundances in all three clouds can be reproduced via a pure gas-phase mechanism, albeit with a increased C/O ratio, these results suggest that the grain chemistry may not dominate the production of all species. For example it is thought that the CO molecule is not produced at all on grain surfaces and but rather is produced in the gas-phase and frosts onto the grain mantles (Whittet 1993).

7.4.2 Other Possibilities

A relatively recent development in astrochemistry is the demonstration that two steady state solutions, or bistability, can exist depending on the local cosmic ray rate, the density of molecular hydrogen, and the depletion of heavy elements (Le Bourlot et al 1993). These solutions are characterized by two separate degrees of ionization, with one solution, the high ionization phase (HIP) producing large amount of neutral carbon and carbon-bearing radicals, while the other solution, the low ionization phase (LIP) provides larger abundances of saturated molecules and molecular ions.

The large amounts of neutral carbon present in the HIP naturally provides an alternate solution for the large C/CO ratios measured in molecular clouds (Flower et al 1994). However, it is not clear whether a bistable steady state solution would apply to the chemistry observed in dense cores. For instance the characteristic chemical age implied by our observations is far from equilibrium, t $\sim 10^5$ years for $n(H_2) = 10^6$ cm^{-3}. In addition, these models have typically only been applied to dark clouds, since the bistable solutions, for typical cosmic ray rates and elemental depletions, occur near $n(H_2) \sim 10^4$ cm^{-3}, the density generally ascribed to dark cloud cores. Therefore it is difficult to apply these models to GMC cores where densities are $\gg 10^4$ cm^{-3} and it is unlikely that bistability applies to the density

regimes covered in our survey. Bistable solutions could be relevant to low density envelopes of clumps or in the interclump medium, hence bistability may provide an alternate solution to the extent of neutral carbon emission.

The chemical ages inferred for the high densities observed in this study (t $\sim 10^5$ yr for $n(H_2) = 10^6$ cm^{-3}; Chapter 6) strongly suggest that a dynamical solution may be required to provide an explanation for the neutral carbon problem in the dense interior of cloud cores. The solution proposed earlier, one of selective depletion onto grain surfaces, includes a dynamical link because it invokes the depletion of oxygen onto grain surfaces during the collapse of a diffuse component (when the abundance of atomic H is greater) to a denser state. This type of dynamical model, allowing the density and temperature to vary according to the equations of motion and energy balance has been examined by several authors, examples are Gerola and Glassgold (1978), Tarafdar et al (1985), and Chièze, Pineau des Forêts, & Herbst (1991). One key parameter in these approaches is the time necessary for the density to increase by a factor of 10. Prasad, Tarafdar, Villere, & Huntress (1987) addressed this question and found that the lifetime of the cores decreases as the core density is increased. For instance the time required to change the central density from $n(H_2) = 10^4$ to 10^6 cm^{-3} is $\sim 10^5$ yr (Prasad et al 1987). Thus clouds will spend most of their lifetime in a diffuse state and pass through the dense states in a short timescale. The timescale to increase the density from 10^4 to 10^6 cm^{-3} is somewhat similar to the timescale observed for the chemical interactions in Orion, M 17, and Cepheus A. At these times (t $\sim 10^5$ yr) a large amount of the atomic carbon co-exists with CO, and thus collapse models prove to be a rich source of complex species (Prasad et al 1987; Chièze et al 1991). Therefore the correspondence of timescales and the increased abundances of complex species may indicate that GMC cores are dynamically evolving objects. These results are certainly intriguing and may apply to processes ongoing in GMC

cores, however, given the complexity of the problem, these models should be taken as a guide to effects that may occur in the linking between dynamics and chemistry.

Another approach is to model the effects of turbulent diffusion on the chemistry (Xie, Allen, & Langer 1995). With the large line widths observed for these cores ($\Delta v \sim 3 - 5$ km s^{-1}) turbulent diffusion is significant and must influence chemical interactions at some level. The model of Xie et al (1995) is able to reproduce the observed amount of carbon and produces significant amounts of neutral carbon in the cloud interior, which may lead to the formation of complex species. One important question in addressing the relevance of this work to the chemical evolution of GMC cores is whether the dense clumps are turbulent. If clumps are structures with thermal linewidths moving around in a turbulent velocity field then turbulence will only effect the outer layers of the clumps that are interacting with the turbulent interclump medium and the dense interiors will remain unaffected. A direct comparison between the Xie et al (1995) model and our observations is impossible because the maximum density in their model is only $n(H_2) = 3 \times 10^4$ cm^{-3}. We will discuss below a method that may help in discriminating the effects of turbulent chemistry in dense clumps.

The final dynamical model that may be applicable to GMC cores is one in which the interclump gas periodically collapses to produce clumps. The clumps live for $\sim 10^5$ yr, after which they are destroyed by stellar winds, thereby preventing the chemistry from reaching steady state (Charnley et al 1988a,b). One interesting facet of these models is that a chemistry attains a limit after several clump/wind cycles. For these models to be applicable to dense GMC cores a significant fraction of the volume must be dominated by wind blown bubbles. Given the evidence for arc and shell structures in the large scale maps of Orion by Heyer et al (1992) and Gem OB1 (Carpenter et al 1995) some long term linking

between stellar winds and cloud material is not unreasonable. Indeed the chemical timescale of $\sim 10^5$ yr is quite close to the observed lifetimes of molecular outflows of 2×10^4 yr (Snell 1984), which could imply that many outflows are interacting with the cloud material and "re-starting" the chemical clock. While the application of these models to GMC cores cannot be ruled out, we note that the arc and ring structures observed by Carpenter et al (1995) in Gem OB1 are rather extended, with a diameter of ~ 9 pc, which is *at least* a factor of 10 larger than the size scales probed in this work.

The amount of carbon that is produced is not satisfactory to discriminate between these models, because each model produces C/CO ratios close to the observed values. Instead we may consider examining the abundances of oxygen-bearing molecules, such as H_2O, O_2, SO, and CH_3OH. When atomic carbon is cycled into the gas phase through any mechanism, the abundances of oxygen containing molecules are lowered, mainly by reactions of species such as OH, O_2, and SO with atomic carbon. The sharp drop in the abundance of SO when the C/O ratio is increased demonstrates how dramatic these effects can be (see Figure 6.11). Therefore a crucial test for these models is whether they can *both raise the amount of carbon to produce complex molecules and still provide enough oxygen-bearing molecules to match observations.* The species that will be particularly useful are SO, CH_3OH, as well as O_2 and H_2O which should be observed by SWAS. As an example of these effects, for the bistability models in the HIP, which has a large C/CO ratio, the abundance of SO is incredibly small. Xie, Allen, & Langer (1995) also predict that O_2 and H_2O will be anticorrelated with the strength of turbulence.

7.5 The Relation of Physical Conditions and Abundance Variations

One critical question is whether any of the abundance variations observed in Orion, M 17, or Cepheus A can be related to changes in physical variables, such as

density, temperature, or ultraviolet field intensity. The fact that within a single cloud (excluding KL/BN and the Bar in Orion) abundances are not changed by more than factors of a few suggests that variations in the physical properties in the quiescent gas in each cloud are not a dominant factor. However, there still may be some correlation between physical and chemical variations, for example the drop in temperature between the NC and the CC in M 17 may change the abundances of some species.

To examine these questions we have chosen to compare the relative abundance changes between the RIP and KL/BN in Orion, and the NC and CC in M 17. These positions were chosen because the RIP in Orion and the CC in M 17 are similar in that both positions are exposed to reduced UV fields and have colder temperatures ($T_k \sim 30$ K). In contrast KL/BN and the NC exemplify more active regions exposed to large UV fields with hotter temperatures ($T_k \sim 50$ K). Therefore this comparison between "active" (KL/BN, NC) and "inactive" regions (RIP, CC) is more likely to emphasize any abundance differences due to changing physical conditions. Table 7.1 presents the ratio of relative abundances for the KL/BN/RIP and NC/CC or active/inactive.

One trend is that the abundances of radicals in both Orion and M 17 are greater in inactive regions. The trend is also observed for molecular ions which are typically more abundant in inactive cores. A different gradient is observed for CH_3C_2H which tends to be more abundant in active regions. The strength of this analysis is that these trends are observed in *both* cores. This is important because as discussed in Chapter 4 an abundance change of a factor of two is only a marginal result. However, the abundance of C_2H and CN is found to decline in both Orion and M 17, with higher abundances in regions with colder temperatures and lower UV fields, argues that this trend is probably real.

To examine whether the chemical models with physical variations taken into account can reproduce these observations. we have divided the "active" 1-D model for KL/BN with the predicted relative abundances for the "inactive" model for the RIP. These ratios are presented in Table 7.1 for C/O $\sim$ 1.0. If we examine the trends which agree with the theory first, the decline of the radicals is reproduced for both CN and C_2H. This drop in abundance is not due to the radiation field, but rather to a decrease in temperature, since the neutral-neutral destruction reactions for these species are high at larger temperatures. For HNC and CH_3C_2H, the models also adequately reproduce the observed gradient, although the abundance gradient for CH_3C_2H in M 17 is greater than predicted.

However the theory predicts a gradient for HCO^+, and N_2H^+ that is in the opposite direction of the observations. The theory predicts a trend in which molecular ions are more abundant in "active" regions, which is primarily due to the inverse temperature dependence of recombination reactions. The UV field in the 1-D models does not have much of an effect because the shielded regions give the largest contribution to the computed column densities. The only way the 1-D model can produce an abundance gradient in the same direction as the observations is to have very small clumps, such that the radiation field creates electrons where there are more UV photons (eg. KL/BN, NC), and these electrons then destroy the ions. However, as demonstrated in Chapter 6, smaller clumps will have a detrimental effect on the abundances of neutral molecules. Obviously the situation is very complex and the solution to these puzzling trends probably lies in some dynamical or turbulent linking between the physical structure and the chemical evolution that has not been included in these relatively simple models.

7.6 Summary

In this chapter we have examined the chemical evolution of GMC cores by comparing theoretical chemical models with relative abundances measured in

Table 7.1. Relationship between Physical Conditions and Abundance Variations

	Active/Inactive[a]	Orion	M17
Species	C/O = 1.0 (Theory)	KL/RIP	NC/CC
Observations that Agree with Theory			
CN	0.7	0.6	0.4
C_2H	0.7	0.6	0.6
HNC	0.7	0.4	0.9
HC_3N	0.5	0.9	0.7
CH_3C_2H	1.7	1.5	2.3
SO	0.8	>7.7	0.8
Observations that Disagree with Theory			
HCO^+	2.0	0.7	1.0
N_2H^+	2.0	0.1	0.6
CS	2.0	1.4	0.8
CH_3OH	2.0	>3.9	0.4
HCN	0.9	>2.4	0.4

[a]Active: $n(H_2) = 10^5$ cm^{-3}; $\chi = 10^5$; $T_k = 50$ K

[a]Inactive: $n(H_2) = 10^5$ cm^{-3}; $\chi = 10^3$; $T_k = 25$ K

Orion, M 17, and Cepheus A. We have found that the chemistry in GMC cores is similar; with the greatest agreement for all clouds requiring a combination of early times and C/O > 0.4. In this chapter we have used a density of $n(H_2) = 10^5$ cm^{-3} for the theoretical chemical models. However the measured densities in these cores is typically an order of magnitude greater or $n(H_2) = 10^6$ cm^{-3}. In Chapter 6 we demonstrated that chemical timescales are dependent on the density therefore for the derived density of $n(H_2) \sim 10^6$ cm^{-3}, the chemical age that is inferred for GMC cores is $t \sim 10^5$ yrs.

To raise the C/O ratio we have invoked selective depletion of oxygen relative to carbon on grains surfaces. This mechanism is consistent with current observations of water ice features and with chemical theory. To examine the possible influence of grains on the chemistry in these dense cores we utilized a model of gas phase chemistry including grain surface depletion and desorption. This model showed that the inclusion of grains into the chemistry typically lowers molecular abundances and therefore an efficient desorption mechanism is required.

To remove species from the mantle and allow for an active gas-phase we suggests two possible solutions: simple thermal evaporation and lower binding energies to a CO ice dominated mantle. We have also examined the utility of other chemical models, including processes such as turbulence or dynamics, to these observations. We find that some of these models (turbulence, incorporating dynamical evolution) models could apply to the chemistry of GMC cores and suggest a possible method to discriminate between the different models.

Chapter 8

Conclusions

This thesis has presented a detailed examination of the physical and chemical structure of three giant molecular cloud cores. In this section we will summarize the results and examine the implications of this work on the chemical and physical evolution of molecular cloud cores.

8.1 Summary

8.1.1 Temperature Structure

To determine the temperature of the cloud cores we have observed the J = $6_K \rightarrow 5_K$ (K = 0,1,2) transitions of the symmetric top molecule CH_3C_2H in Orion A, M 17, and Cepheus A. To investigate the use of CH_3C_2H as a temperature probe we have first examined the excitation of methyl acetylene through statistical equilibrium calculations. The excitation models have shown that CH_3C_2H is an excellent tracer of the temperature of the *dense* gas in molecular clouds. We have utilized the theoretical analysis and the observations to derive kinetic temperature for numerous positions in each core. The temperature structure is similar in all three cores with higher temperatures found closest to the luminous young stars and with a smooth temperature decrease away from these sources.

We have also compared the temperatures derived from two different thermometers: CH_3C_2H and ^{12}CO. In two clouds, Orion A and M 17, the comparison between the two thermometers shows significant differences, with the CO excitation temperatures much larger than those inferred from methyl acetylene. This temperature difference between CO and CH_3C_2H is suggested to be the result of a line of sight temperature gradient and therefore reflects differences

in the emission regions along the line of sight. The CO emission probably arises from gas near the front surface of the clouds, heated by the luminous external heating sources, while the methyl acetylene emission arises from cooler gas deeper within the clouds cores. In Cepheus A the results are more ambiguous because of the presence of self absorption features seen in the CO spectra.

8.1.2 Density Structure

We have observed the J = 4 → 3, J = 10 → 9, J = 12 → 11, and J = 16 → 15 transitions of HC_3N in the Orion A, M 17, and Cepheus A cloud cores. We have used these data with temperatures derived from CH_3C_2H and a non-LTE model for the excitation of HC_3N to obtain measurements of the density of molecular hydrogen in GMC cores. Densities were determined for 133 positions over a $4' \times 12'$ region in Orion, 55 positions over a $4' \times 5'$ area in M 17, and 14 positions within a $4' \times 5'$ region in Cepheus A. The density found for each core is very similar; within the errors the densities in each core are consistent with a constant value of $n_{H_2} \sim 10^6$ cm^{-3}.

Despite of the use of an optically thin tracer and the inclusion of an improved source temperature model, the density within each cloud core shows no evidence of large scale variations. These observations are consistent with the results of previous efforts which utilized other tracers of the dense gas and assumed a constant temperature for the cloud. The lack of density variations provides one piece of evidence that molecular clouds have a clumped structure, such that each antenna beam encompasses numerous dense clumps. The clumps fill only a small percentage of the total volume of the cloud, with the volume filling factor decreasing from the center of the cloud to the edge producing the observed variation in column density. Further evidence that clouds are clumpy comes from an examination of the size scale of the cores implied by the inferred density and the $C^{18}O$ column density. This analysis demonstrates that unless these cores have

a strikingly (>10:1) flattened geometry, each with the short axis along the line of sight, then the dense gas must be clumped and is filling only a small fraction of the volume ($\lesssim$5%).

8.1.3 Chemical Structure

The temperatures and densities determined directly from the CH_3C_2H and HC_3N observations were used to derive accurate relative abundances for 12 species for two positions in M 17 and Cepheus A, and for six positions in Orion A. Although abundance differences exist, in general, chemical abundances are found to be fairly similar both within and among GMC cores. There are some exceptions to the general agreement. The most significant trend in abundances within a single cloud is observed in Orion between the RIP and both 4′S and the Bar. In 4′S and the Bar the abundances of ions are decreased by factors of 3 to 10 from the relative abundances observed in the RIP, while some species (CH_3C_2H, HC_3N, CH_3OH, and HNC) are not observed at all in the Bar.

Some subtle abundance variations were also observed, in M 17 and Cepheus A relative abundance gradients are observed that could be related to physical features (e.g. UV field in M 17; outflows in Cepheus A). However these variations are not large and are within the estimated error ~50%. In addition, the relative abundances HCO^+, CH_3C_2H, and HNC are the same, to within a factor of four, for any position in Orion, M 17, or Cepheus A. Therefore these species appear to be least affected by the varying physical properties of these GMC cores.

8.1.4 Comparisons with Chemical Theory

We have developed two different chemical models to compare with the observations. These models were compared to the relative abundances measured at the radical-ion peak in Orion and then applied to other positions in Orion, M 17, and Cepheus A. The first chemical model computed abundances only in the dense

well shielded interiors of the cloud cores. The second more complicated model integrated abundances of the different species as a function of depth in the presence of an enhanced radiation field, thereby incorporating line of sight effects on the chemistry. The model also attempted to mirror real clouds by enhancing the radiation field only on one side of the cloud. The other side of the cloud, facing away from the newly formed stars, is impinged by the normal ISRF.

Neither model was able to reproduce the observed abundances of molecular species at any time. While agreement can be found for single species at a particular time, no single time gives a good fit to the data. In order to obtain a better match between theory and observations the model abundances must be increased. One method to increase abundances is to provide a greater amount of free neutral carbon, which is the building block for most simple and complex carbon-bearing species, in the gas-phase. Two possible solutions were examined: 1) clumps and 2) raising the initial gas-phase C/O ratio above the value measured towards diffuse clouds of C/O $\sim$0.4.

A number of arguments have been presented that imply that these cloud cores have a clumpy structure. This study found that the inclusion of clumps into the chemical model can reproduce the observed abundances of C^+ and C. However this model has a detrimental effect on the abundances of most other species. Because the enhanced photodestruction rates destroy molecules present in small clumps, a clumpy model presents a poorer match to the observations than a non-clumpy model.

Theoretical 1-D models with a range of C/O ratios were compared to the relative abundances measured towards the RIP and KL/BN in Orion, as well as the northern condensation in M 17 and 1.5′S in Cepheus A. Good agreement between model and observations was found for early times and C/O $\sim$ 0.8. Using the measured density of $n(H_2) = 10^6$ cm^{-3} the chemical age inferred for the three

GMC cores is t $\sim 10^5$ years. The CS/SO ratio is also suggested to be a useful probe of the amount of carbon to oxygen available in the gas-phase and this ratio produces similar results to that inferred from the match between the theory and observations with other species (eg. HCN, HNC, CN).

8.2 Implications

The primary goal of this thesis is to characterize the physical and chemical state of giant molecular cloud cores. In the process we paint a very complex picture of the physical and chemical structure of molecular clouds. Many of the results of this work have built upon and extended the work of others. For instance the "neutral carbon problem" is a well documented observational result and has been a problem plaguing astrochemistry for several years. But this study observed numerous species, placing greater constraints on chemical models, and found that similar problems exist for the abundances of the observed molecules. This problem can be alleviated by a combination of early time chemistry and a C/O ratio greater than 0.4. To raise the gas-phase C/O ratio we invoked selective depletion of oxygen relative to carbon from the gas-phase due to the formation of H_2O on grain surfaces, effectively raising the initial gas-phase C/O ratio. Since a large abundance of atomic hydrogen is required to react efficiently on grain surfaces with oxygen and produce water ice, this mechanism will produce the H_2O ice in the early stages of the cores evolution prior to the conversion of all the atomic hydrogen to molecular form (Tielens et al 1991). Thus chemistry on grain surfaces may play an important role in the chemical evolution of GMC cores.

One unique contribution of this work to our fundamental understanding of the physics and chemistry of GMC cores is the systematic incorporation of the analysis of the physical structure into the examination of the chemical evolution. For instance, none of the previous efforts in modeling the chemistry of the quiescent ridge in Orion have used a density as high as $n(H_2) = 10^6$ cm^{-3}. Knowledge of the

density is particularly important in studies of the chemical evolution of molecular clouds because the density sets the timescales for chemical interactions and therefore plays a crucial role in the chemical history of material in GMC cores. The observed densities of $n(H_2) \sim 10^6$ cm^{-3} were found to imply that the dense gas in the cores is in a chemically young state, with a characteristic age of $t \sim 10^5$ yr. One problem inherent in time dependent chemical studies is in ascribing this "age" to the core, because in terms of the chemistry the $t = 0$ state is set by some event which occurred beforehand. Thus it is uncertain whether chemical timescales are reflective of the age of the core itself, or possibly the chemical age is amount of time that has elapsed since some dynamical event, such as an outflow, has reset the chemical clock. Another possibility that must be considered is inaccuracies in some key reactions in the theoretical models.

As we argued in Chapter 6, although certain parts of chemical reaction networks may be incomplete or inaccurate, it is unlikely that one aspect of the models will change; that certain stable species act as "endpoints" in the chemical evolution. For the gas-phase these are CO (carbon and oxygen), O_2 (oxygen), N and N_2 (nitrogen). The fact that CO is observed to be widely abundant, in diffuse and dense clouds, suggests that CO is indeed a chemically stable molecule. Therefore to provide enough carbon in the gas-phase either CO must be destroyed or early timescales prior to the formation of stable species must be invoked.

This suggests two possible scenarios for the chemical and physical evolution of GMC cores. In the former scenario the cores could have ages greater than inferred from the chemistry because some process, such as shocks, would destroy the CO in the dense gas and recycle the carbon. Thus the short characteristic age implies that a fundamental part of the chemistry, such as grain chemistry, turbulence, or dynamical cycling of material due to outflows (Norman and Silk 1980) is not included in our model. In the second scenario the young chemical age could imply

something fundamental about the structure and/or chemistry of molecular clouds, such as GMC cores being intrinsically young objects.

It is certainly possible that the age of the dense cores is indeed 10^5 yr. Dense cores are believed to form by compression of expanding H II regions and, since the formation process itself could trigger more massive star formation, which would quickly disperse the dense cores, cloud cores could be short lived objects (Carpenter et al 1995). However the chemical age inferred for the cores is rather short, and the timescale will only get smaller, and more unphysical ($\ll 10^5$ yr), if densities are slightly greater.

If the cores themselves are not short lived then another possibility is that the cores, which are composed of both low density and and high density gas, are older than the chemical interactions of the gas composing the core. The observations in Chapter 3 suggest that the dense gas is segregated into small clumps. Since the emission from all of the molecules observed in this study is believed to come from the clumps then this would imply that the clumps are intrinsically young objects with ages $< 10^5$ yrs. This structure, with an older core composed of short lived clumps, is possible if there is a continuous interchange between the interclump medium, which is dominated by UV photons and therefore is a rich source of C^+ and C, and the clumps. New clumps will therefore be created and destroyed in a short timescale of $\sim 10^5$ yrs, and the age of the entire core could be much older than the clumps themselves. We note that in the dynamical models of Tarafdar et al (1985) and Chièze, Pineau des Forêts, & Herbst (1991) the compression of low density material to a higher density is in itself a rich source of complex species (see Chapter 7).

The destruction processes to return clump material to the interclump medium could simply be the formation of star. Another possible destruction mechanism is that some clumps are transient features and dissipate prior to the formation of a

star. When the clumps form some may not be gravitationally stable and instead will break up prior to the formation of a star. Some evidence of unbound dense clumps is found in the high resolution study of TMC1 by Langer et al (1995), whether such features exist in GMC cores is an open question and one worthy of further investigation.

While the destruction processes are easier to determine a continuous formation process for clumps from compression of the interclump medium is more speculative. A recent study of sequential star formation in a turbulent medium by Elmegreen, Kimura, and Tosa (1995) found that massive cores can form behind a shock front induced by an expanding H II region. While this model is complex and relies on star formation in a pre-existing turbulent medium it does suggest that dense cores are continuously growing by addition of new clumps. The new clumps form from low density turbulent material behind the shock. The growth of the core is then halted by the formation of an embedded cluster. This scenario is highly speculative but, given the constraints placed on chemical interactions by the formation of stable molecules, one possible solution that must be considered is that the clumps are themselves young features.

8.2.1 Future Work

This work has pointed out several avenues that warrant further investigation. One question is whether other observations will support the conclusion of high C/O ratios in GMC cores. This ratio has been shown to have a significant impact on the abundances of simple oxygen molecules (eg. SO). However the simple oxygen bearing species that this ratio will have the greatest effect on are O_2 and H_2O, because these species are possibly the dominant reservoir of atomic oxygen. In particular current chemical theory predicts that the O_2 will be the dominant reservoir of oxygen. The dependence of the O_2 abundance on the C/O ratio is quite dramatic, for C/O = 0.4, the abundance of O_2 in equilibrium is $X(O_2) = 9$

$\times 10^{-5}$, while for C/O = 1.0 the abundance is only $X(O_2) = 1 \times 10^{-7}$. Therefore O_2 (and H_2O) is a potentially important probe of the amount of oxygen in interstellar clouds. Both H_2O and O_2 are not currently observable from the ground. However, through the observations of O_2, H_2O, and atomic carbon in Orion, M 17, and Cepheus A by the Submillimeter Wave Astronomy Satellite (SWAS) we will be able to investigate this question in detail. Another method of investigation of the C/O ratio in molecular cores is to use the CS/SO ratio to determine the C/O ratio in molecular clouds. This project would examine the uses of the C/O ratio by observing CS and SO in many clouds, sampling a range of conditions. These observations can be combined with the observations of key oxygen and carbon species by SWAS. For instance a plot of CS/SO against O_2/CO, two ratios that are highly dependent on the amount of gas-phase carbon and oxygen, would be a potentially powerful method to investigate the carbon and oxygen content of GMC cores.

Other interesting efforts should be directed to extending these observations to the highest resolution possible. For instance near the H II region/molecular cloud interface in M 17 our observations imply that there are small scale abundance variations. High resolution observations of several molecules at the interface will enable an examination of possible effects on the chemistry induced by the changing UV field. The inclusion of molecules, such as CN and C_2H which appear to tracers of the UV field, would be also be useful in examining the effects of radiation on the chemistry. In addition, as more information of molecules frozen on grain surfaces become available, through high resolution ground based or space based observations (ISO), a careful accounting of the molecular abundances in the gas-phase and solid state should be undertaken. In this regard we will propose to observed several molecules along lines of sight where molecular depletions have

been measured. The aim of this study will be to characterize the extent of the link between chemistry occurring on grain surfaces and on the surfaces of grains.

Appendix A

CS/SO Ratio as a Tracer of the C/O Ratio

Figure 6.11 shows that the predicted CS/SO ratio has a strong dependence on the initial amount of carbon and oxygen allowed in the gas-phase. This figure demonstrates that the CS/SO ratio is greater at early times and for a larger C/O ratio. In this appendix we will outline the principal mechanisms for this dependence. Since the abundance of CS exhibits no significant change with either time or with C/O ratio (see Figure 6.9) the principle culprit is the abundance of SO which is lower both at early times and for high C/O ratios.

SO is produced via neutral neutral reactions of sulfur with simple oxygen bearing molecules,

$$S + OH \rightarrow SO + H, \tag{A.1}$$

$$S + O_2 \rightarrow SO + O, \tag{A.2}$$

although a third path contributes at early times,

$$HS + O \rightarrow SO + H. \tag{A.3}$$

Of these paths, reaction A.1 dominates the early time formation, while the reaction with O_2 will dominate at late times. These formation reactions give an important clue to why the abundance of SO peaks at later times. Recent chemical networks predict that O_2 will be the primary reservoir for neutral oxygen, in fact, the O_2 abundance at equilibrium in these models is close to the abundance of CO,

$X(O_2) \sim 9 \times 10^{-5}$. Therefore, the abundance of SO will closely follow the time dependence of the O_2 molecule, which shows a steady rise with time.

The final link in this network is principal destruction path for SO at early times, which is a reaction with neutral carbon to produce CS. A destruction path linked to C will preferentially destroy SO at the early times leading to greater amounts of CS at these times (see Figure 6.9). This path rapidly becomes insignificant when the abundance of neutral carbon drops shortly after 10^5 yr creating the two separate solutions between 10^5 yr and 3×10^5 yr observed in Figure 6.11.

This discussion illustrates why the CS/SO ratio is high at early times but, it does not explain the dependence on the C/O ratio. The dependence is a result of a drop in the abundance of O_2 and OH for greater C/O ratios. For example the abundance of O_2 at equilibrium for C/O = 1.0 is $X(O_2) = 1 \times 10^{-7}$, which is significantly lower than the abundance for C/O = 0.4 listed earlier. Therefore, the higher CS/SO ratios for a larger C/O ratio is due to a drop in the formation of SO because the excess carbon is rapidly destroying the simple oxygen molecules at early times to produce mostly CO.

Appendix B

Gas-Phase Chemistry in Dense Interstellar Clouds including Grain Surface Molecular Depletion and Desorption

B.1 Introduction

In this appendix we present a brief discussion of gas phase chemistry including the effects of grain depletion and desorption in regions exposed to enhanced ultraviolet (UV) flux. This work has been presented in Bergin, Langer, & Goldsmith (1995; hereafter BLG) and used a smaller chemical network which enables an examination of the general effects of including gas-grain interactions on the chemical evolution but does not allow for a direct comparison to be made. For a more detailed discussion of the gas-grain model see BLG.

Many of the current theoretical efforts incorporating grains into chemical models, including the work by Hasegawa & Herbst (1993) and Hasesgawa, Herbst, & Leung (1992), have concentrated on studying effects of grain surface chemistry on the chemical evolution of molecular clouds in dense well shielded regions. In this appendix we extend the theoretical models to the exterior regions of molecular clouds in addition to the dense well shielded interior. We model how molecular grain mantles evolve as a result of the competition between the processes of depletion and desorption, in order to examine the time history of molecular abundances on the mantle as a function of cloud depth (visual extinction).

In our models we have initially taken the somewhat restrictive view of not allowing reactions on the grain mantle, since the addition of surface reactions adds additional complexity and uncertainty. The exclusion of surface reactions is certainly an approximation, since reactions on the surfaces of grains are thought to

form molecular hydrogen (Hollenbach & Salpeter 1970). However, the observations of solid CO embedded in a nonpolar matrix provides some evidence of molecules that were directly deposited on the grains from the gas phase and not created by surface processes (Tielens et al 1991; Whittet 1993).

B.2 Chemical Model

B.2.1 Gas Phase Chemistry

As mentioned earlier the chemical reaction network is smaller than the network presented in Chapter 6. In particular the reaction network for gas phase reactions consists of the major formation and destruction pathways for carbon-, oxygen-, and nitrogen-bearing species. The reaction set links 82 species through a network of 1072 reactions first compiled by Viala (1986) and later updated by Benayoun, Nercessian, & Viala (1991). Since we are modeling both the edges of clouds and interior regions the chemical reaction scheme includes the photodissociation and photoionization of molecules. The transition from atomic to molecular form for most molecular species occurs much deeper in the cloud than that for H to H_2. Therefore we have not included the effects of H_2 self-shielding. In our model the molecular hydrogen density remains constant in time. The main destruction process for H_2 is cosmic ray ionization ($\zeta = 2.0 \times 10^{-17}$ s^{-1}) and the main formation path is immediate H_2 formation when a hydrogen atom sticks to a grain.

B.2.2 Gas-Grain Interactions

B.2.2.1 Depletion and Binding

The rate of deposition of a molecule in the gas phase onto a grain surface is

$$k_{dep} = \pi a^2 \overline{v} S n_{gr} \ \ (s^{-1}). \tag{B.1}$$

where a is the grain radius, $\overline{v}$ is the mean thermal velocity, S is the sticking coefficient, and n_{gr} the space density of grains. We have used "classical" grains of

radius 1000 Å and space density $n_{gr} = 1.3 \times 10^{-12} \mathrm{n}(H_2)$ cm^{-3}. We have assumed a sticking coefficient of 1.0 for all neutral atoms and molecules except atomic and molecular hydrogen.

We have adopted the binding energy scheme of Hasegawa, Herbst & Leung (1992) who assumed that all molecules are physisorbed onto the surfaces of grains. The values chosen for binding energies are highly uncertain, since few have been measured in the laboratory and the binding surface may change as grains evolve. The choice of E_b is critical since the desorption processes are highly dependent on the binding energy.

B.2.2.2 Desorption

One of the more uncertain aspects of modeling gas-grain chemical interactions is determining the dominant mechanism that removes species from the mantles. Several studies have been performed, proposing many different desorption mechanisms (c.f. Leger, Jura, & Omont 1985, and Schutte & Greenberg 1991). To assess the effectiveness of different desorption mechanisms throughout the cloud, we have included three potentially important desorption mechanisms: thermal evaporation, cosmic ray induced heating, and direct photodesorption (see Section 2.2.2 in BLG).

B.2.3 One Dimensional Chemical Model

The coupled differential equations governing the gas-grain chemical evolution were solved using a variant of the Gear (1971) algorithm: LSODE (Hindmarsh 1980). This code, which is a linear implicit multistep method, utilized variable time step and error control techniques to preserve numerical accuracy during the integration. The adjustable variables for a given calculation are the space density of *molecular* hydrogen, n(H_2), the factor by which the UV radiation is enhanced, χ, the gas temperature, T_{gas}, the dust temperature, T_{dust}, and the visual extinction

to the center of the cloud, A_v. τ_V is the visual extinction proceeding from edge to center such that $\tau_V^{max} = A_V$.

A one dimensional cloud model was constructed by running a one dimensional time dependent calculation up to 10^7 yr with fixed physical conditions for a given visual extinction (see discussion of 1-D model in Chapter 6). For the initial conditions we use depleted elemental abundances based for the most part on observations in the diffuse cloud towards ζ Ophiuchi (Savage, Cardelli, and Sofia 1992, see also Graedel et al 1982). These abundances (Table 1 in BLG) represent moderate depletions (~ 0.2) for C, N, O, while the heavier metals are significantly depleted.

The one dimensional model of gas phase chemistry including grain depletion and desorption was run for a single cloud model, labeled the standard model, where physical parameters were kept constant throughout the cloud. The physical conditions of the standard model are n(H_2) = 10^4 cm^{-3}, T_{gas} = 20 K, T_{dust} = 10 K, and $\chi = 1.0$. The calculations included all desorption processes discussed earlier unless otherwise noted.

B.3 Time Dependence

To show the limiting case of total depletion we performed one calculation of standard model without cosmic ray desorption, similar to the results presented by Iglesias (1977) and Brown & Charnley (1990). This is presented in Figure B.1 for deep in the cloud (τ_V = 10.3 mag) where photoprocesses can be neglected. Thermal evaporation is therefore the only relevant desorption mechanism. Since at T_{dust} = 10 K the timescale for thermal evaporation is much greater than the depletion timescales, all molecules are seen to disappear from the gas phase at the characteristic depletion time of $\sim 10^6$ years. These results remain essentially unchanged for T_{dust} up to $\sim$ 20 K. A characteristic of most ion-molecule models in the gas phase is that O_2 and N_2 peak in the gas phase at much later times than

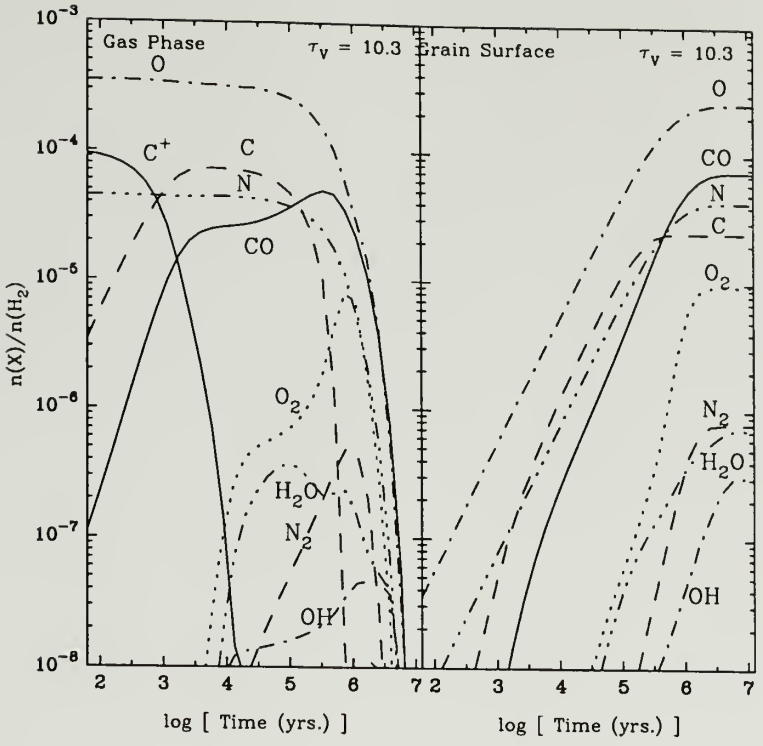

Figure B.1. Time evolution of gas phase and grain surface abundances for major reservoirs of carbon, oxygen, and nitrogen (abundances are relative to H_2). The physical conditions are for the standard model but thermal evaporation off of 10 K dust grains is the only desorption process.

CO, which quickly locks up most of the carbon (Graedel et al 1982, Langer and Graedel 1989). *Thus, the mantle composition reflects the gas phase abundances at earlier times and is dominated by atomic oxygen and CO. H_2O remains a trace species on the mantle where its fractional abundance remains below* 10^{-6}.

Our standard model includes all desorption processes and these modify the time dependent evolution significantly. The results are shown in Figure B.2 for species which represent the dominant reservoirs of carbon, oxygen, and nitrogen in the interior ($\tau_V = 10.3$ mag) and near the edge of the cloud ($\tau_V = 2.1$ mag). *The most striking feature in Figure B.2 is that deep in the cloud ($\tau_V = 10.3$ mag), the*

molecules, including highly polar H_2O, remain in the gas phase despite the high depletion rate . This is in contrast to Figure B.1 that indicated that all molecules disappear from the gas phase after $\simeq 10^6$ yr. The persistence of molecules in the gas phase at all times is due to cosmic ray desorption (discussed in section 2.2.2). The grain surface composition has been highly modified by the cosmic rays, which quickly remove the weakly bound atoms and allow formation of molecular oxygen and nitrogen in the gas phase. These species subsequently deplete onto the grain surface. Hence the composition of the molecular grain mantle is dominated by O_2 and CO, in contrast to the case excluding cosmic ray desorption where O and CO are the most abundant species present in the mantle.

We can examine these effects for various species more closely by comparing the timescales for depletion and desorption listed in Table B.1. Since the timescales for cosmic ray desorption are highly dependent on the binding energy, there exists a wide range of values: the strongly bound water molecule shows the cosmic ray desorption timescale, $t_{cr} > t_{dep}$, the depletion timescale. The intermediate binding of CO exhibits $t_{cr} \approx t_{dep}$, while the weakly bound carbon atom has $t_{cr} < t_{dep}$. In our model, the gas phase chemistry is strongly influenced by the desorption of atoms from the surface. *Since atoms have low binding energies, cosmic ray desorption rapidly removes the atoms from the surface allowing an active gas phase chemistry to continue for very long times.* In the work by Hasegawa & Herbst (1993) this effect is absent because the atoms are assumed to undergo rapid catalytic reactions on the grain surfaces processing them to molecules which have higher binding energies.

The lower panel in Figure B.2 shows the chemical evolution at $\tau_V \sim 2$ mag, where photoprocesses play a more important role. However, even at low extinctions, the process of cosmic ray desorption dominates over photodesorption. As an example, for CO $t_{cr} = 2.2 \times 10^6$ yr is less than the photodesorption

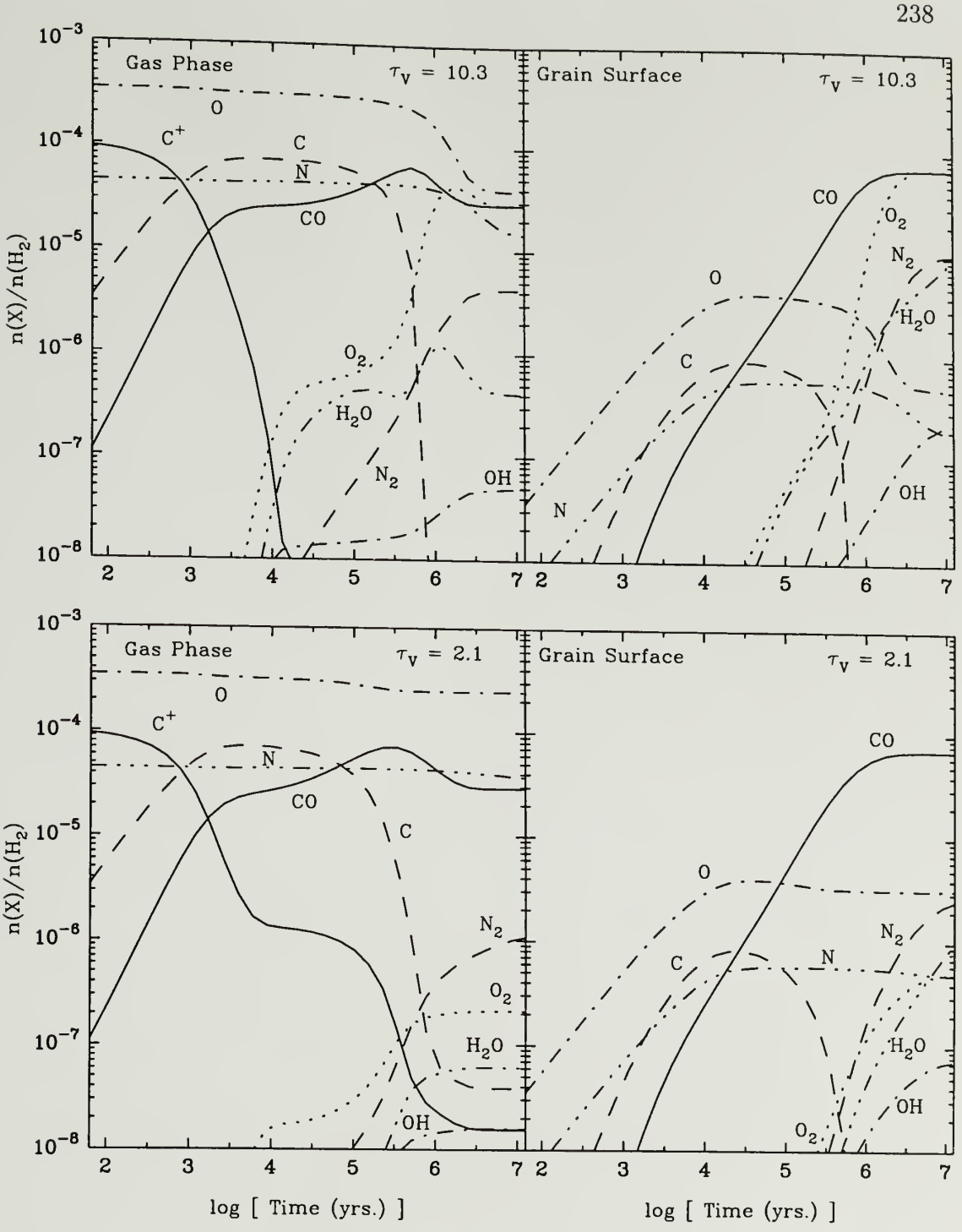

Figure B.2. Time evolution of gas phase and grain surface abundances (abundances are relative to H_2) for major reservoirs of carbon, oxygen, and nitrogen for the standard model at $\tau_V = 10.3$ mag (upper panel) and $\tau_V = 2.1$ mag (lower panel).

Table B.1. Relevant Timescales in yrs.[a]

Timescale	C	CO	H_2O
τ_{dep}^{b}	7.8(5)	8.6(5)	6.9(5)
$\tau_{ph}(A_v = 2.0)$	6.0(7)	6.0(7)	6.0(7)
τ_{cr}^{b}	7.4(3)	2.2(6)	1.3(10)

[a]Numbers are written in the form a(b) = a × 10^b.
[b]τ_{dep} and τ_{cr} calculated at n(H_2) = 10^4 cm^{-3}

timescale (at $\tau_V = 2.1$ mag) of 6.0×10^7 yr. The important mechanism at low extinctions is not photodesorption but photodestruction, which keeps the oxygen and nitrogen in atomic form. Cosmic ray grain surface desorption then maintains O and N in the gas phase, leaving the strongly self-shielded CO molecule and trace amounts of O, N_2 and H_2O on the grain mantles.

Thus, for molecular cores with densities near n(H_2) $\sim 10^4$ cm^{-3} cosmic ray desorption can play a significant role in removing molecules from the grain mantles both in the cloud interiors and in exterior regions. This examination therefore supports the conclusions of Leger et al (1985) and Willacy and Williams (1993) that cosmic-ray desorption allows an active chemistry, deep in the cloud, at times greater than the depletion timescale.

B.4 The Dependence of Molecular Depletion on Physical Conditions

Depletion is highly dependent on the physical conditions of the parent cloud. For example the depletion timescale presented in Table B.1 is inversely dependent on the density, as such, in GMC cores with n(H_2) $\sim 10^6$ cm^{-3} the depletion timescale is very short, $\tau_{dep} \sim 10^4$ yr. Therefore gas-grain interactions could play a dominant role in the chemical evolution, unless some mechanism can be found to remove molecules from the grain mantle. In this section we examine the dependence of depletion on the density and apply these results to observed molecular ice abundances. In the following paragraphs we will refer to depletion as defined by the percentage of the total abundance of a species (gas phase + surface

abundance) that is present on the grain surface. A molecule that shows a depletion of 90% will have 90% of the total abundance of that species on the grain surface and would be considered significantly depleted from the gas phase.

Observations along lines of sight towards field stars in Taurus by Whittet et al (1989) have revealed depletions on the order of 5 - 40%. These results are towards obscured stars that are presumably not associated with the cloud, it is likely that they are probing quiescent material. Thus we assume that a dust temperature of 10 K may be representative for the observations towards the most obscured stars which exhibit the highest depletions. With this assumption it is worthwhile to examine at what density our model agrees with the observed CO depletions, and whether at these densities millimeter observations may miss a significant fraction of molecular material.

To illustrate this, we plot in Figure B.3 the depletion as a function of density to examine at what density different molecules will be significantly depleted from the gas phase. This figure shows that both CO and O_2 are quickly depleted below a level of 50% by $n(H_2) = 3000$ cm^{-3}, while the highly bound species CN, HCN, and H_2O all show significant amounts of gas phase depletion for all densities. Thus for densities typical of GMC cores, $n(H_2) \sim 10^6$ cm^{-3}, almost all of the CN and HCN should reside solely on the grain surfaces. However, these results are uncertain, since the depletion of a given species is a strong function of the binding energy, and even a modest change in E_b (which are mostly unknown) will have a large effect.

Some binding energies have been measured in the laboratory for CO in an H_2O matrix (Sandford & Allamandola 1990) and CO in a pure CO matrix (Sandford & Allamandola 1988). We have used these binding energies to examine the interdependence of depletion and binding energy for the CO molecule. We present these results in Figure B.4, showing depletion as function of density and binding energy. The dashed line in the figure is the nominal depletion estimated by Whittet

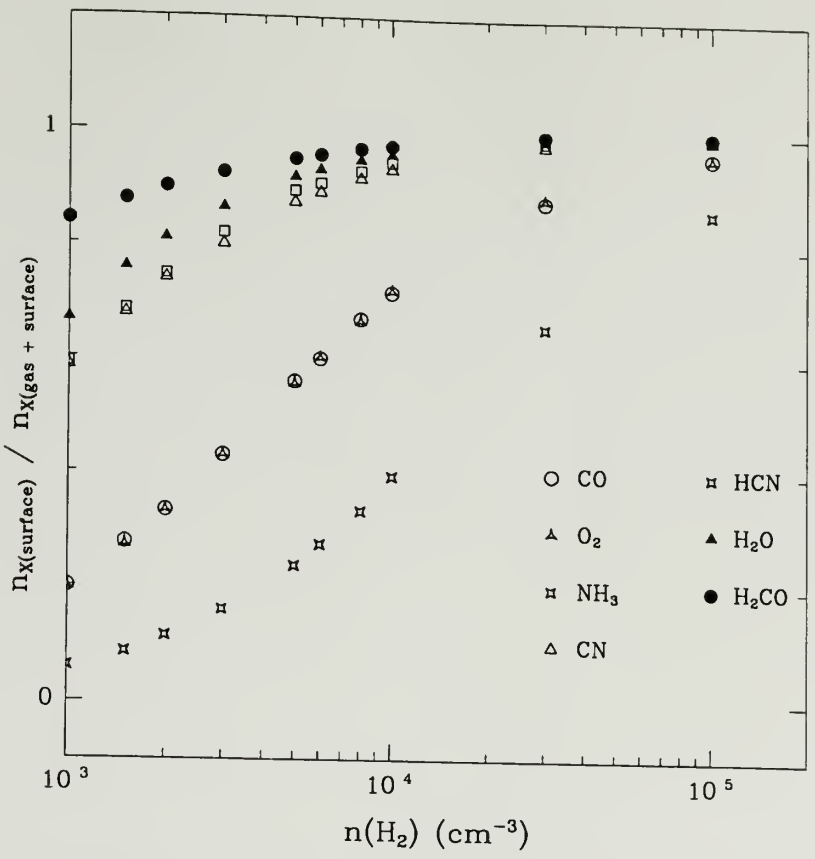

Figure B.3. Depletion from the gas phase for selected species as a function of density at 10^7 yr for $T_{dust} = 10$ K, $\chi = 1.0$, $T_{gas} = 20$ K. $n_{X(surface)}/n_{X(gas+surface)}$ is defined as 1 = 100 percent depletion.

et al (1989) in Taurus. The most striking feature in this figure is that the CO molecule is easily accreted and held on a water mantle. In fact, for all densities, the depletions of CO in a water mantle are much larger than observed. Our model thus suggests that the CO ice observed in molecular clouds must be binding in a mantle with a binding energy less than 1740 K. This conclusion is consistent with the observations of nonpolar and polar ice features, since CO is more abundant in the nonpolar layer which is not dominated by H_2O (Tielens et al 1991)

The binding of CO in the nonpolar mantle may also be inconsistent with the binding energies used in this work, which are for SiO_2 mantles. At high densities, even a binding energy for CO to an SiO_2 surface of $\sim$ 1200 K produces high depletion. It is somewhat hard to categorize the actual densities along these lines

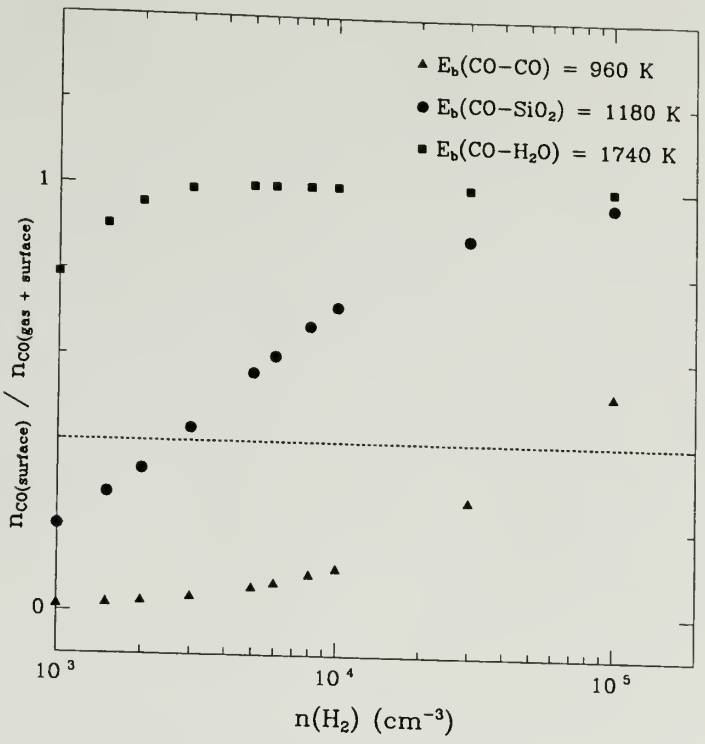

Figure B.4. Depletion of CO from the gas phase at 10^7 yr as a function of molecular hydrogen density for three different binding surfaces: CO binding on a pure CO surface, CO binding on a SiO_2 surface, and CO binding onto a water ice surface. $n_{CO(surface)}/n_{CO(gas+surface)}$ is defined as 1 = 100 percent depletion.

of sight, since space densities are difficult to infer from extinction measurements. However, various indications of the densities towards some of the field stars in Taurus are in the literature. Two of the stars in the survey by Whittet et al (1989), Elias 15 (A_V = 13.3 mag) and Elias 16 (A_V = 23.9 mag), are in portions of the Heiles' Cloud 2 mapped by Cernicharo, Guélin, & Askne (1984) in the $J = 1 \rightarrow 0$ transition of HCO^+ and its isotopic variant $H^{13}CO^+$. Both of these field stars are within the contours of the HCO^+ emission (the beam size is $\sim 5'$) and Elias 15 is coincident with a local maximum in the $H^{13}CO^+$ map. These observations thus suggest the densities are $>10^4$ cm^{-3}, since HCO^+ and in particular $H^{13}CO^+$ would be hard to excite at densities below this value.

If these densities are representative of the material where CO ice features are observed, then pure CO ice seems to best reproduce observations. For CO-CO

binding, depletions > 50% do not occur until $n(H_2) > 5 \times 10^4$ cm^{-3} which is not unrealistic for lines-of-sight with large extinction. In fact, for two sources listed in Table 4 the observations of the nonpolar component exhibit ice features consistent with pure CO ice. *If CO (or O_2) is the dominant component of the nonpolar ice then the binding energies for most species would be reduced to values that may allow a significant portion to remain in the gas phase, even at the high densities observed in GMC cores.* Of course these results are dependent on the desorption model and on the absence of competing reactions on the surface of the grain.

References

Allamandola, L. J., Sandford, S. A., Tielens, A. G. G. M., & Herbst, T. M. 1992, *ApJ*, **399**, 134.

Askne, J., Höglund, B., Hjalmarson, Å., & Irvine, W. M. 1984, *A&A*, **130**, 311.

Batrla, W., Wilson, T. L., Bastien, P., & Ruf, K. 1983, *A&A*, **128**, 279.

Bauer, A., Boucher, D., Burie, J., Demaison, J., & Dubrulle, A. 1979, *J. Phys. Chem. Ref. Data*, **8**, 537.

Beichmann, C. A., Becklin, E. E., & Wynn-Williams, C. G. 1979, *ApJ*, **232**, L47.

Bergin, E.A., Langer, W.D., & Goldsmith, P. F. 1995, *ApJ*, **441**, 222..

Bettins, R. P. A., Lee, H. -H., Herbst, E. 1995, *ApJ*, in press.

Bevington, P. R. & Robinson, D. K. 1992, *Data Reduction and Error Analysis for the Physical Sciences* (McGraw-Hill: New York).

Blake, G. A., Sutton, E. C., Masson, C. R., & Phillips, T. G. 1987, *ApJ*, **315**, 621.

Boreiko, R. T., Betz, A. L., & Zmuidzinas, J. 1988, *ApJ*, **325**, L47.

Brown, P. D., Charnley, S. B., & Millar, T. J. 1988, *MNRAS*, **231**, 409.

Brown, R. D., & Rice, E. H. N. 1986a, *MNRAS*, **223**, 423.

Brown, R. D., & Rice, E. H. N. 1986a, *MNRAS*, **223**, 405.

Burton, M. G., Hollenbach, D. J., & Tielens, A. G. G. M., 1991, *ApJ*, **365**, 620.

Carpenter, J. M., Snell, R. L., & Schloerb, F. P. 1995,*ApJ*, in press.

Castets, A., Duvert, G., Dutrey, A., Bally, J., Langer, W. D., & Wilson, R. W. 1990, *A&A*, **234**, 469.

Cazzoli, G. Corbelli, G., Degli Esposti, C., & Favero, P. G. 1985, *Chem. Phys. Letters*, **118**, 164.

Charnley, S.B., Dyson, J.E., Hartquist, T.W., & Williams, D.A. 1988a, *MNRAS*, **231**, 269.

Charnley, S.B., Dyson, J.E., Hartquist, T.W., & Williams, D.A. 1988b, *MNRAS*, **231**, 269.

Chiar, J. E., Whittet, D. C. B., Adamson, A. J., & Kerr, T. H. 1995, *BAAS*, **26**, 1459.

Chieze, J.-P., Pineau des Forêts, G., & Herbst, E. 1991, *ApJ*, **373**, 110.

Churchwell, E., & Hollis, J. M. 1983, *ApJ*, **272**, 591.

Colomé C., & Harvey, P. M. 1995, *ApJ*, in press.

Cuhna, K & Lambert, D. L. 1992, *ApJ*, **399**, 586.

Cummins, S. E., Green, S., Thaddeus, P., & Linke, R. A. 1983, *ApJ*, **266**, 331.

Cummins, S. E., Linke, R. A., & Thaddeus, P. 1986, *ApJS*, **60**, 819.

Elmegreen, B. G., Kimura, T., Tosa, M. 1995, IBM Research Report #RC 20035 (88269).

Erickson, N. R., Goldsmith, P. F., Novak, G., Grosslein, R. M., Viscuso, P. J., Erickson, R. B., & Predmore, C. R. 1992, *IEEE Trans Microwave Theory Tech*, **40**, 1.

Falgarone, E., Puget, J. L., & Perault, M. 1992, *A&A*, **257**, 715.

Felli, M., Churchwell, E., & Massi, M. 1984, *A&A*, **136**, 53.

Flower, D. R., Le Bourlot, J., Pineau des Forêts, & Roueff, E. 1994, *A&A*, **282**, 225.

Frerking, M. A., Langer, W. D., & Wilson, R. W. 1982, *ApJ*, **262**, 590.

Fuente, A., Martin-Pintado, J., Cernicharo, J., & Bachiller, R. 1993, *A&A*, **276**, 473.

Fuente, A., Cernicharo, J., Garcia-Burillo, S., & Tejero, J. 1993, *A&A*, **275**, 558.

Fuller, G. A., & Myers P. C. 1993, *ApJ*, **418**, 273.

Gatley, I., Becklin, E. E., Sellgren, K., & Werner, M. W. 1979, *ApJ*, **233**, 575.

Gear, C. W. 1971, *Numerical Initial Value Problems in Ordinary Differential Equations*, (Englewood Cliffs, N.J.: Prentice-Hall).

Genzel, R., Reid, M. J., Moran, J. M., & Downes, D. 1981, *ApJ*, **296**, 766.

Genzel, R., & Stutzki, J. 1989, *ARA&A*, **27**, 41.

Goldsmith, P. F. 1995, *The Clumpy Structure of Molecular Clouds*, in Festschrift for C. H. Townes, R. X. Chiao, ed. (AIP).

Goldsmith, P. F., Bergin, E. A., & Lis D. C. 1995, *ApJ*, in preparation.

Goldsmith, P.F., Margulis, M., Snell, R.L., & Fukui, Y. 1992, *ApJ*, **385**, 522.

Goldsmith, P.F. 1991, in IAU Symp. No. 147, Fragmentation of Molecular Clouds and Star Formation, ed. E. Falgarone, F. Boulanger, & G. Duvert, (Dordrecht: Kluwer), 177.

Goldsmith, P.F., Snell, R.L., Hasegawa, T., & Ukita, N. 1987, *ApJ*, **314**, 525.

Goldsmith, P. F., Irvine, W. M., Hjalmarson, Å, & Elldér. J. 1986, *ApJ*, **310**, 383.

Goldsmith, P.F., Langer, W.D., & Wilson, R.W. 1986, *ApJ*, **303**, L11.

Goldsmith, P.F., Irvine, W.M., Hjalmarson, Å., & Elldér, J. 1986a, *ApJ*, **310**, 383.

Goldsmith, P. F., Snell, R. L., Deguchi, S., & Krotkov, R. 1982, *ApJ*, **260**, 147.

Goldsmith, P. F., Arquilla, R., Schloerb, F. P., & Scoville, N. Z. 1982 in Regions of Recent Star Formation, eds. R. S. Roger & P. E. Dewdney (Dordrecht: D. Reidel), 295.

Goldsmith, P. F., Langer, W. D., Schloerb, P. F., & Scoville, N. Z. 1980, *ApJ*, **240**, 524.

Goldsmith, P. F., Langer, W. D. 1978, *ApJ*, **222**, 881.

Graedel, T. E., Langer, W. D., & Frerking, M. A. 1982, *ApJS*, **48**, 321.

Greaves, J. S., & White, G. J. 1992, *MNRAS*, **259**, 457.

Greaves, J. S., White, G. J., & Williams, P. G. 1992, *A&A*, **257**, 731.

Green, S. 1994, *ApJ*, **434**, 188.

Green, S. 1986, *ApJ*, **309**, 331.

Green, S. 1975, *ApJ*, **201**, 366.

Green, S., & Chapman S. 1978, *ApJ*, **37**, 169.

Green, S., & Thaddeus, P. 1974, *ApJ*, **191**, 653.

Grim, R.J.A., Baas, F., Geballe, T.R., Greenberg, J.M., & Schutte, W. 1991, *A&A*, **243**, 473.

Güsten, R., Chini, R., & Neckel, T. 1984, *A&A*, **138**, 205.

Güsten, R., & Fiebig, D. 1988, *A&A*, **204**, 253.

Harris, A. I., Stutzki, J., Genzel, R., Lugten, J. B., Stacey, G. J., & Jaffe, D. T. 1987, *ApJ*, **322**, L49.

Hasegawa, T. I., Herbst, E., & Leung, C. M. 1992, *ApJS*, **82**, 167.

Hayashi, S. S., Hasegawa, T., & Kaifu, N. 1988, *ApJ*, **332**, 354.

Herbst, E. & Leung, C. M. 1989, *ApJS*, **69**, 271.

Herbst, E. 1983, *ApJ Suppl. Ser.*, **53**, 41.

Heyer, M. H., Morgan, J., Schloerb, F. P., Snell, R. L., & Goldsmith, P. F. 1992, *ApJ*, **395**, L99.

Hindmarsh, A. C. 1980, *ACM SIGNUM Newsletter*, **15**, 10.

Ho, P. T. P., & Townes, C. H. 1983, *ARA&A*, **21**, 239.

Hobson, M. P., Jenness, T., Padman, R., & Scott, P. F. 1994, *MNRAS*, **266**, 972.

Hogerheijde, M. R., Jansen, D. J., & van Dishoeck, E. F. 1995, *A&A*, in press.

Hollenbach, D. J., Takahashi, T., & Tielens, A. G. G. M. 1991, *ApJ*, **377**, 192.

Hughes, V. A., & Wouterloot, J. G. A. 1984, *ApJ*, **276**, 204.

Icke, V., Gatley, I., & Israel, F. P. 1980, *ApJ*, **236**, 808.

Iglesias, E. 1977, *ApJ*, **218**, 697.

Irvine, W. M., Goldsmith, P. F., & Hjalmarson, Å. 1987, in Interstellar Processes, eds. D. J. Hollenbach & H. A. Thronson, Jr. (Dordrecht: D. Reidel), 561.

Keene, J. 1995, in Proc. of the 2nd Cologne-Zermatt Symposium, in press.

Keene, J., Hildebrand, R. H., & Whitcomb, S. E. 1982, *ApJ*, **252**, L11.

Kleinmann, D. E., & Wright, E. L. 1973, *ApJ*, **185**, L131.

Kuiper, T. B. H., Kuiper, E. N., Dickinson, D. F., Turner, B. E., & Zuckerman, B. 1984, *ApJ*, **276**, 211.

Kutner, M. L., & Ulich, B. L. 1981, *ApJ*, **250**, 341.

Lada, C. J., Lada, E. A., Clemens, D. P., & Bally, J. 1994, *ApJ*, **429**, 694.

Langer, W. D., Velusamy, T., Kuiper, T. B. H., Leven, S., & Olsen, E. 1995, *ApJ*, in press.

Langer, W. D., & Graedel, T. E. 1989, *ApJS*, **69**, 241.

Langer, W. D., Graedel, T. E., Frerking, M. A., & Armentrout, P. B. 1984, *ApJ*, **277**, 581.

Le Bourlot, J., Pineau des Forêts, G., & Roueff, E. 1995, *A&A*, **297**, 251.

Leung, C. M., Herbst, E., & Huebner, W. F. 1984, *ApJS*, **56**, 231.

Loren, R. B., & Mundy, L. G. 1984, *ApJ*, **286**, 232.

Mangum, J. G., Wooten A., Loren, R. B., & E. J. Wadiak 1990, *ApJ*, **348**, 542.

Mangum, J. G., Wootten, A., & Plambeck, R. L. 1993, *ApJ*, **409**, 282.

Martin, H. M., Sanders, D. B., & Hills, R. E. 1984, *MNRAS*, **208**, 35.

Masson, C. R. & Mundy, L. G. 1988, *ApJ*, **324**, 538.

McKee, C.F. 1989, *ApJ*, **345**, 782.

McMullin, J. P., Mundy, L. G., & Blake, G. A. 1993, *ApJ*, **405**, 599.

Meixner, M., Haas, M. R., Tielens, A. G. G. M., Erickson, E. F., & Werner, M. W. 1992, *ApJ*, **390**, 499.

Meixner, M. & Tielens, A. G. G. M. 1993, *ApJ*, **405**, 216.

Menten, K. M., Walmsley, C. M., Henkel, C., & Wilson, T. L. 1988, *A&A*, **198**, 253.

Mezger, P. G., Wink, J. E., & Zylka, R. 1990, *A&A*, **228**, 95.

Millar, T. J., Rawlings, J. M. C., Bennet, A., Brown, P. D., & Charnley, S. B. 1991, *A&A Suppl Ser*, **87**, 585.

Millar, T. J., Herbst, E., & Charnely S. D. 1991, *ApJ*, **369**, 147.

Millar, T. J., Leung, C. M., & Herbst, E. 1987, *A&A*, **183**, 109.

Millar, T. J., & Freeman, A. 1984, *MNRAS*, **207**, 405.

Mittaz, J. P. D., Penston, M. V., & SNijders, M. A. J. 1990, *MNRAS*, **242**, 370.

Moriarty-Schieven, G. H., Snell, R. L., & Hughes, V. A. 1991, *ApJ*, **374**, 69.

Morris, M., Turner, B. E., Palmer, P., & Zuckerman, B. 1976, *ApJ*, **205**, 82.

Morris, M., Snell, R. L., & Vanden Bout, P. A. 1977, *ApJ*, **216**, 728.

Mundy, L. G., Evans, N. J., Snell, R. L., & Goldsmith, P. F. 1987, *ApJ*, **318**, 392.

Mundy, L. G., Scoville, N. Z., Baath, L. B., Masson, C. R., & Woody, D. P. 1986, *ApJ*, **304**, L51.

Norman, C. & Silk, J. 1980, *ApJ*, **238**, 138.

Ohishi, M., Irvine, W. M., Kaifu, N. 1992, in *Astrochemistry of Cosmic Phenomena*, IAU Sym. 150, ed P.D. Singh (Dordrecht: Kluwer), 561.

Padman, R., Scott, P. F., Vizard, D. R., & Webster A. S. 1985, *MNRAS*, **214**, 251.

Perault, M., Falgarone, E., & Puget, J. L. 1985, *A&A*, **152**, 371.

Phillips, J. P., & Mampaso, A. 1991, *A&A Suppl. Ser.*, **88**, 189.

Phillips, T. G., & Huggins, P. J. 1982, *ApJ*, **251**, 533.

Phillips, T. G., Knapp, G. R., Huggins, P. J., Werner, M. W., Wannier, P. G., Neugebauer, G., & Ennis, D. 1981, *ApJ*, **245**, 512.

Pineau des Forêts, G. , Roueff,, E., & Flower, D. R. 1992, *MNRAS*, **258**, 45P.

Prasad, S.S., Tarafdar, S.P., Villere, K.R., & Huntress, W.T., Jr. 1987, in *Interstellar Processes*, ed. D.J. Hollenbach and H.A. Thronson, Jr., (Dordrecht: Kluwer), 631.

Prasad, S. S., & Huntress, W. T., Jr 1980a, *ApJS*, **43**, 1.

Prasad, S. S., & Huntress, W. T., Jr 1980b, *ApJ*, **239**, 151.

Roberge, W. G., Jones, D., Lepp, S., & Dalgarno, A. 1991, *ApJS*, **77**, 287.

Rodriguez-France, A., Martin-Pintado, J., Gomez-Gonzalez, J. & Planesas, P. 1992, *A&A*, **264**, 592.

Rodriguez, L. F., Ho P. T. P., & Moran, J. M. 1980, *ApJ*, **240**, L149.

Sandford, S. A., & Allamandola, L. J. 1993, *ApJ*, **417**, 815.

Sandford, S. A., Allamandola, L. J., Tielens, A. G. G. M., & Valero, G. J. 1988, *ApJ*, **329**, 498.

Sargent, A. I. 1977, *ApJ*, **218**, 736.

Savage, B. D., Cardelli, J. A., & Sofia, U. J. 1992, *ApJ*, **401**, 706.

Schloerb, F. P., Snell, R. L., & Young, J. S. 1983, *ApJ*, **267**, 163.

Schloerb, F. P., Goldsmith, P. F., & Scoville, N. Z. 1982, in Regions of Recent Star Formation, eds. R. S. Roger & P. E. Dewdney (Dordrecht: D. Reidel), 439

Schutte, W. A., & Greenberg, J. M. 1991, *244*, **190**,

. Scoville, N. Z., & Kwan, J. 1976, *ApJ*, **206**, 718.

Sellgren, K., Smith, R. G., & Brooke, T. Y. 1994, *ApJ*, **433**, 179.

Simon, T., & Joyce, R. R. 1983, *ApJ*, **265**, 864.

Sims, I. R. Queffelec, , J.-L., Defacnce, A., Rebrion-Rowe, C., Travers, D., Rowe, B. R., & Smith, I. W. M. 1992, *J. Chem. Phys*, **97**, 8798.

Sims, I. R. Queffelec, , J.-L., Defacnce, A., Rowe, B. R., Herbert, L., Karthauser, J., & Smith, I. W. M. 1993, *J. Chem. Phys*, **100**, 4229.

Sims, I. R. Queffelec, , J.-L., Defacnce, A., Rebrion-Rowe, C., Travers, D., Rowe, B. R., & Smith, I. W. M. 1994a, *J. Chem. Phys*, **100**, 4229.

Sims, I. R., Smith, I. W. M., Bocherel, P., DeFrance, A., Tavers, D., & Rowe, B. 1994b, *J. Chemi. Soc. Faraday Trans*, **90**, 1473.

Skatrud, D. D., De Lucia, F. C., Blake, G. A., & Sastry, K. V. L. N. 1983, *J. Mol. Spec.*, **99**, 35.

Snell, R. L., Erickson, N. R., Goldsmith, P. F., Ulich, B. L., Lada, C. J., Martin, R. N., & Schulz, A. 1986, *ApJ*, **304**, 780.

Snell, R. L., Scoville, N. Z., Sanders, D. B., & Erickson, N. R. 1984, *ApJ*, **284**, 176.

Snell, R. L. 1981, *ApJS*, **45**, 121.

Snell, R. L., Mundy, L. G., Goldsmith, P. F., Evans, N. J., & Erikson, N. R. 1984, *ApJ*, **276**, 625.

Sorrell, W. H. 1992, *Comm. Astrophys.*, **16**, 123.

Stacey, G. J., Jaffe, D. T., Geis, N., Harris, A. I., Poglitsch, A., Stutzki, J., & Townes, C. H. 1993, *ApJ*, **404**, 219.

Staude, H. J., & Elsasser H. 1993, *A&ARev*, **5**, 165.

Stutzki, J., & Güsten, R. 1990, *ApJ*, **356**, 513.

Stutzki, J., Stacey, G. J., Genzel, R., Harris, A. I., Jaffe, D. T., & Lugten, J. B. 1988, *ApJ*, **332**, 379.

Sutton, E. C., Blake, G. A., Genzel, R., Masson, C. R., & Philips, T. G. 1986, *ApJ*, **311**, 921.

Swade, D.A. 1989a, *ApJ Suppl.*, **71**, 219.

Swade, D.A. 1989b, *ApJ*, **345**, 828.

Swade, D.A., & Schloerb, P.F. 1992, *ApJ*, **392**, 543.

Tauber, J. A., Lis, D. C., Keene, J., Schilke, P., & Buttgenbach, T. H. 1995, *A&A*, **297**, 567.

Tauber, J. A., Tielens, A. G. G. M., Meixner, M., & Goldsmith P. F. 1994, *ApJ*, **422**, 136.

Tauber, J. A., & Goldsmith, P. F. 1990, *ApJ*, **356**, L63.

Taylor, D. K. 1989, PhD Thesis, University of Massachusetts.

Taylor, D. K. & Dickman, R. L. 1989, *ApJ*, **341**, 293.

Tielens, A. G. G. M., Tokunaga, A. T., Geballe, T. R., & Bass, F. 1991, *ApJ*, **381**, 181.

Tielens, A. G. G. M., & Hollenbach D. 1985a, *ApJ*, **291**, 722.

Tielens, A. G. G. M., & Hollenbach D. 1985b, *ApJ*, **291**, 747.

Townes, C. H. & Schawlow, A. L. 1955, Microwave Spectroscopy (New York: Dover)

Turner, B.E., & Thaddeus, P. 1977, *ApJ*, **211**, 755.

Turner, B. E., & Gammon, R. H. 1975, *ApJ*, **198**, 71.

Ungerechts, H., Bergin, E. A., Goldsmith, P. F., Irvine, W. M., Schloerb, F. P., & Snell, R. L. 1993a, in Proceedings of the Zermatt Symposium, in press.

Ungerechts, H., Bergin, E. A., Goldsmith, P. F., Irvine, W. M., Schloerb, F. P., & Snell, R. L. 1995, in preparation.

Ungerechts, H., Bergin, E. A., Carpenter, J., Goldsmith, P. F., Irvine, W. M., Lovell, A., McGonagle, D., Schloerb, F. P., & Snell, R. L. 1992, in The Astrochemistry of Cosmic Phenomena, ed. P.D. Singh (IAU Symposium 150), 271.

van Dishoeck, E.F., Blake, G.A., Draine, B.T., & Lunine, J.I. 1991, in *Protostars and Planets III*, ed. E.H. Levy, J.I. Lunine, and M.S. Matthews, (Tuscon: University of Arizona Press).

van Dishoeck, E. F. & Black, J. H. 1988, *ApJ*, **334**, 771.

Vanden Bout, P. A., Loren, R. B., Snell, R. L., & Wooten, A. 1983, *ApJ*, **271**, 161.

Vialla, Y. P. 1986, *A&AS*, **64**, 391.

Vogel, S.N., Genzel, R., & Palmer, P. 1987, *ApJ*, **316**, 243.

Walmsley, C. M., & Ungerechts, H. 1983, *A&A*, **122**, 164 .

Wang, T. Y., Wouterloot, J. G. A., & Wilson, T. L. 1993, *A&A*, **277**, 205.

Wang, Y., Jaffe, D. T., Evans, N. J., Hayashi, M., Tatematsu, K., & Zhou, S. 1993, *ApJ*, **419**, 707.

Weliachew, T. Emerson, D. T., Foreveille, T., Beijing, J. H., Wright, M. C. H., Ellder, J. 1985, *A&A*, **153**, 139.

Werner, M. W. 1982, in Symposium on the Orion Nebula to Honor Henry Draper, eds. A.E. Glassgold, P.J. Huggins, & E.L. Schucking, eds. Ann. NY Acad. Sci., 395, 79.

White, G. J., & Sandell G. 1995, *A&A*, submitted.

Whittet, D. C. B. 1993, in *Dust and Chemistry in Astronomy*, eds. T. J. Millar & D. A. Williams, (Bristol: Institute of Physics), 9.

Willacy, K., & Williams, D. A. 1993, *MNRAS*, **260**, 635.

Williams, D. A. 1993, in *Dust and Chemistry in Astronomy*, eds. T. J. Millar & D. A. Williams, (Institute of Physics Publishing: Bristol), 143.

Williams, D. A. & Hartquist, T. W. 1984, *MNRAS*, **210**, 141.

Wilner D. J., Wright, M. C. H., & Plambeck R. L. 1994, *ApJ*, **422**, 642.

Xie, T., Allen, M., & Langer, W. D. 1995, *ApJ*, **440**, 674.

Zhou, S., Evans, N. R., Gusten, R., Mundy, L. G., & Kutner, M. L. 1991, *ApJ*, **372**, 518.

Zhou, S., Evans, N.J., II, & Mundy, L.G. 1990, *ApJ*, **372**, 518.

Ziurys, L. M., Martin, R. N., Pauls, T. A., & Wilson, T. L. 1980, *A&A*, **104**, 288.

Zuckerman, B. 1973, *ApJ*, **183**, 863.